

Adsorbed films of methyl halides on magnesium oxide and boron nitride

Dissertation
zur Erlangung des Doktorgrades
der Mathematisch-Naturwissenschaftlichen Fakultät
der Christian-Albrechts-Universität
zu Kiel

vorgelegt von
Michael Sprung

Kiel
2001

Referent:.....

Koreferenten:.....

.....

Tag der mündlichen Prüfung:.....

Zum Druck genehmigt: Kiel,.....

Dekan

Abstract:

This thesis presents a systematic study of the behavior of adsorbed films of three methyl halides (CH_3Cl , CH_3Br and CH_3I) on boron nitride and magnesium oxide. The thermodynamic and structural properties were investigated using two experimental techniques, volumetric adsorption isotherms and x-ray powder diffraction. The results of these investigations are compared to the ones obtained with graphite as substrate. Knorr presented a good summary of the graphite studies [Kno92].

The study of thin adsorbed films composed of polar molecules is motivated by a search for electrostatic ordering phenomena in two dimensions (2D). The methyl halides are a group of polar methane derivatives that allow a systematic variation of two important parameters, molecular size and dipole moment. While the majority of previous physisorption investigations used graphite as a substrate (e.g. [Tho69]), the situation has changed recently because the availability of high quality powders of MgO and BN has increased (e.g. [Kun01]). The use of MgO makes it also possible to compare results of adsorbed films under the influence of different surface geometries.

Adsorption isotherms have been used to study properties of adsorbed films for many years. This technique is used to gather information about the substrate (e.g. the surface area and the quality of the powder) and the adsorbate (e.g. molecular adsorption areas and wetting behavior). While only the molecular adsorption areas of the methyl halides on BN were determined, the studies of methyl halides on MgO are more detailed. It is shown that CH_3Cl and CH_3Br on MgO grow in up to two distinct layers and exhibit triple point wetting. The onset temperatures for the second layer are determined for both adsorbates and a possible dewetting transition is predicted for CH_3Cl near 100K. On the other side, the adsorption isotherms of CH_3I show no evidence for the appearance of a second layer or triple point wetting.

X-ray and/or neutron powder diffraction are powerful tools for investigating the structural properties of 3D objects. These methods can also be used to investigate thin, almost 2D matter (i.e. adsorbed films). The theory for the powder diffraction from layered (nominally 2D) matter was originally proposed by Warren [War41]. He showed that the diffracted signal from a layered solid has a characteristic lineshape, often referred to as the ‘*Warren profile*’.

As noted above, the monolayer structures of CH_3Cl , CH_3Br and CH_3I have been investigated using high quality powders of BN and MgO. This thesis proposes solutions for structures of all three methyl halides on BN. These structures are similar to the ones observed on graphite. The situation is more complex if MgO is used as substrate. Methyl chloride and methyl bromide exhibit similar diffraction profiles. Both contain features that can be related to a disordered (liquid-like?) phase and a 2D solid. For CH_3I two phases, a disordered phase and a commensurate 2D solid, coexist below 147K. The unit cell of the solid phase is rectangular and centered and contains 12 molecules.

Kurzfassung:

Im Rahmen dieser Arbeit wurde eine systematische Untersuchung zum Verhalten von adsorbierten Filmen dreier Methylhalogenide (CH_3Cl , CH_3Br and CH_3I) auf Magnesiumoxid und Bornitrid durchgeführt. Volumetrische Adsorptionsisothermen und Röntgenpulverdiffraktion wurden als experimentelle Methoden eingesetzt, um thermodynamische und strukturelle Informationen zu gewinnen. Die Resultate dieser Untersuchungen werden mit Messungen verglichen, bei denen Graphit als Substrat eingesetzt wurde [Kno92].

Die Motivation zur Untersuchung von dünnen adsorbierten Filmen polarer Moleküle ist in der Suche nach elektrostatischer Ordnung in zwei Dimensionen begründet. Die Methylhalogenide sind polare Derivate des Methans, die es ermöglichen zwei wichtige Parameter, Molekülgröße und Dipolmoment, systematisch zu verändern. Im Gegensatz zu früheren Untersuchungen dieser Art, die sich auf den Einsatz von Graphite als Substrate beschränken mußten (e.g. [Tho69]), ist es nun möglich geworden, MgO und BN als Substrate zu nutzen (z.B. [Kun01]). Durch den Einsatz von MgO ist es möglich geworden, Vergleiche des Adsorptionsverhalten unter dem Einfluß verschiedener Oberflächengeometrien zu ziehen.

Adsorptionsisothermen werden seit langer Zeit genutzt, um die Eigenschaften adsorbierter Filme zu untersuchen. Sie erlauben es, Informationen über das Substrat (z.B. die Oberfläche und die Qualität des Pulvers) und das Adsorbat (z.B. die molekulare Adsorptionsfläche oder das Benetzungsverhalten) zu gewinnen. Im Gegensatz zu den Messungen auf BN, bei denen nur die molekulare Adsorptionsfläche bestimmt wurde, sind die Messungen mit MgO als Substrat detailreicher. CH_3Cl und CH_3Br auf MgO wachsen in bis zu zwei Lagen auf und zeigen Anzeichen für vollständige Benetzung am Tripelpunkt. Die Temperaturen, oberhalb derer sich eine zweite Lage bildet, konnten für beide Adsorbate bestimmt werden. Zusätzlich wird für CH_3Cl die Möglichkeit eines Entnetzungsphasenüberganges vorhergesagt. Methyljodid zeigt keine Anzeichen einer zweiten Lage oder vollständiger Benetzung.

Röntgen- und Neutronenpulverdiffraktion sind geeignete Untersuchungsmethoden, um strukturelle Eigenschaften dreidimensionaler Objekte zu studieren. Sie können aber auch genutzt werden, um dünne, fast zweidimensionale Filme zu untersuchen. Warren begründete die Pulverdiffraktionstheorie dieser Filme und zeigte, dass das Diffraktionssignal einer festen zweidimensionalen Phase durch eine charakteristische Profilform, das 'Warren Profil', ausgezeichnet ist [War41]. Diese Arbeit präsentiert Strukturvorschläge für CH_3Cl , CH_3Br und CH_3I auf BN. Diese Monolagenstrukturen weisen starke Ähnlichkeiten zu denjenigen auf Graphitoberflächen auf. CH_3Cl und CH_3Br auf MgO zeigen Anzeichen einer ungeordneten und einer geordneten, kommensurablen Phase. Die feste Phase des Methyljodid formt eine rechtwinklige, zentrierte Einheitszelle, die kommensurabel mit dem MgO Substrat ist. Sie enthält 12 Moleküle, deren Positionen mit Simulationsrechnungen bestimmt wurden.

Contents:

1. Introduction	1
2. Theory	5
2.1 X-ray powder diffraction of 2D systems	5
2.1.1 Introduction of the Schildberg algorithm	8
2.1.2 The powder averaging function $P(u, \theta_{\text{Mos}})$	10
2.1.3 The intensity distribution function $J(Q, u, \omega)$	12
2.1.4 The \bar{Q} -dependent structure factor $S(Q, u, \omega)$	13
2.2 Thermodynamic study of physisorbed films	16
2.2.1 Models of adsorption processes	18
2.2.2 The 2D compressibility K_{2D}	23
2.2.3 The isosteric heat of adsorption Q_{st}	24
2.3 Commensurability	25
3. Experimental Setup	27
3.1 Thermodynamic experiments	27
3.2 X-ray powder diffraction experiments	30
3.2.1 X-ray diffraction cell	31
3.2.2 The beamline X7B at the NSLS	32
3.2.3 X-ray image plate detector systems	33
3.2.4 Xenon on graphite: A test experiment	36
3.3 The adsorbates	40
3.3.1 Chloromethane	41
3.3.2 Bromomethane	42
3.3.3 Iodomethane	43
3.4 The substrates	43
3.4.1 Boron nitride	44
3.4.2 Magnesium oxide	46

4. Thermodynamic measurements	51
4.1 Adsorption isotherms on magnesium oxide	52
4.1.1 Methyl chloride on magnesium oxide	52
4.1.2 Methyl bromide on magnesium oxide	61
4.1.3 Methyl iodide on magnesium oxide	65
4.2 Adsorption isotherms on boron nitride	67
4.2.1 Monolayer capacities of methyl halides on boron nitride	67
4.2.2 Methyl chloride on boron nitride	69
5. Structural investigations	71
5.1 Methyl halides on graphite: A summary	71
5.1.1 Methyl chloride	72
5.1.2 Methyl bromide	73
5.1.3 Methyl iodide	73
5.2 Methyl halides on boron nitride	74
5.2.1 Methyl iodide on BN	74
5.2.2 Methyl bromide on BN	84
5.2.3 Methyl chloride on BN	88
5.3 Methyl halides on magnesium oxide	92
5.3.1 Methyl iodide on MgO	93
5.3.2 Methyl bromide and methyl chloride on MgO	111
6. Summary and interpretation	119
Appendixes	127
References	131
Lebenslauf	149
Eidesstattliche Versicherung	151
Danksagung/Acknowledgements	153

Chapter 1

Introduction

The adsorption of gas on the surface of materials is a long known phenomenon. In the late 18th century Fontana und Scheele tried adsorption experiments on charcoal [Ger82]. While there are a multitude of reasons why the adsorption of gases is an important and interesting topic, two come to mind immediately. First, it provides framework and methodology for measuring the surface area of a powdered or porous material. This is an important parameter in many technological areas, e.g. powders exhibiting large surface areas are used as filters in smoke stakes to reduce the excess gases and the catalytic properties of powders often scale with this area. Secondly, adsorbate systems can be used as models to study and understand the behavior of thin (almost) two-dimensional (2D) matter.

At the beginning of the 20th century many theories concerning adsorption were being developed. It was shown that translational long-range order is limited in 2D (e.g. [Pei34], [Pei35], [Lan37]) and (statistically and thermodynamically) models for different types of adsorption behavior were proposed (keywords are e.g. Henry's law, van der Waals isotherm or BET isotherm). Brunauer developed a system to classify isotherms [Bru45]. He found that a set of five different types could be used to classify all the isotherms of different shape that had been observed. Frenkel, Halsey and Hill (FHH) demonstrated that it is possible to study wetting behavior using volumetric adsorption isotherm. Summaries of these early works can be found e.g. in the book of Young '*Physical Adsorption of gases*' [You62] or in the book '*Films on solid surfaces*' by Dash [Das75].

However, only after the availability of uniform high-quality substrates was it possible to explore the rich variety of phases in thin adsorbed films. Thomy and Duval [Tho69] used adsorption isotherms to study rare gases and methane physically adsorbed on Grafoil, a crystalline exfoliated graphite material produced by Union Carbide. This groundbreaking series of experiments led to new interest to experimentally and theoretically study adsorption phenomena. Graphite proved to be an almost ideal substrate for these investigations. It was easy to handle, relatively inert and easy to keep clean. Furthermore, it exhibited a large surface to volume ratio and the relatively small scattering cross section made structural investigations of adsorbed films using powder diffraction techniques possible. Multiple overview articles of

studies on graphite are available today (e.g. [Bir86], [Sin87], [Shr92] or [Tho94]). While studies on graphite blossomed, it took more than a decade before other substrates, which exhibited a different surface geometry, of comparable quality became available, e.g. MgO [Das78]. Coulomb, Sullivan and Vilches [Cou84] performed adsorption experiments on highly uniform ‘smoke’ MgO powders similar in quality to those by Thomy and Duval [Tho69] and more recently the group of Aldo Migone started to study adsorbed films on BN [Alk91]. Nevertheless, the difficulties involved in the sample preparation and handling have kept the number of studies on these powdered materials small compared to the number of graphite studies.

The study of thin adsorbed films has revealed many interesting phenomena. A few of these should be mentioned here. A theory that received much attention was that by Kosterlitz and Thouless who proposed that a 2D solid phase could melt continuously [Kos73]. Experimental evidence for this theory was found e.g. on the system ethane on graphite [Gay85]. Kosterlitz, Thouless, and later Halperin, Nelson and Young (KTHNY) suggested also that the melting of a 2D solid might be a two-step process ([Kos73], [Hal78] and [You79]). Here the transition from 2D solid to 2D liquid takes place via an intermediate phase (designated as a ‘*hexatic*’ phase for a six-fold solid). This new type of state exhibits short-range spatial order but long-range bond directed order. In addition to melting, wetting theories were also developed (e.g. [Pan83], [Git84]) and transitions between commensurate and incommensurate solid phases were observed. More recent information on this topic can be found e.g. in a book by Bruch, Cole and Zaremba [Bru97] or in the ‘*Handbook of surface science*’ [Ein96], [Suz96].

The development of a new process to produce large quantities of high quality powders of pure and doped metal oxides [Kun01] enabled the Materials Chemistry group at BNL to study adsorbed films on MgO. For example, extensive studies were performed concerning the properties of CH₄ on MgO using adsorption isotherm techniques and elastic and inelastic neutron diffraction (e.g. [Lar98], [Fre00]). The behavior of ammonia films was investigated on MgO [Joh99] and graphite [Lar97]. The latter displayed an interesting anomalous wetting behavior. But also questions were studied such as ‘*Why do vertical steps reappear in adsorption isotherms?*’ [Phi93].

Starting with the dissertations of Degenhardt [Deg88] and Schildberg [Sch89] multiple systems of adsorbed films have been studied using x-ray and neutron diffraction experiments in Kiel. The behavior of methyl chloride and tetramethyl metals (M(CH₃)₄, M=Sn, Ge and Pb) was studied on graphite ([Opp92], [Gri94], [Sue95] and [Str98]). In addition, several contributions to the diffraction theory of 2D systems were developed [Sch89], [Str97].

The methyl halides are a group of polar derivatives of methane. Studies involving adsorbed films of these molecules on graphite have been performed and a summary of these results is available [Kno92]. The driving force behind the study of adsorbed films of polar molecules is to gain information of 2D electrostatic ordering. The methyl halides are a good

match for this purpose because both the molecular size and dipole moment varies within this group of molecules.

This thesis undertook a systematic investigation of structural properties and thermodynamics of adsorbed films of methyl halides on MgO and BN. It concentrated on the behavior of three adsorbates (CH_3R , $\text{R}=\text{Cl}$, Br and I) under the influence of substrates with different surface geometry. The goal was to make comparisons with the results already gained on graphite.

While BN is similar to graphite, the (100) surface of MgO crystals is different. Both, graphite and BN are layered materials with a hexagonal structure in the plane. The in-plane unit cell of BN is about 2% larger than the one of graphite. This structural similarity is why it is expected that many structural properties of adsorbed films will be similar, too. However, if distinct changes in the structure are observed, they are probably related to the small difference between the in-plane lattice constants, even though the differences in the interaction between the adsorbed molecule and the substrate surface atoms should not be excluded.

Investigating adsorbed films of these polar molecules on MgO has several interesting aspects. The ionic character of the MgO introduces an interesting aspect into the interaction between adsorbate and substrate. The four-fold character of the MgO (100) surface offers strong contrast to the hexagonal surfaces of graphite and BN. And finally, the study of polar molecules might provide additional information important for understanding the more complex surface interactions of gases such as SO_x and NO_x , where the catalytic properties of MgO play a significant role.

Two experimental techniques were utilized to study methyl halides adsorbed films on MgO and BN. Volumetric adsorption isotherms were used to determine the adsorption areas of the substrate, the molecular areas of the adsorbate and some thermodynamic quantities of the adsorbed system such as the isosteric heat of adsorption and the 2D compressibility. In addition, layering transitions and the wetting behavior near the triple point were investigated for CH_3Cl on MgO and BN and for CH_3Br and CH_3I on MgO.

X-ray powder diffraction was used to determine the structural properties of monolayers of methyl halides adsorbed on both substrates. The use of an image plate detector system was employed for the first time in studies of adsorbed films at the NSLS. Temperature and coverage dependent measurements are undertaken to investigate the monolayer structures of CH_3Cl , CH_3Br and CH_3I on MgO and BN.

This thesis is divided into six chapters. Besides this brief introduction, they are structured in the following way:

- The second chapter provides a short theoretical background of properties of 2D systems. It develops a mathematical algorithm subsequently used to analyze the structure of adsorbed films with x-ray or neutron powder diffraction. In addition, it is shown

which thermodynamic quantities can be obtained using volumetric isotherms and what other information (e.g. molecular areas of the adsorbed species, phase transitions and wetting behavior) is accessible. Some thoughts are given to the influence of the adsorbate-substrate interaction. Here, the terms commensurate and incommensurate are introduced and discussed.

- The next chapter describes the experimental equipment and setups used to investigate the adsorption properties. It discusses the sample environment used to study adsorption isotherms and the x-ray powder diffraction (XPD) setup at X7B of the NSLS in detail. A comprised set of information is also presented describing the adsorbate-substrate systems that were investigated.
- The thermodynamic investigations are summarized in Chapter 4. Extensive adsorption isotherm studies of the three methyl halides on the (100) surface of magnesium oxide are presented along with information concerning the thermodynamic properties of films adsorbed on the hexagonal basal plane of boron nitrate.
- Chapter 5 discusses measurements of the structural properties of adsorbed films of methyl halides. It starts by summarizing the known structures of methyl halides on graphite. Then, the structures of these methyl halides on boron nitrate are described, followed by investigations of the structures of the methyl halides on the (100) surface of magnesium oxide.
- A summary and interpretation of the results of this thesis follows. Finally, the closing remarks include some interesting questions that remain unanswered and possibilities for future studies are discussed.

Chapter 2:

Theory

The combination of thermodynamic measurements with structural probes like x-ray or neutron diffraction to investigate adsorbed films provides insight into adsorbate-adsorbate and adsorbate-substrate interactions. This chapter presents a theoretical background to understand the x-ray scattering and thermodynamic behavior of films of methyl halides adsorbed on boron nitrate and magnesium oxide.

2.1 X-ray powder diffraction of 2D systems

X-Ray Powder Diffraction (XPD) is a powerful tool to investigate structural properties of materials. The theory is well developed for 3D systems and detailed summaries are widely available (e.g. [War69], [Gui94]). Conceptually, the experimental process is straightforward: A monochromatic beam hits a powder sample composed of a large number of small crystallites with random orientations. This beam is then diffracted from the crystal planes (characterized by sets of the Miller indices h, k, l) of individual particles resulting in diffracted intensity distributed on cones of angle $2\theta_{hkl}$ around the incident beam direction (Fig. 2.1).

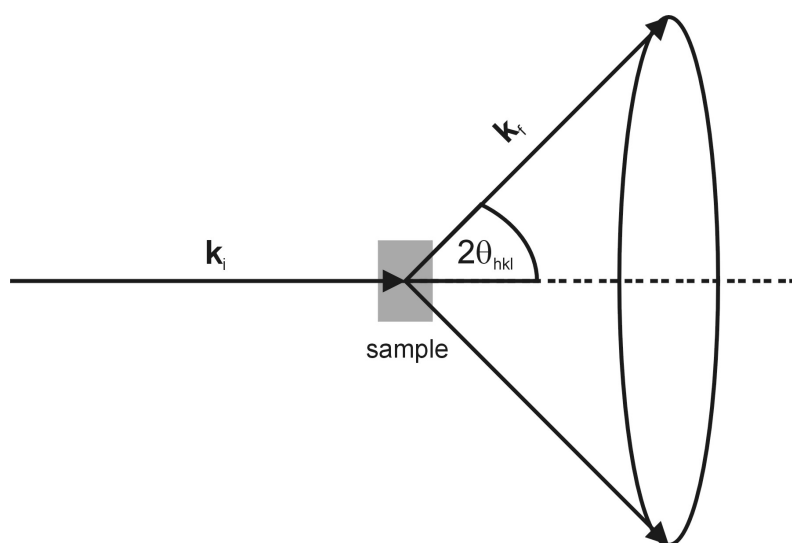


Figure 2.1: Schematic view of the diffraction from a sample consisting of many small crystallites.

Before the mathematical formalism appropriate to describe the powder diffraction from 2D systems is developed, it is worth mentioning two problems that are frequently encountered in XPD experiments. First, sometimes the intensity scattered from different crystal planes (i.e. planes of different sets of hkl) is distributed over (nearly) the same cone because the scattering derives from planes that are separated by (almost) the same distances. This results in overlap of reflections. Second, a non-uniform distribution of the scattered intensity around the cones can be observed if the powder particles have a preferred orientation. For example, this effect is sometimes observed if powders consisting of plate like crystals (like some graphite modifications) are used.

Furthermore, geometrical effects introduced by the experimental setup, the Lorentz polarization factor or the Debye-Waller factor also influence the behavior of $I(Q)$. These effects are very similar to the effects observed for 3D samples and more information can be found in the monographs mentioned earlier [War69], [Gui94].

The diffracted signal from a very thin (almost 2D) film differs significantly from the signal recorded from a bulk (3D) sample. The basis for this distinction derives from the fact that only two Laue or Bragg conditions need to be satisfied. This results in a reciprocal space composed of a lattice of rods (not spots as in the case of 3D systems). Thus, the diffracted intensity of one crystallite is no longer localized in a spot on the diffracted cone; instead it is distributed onto tangents. The integration of the intensity from the cone leads to a characteristic Q -dependant lineshape, the ‘Warren profile’ [War41]. Figures 2.2 and 2.3 illustrate this graphically.

The theory of the diffraction of 2D systems has evolved since Warren’s first description. Methods for including preferred orientation and multilayer effects have been derived [Kje76], [Tau77]. Dutta and Sinha proposed an analytic form of the structure factor of a two-dimensional lattice [Dut81]. Using this information, the paper by Stephens et al. [Ste84] discusses the use of a modified intensity distribution function (a sum of a Gaussian and Lorentzian, instead a Gaussian only [War41]) and effects of domain structures. Schildberg and Lauter used a more mathematical approach to include the effects of preferred orientation and developed equations for calculating the intensity distribution functions containing Gaussian, Lorentzian and Lorentzian Squared components and then used these to incorporate a \vec{Q} -dependence into the structure factor calculations for unit cells containing two atoms [Sch88], [Sch89]. Strzelczyk et al. extended the structure factor calculations for unit cells containing more than two atoms [Str97], [Str98].

The analysis of the diffraction data proceeded along the lines of the approach from Schildberg and Lauter, but it was found that certain approximations, especially in the implementation of the \vec{Q} -dependent structure factor, could lead to results that were unable to reproduce the experimental data; e.g. when a short coherence length and a large unit cell are combined.

Figure 2.2: In 2D the discrete diffraction spots normally distributed around the Ewald's surface are depicted into tangents (2D-rods). The intensity as a function of Q is obtained by integrating around α . In a real system, the rods have a finite width and an intensity distribution, which varies perpendicularly across them. This intensity distribution function is often approximated using Gaussian, Lorentzian and Lorentzian square functions.

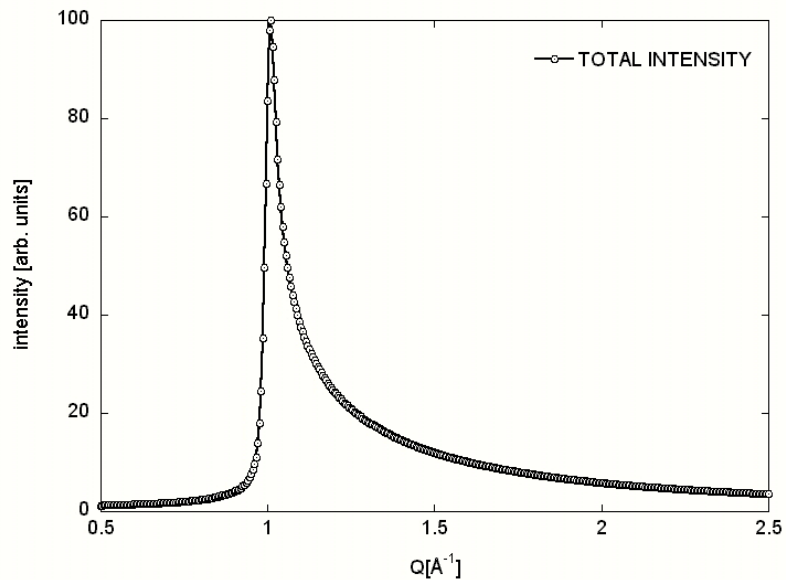
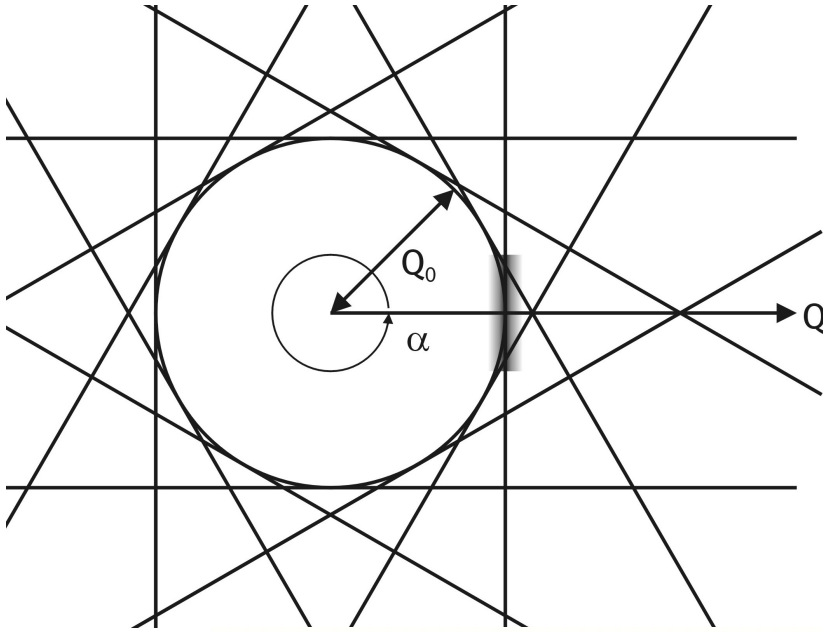


Figure 2.3: Characteristic ('Warren') lineshape after integrating over α at $Q_0 = 1 \text{ \AA}^{-1}$ of a 2D structure with a coherence length of $L_G = L_L = L_S = 250 \text{ \AA}$ and an intensity distribution function consisting of equal parts ($p_G = p_L = p_S$) of Gaussian, Lorentzian and Lorentzian Square functions (see Equations 2.8 and 2.27). An isotropic powder average was used.

For this reason the algorithm employed by Schildberg and Lauter was extended. This approach avoids some of the difficulties they encountered. The following sections describe the mathematical formalism used to describe the powder diffraction of 2D systems.

First, it gives an introduction into Schildberg's approach [Sch88]. It starts with a description of the coordinate system and derives some properties of the scattering vector \vec{Q} , before it addresses how to solve the Q-dependent intensity distribution problem for 2D systems. The second part concentrates on developing a new powder averaging function. The third section presents expressions for describing the intensity distribution functions. Finally, the problem of implementing the \vec{Q} -dependent structure factor into these calculations is discussed.

2.1.1 Introduction of the Schildberg algorithm:

Only a very brief overview is given in this section, since it follows closely the description presented by Schildberg and Lauter [Sch88]. The following definitions are normally made to describe an (elastic) diffraction experiment:

$$\vec{k}_i: \text{Incoming wavevector} \quad |\vec{k}_i| = 2\pi / \lambda \quad \lambda: \text{Wavelength} \quad 2.1$$

$$\vec{k}_f: \text{Outgoing wavevector} \quad |\vec{k}_i| = |\vec{k}_f| \quad 2.2$$

$$\vec{Q}: \text{Scattering vector} \quad \vec{Q} = \vec{k}_i - \vec{k}_f \quad 2.3$$

a) The coordinate system

A Cartesian coordinate system is defined such that the x-axis is parallel to the scattering vector \vec{Q} , and the wavevectors, \vec{k}_i and \vec{k}_f , are lying in the xy-plane. A graphical view of this coordinate system is given in figure 2.4.

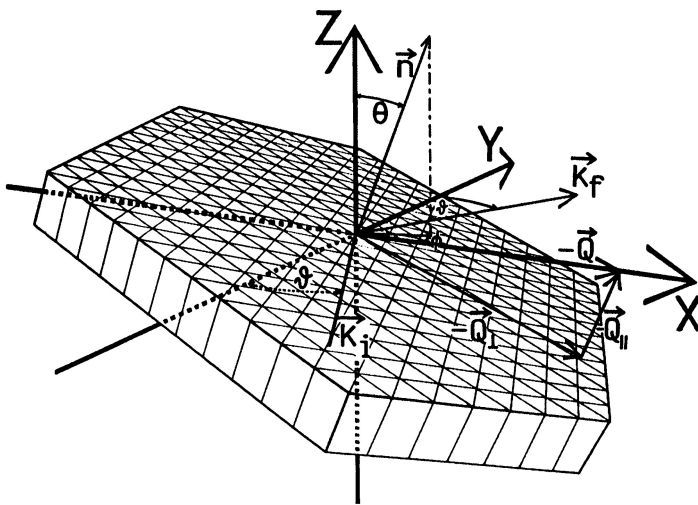


Figure 2.4: Schematic view of the coordinate system [Sch88]. The scattering vector \vec{Q} is parallel to the x-axis and the wavevectors, \vec{k}_i and \vec{k}_f , are in the xy-plane. A unit vector $\vec{n}(\theta, \varphi)$ normal to the surface describes the orientation of the crystal.

The orientation of a crystallite is described using a unit vector, \vec{n} , normal to the crystal surface using the spherical coordinates θ and φ , where $0 \leq \theta \leq \pi$ and $0 \leq \varphi \leq 2\pi$. In a Cartesian coordinate system this vector is given by:

$$\vec{n}(\theta, \varphi) = (\sin \theta \cos \varphi, \sin \theta \sin \varphi, \cos \theta) \quad 2.4$$

b) Properties of the scattering vector \vec{Q}

i) In this geometry, where the detector is positioned in the xy-plane, only the part of the scattering vector $\vec{Q} = (Q, 0, 0)$ perpendicular to \vec{n} , \vec{Q}_\perp , contributes to the scattered intensity since the Bragg rods are parallel to \vec{n} . After substituting a dimensionless quantity $u(\theta, \varphi) = \sqrt{\cos^2 \theta + \sin^2 \theta \sin^2 \varphi}$, with $0 \leq u \leq 1$, the modulus of \vec{Q}_\perp is found to be:

$$Q_\perp = u Q \quad 2.5$$

ii) If a Cartesian coordinate system (x' , y' and z') is defined for each lattice vector \vec{Q}_0 (one for each combination of hkl) and the angle $-\pi/2 \leq \omega \leq \pi/2$ enclosed between \vec{Q}_0 and \vec{Q}_\perp describes the rotation of the crystal plane around \vec{n} , then the scattering vector \vec{Q} is defined as:

$$\vec{Q}(Q, u, \omega) = Q \begin{pmatrix} +u \cos \omega \\ -u \sin \omega \\ \sqrt{1-u^2} \end{pmatrix} \quad 2.6$$

iii) The square of the difference vector between a lattice vector \vec{Q}_0 and \vec{Q}_\perp as a function of ω and u can be approximated for $-\pi/2 \leq \omega \leq \pi/2$ by:

$$\begin{aligned} (\vec{Q}_\perp(Q, u, \omega) - \vec{Q}_0)^2 &= u^2 Q^2 + Q_0^2 - 2uQQ_0 \cos \omega \\ &\approx u^2 Q^2 + Q_0^2 - 2uQQ_0 \cdot \left(1 - \frac{4}{\pi^2} \omega^2\right) = (uQ - Q_0)^2 + \frac{8}{\pi^2} uQQ_0 \omega^2 \end{aligned} \quad 2.7$$

The used approximation for $\cos \omega$ has the advantage that it is exact for $\omega = 0, \pm \pi/2$ and it is positive for all other values of ω .

c) The intensity distribution $I(Q)$

The goal is to model the scattered intensity $I(Q)$ for one 2D reflection within this coordinate system. To achieve this, the intensity diffracted from all crystallites has to be integrated. Both, the orientation of all particles described by the normal vector \vec{n} and the orientation of the crystal plane around \vec{n} have to be considered. This leads to a double integral over u and ω [Sch88]:

$$I(Q) = \int_{u=0}^1 P(u, \theta_{Mos}) \cdot \int_{\omega=-\pi/2}^{\pi/2} |S(Q, u, \omega)|^2 J(Q, u, \omega) d\omega du \quad 2.8$$

This equation introduces the three functions $P(u, \theta_{Mos})$, $S(Q, u, \omega)$ and $J(Q, u, \omega)$. The powder averaging function $P(u, \theta_{Mos})$ is used to describe the powder particle distribution (e.g. effects of preferred orientation are included). The square of the modulus of the structure factor $S(Q, u, \omega)$ describes how the distribution of the molecules within the unit cell (including the Q -dependent atomic form factors for x-rays) contributes to the scattered intensity. Finally, the function $J(Q, u, \omega)$ describes how the intensity is distributed across the Bragg rods (here, parameters such as the coherence length are included).

In the following sections, these three functions are described in more detail and formulas useful for solving equation 2.8 are derived.

2.1.2 The powder averaging function $P(u, \theta_{Mos})$

Since a powder sample consists of many small crystallites, a powder averaging function $P(u, \theta_{Mos})$ has to be developed to account for the diffraction signal from these particles. Often a 'real' powder is best described as a combination of an isotropic part (P_I) and a component with preferred orientation (P_A). This leads to the following expression using p to describe the isotropic fraction of the powder:

$$P(u, \theta_{Mos}) = p P_I(u) + (1 - p) P_A(u, \theta_{Mos}) \quad 2.9$$

The normalized powder averaging function for an isotropic powder $P_I(u)$ is given in equation 2.10 (it was derived solving Equation 2.12 without the Gaussian distribution function) [Sch88]:

$$P_I(u) = \frac{u}{\sqrt{1 - u^2}} \quad 2.10$$

In the case of a powder with a preferred orientation, it is possible to find an average particle direction and to describe the orientation of a single crystallite with respect to this average direction by a tilt angle θ . The distribution of the preferred ordered particles $D(\theta)$ is often described by a Gaussian function:

$$D(\theta) = \exp\left(-\left(4 \ln 2\right) \frac{\theta^2}{\theta_{Mos}^2}\right) \quad 2.11$$

Where θ_{Mos} is defined as FWHM of this Gaussian distribution function. In order to derive the powder averaging for a powder with preferred orientation described by $D(\theta)$, the following equation has to be solved [Sch88]:

$$P_A(u, \theta_{Mos}) = N(\theta_{Mos}) \frac{u}{\sqrt{1-u^2}} \int_{\theta=\arccos(u)}^{\pi/2} d\theta \frac{\sin(\theta)}{\sqrt{u^2 - \cos^2(\theta)}} \exp\left(- (4 \ln 2) \frac{\theta^2}{\theta_{Mos}^2}\right) \quad 2.12$$

The integration over the spherical coordinates, $0 \leq \theta \leq \pi$ and $0 \leq \varphi \leq 2\pi$, was performed by substituting the dimensionless quantity $u(\theta, \varphi) = \sqrt{\cos^2 \theta + \sin^2 \theta \sin^2 \varphi}$ with the limits $0 \leq u \leq 1$ (see figure 2.5).

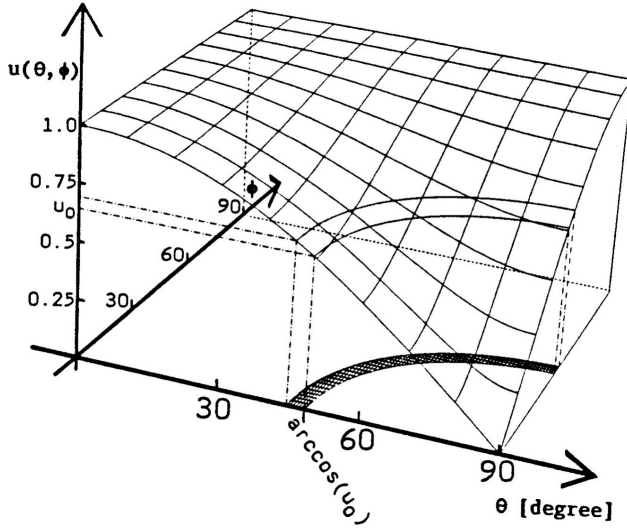


Figure 2.5: Graph of the quantity $u(\theta, \varphi) = \sqrt{\cos^2 \theta + \sin^2 \theta \sin^2 \varphi}$ to visualize how the integration limits for equation 2.12 were developed [Sch88].

The function $N(\theta_{Mos})$ normalizes the integral of $P_A(u, \theta_{Mos})$ over u from $0 \leq u \leq 1$. Equation 2.12 solvable by substituting $x = \arccos(u^{-1} \cos \theta)$ and using the approximation:

$$\arccos^2(u \cos(x)) = \arccos^2(u) + \left(1 - \frac{4}{\pi^2} \arccos^2(u)\right) x^2 \quad 2.13$$

This leads to the following function:

$$P_A(u, \theta_{Mos}) = N(\theta_{Mos}) \frac{\sqrt{\pi}}{2} \frac{u}{\sqrt{1-u^2}} \exp\left(-4 \ln 2 \frac{\arccos^2(u)}{\theta_{Mos}^2}\right) \cdot \sqrt{\frac{\theta_{Mos}^2}{4 \ln 2 \left(1 - \frac{4}{\pi^2} \arccos^2(u)\right)}} \operatorname{erf}\left(\frac{\pi}{2} \sqrt{\frac{4 \ln 2 \left(1 - \frac{4}{\pi^2} \arccos^2(u)\right)}{\theta_{Mos}^2}}\right) \quad 2.14$$

Although the error function $\operatorname{erf}(x)$ is itself an integral, Equation 2.14 can still be implemented into equation 2.8 using the approximation of an inverse polynomial function for $\operatorname{erf}(x)$ (see e.g. ‘Handbook of mathematical functions’, [Abr72]).

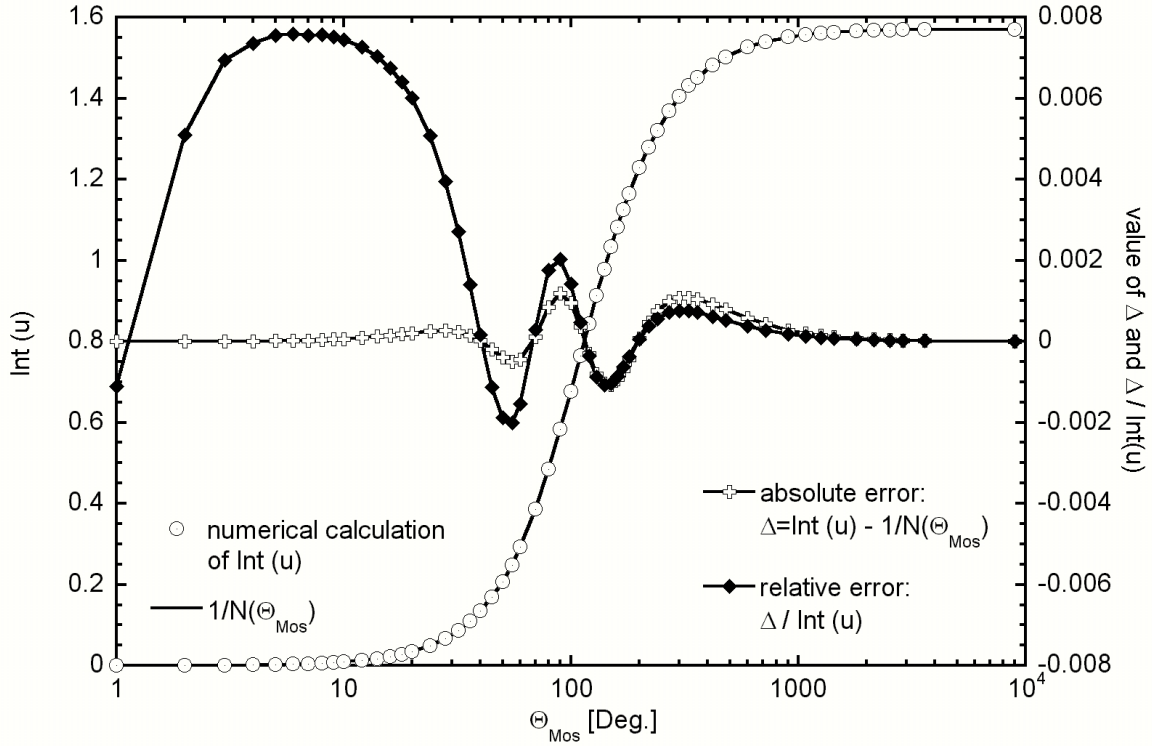


Figure 2.6: Numerical calculation of $Int(u)$ (circles) and the normalization function $N(\theta_{Mos})$ (Equation 2.15) for different values of θ_{Mos} . In addition, the absolute (crosses) and the relative error (rhombuses) are shown using the right y-scale.

The integral of Equation 2.14 over u from $0 \leq u \leq 1$ ($Int(u) = \int_{u=0}^1 du P_A(u, \theta_{mos}) / N(\theta_{mos})$) has been numerically calculated for many values of θ_{Mos} and it was found that it could be normalized by expressing $N(\theta_{Mos})$ as a sum of a Gaussian and a Lorentzian function for all values of θ_{Mos} (see Figure 2.6):

$$N(\theta_{Mos}) = \left(\frac{\pi}{2} \left[1 + 0.2834598 \exp\left(-\frac{\theta_{Mos}^2}{0.91723^2}\right) - \frac{1.2834593}{1 + 0.40190 \theta_{Mos}^2} \right] \right)^{-1} \quad 2.15$$

2.1.3 The intensity distribution function $J(Q, u, \omega)$

The distribution of scattered intensity at each 2D reflection is related to factors such as the crystal sizes and other imperfections of the substrate and the extend of the spatial ‘long range’ order of the two-dimensional systems [Pei34], [Pei36] and [Lan37]. The intensity distribution across a Bragg rod has been described as a sum of Gaussian (G), Lorentzian (L) and Lorentzian Square (S) functions (e.g. [War41], [Ste84] and [Sch88]):

$$J(Q, u, \omega) = p_G \cdot J_G(Q, u, \omega) + p_L \cdot J_L(Q, u, \omega) + (1 - p_G - p_L) \cdot J_S(Q, u, \omega) \quad 2.16$$

$$J_G(Q, u, \omega) = \frac{1}{\pi} \cdot A_G \cdot \exp\left(-A_G \cdot \left(\bar{Q}_\perp(Q, u, \omega) - \bar{Q}_0\right)^2\right) \quad 2.17$$

$$J_L(Q, u, \omega) = \frac{1}{\pi} \cdot \frac{A_L}{\ln(1 + A_L \cdot Q_{max}^2)} \cdot \frac{1}{1 + A_L \cdot \left(\bar{Q}_\perp(Q, u, \omega) - \bar{Q}_0\right)^2} \quad 2.18$$

$$J_S(Q, u, \omega) = \frac{1}{\pi} \cdot A_S \cdot \frac{1}{\left(1 + A_S \cdot \left(\bar{Q}_\perp(Q, u, \omega) - \bar{Q}_0\right)^2\right)^2} \quad 2.19$$

Equations 2.17 and 2.19 are normalized in two dimensions (u, ω). However, for the Lorentzian function (2.18) only a quasi normalization can be performed, because the integral diverges. Here, the normalization is performed using the factor $1/\ln(1 + A_L \cdot Q_{max}^2)$, where Q_{max} stands for the upper integration limit. The variables A_G , A_L and A_S are related to the coherence lengths L_G , L_L and L_S of the 2D film:

$$A_G = \frac{L_G^2}{\pi^2} \cdot \ln 2 \quad A_L = \frac{L_L^2}{\pi^2} \quad A_S = \frac{L_S^2}{\pi^2} \cdot (\sqrt{2} - 1) \quad 2.20$$

For convenience, the Q and u dependent functions $C_{G, L, S}$ and $D_{L, S}$ are introduced:

$$C_{G, L, S} = \frac{8}{\pi^2} \cdot A_{G, L, S} \cdot u Q Q_0 \quad 2.21$$

$$D_{L, S} = 1 + A_{L, S} \cdot (uQ - Q_0)^2 \quad 2.22$$

2.1.4 The \bar{Q} -dependent structure factor $S(Q, u, \omega)$

Whereas the position of a reflection can be calculated from the unit cell dimensions, the arrangement of the molecules within the unit cell determines the intensity of a reflection. The molecule configuration is included in the structure factor $S(Q, u, \omega)$. If a unit cell is considered that contains NM molecules with NA atoms, then the \bar{Q} -dependent structure factor can be written as [War69]:

$$S(Q, u, \omega) = \sum_{i=1}^{NM} \sum_{j=1}^{NA} f_j(Q) \exp\left(-i \bar{Q}(Q, u, \omega) \cdot \vec{r}_{ij}\right) \quad 2.23$$

The (for x-rays Q -dependent) atomic form factors f_j are tabulated (e.g. [Int74]) and can be easily included into the calculations. For neutron powder diffraction data, the coherent scattering lengths of the atoms have to be used. The modulus of the square of the structure factor can be calculated as:

$$\begin{aligned}
|S(Q, u, \omega)|^2 &= \text{Re}^2(S) + \text{Im}^2(S) \\
&= \left(\sum_{i=1}^{NM} \sum_{j=1}^{NA} f_j(Q) \cos(\vec{Q}(Q, u, \omega) \cdot \vec{r}_{ij}) \right)^2 \\
&\quad + \left(\sum_{i=1}^{NM} \sum_{j=1}^{NA} f_j(Q) \sin(\vec{Q}(Q, u, \omega) \cdot \vec{r}_{ij}) \right)^2 \\
&= \sum_{i=1}^{NM} \sum_{j=1}^{NA} \sum_{k=1}^{NM} \sum_{l=1}^{NA} f_j(Q) f_l(Q) \cos \left(\frac{u Q (\Delta x_{ijkl} \cos \omega - \Delta y_{ijkl} \sin \omega)}{+\sqrt{1-u^2} Q \Delta z_{ijkl}} \right)
\end{aligned} \tag{2.24}$$

The following abbreviations were used in Equation 2.24. The vector \vec{r}_{ij} marks the position of atom j of molecule i and Δx_{ijkl} , Δy_{ijkl} and Δz_{ijkl} are the distances between the atom j of molecule i and atom l of molecule k along the x-axis, y-axis and z-axis.

$$\begin{aligned}
\vec{r}_{ij} &= \begin{pmatrix} x_{ij} \\ y_{ij} \\ z_{ij} \end{pmatrix} & \Delta x_{ijkl} &= x_{ij} - x_{kl} \\
& & \Delta y_{ijkl} &= y_{ij} - y_{kl} \\
& & \Delta z_{ijkl} &= z_{ij} - z_{kl}
\end{aligned} \tag{2.25}$$

Equation 2.8 requires solving the integral over ω , $Int(\omega)$:

$$Int(\omega) = \int_{\omega=-\pi/2}^{\pi/2} |S(Q, u, \omega)|^2 \cdot J(Q, u, \omega) \cdot d\omega \tag{2.26}$$

Therefore the ω -dependence of $|S(Q, u, \omega)|^2$ is investigated in more detail. Only the cosine term in Equation 2.24 is ω dependent and the part $\sqrt{1-u^2} Q \Delta z_{ijkl}$ is a phase shift in ω . The effect of the other part $u Q (\Delta x_{ijkl} \cos \omega - \Delta y_{ijkl} \sin \omega)$ is more complex (Figure 2.7).

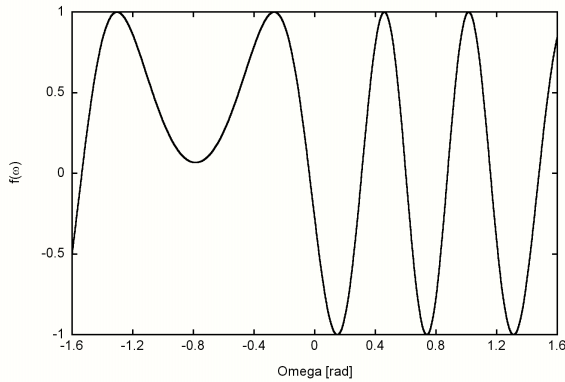


Figure 2.7: Sample graph of the behavior of ω of the cosine term in Equation 2.24

$$f(\omega) = \cos \left(\frac{+u Q \Delta x_{ijkl} \cos \omega - u Q \Delta y_{ijkl} \sin \omega}{+\sqrt{1-u^2} Q \Delta z_{ijkl}} \right)$$

For this plot $u = 0.9$, $Q = 3.0 \text{ \AA}^{-1}$ and $\Delta x_{ijkl} = 3.0 \text{ \AA}$, $\Delta y_{ijkl} = 3.0 \text{ \AA}$, $\Delta z_{ijkl} = 2.0 \text{ \AA}$ were used.

The Figure 2.7 shows that this cosine term can become oscillatory. This behavior makes it unlikely that an analytic expression for $Int(\omega)$ can be found. Furthermore, a simple quadratic Taylor expansion of the structure factor around $\omega=0$ that was used in the original Schildberg algorithm is only able to describe this behavior in a very narrow interval in ω .

Nevertheless, in certain cases, it may be possible to solve $Int(\omega)$, if the \bar{Q} -dependence of the structure factor is only weakly ω dependent. An example for such a case is the investigation of a solid phase, where the coherence length is large and the unit cell is small. Then the modulus of $S(Q,u,\omega)$ can be approximated by $S(Q,u,\omega=0)$ and be removed from the ω integral, since equations 2.17-2.19 peak sharply at $\omega=0$ for long coherence lengths and fall off to zero at other values of ω . In these cases, $Int(\omega)$ is solvable and the result is given by equation 2.27.

$$\begin{aligned}
 Int_{\omega}(Q,u) &= \int_{\omega=-\pi/2}^{\pi/2} J(Q,u,\omega) \cdot d\omega & 2.27 \\
 &= p_G \cdot \frac{1}{\pi} \cdot A_G \cdot \exp\left(-A_G \cdot (uQ - Q_0)^2\right) \cdot \sqrt{\frac{\pi}{C_G}} \cdot \operatorname{erf}\left(\frac{\pi}{2} \sqrt{C_G}\right) \\
 &+ p_L \cdot \frac{1}{\pi} \cdot \frac{A_L}{\ln(1 + A_L \cdot Q_{max}^2)} \cdot \frac{2}{\sqrt{D_L \cdot C_L}} \cdot \arctan\left[\frac{\pi}{2} \sqrt{\frac{C_L}{D_L}}\right] \\
 &+ (1 - p_G - p_L) \cdot \frac{1}{\pi} \cdot A_S \cdot \left(\frac{\arctan\left[\frac{\pi}{2} \sqrt{\frac{C_S}{D_S}}\right]}{\sqrt{C_S \cdot D_S^3}} + \frac{2\pi}{4D_S^2 + \pi^2 \cdot D_S \cdot C_S} \right)
 \end{aligned}$$

This function can be readily calculated and used to determine the lineshape of the diffracted intensity from a 2D film.

A different approach to solve $Int(\omega)$ is to split the integral into a sum of integrals over smaller regions of ω . For each of these smaller parts, the square of the modulus of the structure factor can be approximated by a Lagrange interpolation formula [Abr72].

Since it is possible to solve $Int(\omega)$ for products of (at least) fourth order polynomials in ω with the intensity distribution function $J(Q,u,\omega)$, a five point Lagrange interpolation formula is used to approximate $|S(Q,u,\omega)|^2$. The Lagrange method uses five equally spaced points $[(x_1, f_1), (x_2, f_2), (x_3, f_3), (x_4, f_4), (x_5, f_5)]$ along the x-axis over the interval from x_1 to x_5 to determine the best fourth order polynomial as approximation. Using the notation $\Delta = x_{i+1} - x_i$ and the formulas to calculate the prefactors W_i given in Appendix A, the Lagrange polynomial is given by:

$$P(x) = \frac{1}{24\Delta^4} (W_4 x^4 + W_3 x^3 + W_2 x^2 + W_1 x^1 + W_0 x^0) \quad 2.28$$

The error of this approximation as a function of the interval size $c = (x_5 - x_1)$ and the parameter $d = uQ r_{xy}$ with $r_{xy} = \sqrt{\Delta x_{ijkl}^2 + \Delta y_{ijkl}^2}$ can be estimated. If the interval size is chosen in a way such that

$$c = (x_5 - x_1) \leq (d^2 + 215d^4 + 327d^6 + 90d^8 + d^{10})^{-1/10} \quad 2.29$$

then the error of the approximation is less than 1%.

$$|\varepsilon| \leq \frac{(x_5 - x_1)^5}{120} \cdot \sqrt{d^2 + 215d^4 + 327d^6 + 90d^8 + d^{10}} \quad 2.30$$

A new maximum interval size has to be calculated for each $d = uQr_{xy}$ to keep the calculation times as low as possible.

Using $M = \pi / c = \pi / (b_m - a_m)$ for the total number of intervals and the following abbreviations $a_m = -\pi/2 + (m-1) \cdot c$ and $b_m = -\pi/2 + m \cdot c$ with $m = 1, \dots, M$, $Int(\omega)$ can be calculated as:

$$Int(\omega) = \sum_{m=1}^M \left(W_0 \int_{a_m}^{b_m} J(Q, u, \omega) d\omega + W_1 \int_{a_m}^{b_m} \omega \cdot J(Q, u, \omega) d\omega + W_2 \int_{a_m}^{b_m} \omega^2 \cdot J(Q, u, \omega) d\omega \right. \\ \left. + W_3 \int_{a_m}^{b_m} \omega^3 \cdot J(Q, u, \omega) d\omega + W_4 \int_{a_m}^{b_m} \omega^4 \cdot J(Q, u, \omega) d\omega \right) \quad 2.31$$

Since a new approximation of the structure factor is generated for each interval, all five terms of Equation 2.31 must be considered. This leads to extensive calculations times. All 15 integrals of the product of Gaussian, Lorentzian and Lorentzian Square functions with up to fourth order terms of ω are listed in Appendix B.

2.2 Thermodynamic study of physisorbed films

The term adsorption (desorption) describes the formation (removal) of surface excess in a system consisting of a gas (the adsorbate) and a solid or liquid surface (the substrate or adsorbent) in equilibrium. It can be broadly divided into two classes, chemisorption and physisorption. In the former case, chemical bonds between adsorbate and substrate are formed creating a chemical compound on the outermost layer of the substrate. Physisorption, on the other hand, does not involve electron transfer between adsorbate and substrate. Molecular interactions like e.g. the van der Waals interaction, dipole-dipole interactions of polar adsorbate molecules or ion-ion interactions of ionic substrates are responsible for this process. The focus of this section is on physisorbed systems since all here investigated systems belong into this class. Some classic books like ‘Physical adsorption of gases’ of Young and Crowell [You62] and ‘Films on solid surfaces’ of J. G. Dash [Das75] and more recently the book ‘Physical Adsorption: Forces and Phenomena’ of Bruch, Cole and Zaremba [Bru97] give an overview of this topic.

A good method to study these adsorption (desorption) processes is the volumetric isotherm. The amount adsorbed Ω (i.e. the number of gas molecules adsorbed) is monitored as a function of pressure p at a constant temperature T . Once a state of equilibrium between adsorption and desorption rate is established, the chemical potential of the adsorbed film μ_f and the gas μ_g are equal. Isotherms are recorded from zero pressure up to the saturation vapor pressure (SVP or p_0) of the adsorbate. When the SVP is reached, then the adsorbed phase and the bulk phase are indistinguishable by adsorption isotherm techniques.

Isotherms can be used to provide valuable information about the thermodynamics of an adsorbed film. They can examine large portions of a phase diagram and also help to characterize certain properties of the substrate. The surface area (often proportional to the reactivity), the surface uniformity and the porosity are some typical quantities of interest.

Isotherms have traditionally been used to provide information about the status of the adsorbed film. Figure 2.8 shows a schematic ‘picture’ of the microscopic status of an adsorbed film as it relates to various locations on the adsorption isotherm. First, at coverages of $\Omega < 1$, the pressure remains near zero while the amount adsorbed increases. This vertical riser relates to the formation of the first adsorbed layer. Second, at $\Omega \sim 1$, the pressure rises and basically no particles are adsorbed. This horizontally portion relates to the completion of the first layer. Third, at $\Omega > 1$, the pressure reaches a certain value and stays constant while the amount adsorbed increases again. This behavior relates to the formation of a second layer.

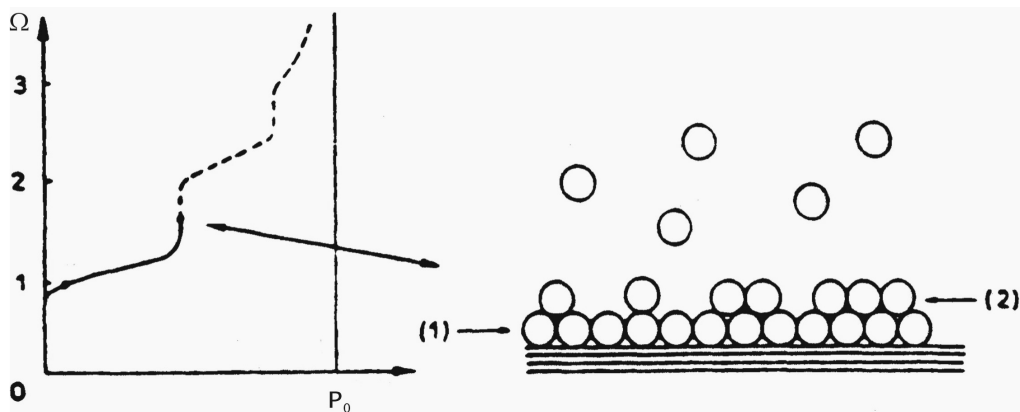


Figure 2.8: Information about the film status examined with an adsorption multilayer isotherm. The amount adsorbed Ω is shown as a function of pressure [left]. The saturation vapor pressure is p_0 . A schematic representation of the corresponding status of the film is shown on the right side.

Even though more distinct layers are observable in multilayer isotherm on high quality substrates, the difference between the film chemical potential and the bulk chemical potential of the adsorbate decreases each time and at some point the formation of bulk material will occur. In addition, effects of capillary condensation might influence the growth of the film.

In the following sections, several adsorption models are described and it is discussed how they are used to explain isotherm data. The purpose is to describe the methods used to derive some of the thermodynamic information contained in adsorption isotherms.

2.2.1 Models of adsorption processes

Brunauer [Bru45] introduced a classification for isotherms below the critical temperature of the gas. The five basic classes are shown in Figure 2.9. Where as type I, II, III are typical for adsorption processes **on** outside surfaces of a substrate, the types IV and V are characteristic for adsorption **in** porous adsorbents or others effects of capillary condensation are present. Type I isotherms are associated with systems where the amount adsorbed does not exceed one layer before bulk material forms. Type II and III isotherms involve the formation of multi-layer.

Different models have been proposed to explain the different shapes (or at least parts there of) of the isotherm types I-III. It is useful to discuss some of them even though most of these models are unable to describe an isotherm over the total recorded range.

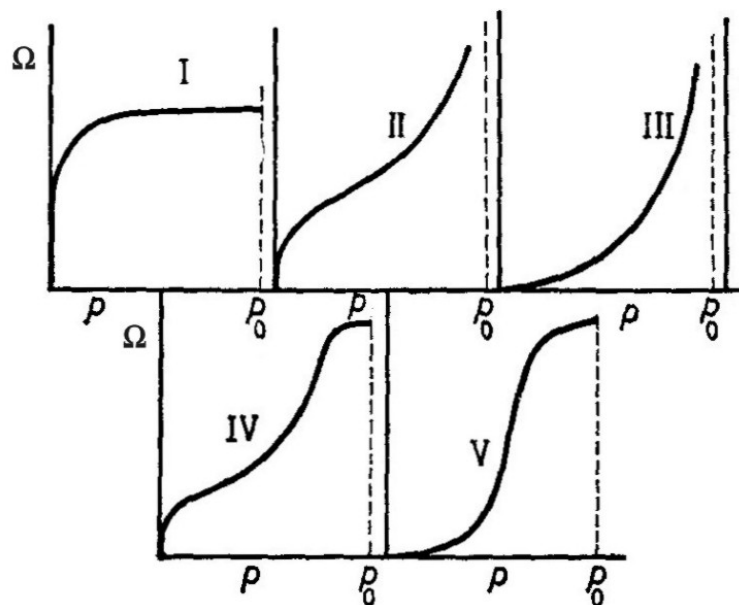


Figure 2.9: Brunauer's classification of isotherms [Bru45]. The following abbreviations are used: Ω describes the amount adsorbed, p is the equilibrium pressure between adsorbate and sample and p_0 is the saturation vapor pressure of the adsorbate.

a) Henry's Law

The adsorption behavior at very low coverages is often referred to as Henry's law regime. Henry's law predicts a linear dependence of coverage Ω as a function of pressure p .

$$\Omega = \alpha \cdot p$$

2.32

Since this model does not include any lateral interactions between adatoms, it should only be applicable at low coverages, i.e. below 0.1 monolayer of a close-packed structure of the adsorbate. In this case, the adsorbate-adsorbate distance would be three times larger than in a typical bulk structure.

b) Langmuir isotherm

The model of an ideal localized **monolayer** is often referred to as Langmuir isotherm. The substrate surface is divided into N identical adsorption sites and the coverage Ω is defined as the ratio of the occupied adsorption sites M to the total number of sites.

$$\Omega = \frac{M}{N} \quad 2.33$$

From the kinetic theory of gases the number of molecules, n , hitting a unit surface in unit time is proportional to the pressure p by:

$$n = \frac{p}{\sqrt{2\pi m k_B T}} \quad 2.34$$

where m is the molecular mass, k_B is the Boltzmann constant and T stands for the temperature.

The probability that a molecule hits the surface at an unoccupied adsorption site and condenses is given by α_a and E_a describes the adsorption energy, then the adsorption rate R_a can be written in a form proportional to the pressure p and the number of free adsorption sites $(1-\Omega)$ as:

$$R_a = \alpha_a \cdot e^{-E_a/RT} \cdot n \cdot (1-\Omega) = k_a \cdot p \cdot (1-\Omega) \quad \text{with } k_a = \frac{\alpha_a}{\sqrt{2\pi m k_B T}} \cdot e^{-E_a/RT} \quad 2.35$$

The desorption rate R_d is defined as the product of the probability of evaporation k_d and the number of molecules adsorbed Ω .

$$R_d = k_d \Omega \quad 2.36$$

In equilibrium the adsorption and desorption rate are equal. This leads to the expression:

$$\Omega = \frac{\gamma p}{1 + \gamma p} \quad \text{with } \gamma = \frac{k_a}{k_d} \quad 2.37$$

Equation 2.37 is the Langmuir isotherm.

c) BET isotherm

The most widely used approach to describe multilayer isotherms is the BET method developed by Brunauer, Emmet and Teller [BET38] or a variation of it. It is an extension of the Langmuir isotherm theory described above. The general idea behind the BET isotherm is that molecules can adsorb on occupied adsorption sites. The following assumptions are made:

a) The number of adsorption sites on the surface N is equal for each layer. If M_j describes the number of adsorption sites covered by j layers of adsorbate molecules (e.g. M_0 is the number of free adsorption sites on the surface) than the number of surface adsorption sites N and the number of adsorbed molecules N_a can be expressed as:

$$N = \sum_j M_j \qquad N_a = \sum_j j M_j \qquad 2.38$$

The case $N_a=N$ is defined as ‘*the amount adsorbed needed to complete a monolayer*’. Some attention is needed at this point since the number of adsorption sites on the substrate surface N depends on the adsorbate/substrate system and **not** on the substrate alone.

b) The adsorption and desorption rate of the first layer is described by the adsorption energy E_a , the adsorption constant k_a and the desorption constant k_d . This is identical to the Langmuir isotherm case.

c) All further layers are described in the following way. The heat of adsorption of these layers is equal to the heat of liquefaction E_L and the ratios of the adsorption constants and desorption constants are also equal.

$$E_2 = E_3 = \dots = E_j = \dots = E_L \qquad \frac{k_a^2}{k_d^2} = \frac{k_a^3}{k_d^3} = \dots = \frac{k_a^j}{k_d^j} = \dots = \gamma_1 \qquad 2.39$$

Using these assumptions the equilibrium conditions are written as:

$$k_a \cdot p \cdot M_0 = k_d \cdot M_1 \qquad k_a^j \cdot p \cdot M_{j-1} = k_d^j \cdot M_j \qquad \text{for } j \geq 2 \qquad 2.40$$

These expressions can be used to express the M_j as a function of unoccupied substrate surface adsorption sites M_0 .

$$M_j = \gamma_1^{j-1} \cdot p^j \cdot \gamma \cdot M_0 \qquad 2.41$$

Combining the equations 2.38 and 2.41 the relative amount adsorbed Ω in adsorbed monolayers as a function of pressure p is:

$$\Omega = \frac{N_a}{N} = \frac{\gamma p}{(1 - \gamma_1 p) \cdot (1 + (\gamma - \gamma_1) p)} \qquad 2.42$$

For adsorption isotherms it is often useful to express the amount adsorbed Ω as a function of the relative pressure p/p_0 . This can be done for a very thick film by using the following approximations, $M_{j-1} \approx M_j$ and $p \approx p_0$, then the equilibrium condition is reduced to:

$$\gamma_1 = \frac{k_a^j}{k_d^j} \approx \frac{1}{p_0} \qquad 2.43$$

By expressing γ as a product of γ_1 and another constant c ($\gamma = c \cdot \gamma_1$) it is then possible to derive the following expression for the relative amount adsorbed in monolayer adsorbed of the BET isotherm:

$$\Omega = \frac{c \cdot p/p_0}{\left(1 - p/p_0\right) \cdot \left(1 + (c-1) \cdot p/p_0\right)} \quad 2.44$$

The magnitude of the parameter c determines the shape of the monolayer step. Figure 2.10 displays the shape of the BET isotherms for different values of c . These curves converge at higher relative pressures.

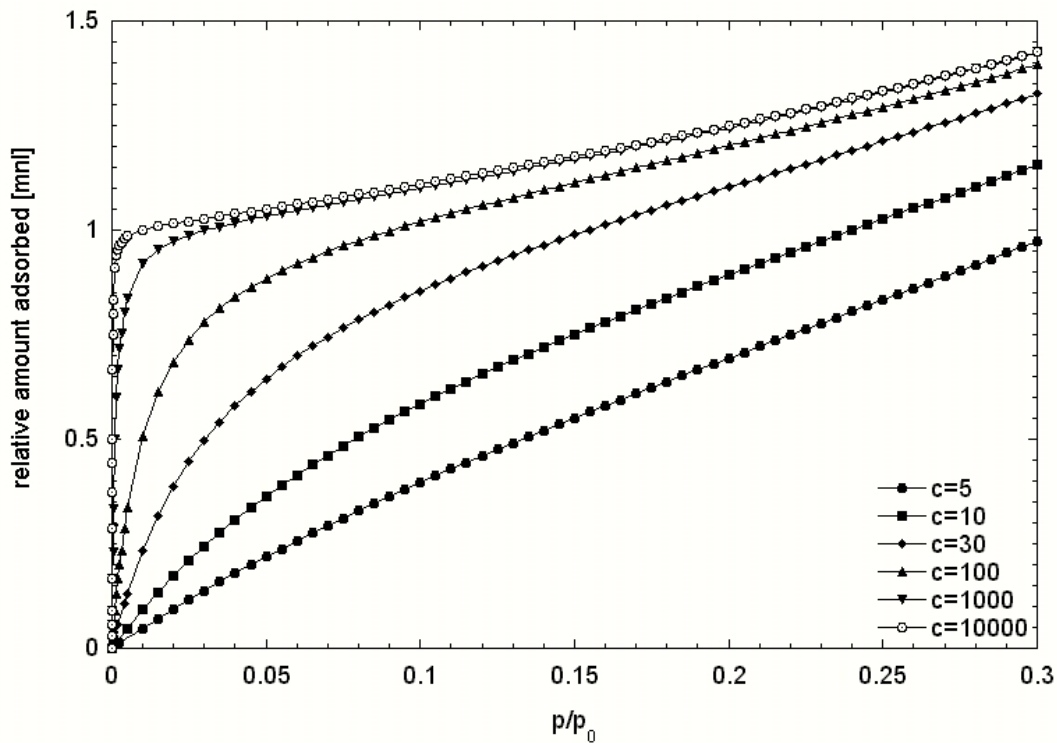


Figure 2.10: BET isotherms as a function of relative pressure p/p_0 [see formula 2.44]. The parameter c has been varied to show its influence on the shape of the monolayer step.

d) Van der Waals isotherm

Frenkel [Fre46], Halsey [Hal48] and Hill [Hil49] independently proposed that the long range van der Waals interaction between substrate and adsorbate could be used to describe the behavior of thick physisorbed films. This approach is often referred to as the FHH theory and it predicts the isotherm shape near the saturation pressure p_0 of the form:

$$-k_B T \cdot \ln\left(\frac{p}{p_0}\right) = \frac{c}{d^s} \quad 2.45$$

with $c > 0$ and the exponent $s = 3.0$. The film thickness is represented by d . Equation 2.45 is also called the van der Waals isotherm.

Discussion of these adsorption models

These models are not detailed or sophisticated enough to describe a complete multilayer isotherm (e.g. CH_4 adsorbed on MgO [Fre00] or [Tho94]), but they are still useful in examining certain regions of an isotherm. In addition, more sophisticated models have been developed recently (e.g. [Lys91], [May90], [May96a, b] and [Mec96]). However, these still need to be tested on simple systems such as rare gases on graphite.

One of the important characteristics of a powdered substance is the surface area. Many properties, such as the reactivity of a catalyst or the capacity of a filter, depend on it. The BET theory provides a very good avenue for determining the amount adsorbed at monolayer completion especially if the isotherm is not characterized by a sharp step. When there is a sharp vertical riser indicating the formation of the monolayer and/or the formation occurs at higher relative pressures (e.g. NH_3/MgO), other methods are commonly used to determine the monolayer height of the isotherm. Probably the best known and most widely used is the point B method [Emm37]. To determine the monolayer capacity a line is approximated to the linear almost horizontally part of the isotherm after monolayer completion. The monolayer is treated as complete at the point where the linear fit and the isotherm diverge at low relative pressures p/p_0 .

To calculate the surface area, normally expressed in m^2/g , it is necessary to know the adsorption area per molecule, σ , projected onto the substrate surface. Early models *assumed* a close packing of adsorbate molecules on the surface using distances derived from the densities of the bulk solid or liquid phases. These models produced reasonable results, especially in cases where rare gases were used as adsorbates. However, a more exact determination is possible if the structure of at least one adsorbate is *known* or can be measured on the specific substrate, e.g. using XPD. In this case, one can calculate a reference area per molecule $\sigma_{\text{reference}}$.

If monolayer heights of isotherms of different adsorbates $\Omega_{\text{other material}}$ are compared to the monolayer height of this specific 'reference' material $\Omega_{\text{reference}}$ than it is possible to easily calculate the average area per molecule for these different adsorbates $\sigma_{\text{other material}}$.

$$\sigma_{\text{other material}} = \sigma_{\text{reference}} \cdot \frac{\Omega_{\text{reference}}}{\Omega_{\text{other material}}} \quad 2.46$$

Another region of interest of adsorption isotherms is near the saturated vapor pressure of the bulk material. There the wetting behavior of the adsorbate can be observed. Wetting has been a topic of great interest over the last two decades (e.g. [Pan83], [Git84], [Die85], [Che93], [Col94], [Die97], [Gro97], [Suk97], [Chi98] and [Boj99]). Customarily, the terms ‘*nonwetting*’, ‘*incomplete*’, and ‘*complete*’ wetting are used to describe different modes of film growth on surfaces. If performed carefully the shape of an isotherm near the saturated vapor pressure can be used as a reliable indicator for the growth mode. When only a limited number of adsorption steps are visible or a limited amount of gas was adsorbed before the isotherm reaches the bulk saturation vapor pressure, the film growth is said to be ‘*incomplete*’.

Often an asymptotic increase in layer thickness (‘*complete*’ wetting) is observed near the bulk triple point, T_{triple} (e.g. [Kri84]). This behavior is commonly referred to as triple point wetting. An analysis of the data from a set of isotherms near T_{triple} can help to distinguish between these two wetting modes.

2.2.2 The 2D compressibility K_{2D}

Similarly to the compressibility in three dimensions, a 2D compressibility K_{2D} can be defined as:

$$K_{2D} = -\frac{1}{\sigma} \left(\frac{d\sigma}{d\varphi} \right)_T \quad 2.47$$

In this expression σ is the area occupied per molecule on the surface of the substrate and φ is the 2D spreading pressure. The derivative is taken at constant temperature T . K_{2D} can be determined directly using an adsorption isotherm using the following relations:

a) The change of the molecular area $\sigma = A/N$ can be related to the change in the number of molecules N adsorbed on the surface area A of the substrate by:

$$d\sigma = -\frac{A}{N^2} dN \quad 2.48$$

b) The molecular area can also be expressed using the relationship of the change of the 2D chemical potential $d\mu_{2D} = -SdT + \sigma d\varphi$:

$$\frac{1}{\sigma} = \left(\frac{d\varphi}{d\mu_{2D}} \right)_T \quad 2.49$$

c) In thermodynamic equilibrium, the chemical potentials between the 3D vapor and the 2D film are equal leading to the following two expressions:

$$\mu_{2D} = \mu_g = -k_B T \ln \left(\frac{k_B T}{\lambda^3 p} \right) \quad d\mu_{2D} = d\mu_g = k_B T \frac{1}{p} dp \quad 2.50$$

Here, λ is an abbreviation of the thermal de Broglie wavelength $\lambda = \sqrt{2\pi k_B T}$. By combining the steps above, the following expression for the 2D compressibility is found:

$$K_{2D} = \frac{A}{k_B T} \cdot \frac{p}{N^2} \cdot \frac{dN}{dp} \quad 2.51$$

The 2D compressibility can be used to investigate phase transitions in the film such as melting and layering transitions, since the derivative dN/dp in Equation 2.51 becomes large at isotherm steps. The height and the width of a compressibility peak as a function of chemical potential are changing dramatically at a first order structural change (e.g. melting transition) of an adsorbed layer [Lah92]. Generally speaking, broad and weak maxima of the compressibility are associated with liquid layers whereas solid layers show sharp intense compressibility peaks. Thus monitoring the height and the full width at half maximum (FWHM) of K_{2D} as a function of temperature is a good way to locate melting transitions [Lah92], [Fre00].

The 2D compressibility indicates accurately the turning point of an isotherm step (as a maximum), which can be used to monitor the position of the step as function of pressure. Larher [Lar92] has shown that the enthalpy h and the entropy s of gas and condensed phase can be related to the saturated vapor pressure by:

$$R \cdot \ln p_0 = -\frac{(h_g - h_f)}{T} + (s_g - s_f) \quad 2.52$$

Using Clausius-Clapeyron's equation, this can be related to the pressure dependence p_n of the n th step position as a function of temperature:

$$\log_{10} p_n [\text{Torr}] = -\frac{A_n}{T[\text{K}]} + B_n \quad 2.53$$

By evaluating this function, it is possible to determine layering transitions within the adsorbed film.

2.2.3 The isosteric heat of adsorption Q_{st}

Another important thermodynamic quantity that can be extracted from a set of closely spaced isotherms is the 'isosteric' (constant coverage) heat of adsorption Q_{st} . This quantity represents the work required to bring one molecule from the 3D vapor into the 2D film. It is defined by:

$$Q_{st} = RT^2 \cdot \left. \frac{\partial \ln p}{\partial T} \right|_{\Omega} \quad 2.54$$

The derivative is taken at constant coverage Ω . Because real isotherms are taken at different temperatures, it is necessary to interpolate the experimental data of two isotherms because it is not possible to record these in steps of equal coverage. For CH_4 on MgO, Freitag and Larese

[Fre00] showed that the partial derivative of Equation 2.51 could be replaced by $\Delta \ln p / \Delta T$ if two isotherms are separated by 1-2K. In that study only a weak dependence on the magnitude of the temperature interval was found.

2.3 Commensurability

Incommensurate and *commensurate* are two widely used terms to describe structures of adsorbed films, which are briefly discussed here. These terms refer to the relationship of the adsorbate structure relative to the surface structure.

In the ideal case, one would study the properties of a 2D system without the influence of a substrate. In practice however, the 2D system is approximated by investigating adsorbed films supported by a substrate. Therefore in addition to the adsorbate-adsorbate interaction, the interaction between adsorbate and substrate needs to be considered, the latter, while often treated as small compared to the molecule-molecule interaction cannot be neglected.

In the study of gas solid interactions one often considers the case of molecules interacting with a smooth surface. In this case one describes the influence of a perfectly flat substrate using a potential that only depends on the distance perpendicular to the surface, e.g. a Lennard-Jones potential. However, real surfaces are better described using a potential that varies periodically in the plane, especially close to the surface. This modulation creates positions that are energetically more or less favorable for the adsorbate molecules. Under certain conditions this modulation is strong enough to cause the adsorbate molecules to *lock* into specific positions on the surface. If the adsorbate molecules form structures that maintain a regular relationship with the underlying surface, these lattices are called *commensurate*.

A well-established terminology is used to describe the 2D unit cell of the adsorbate in terms of the substrate surface structure. Two factors (the length of the lattice vectors) and a rotation angle, indicated by R , are traditionally used to describe the commensurate overlayer with respect to the 2D substrate unit cell. Classic examples are the $\sqrt{3} \times \sqrt{3}$ $R30$ structure on graphite (e.g. krypton molecules sitting in the center of the graphite hexagons, see Figure 2.11b) [Ste84] or the $\sqrt{2} \times \sqrt{2}$ $R45$ structure of CH_4 on MgO (the methane molecules are sitting on top of the magnesium sites on the MgO surface, see Chapter 3.4) [Cou85].

Whereas the $\sqrt{3} \times \sqrt{3}$ $R30$ superlattice can be pictured as a ‘Halma’ or ‘Chinese checkers’ board game, the structure of methane on magnesium oxide can be viewed as a ‘chess board’ (magnesium atoms white fields and oxygen atoms black fields) where the methane molecules might only occupy the white fields (see Figure 2.11a).

In these two systems *every* adsorbed molecule occupies an identical adsorption site (e.g. each krypton atom sits in the center of a hexagon of the substrate surface). This situation usually occurs when the adsorbate-substrate interaction is greater than the adsorbate-

adsorbate interaction. However, if the adsorbate-substrate interaction is weaker and comparable in strength to the adsorbate-adsorbate interaction, then the molecular forces dictate the intermolecular distance and adsorbate systems can be found where only every n^{th} molecule interlocks at a regular position relative to the substrate, e.g. molecules might only occupy identical sites every 3rd or 4th lattice site or just in one direction. These are called ‘*weakly commensurate*’ or ‘*1D commensurate*’ structures. Examples here are e.g. H₂O on MgO [Fer96] and the high-density phase of methyl chloride on graphite [Mor91], respectively.

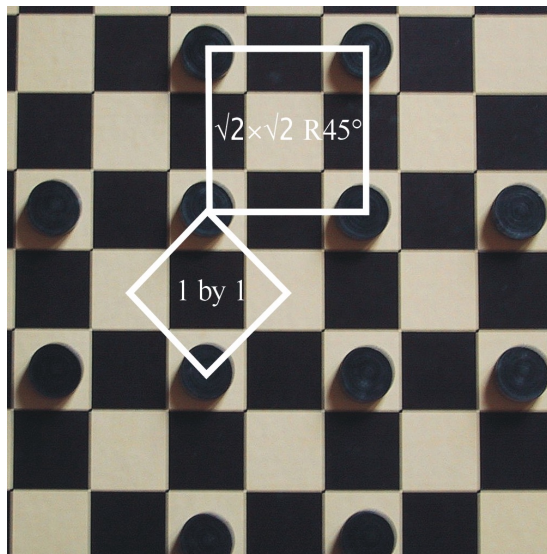


Figure 2.11a: Visualization of the structure of CH₄ on MgO ($\sqrt{2} \times \sqrt{2}$ R45) as a chessboard with occupied white fields.

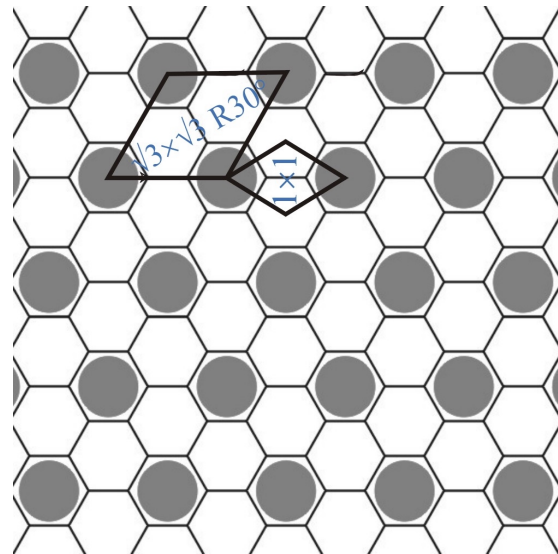


Figure 2.11b: Schematic picture of the $\sqrt{3} \times \sqrt{3}$ R30 superlattice (e.g. krypton on graphite).

In the case where the influence of the adsorbate-substrate interaction is negligible in the plane of the surface (i.e. the adsorbate-adsorbate interaction is dominant and the adsorbate structure is independent of the periodicity of the substrate surface), the overlayer structure is called ‘*incommensurate*’. Incommensurate structures often exhibit strong temperature and coverage dependencies (e.g. Xe/Gr [Hon86]). These structures are sometimes referred to as ‘*floating*’ 2D solids. Novaco and McTague have pointed out that in order to minimize the free energy of the adsorbate-substrate interaction, the entire overlayer has to rotate with respect to the substrate surface. This rotation is commonly referred to as Novaco-McTague rotation [McT79].

There are a number of various interesting aspects of the study of adsorbed film structures, especially the phase transitions between ‘*commensurate*’ and ‘*incommensurate*’. Details of these structural transitions can be found in the monograph by Bruch, Cole and Zaremba [Bru97] or in the chapter ‘*The structure of physically adsorbed phases*’ in the ‘*Handbook of surface science*’ by Suzanne [Suz96].

Chapter 3:

Experimental setup

A wide variety of experimental methods have been used to study the structure and the dynamics of adsorbed films on surfaces. In the case of single crystal surfaces techniques such as LEED (e.g. [Aud92] and [Fer98]), RHEED, helium atom scattering [Fer96], ellipsometry [You93] and x-ray diffraction [Str98] are commonly employed. When the surfaces take the form of a crystalline powder, tools such as x-ray and neutron powder diffraction [Buc89], quasi elastic and inelastic neutron scattering [Lar98], NMR and Mössbauer spectroscopy have also been used. Many researchers have found it useful to combine microscopic measurements with investigations focused on the thermodynamic properties, e.g. complementary adsorption isotherms [Bah95] or heat capacity [Ina91] measurements. While all of these studies involve low temperatures and the use of high-to-ultra high vacuum environments the requirements on the experimental conditions are usually more severe in the case of the single crystal work. In the first two sections of this chapter a characterization of the experimental setups used to measure volumetric adsorption isotherms and to study adsorbed films with x-ray powder diffraction is provided. The later parts will introduce the materials investigated in this study.

3.1 Thermodynamic experiments:

A set of adsorption isotherms recorded over an extended temperature regime can provide a wealth of information concerning the physical properties of a physisorbed system. In addition to providing an overview of the phase diagram, specific information concerning layering, commensurate-incommensurate and melting transitions can also be obtained. Thermodynamic quantities such as the isothermal compressibility and isosteric heat of adsorption can be determined from the measurements since most of them essentially take place in thermodynamic equilibrium.

Figure 3.1 illustrates the simplicity of the equipment needed to measure adsorption isotherms volumetrically. All that is needed to perform these measurements is a sample confined in a constant temperature bath, a gas handling system for dosing *known* quantities of gas onto the sample and accurate pressure readout to monitor the adsorption process. The follow-

ing procedure is used to perform a volumetric isotherm. Known quantities of purified gas are admitted into a calibrated volume at a known pressure from a reservoir. An isolation valve separates the calibrated volume from the sample cell until the desired amount of gas is metered into the calibrated volume. The calibrated volume is connected to the sample cell via a thermally insulated capillary.

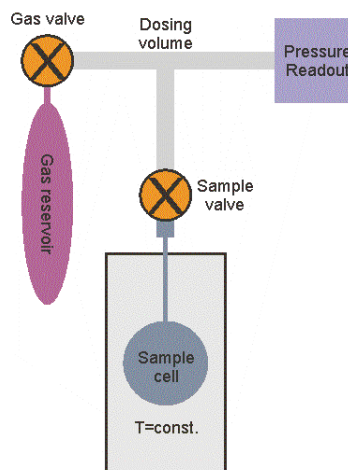
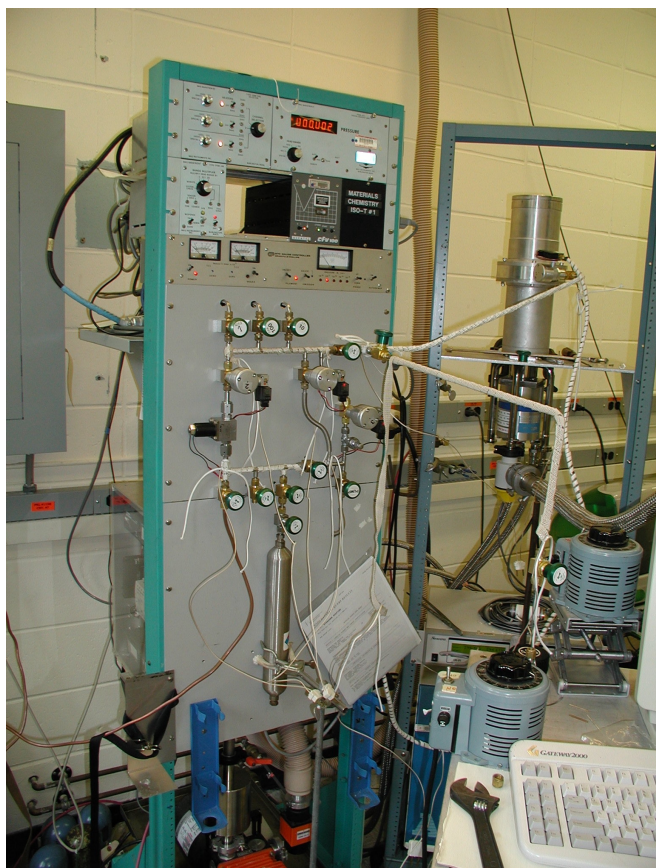


Figure 3.1: Schematic view of the basic experimental setup to record adsorption isotherms [top].

Figure 3.2: Digital image of the gas handling system of Isotherm Machine #1 [left]. A LabView based program controls the machine.

Once the desired “dose” of gas is admitted to the calibrated volume the “initial” gas pressure is recorded. The isolation valve is then opened admitting the gas into the sample cell. The change of pressure inside the calibrated volume is monitored as a function of time. Once the pressure no longer changes noticeably (i.e. after “equilibrium” is reached) the “final” pressure is recorded and the isolation valve is closed. The quantity of gas admitted to the sample cell is determined by subtracting the “final” gas pressure value from the “initial” gas pressure using the ideal gas law (or if needed the van der Waals equation for real gases) along with the appropriate calibrated volume and associated temperature. This procedure is repeated multiple times. A plot of the quantity admitted into the cell versus final pressure is then referred to as an adsorption isotherm.

The actual isotherm machine (gas handling system and computer controlled electronics) used during this work described below is shown in Figure 3.2 [Mur96]. Clearly the apparatus that was employed during this research is more sophisticated and complicated than Figure 3.1 suggests.

The sample cell is mounted on the second stage of a closed cycle helium refrigerator (Displex), which is thermally isolated from the external world by an external vacuum can. A short piece (~15cm long) of thin walled stainless steel capillary (0.5mm diameter) separates the gas handling system from the sample via a vacuum feedthru. An automated pneumatic bellows valve (#1) separates the dosing volume from the sample. The dosing volume is constructed of stainless steel (304) tubing (6mm outer diameter) and a short length of annealed copper tubing (6mm) is used to connect the dosing volume to the Displex.

Commercial high-resolution capacitance manometers manufactured by MKS (Series 690 Baratrons) and originally calibrated with an NIST calibrated dead weight gauge are used to monitor the pressure. A range of manometers between 1-5000Torr was available. Depending on the temperature and the resulting 3D equilibrium vapor pressure P_0 of the adsorbate, the appropriate manometer was chosen. The pressure reading of the manometer is available externally by monitoring the output voltage from the manometer that varies proportionally and linearly with the full-scale pressure reading between 0 and 10V. The voltage output from the manometers is fed to a 16-bit AD board and monitored by a computer.

Two additional pneumatically automated valves are used to automatically dose controlled amounts of gas into the dosing volume and subsequently onto the sample. A combination of an electronically controlled solenoidally actuated flow control valve (MKS 248) followed by another pneumatically automated valve regulates the introduction of gas into the calibrated volume. This configuration makes it possible to slowly admit small quantities of gas into the dosing volume. Some method for gas removal must be provided if the pressure in the calibrated volume still exceeds a certain predetermined “setpoint” value. Another automated valve (#3) followed by a needle valve (used to regulate the pumping speed) connects the dosing volume to a turbomolecular pump based vacuum station for this purpose.

This pump station operates in the very low 10^{-7} mbar range and is used to evacuate the gas handling system and/or the sample cells before or after an isotherm. These high vacuum conditions are well suited for evacuating sample cells and for minimizing sample contamination since the powders used in the isotherm studies described here have large surface areas (1-100m²/g) and do not require UHV conditions.

A Conductus (Neocerra) LTC 21 temperature controller is used to regulate the temperature of the sample to within ± 0.003 K over the entire operating range of the closed-cycle refrigerator (i.e. from 15-325K). This device has two input channels that can be used to control the temperature and independently monitor the temperature of a device using a variety of sensors (e.g. Pt resistors, FeRu resistors or Si diodes) and a three-step heater output (0.5W, 5W and 50W). For the isotherms described here one sensor is mounted on the tip of the cold finger (just below the sample cell), where the heater is also located while the other is on top of the sample cell.

As mentioned above the gas handling system and the temperature controller are computer controlled. The program to monitor the adsorption process was written in LabView, a graphical programming language. This program is user friendly and offers great flexibility to record adsorption isotherms, e.g. three different criteria to decide if the pressure above the sample has reached equilibrium. Figure 3.3 shows an isotherm of CH_4 on MgO as a typical example of the type of measurements that can be made using this apparatus.

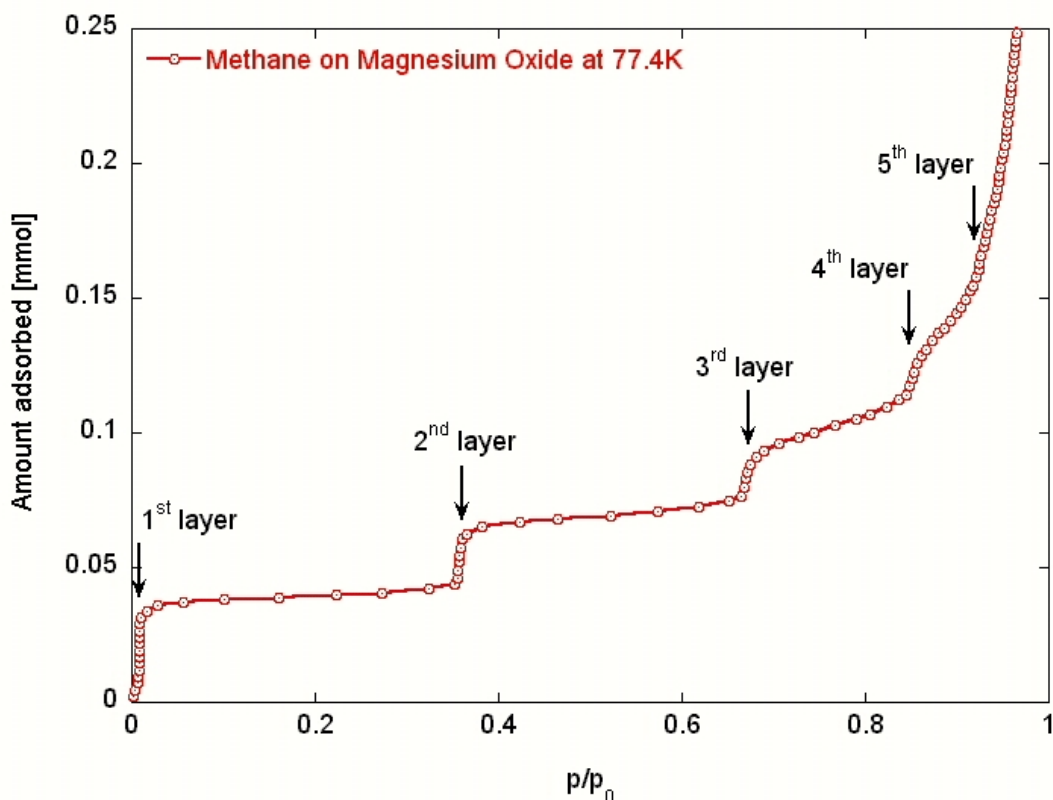


Figure 3.3: Sample isotherm of CH_4 on MgO

3.2 X-ray powder diffraction experiments:

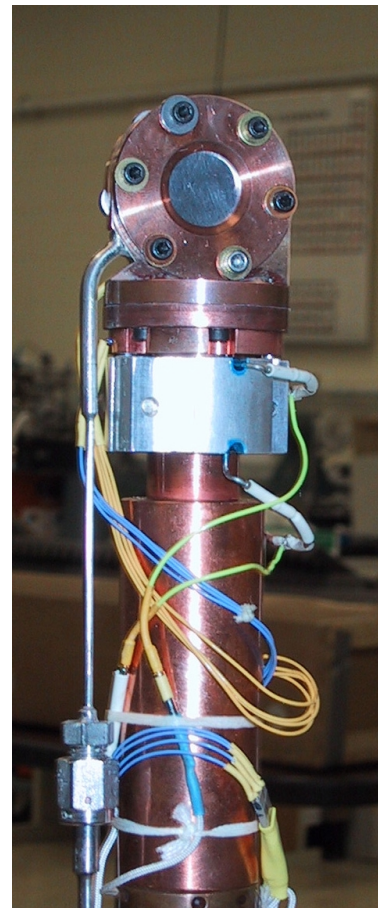
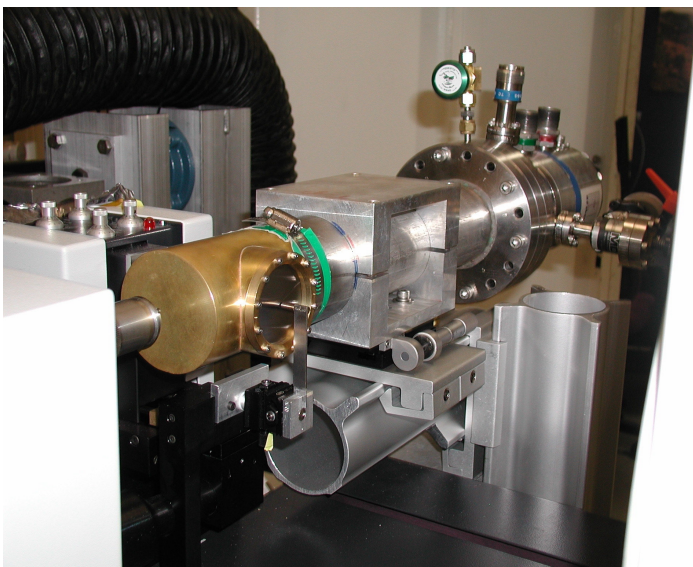
X-ray powder diffraction (XPD) is an excellent tool for investigating the structural properties of an adsorbed film. Here, the diffraction cells, the experimental setup and the Chemistry department's beam line X7B at the NSLS at Brookhaven National Laboratory are briefly described. In addition, some discussion of the use of a 2D image plate detector system to study adsorbed films will be presented.

3.2.1 X-ray diffraction cell:

During the course of this study several improvements were made to the basic design (see e.g. [Opp92]) of the x-ray diffraction cell used to study adsorbed films (see Figure 3.5). The sample is placed inside a copper cell (optimizing the thermal conductivity) between two 0.25mm thick beryllium windows (low x-ray absorption). These windows are attached leak tight onto the cell using indium wire seals. A lead mask with a 2mm pinhole (to remove background scattering from the outside vacuum can) covers the upstream beryllium window. The substrate is loaded through a slit in the bottom of the copper cell after the beryllium windows are attached to prevent powder particles from falling onto the indium seals. This technique for loading the sample results in a higher probability of creating a good vacuum seal. A stainless steel capillary is silver soldered to the copper cell to provide gas access to the substrate. The sample cell is mounted to the cold finger of a closed cycle refrigerator and the capillary is connected using a VCR seal to a vacuum feedthru ring, which is part of the vacuum vessel of the Displex.

Figure 3.5: View of the downstream side of the x-ray diffraction cell [right].

Figure 3.6: Displex used for the x-ray measurements at X7B of the NSLS. The cryostat is mounted behind the MAR345 slit assembly and is adjustable horizontally and vertically.



Two, 2 watt Allen Bradley, 100 Ω carbon resistors, epoxied into an aluminum block with Sty-cast 2850, heat the sample cell. The heater block is mounted between the sample cell and the cold finger. Two platinum resistance thermometers (1000 Ω) are mounted on the sample cell,

one at the bottom and one in front of the upstream beryllium window. The cell temperature is adjusted and regulated using a Conductus (Neocerra) LTC21 controller. The sample temperature is regulated within $\pm 0.003\text{K}$ between 25-300K.

The Displex (Figure 3.6) has also been modified for use in x-ray diffraction studies of adsorbed films using the MAR345 detector table at X7B. A specialized mount (constructed from X tubing) is used to hold the cryostat in front of the MAR345 slit assembly. It provides controlled vertical and horizontal adjustment (with micrometer accuracy) of the Displex position. Such exact mechanical control is needed because the weight and size of the refrigerator makes it difficult to manually align the beam with the pinhole in the lead mask. This is not only important for initial alignment but also to correct for the change in length of the cold finger as the temperature of the cold stage varies. The outer brass vacuum can on the displex also has two thin (0.25mm) indium sealed beryllium windows, a small diameter (1.25cm) window on the upstream side and a 5cm diameter window on the downstream side to minimize beam absorption. This construction allows observing diffraction angles $2\Theta \leq 30^\circ$ corresponding to an observable Q range of about $0.5 \text{ \AA}^{-1} \leq Q \leq 3.5 \text{ \AA}^{-1}$ at a wavelength $\lambda = 0.94 \text{ \AA}$.

In some of the earlier adsorption studies Kapton windows were employed on the vacuum shroud, but these were found to be less desirable because they increased the diffuse background and were difficult to keep leak tight for multiple experimental runs. A small lead beam stop is positioned directly behind the downstream beryllium window to prevent the direct beam and other undesirable low angle signals from reaching the MAR 345 detector and to reduce the background due to air scattering of the direct beam.

3.2.2 The beamline X7B at the NSLS:

Beamline X7B is operated by the Chemistry Department at the NSLS of Brookhaven National Lab. It is one of many bending magnet lines on the x-ray floor. The white beam of the synchrotron is directed unto the sample through a system of mirrors all contained in UHV. Vertical focusing of the beam is accomplished using a rhodium-coated silicon carbide spherical mirror located 5 meters from the x-ray source. The monochromator tank contains a pair of channel cut silicon (111) crystals located 8m from the source. This arrangement allows the user to select a mono-energetic beam ($\Delta E / E = 2 \cdot 10^{-4}$) in the energy range between 5-21keV. Horizontal focusing of the monochromatic beam takes place 13 m from the source using a nickel-plated rhodium coated cylindrical aluminum mirror. The beamline optics was originally designed to be used for single crystal diffraction using micron diameter crystals. It produces a beam whose intensity varies by less than 1% over an area of $0.3 \times 0.3 \text{ mm}^2$ at the sample position (22m from the source).

Like many synchrotron beam lines that specialize in single crystal crystallography or powder diffraction X7B is equipped with range of ancillary equipment (displex, flow coolers, furnaces, etc.). The detector used to collect the scattered x-rays is a MAR345 image plate system that is scanned and erased in situ. Prior to 1997 the beam line used discrete, hand mounted image plates that were exposed and then manually transferred to a Fuji BAS image plate scanner for readout.

3.2.3 X-ray image plate detector systems:

X-ray powder diffraction techniques have been used in the past to investigate the 2D structure of films adsorbed on surfaces. To our knowledge, however, the use of image plate techniques (specifically a MAR345 detector system) to study these systems has not previously been described. It is therefore necessary to review some of the properties of image plate detectors (e.g. [Miy86], [Fuj91], [Iot91], [Hal91], [Ham94] and [Lar99]) as they relate to this study. The image plate itself is a polymer disk, which has a photosensitive phosphor coating (BaFBr:Eu²⁺) that “records” an image of the x-ray diffraction pattern as a distribution of F-centers. The stored image can be read out by measuring the intensity of the fluorescence ($\lambda=390\text{nm}$) when stimulated by a He/Ne laser beam reflected off the surface of the irradiated plate (e.g. using the program ‘*Fit2D*’ [Ham97] developed at ESRF). Bleaching of the color centers and thus erasure of the image plate is accomplished through exposure to UV light.

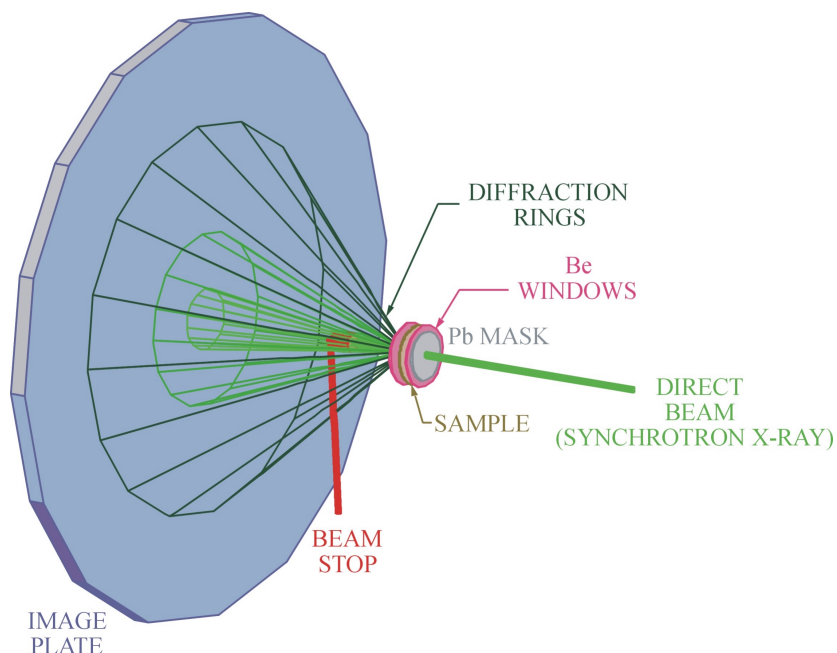


Figure 3.7: Schematic view of a powder diffraction experiment observed with an image plate detector

There are several advantages that area detector systems such as the MAR345 detector or the Fuji BAS image plate/scanner system offer for studying surface films when compared to point detectors such as e.g. a sodium iodide counter. Table 3.1 lists some of the characteristic features of the more advanced MAR345 system. One obvious advantage is that data from the entire Debye-Scherrer cone can be collected and then integrated (Figure 3.7). This reduces data collection time by at least an order of magnitude.

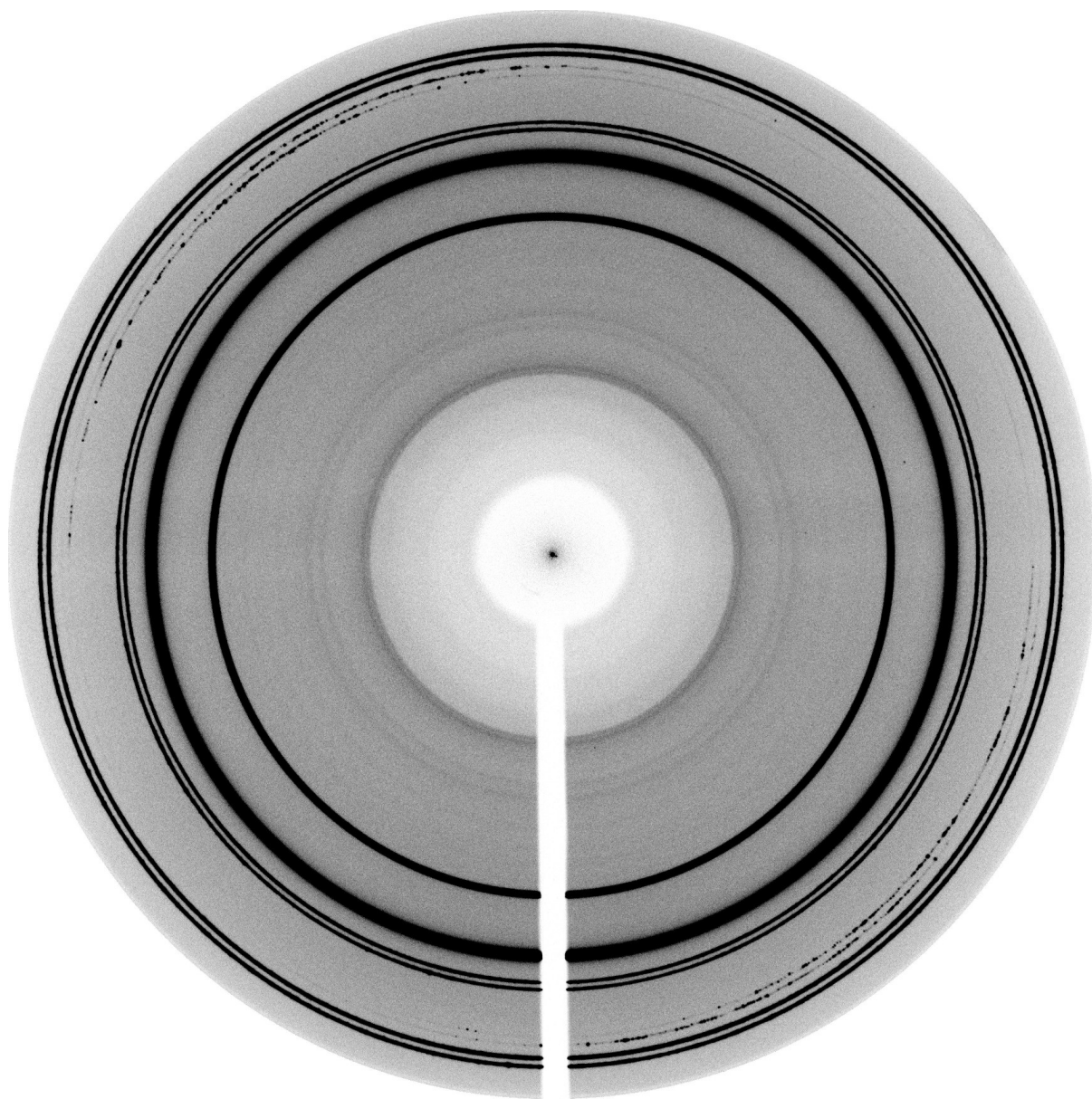


Figure 3.8: Image of a monolayer of CH_3I adsorbed on magnesium oxide observed with the MAR345 detector system.

Figure 3.8 shows x-ray diffraction data recorded for a monolayer film of CH_3I adsorbed on MgO . It should be noted that the main contributions are due to the sample cell and the substrate. The shadow of the beam stop (white), the diffraction of the beryllium windows (the

doublets) and the (111) and the (200) reflections of magnesium oxide (the black rings) are also visible. The gray rings inside of the MgO rings are due to diffraction of the CH₃I film.

The MAR345 detector uses a 16-bit AD converter and can be operated in a low- and high-resolution mode [MAR]. In the low-resolution mode the pixel size is 150 μ m X 150 μ m where each pixel is subdivided into 2 pixels of the size 75 μ m \times 150 μ m thus increasing the dynamic range to effectively 17 bits (0-131071) per pixel. The detector features high detective quantum efficiency (DQE) of about 80-95% for 8-20keV x-rays, a very low noise level of 1-2 photon equivalents and high sensitivity (1 photon at 8keV). The read out and digitization time is about 7 μ sec per pixel.

The main disadvantage of individual (discrete) image plate detectors is the decay of the stored image as a function of time. This effect combined with the ring current dependence of the x-ray intensity at a synchrotron makes the normalization of multiple scans, especially difference measurements, a very difficult task. Other problems are air scattering and accurate repositioning of the image plate.

The MAR345 detector system solves some of these problems. As an integrated system (i.e. the scan unit is build into the detector system) it repositions the image plate perfectly each time. This was not the case for the Fuji system where the image plates of had to be taken off the beamline and carried to the scanner, which didn't allow perfect repositioning. Also, the effects of the signal decay are reduced, because the readout of the plate starts immediately after a scan.

Plate diameter	345mm
Usable detector area	93.480mm ²
Diameter of scanned area	180, 240, 300 or 345mm
Pixel size	150 μ m \times 150 μ m or 100 μ m \times 100 μ m
Dynamic range	17bits (0-131071)
Sensitivity	1 x-ray photon at 8keV
Read out cycles	34s to 108s

Table 3.1: Some specification of the MAR345 image plate detector system [MAR].

Because the diffracted signal from an adsorbed film is orders of magnitude smaller than signal of the substrate, difference measurements are required. The following procedure was employed: A “background” diffraction pattern from the substrate with no gas adsorbed on it was recorded, before a diffraction pattern with the film adsorbed to the substrate was measured. As noted above, this was a new application of the image plate detector system. Therefore a test experiment was performed to examine the usefulness of this approach.

3.2.4 Xenon on graphite: A test experiment

A well-known system, xenon on graphite (see for example [Hei83], [Dim85], [Hon86], [Bir86], [Shr92] [You93] and [Phi97]), has been studied to investigate the suitability of image plate detectors for difference measurements. Two reasons led to the decision to choose this system. First, graphite is a substrate with a high surface area and a low x-ray scattering cross section. It is easy to handle and the probability to have a bad or contaminated sample is low. Second, xenon is a rare gas, available in high purity and a very good x-ray scattering element ($Z=54$).

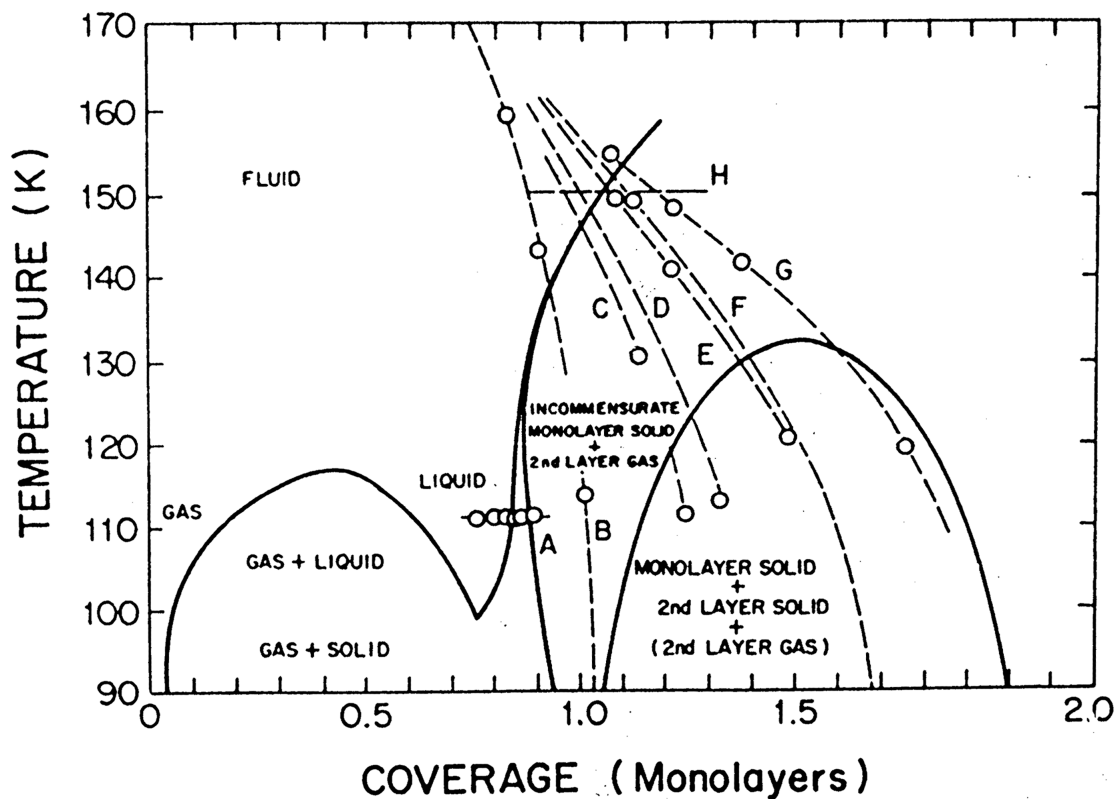


Fig. 3.9: Phase diagram of xenon on graphite between 0 and 2 monolayers. (Fig. 2 from [Hei83])

This system undergoes a liquid to solid transition with increasing coverage (between 0.6 and 1.0 monolayers) at 112K. Heiney *et al* [Hei83] studied this transition with high-resolution x-ray scattering. Going along path A in the phase diagram of xenon on graphite (Figure 3.9) a clear change in the diffraction pattern is observed (Figure 3.10).

A broad Gaussian like diffraction signal is observed at 0.77 monolayers. This signal becomes first more concentrated around $Q \approx 1.6 \text{ \AA}^{-1}$ (scans e and d). Between 0.83 to 0.84 monolayers (scans c and d) the crossover to a Warren lineshape like profile is observed. It

becomes more pronounced for higher coverages and shifts slightly towards higher Q (i.e. the film gets compressed).

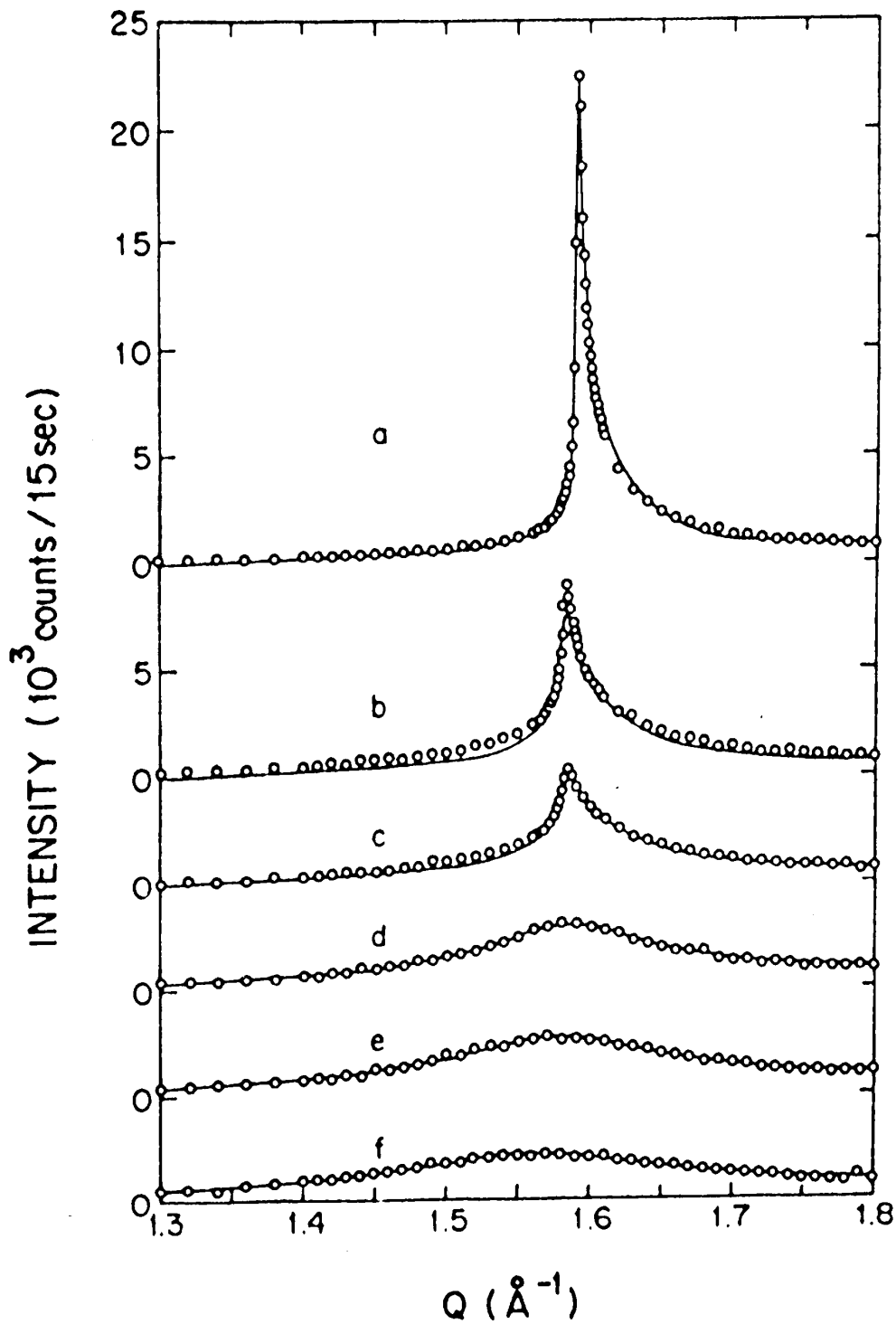


Figure 3.10: Xe (10) peaks with increasing coverage along path A in the phase diagram. The coverages (in units of 1 monolayer) are: f, 0.77; e, 0.81; d, 0.83; c, 0.84; b, 0.86; a, 0.90. (Fig. 11 from [Hei83])

This experiment was repeated with the Fuji BAS image plate detector system. A sample of 0.1g of graphite foam, an isotropic graphite modification from Union Carbide with a specific surface area of $27\text{m}^2/\text{g}$ and about 1000\AA crystal size, was heated under vacuum to 1500°C and loaded into the x-ray diffraction cell. The cell was mounted on the cold finger of a closed cycle helium refrigerator and after the background measurements the gas was dosed onto the sample using an automated gas handling system.

The investigated coverages are indicated as fraction of the monolayer capacity as determined with the B-point method of the Xe/Gr isotherm (Figure 3.11). The monolayer height was estimated to be 7.2Torr .

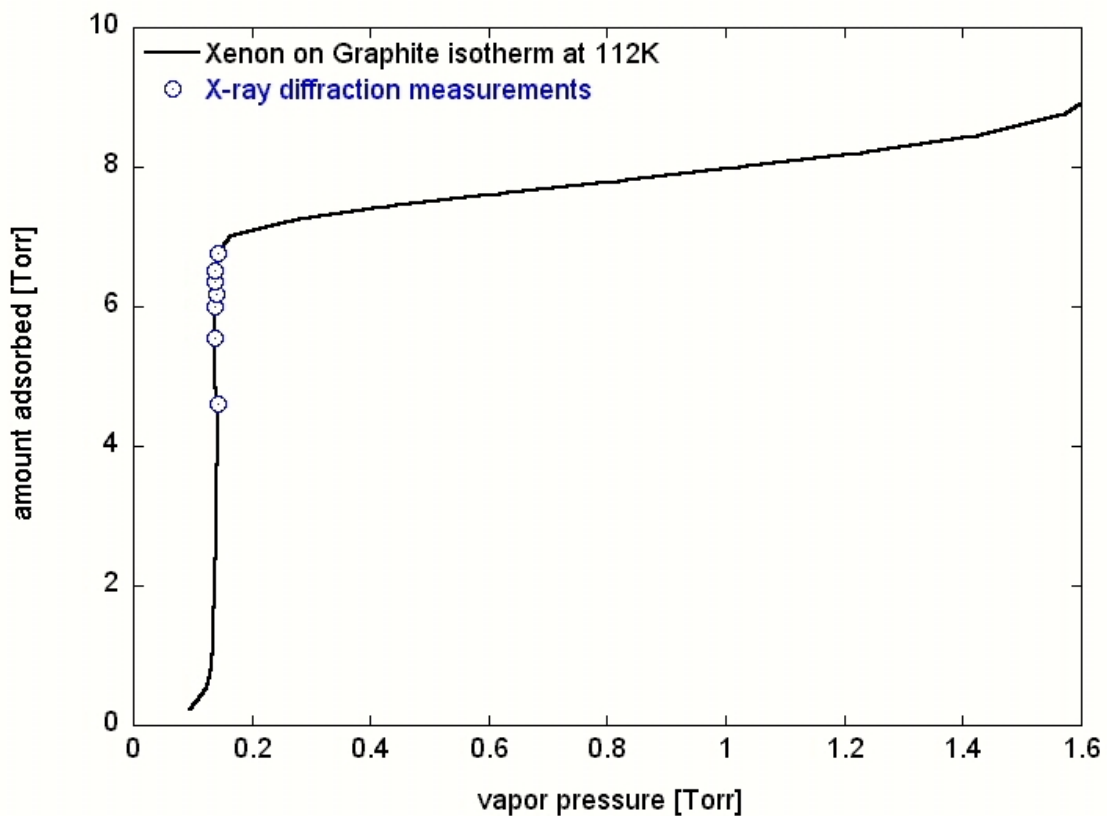


Figure 3.11: Part of the adsorption isotherm of xenon on graphite at 112K. The markers indicate the coverages of the x-ray measurements.

The measurements had an exposure time of 120s and covered a Q range of up to 4\AA^{-1} . The difference plots of the data show clearly the expected behavior of a liquid (broad diffraction signal) to solid (sharp and two-dimensional Warren Lineshape [War41]) transition. Figure 3.12 shows the (1,0) reflection and the inset the (1,1) reflection due to the adsorbed film of xenon.

The image plate data shows about the same statistical uncertainties as the data obtained by Heiney et al. The data collection time for a point detector is around 20s per point (including motor movements) so that the total time for a scan easily adds up to 30min (90 points over a Q range of 2\AA^{-1}). It took about 3-4 min for each scan with the image plate detector (120s exposure and 1-2 min of scanning time). This is a reduction of data collection time of an order of magnitude as predicted. The ability to reproduce the measurements from Heiney et al supports that the use of image plate detectors to study adsorbed films on powdered substances is reasonable.

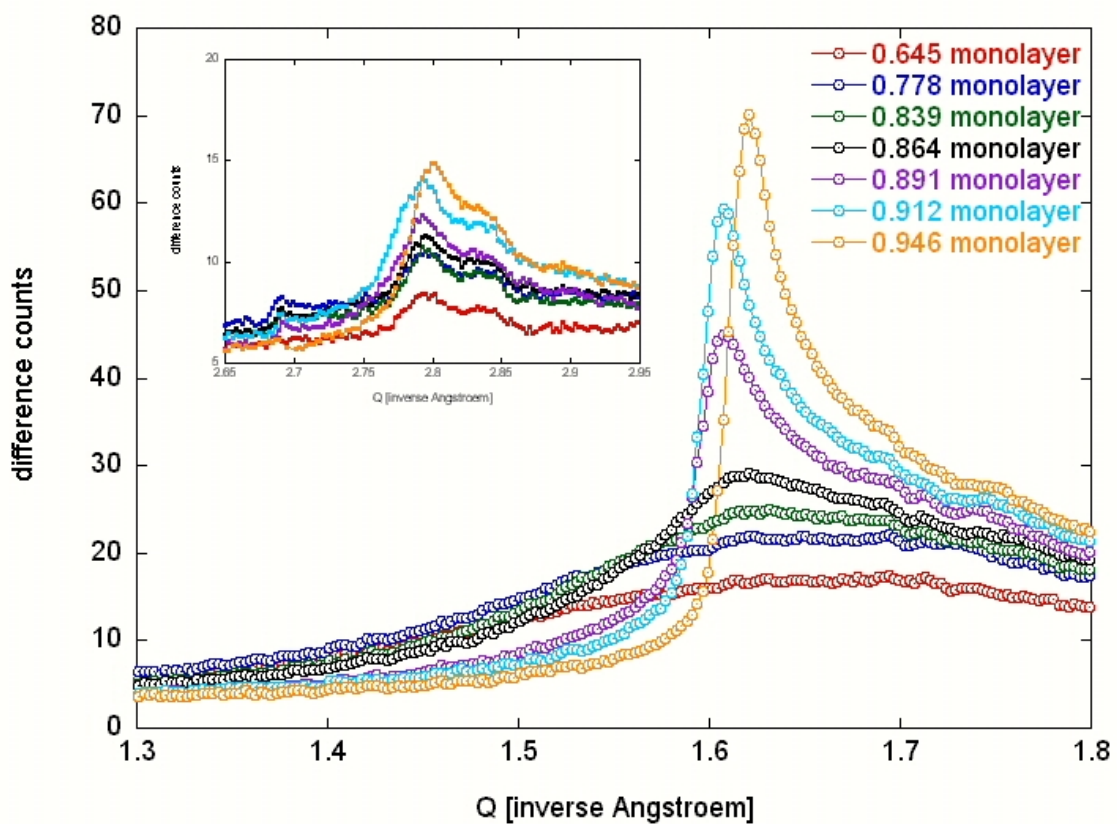


Figure 3.12: Diffraction pattern of xenon on graphite observed with the Fuji BAS image plate detector. The liquid to solid transition going along path A in the phase diagram. The (1,0) reflection (large) and the (1,1) reflection (inset).

3.3 The adsorbates:

The methyl halides are a group of polar derivatives of methane, where halogen atoms (F, Cl, Br or I) are replacing hydrogen atoms of the methane molecule. Their adsorption properties on substrates like graphite, boron nitride or metal oxides (e.g. magnesium oxide) are of interest since size (Figure 3.13) and dipole moment vary. This offers the possibility to study e.g. 2D electric ordering as a function of those two parameters and to gain further information about wetting properties of very thin films of polar molecules.

Furthermore, the adsorption properties of this group of molecules are already well known on graphite [Kno92] and comparisons between adsorption properties on different substrate materials might lead to a better understanding of adsorbate-adsorbate and adsorbate-substrate interactions in general.

Three methyl halides (CH_3Cl , CH_3Br and CH_3I) were examined in this study. From this point on the term ‘methyl halides’ is used to refer to those three molecules. This section provides important background information on the structural and thermodynamic properties (Table 3.2) for each of these molecules.

		CH_3Cl	CH_3Br	CH_3I
Molecular Weight:	²	50.488 grams	94.939 grams	141.94 grams
Boiling point @ 1 atm	³	248.93K	276.71K	315.65K
Freezing point in Air T_{Tr} at 1 atm	³	175.43K	179.55K	206.70K
Transition point	³		173.74 K	
Vapor pressure @ 294.25K	³	510kPa	191kPa	54.4kPa
Vapor pressure at T_{Tr}	²	0.825kpa		
Electric dipole moment	²	1.87D	1.80D	1.65D
Heat of fusion at T_{Tr}	^{3,4}	6.431kJ/mol	5.979kJ/mol	
Heat of sublimation [176K-227K]	⁴			40.2kJ/mol
Heat of fusion at the transition point	⁴		0.473kJ/mol	
$d_{\text{C-H}}$	¹	1.109Å	1.101Å	1.100Å
$d_{\text{C-R}}$ (R=Cl, Br, I)	¹	1.779Å	1.939Å	2.139Å
$\angle\text{H-C-H}$	¹	110.00°	110.48°	110.58°
$\angle\text{H-C-R}$ (R=Cl, Br, I)	¹	108.94°	108.44°	108.34°

Table 3.2: Physical properties of methyl chloride, methyl bromide and methyl iodide [Gor48]¹, [NIST]², [MAT]³, [NBS]⁴.

3.3.1 Chloromethane:

Chloromethane (methyl chloride or CH_3Cl) is a highly flammable, toxic gas with a sweetish, ethereal odor. First prepared about 1830 from methanol, sulfuric acid and sodium chloride, it was later commercially produced in the reaction of methanol with hydrogen chloride or of methane with chlorine. It is used as a catalyst solvent in butyl rubber, in organic synthesis, in the manufacturing of tetramethyllead and as a starting material in the production of organic chemicals such as methyl mercaptan, methylene chloride, chloroform and carbon tetrafluoride. In the past it was also used as a refrigerant, but less toxic and less flammable substances have replaced it.

CH_3Cl has C_{3v} symmetry. The intra-molecule distances are $d_{\text{C-H}} = 1.109 \text{ \AA}$ and $d_{\text{C-Cl}} = 1.779 \text{ \AA}$ and H-C-H and H-C-Cl bond angles of 110.0° and 108.94° respectively [Gor48]. Methyl chloride has a permanent dipole moment of 1.87D due to the highly electro-negative character of the chlorine atom.

Chloromethane forms an orthorhombic bulk crystal structure with $\text{Cmc}2_1$ symmetry at 148K with the following unit cell lattice constants: $a = 6.495 \pm 0.01 \text{ \AA}$, $b = 5.139 \pm 0.01 \text{ \AA}$ and $c = 7.523 \pm 0.01 \text{ \AA}$. This cell contains four molecules [Bur53].

Several vapor pressure studies have been performed on chloromethane. The coefficients for Clausius-Clapeyron's or Antoine's equation have been calculated for various temperature regions [Bah95], [NIST] and [MAT].

$$\log_{10} p [\text{Torr}] = A - \frac{B}{T[\text{K}]} \qquad \log_{10} p [\text{Torr}] = A - \frac{B}{T[\text{K}] + C} \qquad 3.1$$

These values are combined in Table 3.3.

Temperature [K]	A	B	C
130.00—152.00	10.355 ± 0.03	1660 ± 4	
154.00—174.00	10.115 ± 0.02	1622 ± 3	
180.00—190.00	8.055 ± 0.03	1266 ± 5	
191.00—204.00	7.855 ± 0.07	1229 ± 14	
183.15—249.35	7.02964	916.223	-28.47
198.15—278.15	7.10017	951.561	-23.47
303.15—416.25	7.79368	1427.529	45.14

Table 3.3: Coefficients of the Clausius-Clapeyron - or Antoine's equation of the methyl chloride vapor pressure [Bah95], [NIST], [MAT].

3.3.2 Bromomethane:

Bromomethane (methyl bromide or CH_3Br) is practically a nonflammable gas except in the narrow range of 10—16% by volume in air. At room temperature and atmospheric pressure it is a colorless, poisonous gas that in relative high concentrations has a chloroform-like odor.

Bromomethane is produced from methanol and hydrobromic acid in the presence of catalysts or dehydrating agents. It is widely used in organic synthesis, for example in the reaction with magnesium it forms the Grignard reagent, in the Wurtz synthesis (with sodium), and the reaction with alkali alkoxides is used in the Williamson synthesis. It was also widely used as a fumigant, but recognition of the danger associated with its handling and the implications in the depletion of the ozone layer of the atmosphere have led to a total ban of the substance from the year 2005 onward.

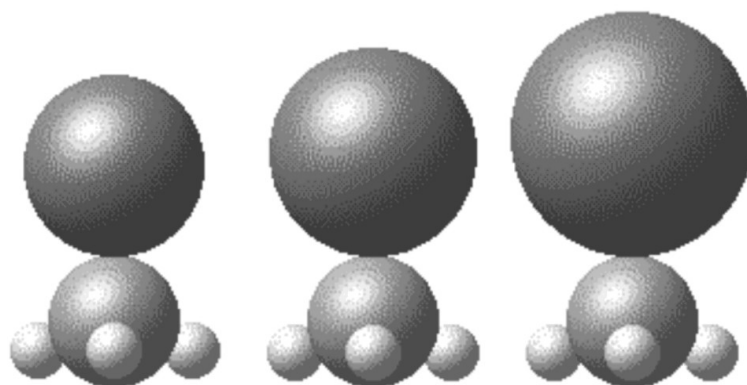


Figure 3.13: Schematic view of methyl halide molecules (CH_3Cl [left], CH_3Br and CH_3I [right]). The diameters are proportional to the relative sizes of the van der Waals radii of the atoms.

Methyl bromide forms two different crystal structures depending on temperature. Below 173.74 K the crystal is orthorhombic with the space group Pnma . The unit cell contains four molecules and has the dimensions: $a = 4.511 \pm 0.010 \text{ \AA}$, $b = 6.504 \pm 0.010 \text{ \AA}$ and $c = 9.350 \pm 0.010 \text{ \AA}$. At temperatures above 173.74 K the α phase exists. It is also orthorhombic, but has the space group $\text{Cmc}2_1$. The dimensions of the unit cell are $a = 6.697 \pm 0.010 \text{ \AA}$, $b = 5.400 \pm 0.010 \text{ \AA}$ and $c = 7.728 \pm 0.010 \text{ \AA}$. It contains four molecules. Both crystal structures show a quasi-two-dimensional character [Kaw73], [Ger86].

Temperature [K]	A	B	C
203.00—276.70	7.14394	1069.708	-25.771

Table 3.4: Coefficients of Antoine's equation of the methyl bromide vapor pressure [NIST].

Only limited vapor pressure measurements have been performed on CH₃Br (Table 3.4). The vapor pressure is extremely low below 200K and thus very difficult to determine.

3.3.3 Iodomethane

Iodomethane (methyl iodide or CH₃I) is a highly toxic colorless liquid at room temperature. It turns brownish upon exposure to light and has a pungent odor. The material is readily adsorbed through the skin so extreme care in handling is necessary.

Methyl iodide is used as an intermediate in the manufacturing of some pharmaceuticals and pesticides. It is also used in methylation processes and in the field of microscopy. Iodomethane has been considered for use as a fire extinguisher and as an insecticidal fumigant to replace methyl bromide.

Temperature [K]	A	B	C
218.00—315.50	7.0306	1177.780	-32.058
315.50—521.00	7.0241	1223.831	-20.179
273.20—307.50	7.1439	1069.708	-25.771

Table 3.5: Coefficients of Antoine's equation of the methyl bromide vapor pressure [NIST].

Methyl iodide forms an orthorhombic structure with the space group Pnma. Kawaguchi et al. investigated it with x-ray diffraction. The dimensions of the unit cell are $a = 4.597 \pm 0.016 \text{ \AA}$, $b = 6.987 \pm 0.012 \text{ \AA}$ and $c = 10.117 \pm 0.011 \text{ \AA}$. The unit cell contains 4 molecules [Kaw73].

Several vapor pressure studies have been carried out for Iodomethane and the results are summarized in Table 3.5. None of the investigations extended below the triple point $T_{Tr}=206.70\text{K}$.

3.4 The substrates:

The adsorption properties of various atoms or molecules on many different materials have been investigated. Metals, metal oxides, graphite in several different modifications and boron nitride are just a few of the substrates used in the past.

While traditional 'surface science' experiments have been performed using single crystals, there are some distinct advantages using crystalline powders for the adsorption of molecular films. Using powders to study adsorbed films allows the establishment of thermodynamic equilibrium or at least quasi-equilibrium conditions. However, these materials need to fulfill certain criteria to be suitable for use in the study of adsorbed films with single crystal or powder methods.

Regardless of the technique, the primary requirement is that the surface geometry of the substance to be investigated should be uniform (i.e. only one crystal plane is exposed to the adsorbate, e.g. only the (100) surface of MgO). This uniformity should extend over sufficiently large areas (i.e. at least a few 1000\AA^2) so that the adsorbed film experiences a uniform interaction with the substrate which is not dominated by imperfections of the crystal (edges and/or defects) thus revealing the ‘true’ behavior of the adsorbate molecules induced by the gas solid interaction.

However, in order to perform successful experiments on these adsorbate-substrate systems with adsorption isotherms and with x-ray or neutron powder diffraction, it necessary to use powders with sufficiently large surface areas ($>1\text{m}^2/\text{g}$) and surface to volume ratios. A large surface area allows to easy monitor and control the number of adsorbed molecules on the substrate surface in the adsorption isotherm studies and a large surface to volume ratio helps to separate the signal of the adsorbed film from the normally strong signal of the substrate in the powder diffraction experiments.

Since these powders would consist of very small particles, the successful investigation of properties of adsorbed films with these experimental techniques depends critically on the right choice of powders, which fulfill both criteria at the same time.

Other important criteria involve the availability, preparation and handling procedures and properties influencing the suitability of different investigation methods, e.g. the scattering cross sections.

Magnesium oxide and boron nitride are two substrates well suited to investigate adsorbed film with adsorption isotherms and XPD. Since both materials are used in this study of the adsorption properties of the methyl halides, a brief review of the properties of these materials is found in the following sections.

3.4.1 Boron nitride:

Boron nitride is used in many different applications (e.g. in cosmetic powders, as a vessel for crystal growth and as functional fillers). It forms as either cubic or hexagonal crystals. The hexagonal form (group $P6_3/mmc$) of boron nitride is very similar to graphite.

It consists of small disk like crystals (Figure 3.14). It is a layered material where individual layers (basal planes) are bound together by the weak van der Waals force. The distance between these layers is $c_{BN} = 6.656\text{\AA}$ ($c_{graphite} = 6.690\text{\AA}$). The hexagonal structure of the basal planes has a lattice constant of $a_{BN} = 2.505\text{\AA}$. This is about 2% larger than the lattice constant of the graphite basal plane $a_{graphite} = 2.457\text{\AA}$. A view of this surface is shown in Figure 3.15. This structural similarity is one of the reasons to investigate adsorbed films on BN. Comparisons to the results on graphite could lead to a better understanding of the adsorbate-substrate interactions.

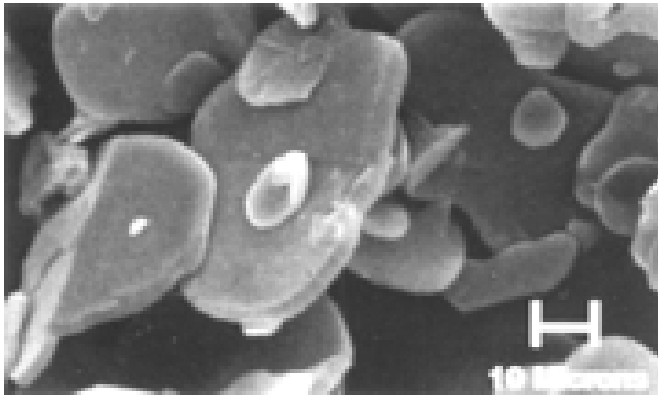


Figure 3.14: Scanning electron micrograph of Boron Nitride powder particles of the powder PT110 of the Advanced Ceramics cooperation. It can be used as example for BN powders in general.

High quality powders with different surface areas (0.1 to $20 \text{ m}^2/\text{g}$) are commercially available. The boron nitride for this study was obtained by Alfa Aesar (BN, 99.5%, metal basis, item#11078, lott#H17F02) in form of a hexagonal 325 mesh powder. Wolfson et al. [Wol96] undertook a comparative study of the quality of different BN powders.

While there are structural similarities between BN and graphite, there are some drawbacks for BN. Unlike the easy sample handling and preparation for graphite powders, boron nitride requires a very rigid sample preparation to remove unwanted materials from the exposed surfaces before adsorption experiments can be performed. Thus, the number of investigated adsorbed systems on BN is relatively small. To our knowledge, only argon (e.g. [Alk91], [Alk92] and [Mig93]), nitrogen ([Alk94], [Shr96]) and krypton ([Dia99], [Li96]) have been used in similar studies so far. However, high quality powders can be prepared using the following procedure:

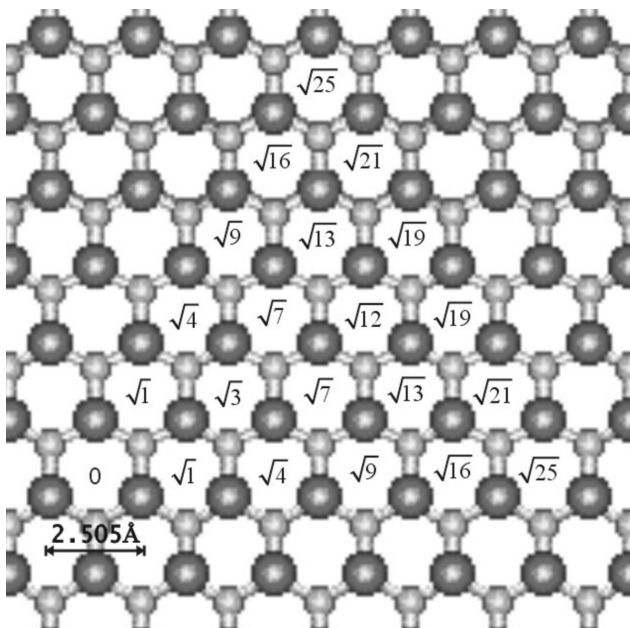


Figure 3.15: Schematic view of the (001) plane of BN. The distance between two neighboring hexagons is $a_{BN} = 2.505 \text{ \AA}$. The numbers in the hexagons are distances from the origin (0) in units of a_{BN} . While the small balls indicate the boron atoms, the nitrogen atoms are shown as the large balls.

The BN samples are loaded into a small alumina crucible that is transferred into a quartz tube, which is stuck into a tube furnace. First a flow (5-10 bubbles per second) of ammonia gas is

run over the sample for a few (at least 3-4) hours at room temperature. After this period the gas flow is stopped and the sample is kept under an atmosphere of ammonia over night. The next day a high flow (10-20 bubbles per second) of ammonia is turned on again while the sample is slowly heated to 1000°C and kept at this temperature for 1-2 hours. After two hours the gas flow is reduced (2-3 bubbles per second) and the sample is cooled to a temperature of 800°C, at which it is held for another 1-2 hours. So prepared the crucible with the powder is removed from the tube furnace. While it is still hot it is transferred in air into another quartz tube and vacuum baked (10^{-7} Torr) at 700°C for 12-16 hours.

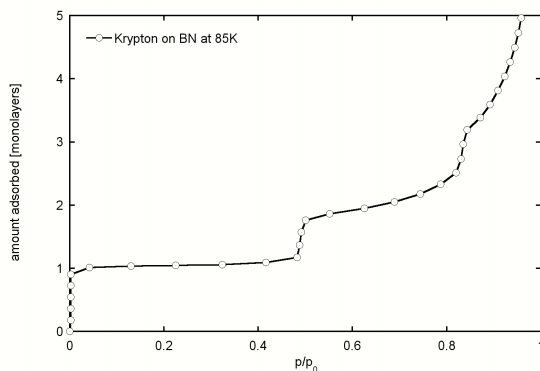


Figure 3.16: Example isotherm of krypton on boron nitride at 85K. The growth of at least three distinct layers is clearly visible.

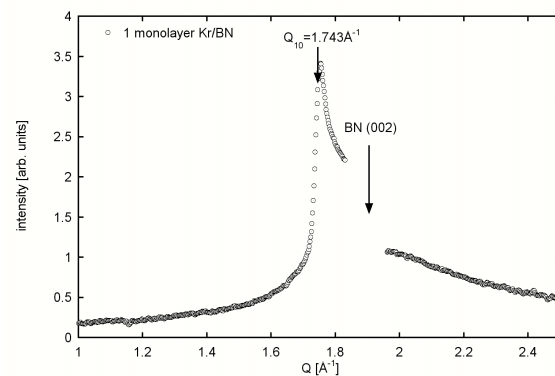


Figure 3.17: Difference spectra of krypton on BN. The spectrum was taken at completion of the isotherm [left].

After the heat treatment in vacuum the sealed quartz tube is transferred to a rare gas filled glovebox and the powder is loaded into a sample cell. Before the sample is used in adsorption experiments it is very important to establish the quality. This can be done using a krypton isotherm. Migone and coworkers have established that high quality BN shows multilayer Kr film growth [Dia99]. The isotherm can be used to determine the surface area of the sample, since diffraction data revealed that the monolayer forms a triangular 2D lattice similar to the incommensurate structure of Kr on graphite [Ste84]. Figure 3.16 and 3.17 show a sample isotherm of krypton on boron nitride and one x-ray diffraction pattern taken at the completion of the monolayer.

3.4.2 Magnesium oxide:

MgO is mainly commercially produced from naturally available minerals like magnesite or from magnesium chloride rich brine or seawater [MMM]. It is a white solid at room temperature. Depending on the starting material different steps are used in the production process, but the steps are essentially the same at the calcination point $[2\text{Mg}(\text{OH})_2 \xrightarrow{\text{heat}} 2\text{MgO} + 2\text{H}_2\text{O}$ (steam)]. Three different commercial grades of magnesium oxide (Figure 3.18) can be pro-

duced depending on the temperature range used at this point. These grades are classified by the reactivity of the powder as ‘dead burned’ (1500-2000°C, surface area: $<0.1\text{m}^2/\text{g}$), ‘hard burned’ (1000-1500°C surface area: $0.1\text{-}1.0\text{m}^2/\text{g}$) and ‘light burned’ (700-1000°C surface area: $1.0\text{-}250\text{m}^2/\text{g}$). TEM examples of these grades are shown in Figure 3.18.



Figure 3.18: TEM picture of dead, hard and light burned MgO [from left]. Clearly visible is the reduced particle size leading to larger surfaces areas [MMM].

Magnesium oxide has multiple industrial uses. It is used in the annealing processes of the steel industry, as filler or acid acceptor in plastic manufacturing, as a binder in grinding wheels. It acts as acid neutralizer for wastewater treatment and precipitates heavy metals. Most interesting for the study of adsorbed films is the use of magnesium oxide as scrubber in smoke stakes to remove e.g. sulfur emissions and to reduce the corrosion of steel pipes. The studies could help understanding the catalytic processes microscopically and subsequently lead to the development of better catalysts.

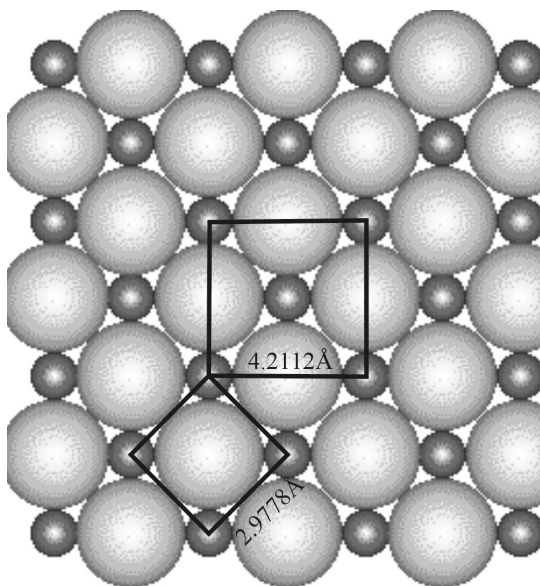


Figure 3.19: View of the (100) surface of magnesium oxide. The 2D unit cell ($a_{\text{MgO-2D}} = 2.9778\text{Å}$) and a projection of the 3D unit cell ($a_{\text{MgO-3D}} = 4.2112\text{Å}$) are shown. While the Mg atoms are marked as small balls, the large ones indicate the oxygen atoms.

A great deal of interest still exists for the study of adsorption on substrates exhibiting four-fold symmetry. Magnesium oxide is an ionic metal oxide with sodium chloride structure.

The three-dimensional lattice constant is $a_{MgO-3D} = 4.2112\text{\AA}$. When magnesium ribbons are burned in air, MgO forms crystallites with almost entirely (100) surface exposure (Figure 3.19). The 2D unit cell of the (100) surface is a centered square with $a_{MgO-2D} = 2.9778\text{\AA}$, which is the distance between two atoms of the same kind (Figure 3.19). Other surfaces are not stable and facet into steps of (100) surfaces [Har99].

The burning of magnesium ribbon to produce MgO powders is a tedious process. Therefore the availability of high quality powders was very limited for a long time. Even though Dash et al [Das78] already reported the production of uniform magnesium oxide smoke, it is not until the mid 1980's ([Cou84], [Cou85] and [Jor85]) when magnesium oxide powders had been successfully produced in quantities large enough to be used as a substrate for the study of physisorbed systems (in this case rare gases and methane). To produce these 'smoke' MgO powders magnesium metal stripes are burned in a mixture of oxygen (~20%) and a rare gas. The rapid reaction speed allows for only a limited control of the particle size and surface area and burning ribbons is not a very effective process to produce larger quantities of MgO. The production of a high quality sample is limited by the purity of the MgO ribbons and the subsequent exposure of the 'smoke' particles to air. These factors limited the number of studies of adsorbed films on magnesium oxide compared to the larger number of systems investigated on graphite.

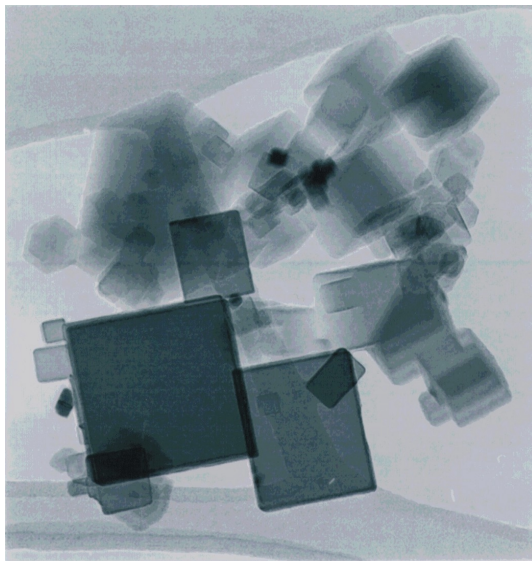


Figure 3.20: TEM picture of a high quality MgO powder produced with the new method by Kunmann and Larese [Kun01]. The length of a side of the large cube is about 2000Å.

Kunmann and Larese developed a new method to produce high quality powders of pure and doped metal oxides (general formula $M_{1-x}R_xO$, where M, R=Mg, Zn, Cr, Cu, Ni, Fe, Ni and Li) with the possibility to control the surface area of these powders between 1-100m²/g [Kun01]. It is a very reliable method that allows the production of large quantities of uniform powders (e.g. the amount needed for neutron experiments or for possible industrial uses as catalysts). Figure 3.20 shows a TEM picture of a magnesium oxide sample produced using

this method. The size of the largest crystal is about 2000Å on a cube side and the predominant crystal shape is cubic (no pyramidal forms are observed).

It was briefly mentioned above that the other reason, why MgO had only a limited role as substrate for adsorption studies to date is due to its high reactivity, especially with water [Alm98], [Hol97], which makes sample handling and preparation a very difficult task. The MgO substrate preparation procedure is described next.

Immediately after the powder is produced it is filled into a quartz tube. This tube is outfitted with a vacuum valve, which allows evacuation using a turbo molecular pump station when it is placed into a tube furnace. The valve is slowly opened and the air is removed from the tube before the sample is slowly heated to slightly above 300°C. At this temperature mostly CO₂ and H₂O are desorbing from the powder. Visual inspection of the sample at this stage finds that the powder is very active (almost ‘boiling’ or ‘bubbling’) as physisorbed gas molecules evolve from the particles. Care must be taken that these particles do not flow into the gas stream and contaminate valves or the pump station. After a few hours of heating and pumping the temperature is raised to around 950°C and the sample is baked *invacuo* for around 36 hours until the pressure reaches the base of the pump station ($\sim 2 \times 10^{-7}$ Torr). Then the valve on the quartz tube is closed and the sample is cooled to room temperature before being transferred into a glovebox. Before use the glovebox has been evacuated and flushed with dry argon (99.998% pure) multiple times (>3) before the quartz tube is opened under argon atmosphere and the sample cell is loaded with the powder. The sealed sample cell is transferred out of the glovebox and the remaining argon is instantly evacuated. Then the cell is leak tested, before it is mounted onto the Displex.

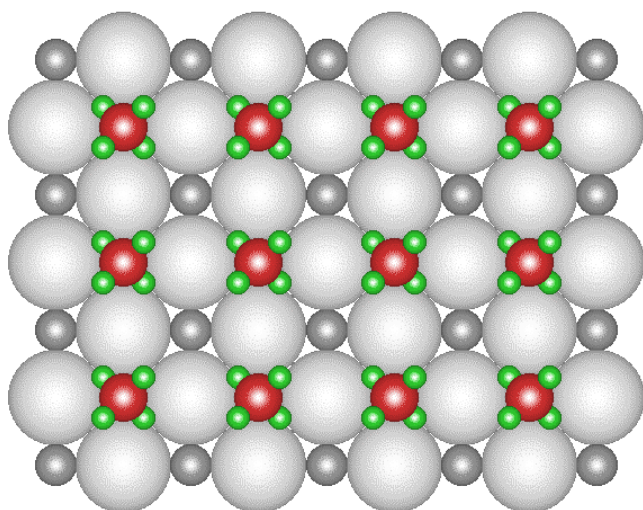


Figure 3.21: $\sqrt{2} \times \sqrt{2}$ $R45^\circ$ commensurate monolayer structure of methane on MgO.

Methane adsorbed on magnesium oxide is an ideal system to test the quality of the powder such as krypton is for BN. This well investigated system (e.g. [Cou85], [Bie87], [Lar98] and [Fre00]) shows a layer-by-layer growth (see Figure 3.3) and forms a solid ($\sqrt{2} \times \sqrt{2}$ $R45^\circ$) square commensurate monolayer structure (Figure 3.21) similar to the (100) plane of bulk

methane at liquid nitrogen temperatures. The main reason for this distinct growth mode is the good match (better than 2%) between the substrate lattice and the bulk crystal distances. The number and sharpness of the adsorption steps and the ratio of the heights (proportional to the gas capacity) of the first and second adsorption step is a good measure for the quality of the sample. Adsorption isotherms of high quality MgO powders will show up to six distinct layers and have nearly equal step height for the first two or three layers.

Chapter 4:

Thermodynamic investigations

This chapter presents the thermodynamic investigations of thin adsorbed films of methyl halides on magnesium oxide and boron nitride. High-resolution volumetric adsorption isotherms recorded over an extended temperature interval have been used as experimental probe to determine thermodynamic quantities and to identify regions of potential phase transitions.

These measurements are experimentally challenging because the methyl halides show interesting adsorption properties at very low saturated vapor pressures. This probably explains why earlier thermodynamic investigations of the methyl halides on graphite using adsorption isotherm techniques [Bah95] and heat capacity measurements [Ina91] were limited to CH_3Cl . Published data of the saturated vapor pressure (SVP) for CH_3Br and CH_3I extending into temperature regimes below the bulk triple points could not be found. This made it difficult to use the SVP as a crosscheck of the sample temperature for these two molecules.

The specifications of the adsorbates used were: a) liquid phase, 99.9% pure CH_3Cl (Matheson), b) 99.8% pure Methyl Bromide (Matheson) and c) CH_3I with a purity better than 99.5% (Sigma-Aldrich). Multiple freeze-thaw distillation cycles were performed to purify the adsorbates before dosed onto the substrate. Successive helium gas expansions were used to determine the ‘dead space’ volume of the sample cell and attached capillary. It was determined to be a few cm^3 depending on the specific sample cell used in the individual experiment and slightly temperature dependent. The adsorption data were corrected for this effect.

The first part of this chapter presents measurements performed on magnesium oxide samples. Sets of adsorption isotherm are shown and analyzed in the order CH_3Cl , CH_3Br and CH_3I . Layering transitions and wetting properties of these films are discussed. The two-dimensional isothermal compressibility and the isosteric heat of adsorption are determined. The second part addresses measurements involving boron nitride as a substrate. These investigations concentrated on searching for a low-density to high-density phase transition of CH_3Cl as it was observed on graphite. These measurements were performed to determine the packing densities of the monolayer films for use in the structural investigations presented later.

4.1 Adsorption isotherms on MgO

As noted earlier all the MgO powders used in this study were synthesized using the new process described in chapter 3 [Kun01]. The powders had a surface area of approximately 8–10 m²/g. At the start of every run a methane isotherm was recorded in order to establish the quality of the MgO sample and to determine the surface area of each batch before the adsorption studies of the methyl halides started. Methane isotherms were repeated at random points between isotherms of the methyl halides to determine if the powder quality was modified/degraded due to the interaction with the adsorbate.

4.1.1 Methyl chloride on magnesium oxide

To determine the wetting properties of methyl chloride on magnesium oxide more than 20 adsorption isotherms were measured on two different MgO samples in the temperature range between 132 < T < 180 K. A subset of these isotherms is shown in Figure 4.1. The amount adsorbed is plotted versus the difference in chemical potential $\mu - \mu_0 \approx T \ln(p/p_0)$.

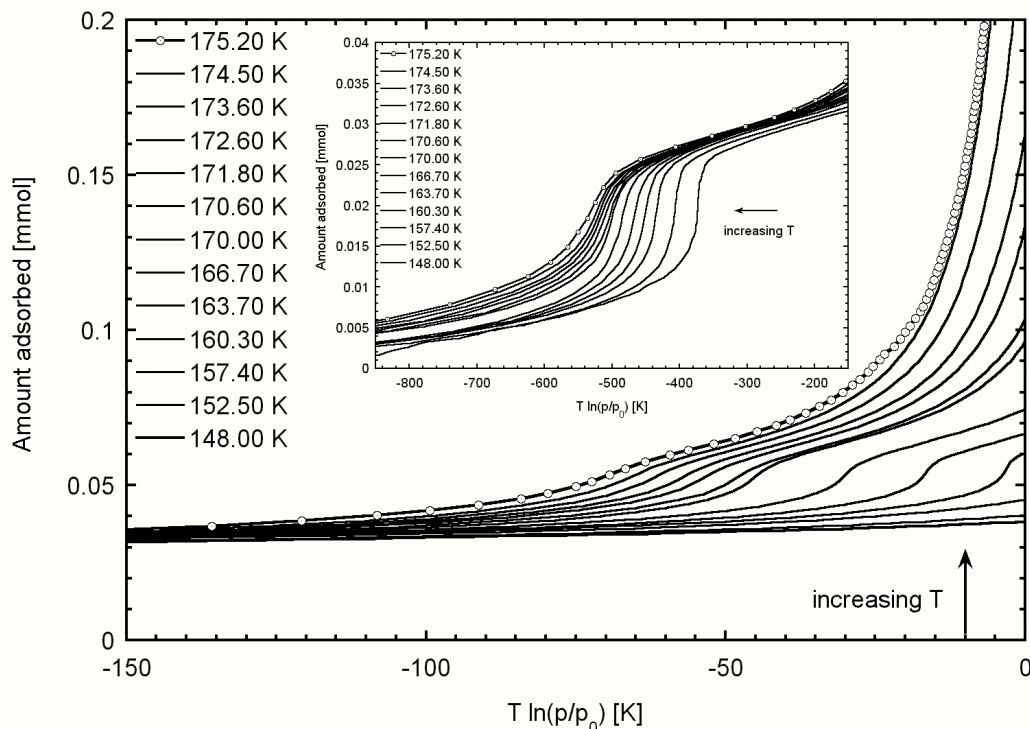


Figure 4.1: A subset of CH₃Cl on MgO isotherms. The amount adsorbed increases near $T \ln(p/p_0) = 0$ as a function of temperature. The inset shows the isotherms in the monolayer regime.

The measurements were restricted to temperatures above 132 K because at lower temperatures, the saturated vapor pressures were too small to be reliably determined and at temperatures below 145 K, the resolution of the 16-bit A-to-D converter of the pressure transducer resulted in a step-wise displacement of the data points near the monolayer adsorption step. In order to analyze these low temperature data they had to be smoothed in this particular region (Figure 4.2). The molecular cross section (see Chapter 2, Equation 2.46) of methyl chloride on the MgO (100) surface was estimated to $\sigma = 23.3 \text{ \AA}^2$ at 168 K by comparing the monolayer step heights of the CH_3Cl and CH_4 isotherms.

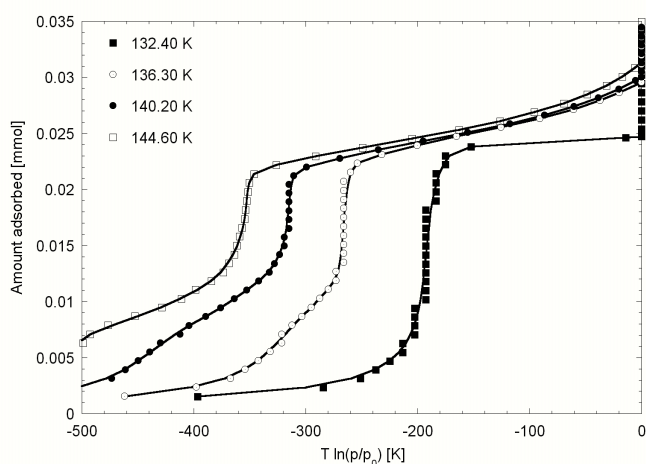


Figure 4.2: Smoothing of the monolayer adsorption step for the low temperature isotherms. The measured data points (indicated with different symbols) show a step-wise curve that resulted from the limited resolution of the A-to-D converter of the pressure transducer. These curve were smoothed (lines) for further analysis.

a) General description

Before turning to a detailed quantitative analysis of the data a few general comments concerning the wetting properties of CH_3Cl on MgO are in order. Several layering/wetting features can be observed. These are indicated by the observation of various features and changes in shape of the isotherms near $T \ln(p/p_0) = 0$. At temperatures below 160.30 K only a single layer forms before evidence of bulk methyl chloride formation appears (i.e. the saturation vapor pressure is reached). This behavior is different from CH_3Cl on graphite, where at low temperatures first a low-density and then a high-density monolayer phase forms. On graphite, this phase transition appeared as a distinct substep in isotherms below 145 K [Bah95]. No evidence of a similar phase change is observed for methyl chloride on magnesium oxide. This change in behavior may not be to surprising since the adsorbate-substrate interaction is significantly different due to the ionic character of the MgO and the four-fold symmetry of the (100) surface as compared to the hexagonal surface structure of graphite.

Also worth mentioning is the movement of the first step position with decreasing temperature towards $T \ln(p/p_0) = 0$ (Figure 4.3a). The 2D compressibility data (analyzed in more detail in the following section) offer the possibility to monitor this behavior. It seems reasonable to wonder whether the observed linear decrease towards lower temperature is an

indication that the film becomes “nonwetting” at low temperatures (a first estimate indicates at around 85K). At higher temperatures a second step appears in the isotherms. By monitoring the location of the maximum of the compressibility corresponding to the second step an reliable estimate for the layering temperature $T_{2nd}=158.9$ K can be obtained as intersection of a linear fit to the data with the x-axis (Figure 4.3b).

The shape of the isotherms also changes near $T \ln(p/p_0) = 0$, however there is no evidence of additional discrete (step-wise) layer formation beyond the second layer. Nevertheless, the shape of the isotherm in this region can be used to distinguish between different wetting modes as mentioned in Chapter 2.

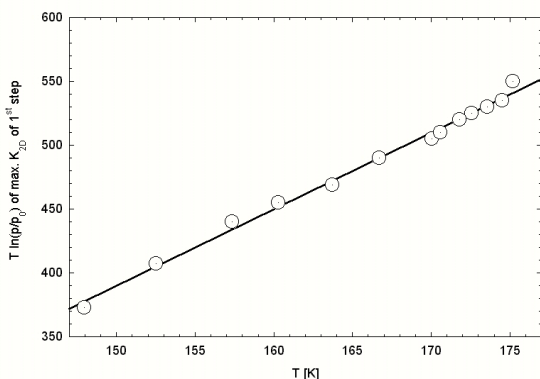


Figure 4.3a: Position of the maximum of the 2D compressibility corresponding to the first step as a function of temperature. The error bars are typically: ± 0.2 in x and ± 5 in y

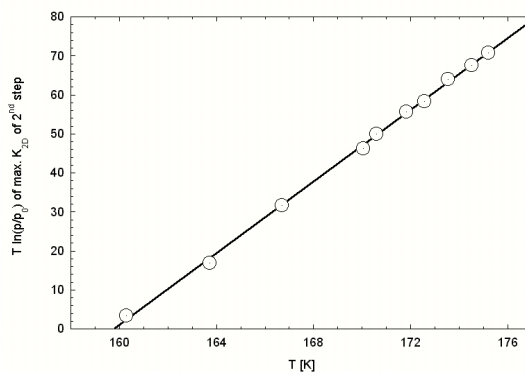


Figure 4.3b: Position of the maximum of the 2D compressibility corresponding to the second step as a function of temperature. The error bars are typically: ± 0.2 in x and ± 1 in y

The wetting is likely referred to as “incomplete” if the amount adsorbed is limited before the bulk saturation vapor pressure (SVP) is reached. This behavior is observed for most of the isotherms. However, two isotherms at 174.50 K and 175.20 K are different. For those isotherms, the SVP was not reached even at the highest coverages (15-20 equivalent layers). This could be an indication that triple point wetting may occur (see Chapter 2.2). The bulk triple point of methyl chloride is $T_{triple}=175.44$ K.

b) The 2D compressibility of methyl chloride on MgO

The 2D isothermal compressibility was calculated from the adsorption isotherm data sets (Equation 2.51). Figure 4.4 shows the compressibility for the first layer as a function of $T \ln(p/p_0)$. Only the data from a subset of the adsorption isotherms is included here. Several comments are appropriate. The figure shows that there is a distinct peak in the compressibility at monolayer completion. The location and shape of this feature is temperature

dependent. As a general trend, the peak moves closer to the bulk chemical potential, decreases in width and grows in height as the temperature decreases. Furthermore, an asymmetric peak shape is observed. The left side of the peaks seems to sit on a plateau, whereas the right side almost drops off to zero.

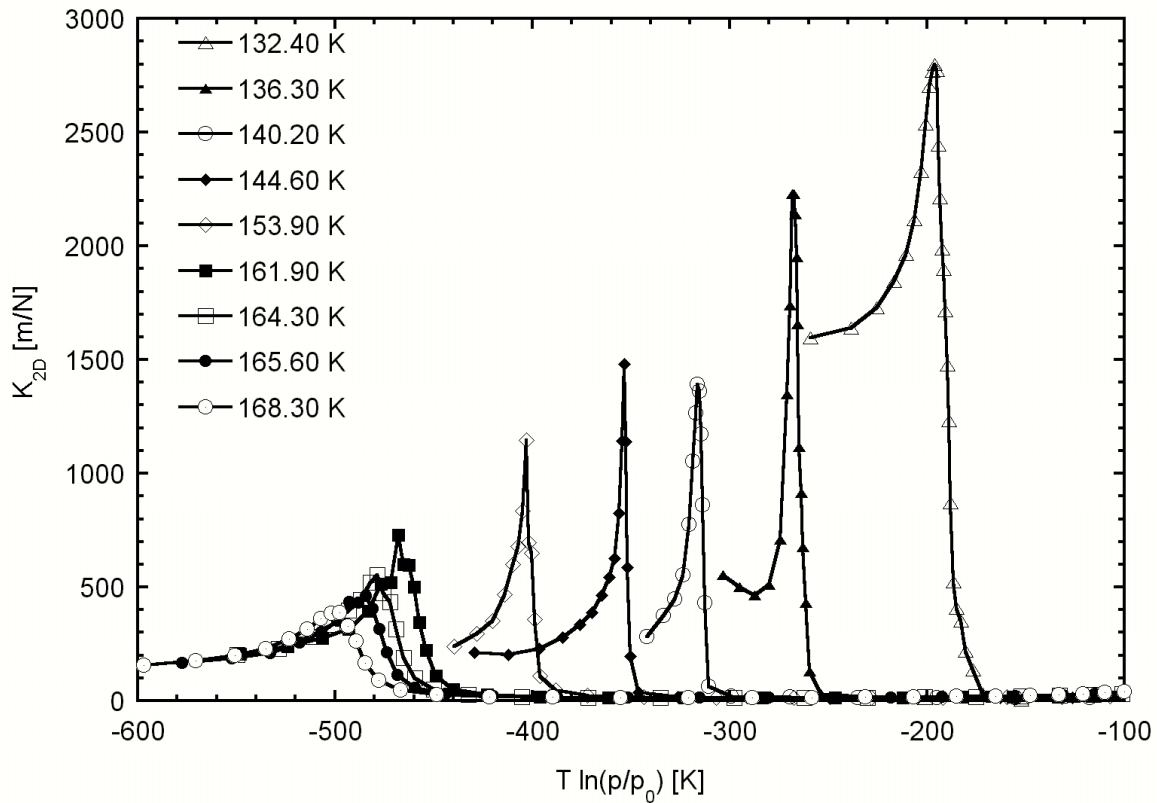


Figure 4.4: 2D compressibility of the first adsorption step of methyl chloride on magnesium oxide as a function of chemical potential.

The phase behavior of the CH_3Cl film was monitored using the compressibility peaks as a function of temperature. The asymmetry of the compressibility as a function of $\mu - \mu_0$ makes it difficult to perform an exact peak analysis. Therefore the difference between the maximum of the peak and half the height of the plateau was defined as the peak height. The result of this analysis is displayed in Figure 4.5. A linear decrease in the peak height with increasing temperature is observed. This gradual increase in the amplitude suggests that the monolayer film does not undergo a discontinuous (first order) structural phase change in this temperature range (see e.g. [Fre00]). Unfortunately, it is not possible to offer additional support to this conjecture by performing an analysis of the peak widths. Here the asymmetry of the compressibility makes it difficult to develop an accurate criterion to describe the width of the K_{2D} feature.

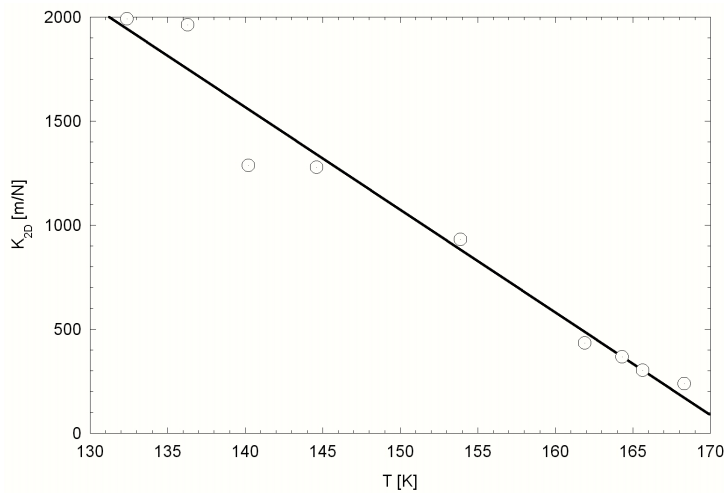


Figure 4.5: The height of the compressibility peak of the monolayer adsorption step is plotted against the sample temperature. The error bars are: ± 0.2 in x and ± 50 in y (with two low temperature exceptions)

A quantitative analysis of K_{2D} is especially difficult at low temperatures because of the low vapor pressures (Figure 4.2). The relative error in position, width and height of K_{2D} introduced larger at temperatures below 145 K and the analysis less reliable.

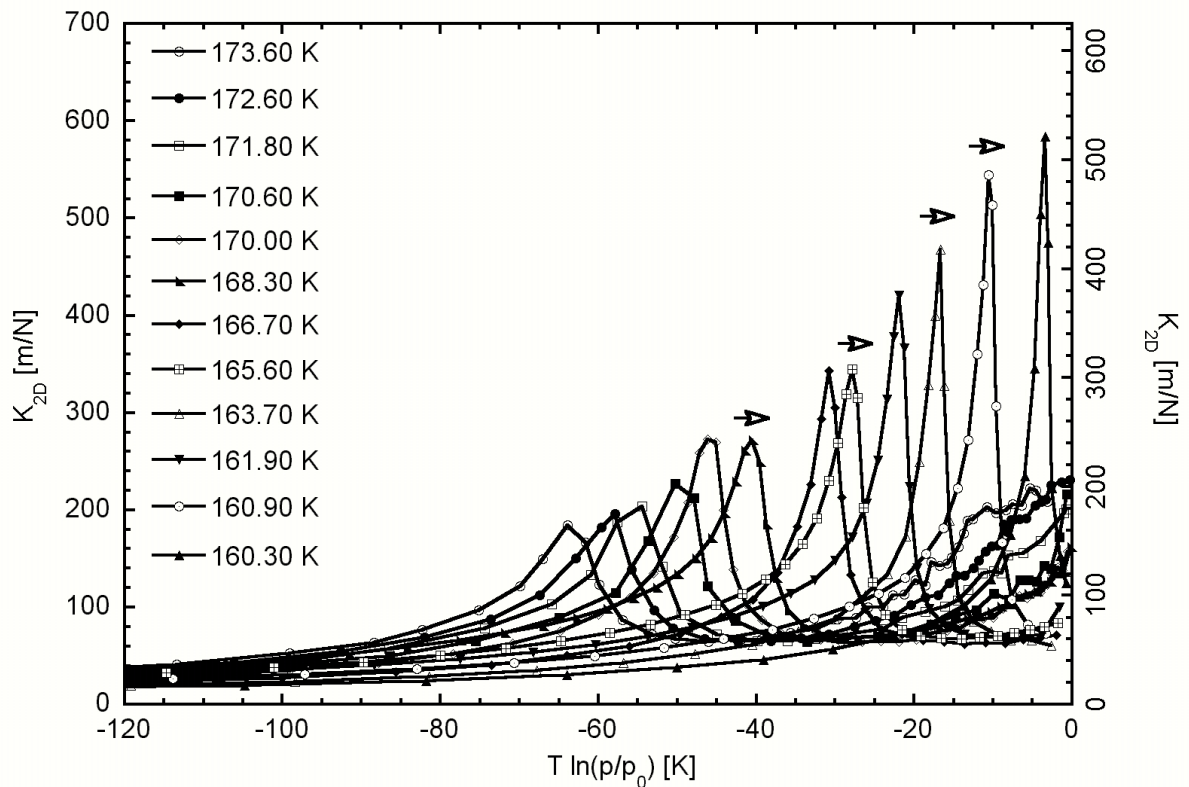


Figure 4.6: Two-dimensional compressibility of the second adsorption step of CH_3Cl on MgO for isotherms above $T_{2\text{nd}}$. Note that the dual scale for compressibility values is induced by the fact that two different samples were investigated.

The compressibility peaks of the second adsorption step were also analyzed. Figure 4.6 shows the 2D compressibility of methyl chloride on MgO for two sets of isotherm measurements at temperatures above T_{2nd} . Since the second step appears at higher absolute pressures, the effects of the limited resolution of the pressure transducer are less important.

As for the first adsorption step, a general trend is observed that the compressibility peak decreases in height, broadens in width and moves toward lower $T \ln(p/p_0)$ with increasing temperature. This is an indication that the thermal energy of the adsorbate molecules increases as a function of temperature and that the disorder of the second layer increases continuously.

A quantitative analysis involving the height and width of these peaks as a function of temperature is displayed in Figures 4.7a and 4.7b where only one set of adsorption isotherm data is shown for clarity. Both figures clearly show a linear dependence. This behavior indicates that also the second layer does not undergo a discontinuous structural phase change over the observed temperature range. The second layer forms probably in a fluid like fashion.

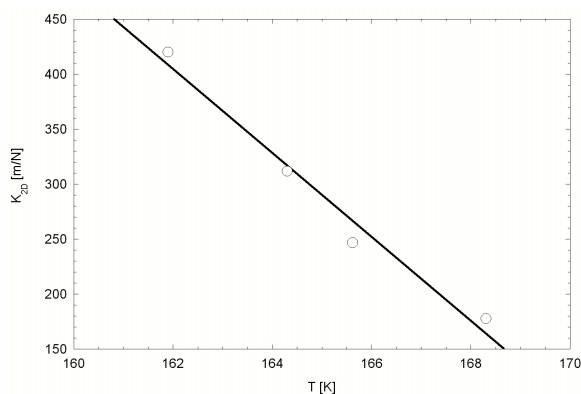


Figure 4.7a: The height of the compressibility peak of the second adsorbed layer plotted versus the sample temperature. The error bars are typically: ± 0.2 in x and ± 20 in y

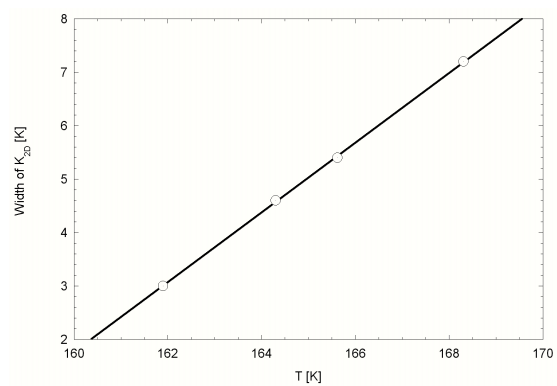


Figure 4.7b: The width of the compressibility peak of the second adsorbed layer plotted versus temperature. The error bars are typically: ± 0.2 in x and ± 0.2 in y

c) The vapor pressure of the adsorption steps

In Chapter 2 it was shown (Equation 2.53) that the vapor pressure of the adsorption steps can be analyzed similarly to the vapor pressure of a bulk material, and can be approximated over a certain temperature range by the Clausius-Clapeyron equation.

Figure 4.8 shows the temperature dependence of the bulk vapor pressure and of the vapor pressure corresponding to the position of the first and second adsorption step in the isotherms. Table 4.1 lists the Clausius-Clapeyron coefficients A and B obtained by a fit of Equation 2.53 to the experimental data.

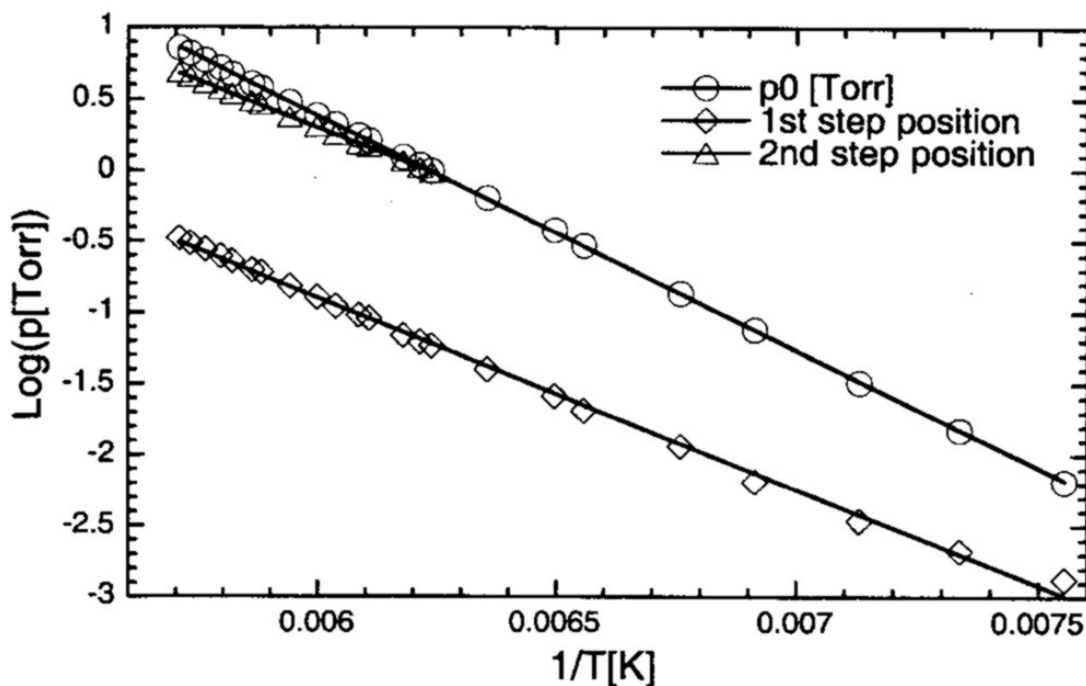


Figure 4.8: Vapor pressure of the adsorption steps as function of temperature. The layering temperature of the second layer was estimated as $T_{2nd}=158.9K$.

Another method often used to estimate the onset temperature of a layering step is to locate where the bulk vapor pressure curve intersects with the vapor pressure curve of that layering step. Whereas the intersection for the second step is within the temperature range covered in the adsorption experiments (i.e. $T_{2nd}=158.9K$), the layering temperature for the first step can only be estimated by extrapolating the fits.

	Saturated vapor pressure of bulk CH_3Cl	Vapor pressure of the 1 st step	Vapor pressure of the 2 nd step
A	1648 ± 3 K	1346 ± 15 K	1313 ± 3
B	10.27 ± 0.03	7.18 ± 0.09	8.18 ± 0.03
R	0.99997	0.9988	0.99994

Table 4.1: Coefficients of the parameters A, B, and R (correlation coefficient) of the Clausius-Clapeyron equation (formula 2.53) as obtained from fits in figure 4.8.

This intersection occurs at ~ 100 K and suggests that a “dewetting” transition may take place for methyl chloride on MgO. Because the vapor pressure is extremely low at $\sim 100K$, it was not possible to verify this prediction experimentally.

d) Wetting behavior of CH₃Cl on MgO near T_{triple}

A more detailed analysis of the methyl chloride film growth on MgO near the bulk triple point (T_{triple}=175.43 K) is a worthwhile undertaking. Figure 4.1 indicates that the amount adsorbed near $T \ln(p/p_0) = 0$ strongly increases with temperature in this region. In Figure 4.9, the film thickness is expressed in layers of CH₃Cl as a function of reduced temperature $t = (T - T_{\text{triple}}) / T_{\text{triple}}$ for several different values of the reduced pressures p/p_0 .

It is interesting to note that even at the highest coverage (limited to about 15–20 equivalent layers in this experiment) the saturated vapor pressure has still not been reached for the isotherms at either 174.50 K or 175.20 K. Although it is not possible to unequivocally state that these data (shown in figure 4.1) represent an asymptotic approach the SVP at $T > 174.5$ K, these data strongly suggest that “complete” wetting takes place at or near T_{triple}.

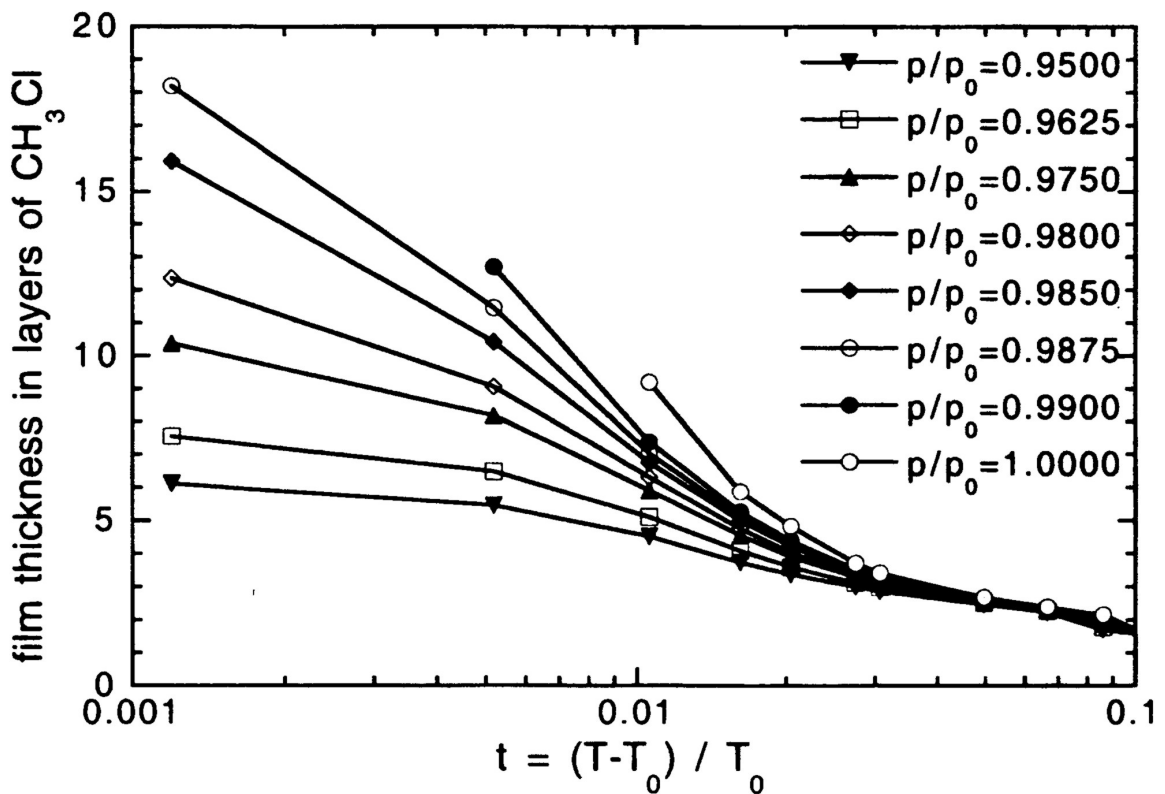


Figure 4.9: Film growth of methyl chloride on MgO as a function of reduced temperature for different reduced pressures p/p_0 . ($T_0 = T_{\text{triple}}$)

Frenkel, Halsey and Hill (FHH) proposed that the long range van der Waals interaction between substrate and adsorbate molecules can be used to describe the behavior of thick physisorbed films (Chapter 2).

Fitting the isotherms at 174.50 K and 175.20 K to the FHH form (Equation 2.45) we find $s = 2.00 \pm 0.08$ and $s = 1.28 \pm 0.12$, respectively. Deviations from the theoretical value

$s=3$ (obtained for nonpolar particles under influence of the van der Waals force) may be related to either the limited coverage range of our measurements or the dipole–dipole interaction between the molecules. Consideration of this additional interaction should reduce the value of the parameter s .

e) The isosteric heat of adsorption

The other thermodynamic quantity that can be readily extracted from a set of closely spaced isotherms is the isosteric heat of adsorption (Chapter 2.2). This quantity represents the work required to bring one molecule from the 3D vapor into the 2D film.

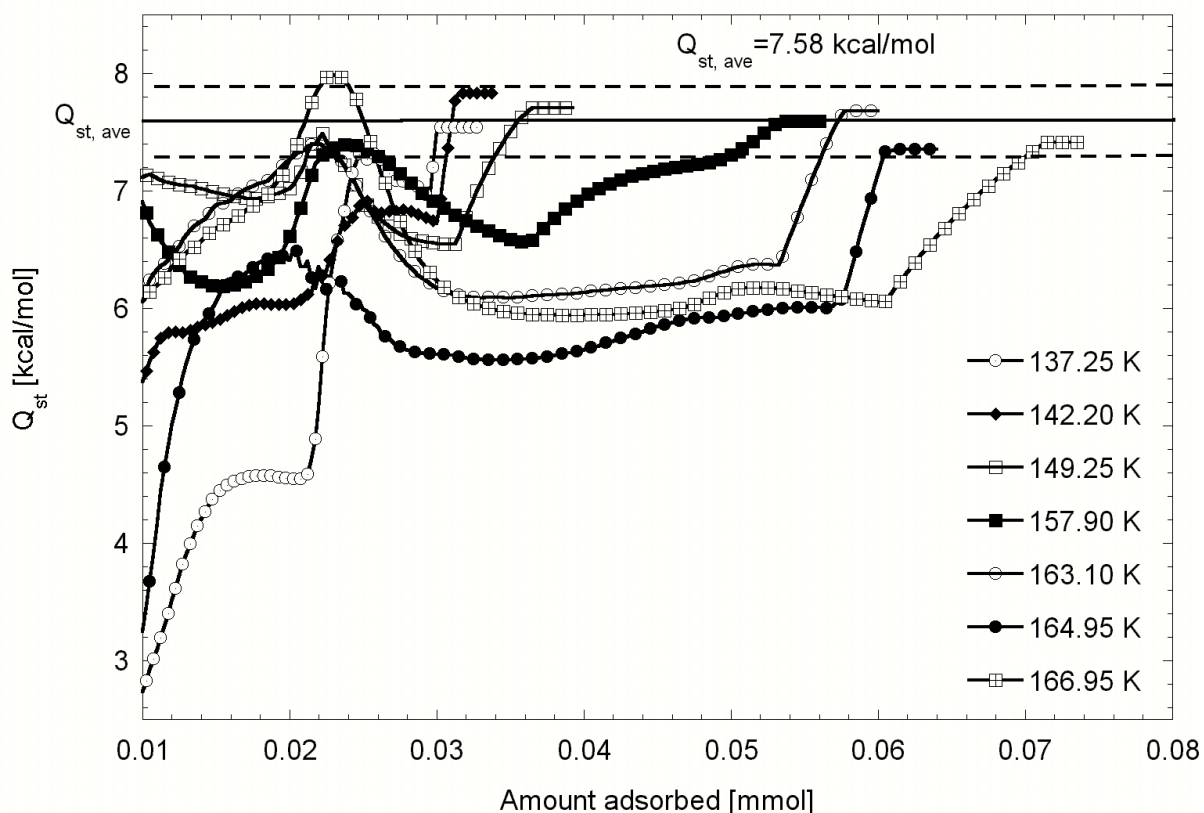


Figure 4.10: Isosteric heat of adsorption from CH_3Cl on MgO .

The calculated heat of adsorption for a subset of the isotherms is shown in Fig. 4.10. This quantity exhibits characteristic maxima after layer completion and this behavior can be observed at $\Omega \approx 0.024$ mmol in the figure. At high coverage, Q_{st} converges for all temperatures towards $Q_{\text{st,ave}} = (7.58 \pm 0.3)$ kcal/mol. Several of Q_{st} plots exhibit a plateau near 6 kcal/mole approaching 7.5 ± 0.3 kcal/mol more slowly as $T \rightarrow T_{\text{triple}}$ with increasing coverage.

Bah and Dupont-Pavlovsky [Bah95] have not included a determination of Q_{st} for CH_3Cl on graphite so no comparison is possible here, but this data can be used to perform a comparison to the heat of vaporization of bulk CH_3Cl . The value of this quantity is reported

as 5.14 kcal/mol at the equilibrium saturation vapor pressure of 1 atm [NBS]. In reference [CRC], the heat of vaporization was determined to be 5.23 to 4.38 kcal/mol over the temperature range from -28.89 °C to 37.78 °C. The measurements taken here were at much lower temperatures and pressures, so a direct comparison with these values is not possible, however, it appears that the values determined are consistent with the published data.

4.1.2 Methyl bromide on magnesium oxide

Multiple isotherms of CH_3Br on MgO were measured on several different samples of MgO over the temperature range of 170.0K to 200.0K. The measurements were limited to temperatures above 170K due to the low vapor pressures of methyl bromide. Figure 4.11 displays a subset of them over the temperature range of 173K to 179K. These data sets are representative of the interesting region involving the wetting behavior.

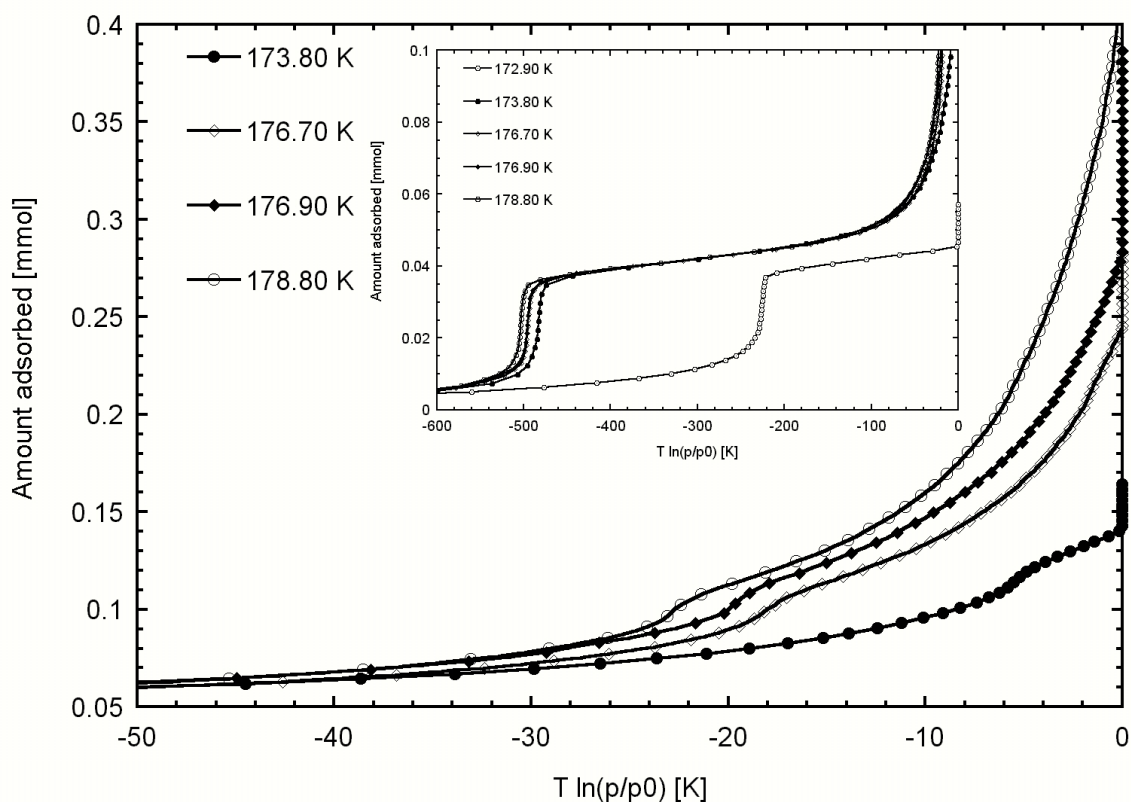


Figure 4.11: A set of bromomethane on magnesium oxide isotherms. The amount adsorbed is plotted as a function of $T \ln(p/p_0)$. The inset illustrates the behavior of the isotherms in the monolayer regime.

As mentioned earlier a determination of the sample temperature of these isotherms using the bulk SVP is not possible because (to our knowledge) no low temperature vapor pressure

curves of methyl bromide are available. One method to use the vapor pressure to check the temperature would be to make an extrapolation of the available vapor pressure curves to lower temperatures, but a discontinuity in the vapor pressure curve was observed near the transition point of the two solid phases of bulk CH_3Br (Chapter 3). The other method is to use the SVP of methane to calibrate the temperature sensor since a small temperature offset normally exists between the actual sample temperature and the temperature reading. This calibration is then applied to the temperatures of the methyl bromide isotherms.

Due to the difficulties associated with the extreme low vapor pressure of methyl bromide near the triple point, only a partial quantitative analysis is presented here.

a) General description

The general behavior of the CH_3Br isotherms (Figure 4.11) is strongly reminiscent of the isotherms of CH_3Cl on MgO . Only one adsorption step is observed at temperatures below 173.80K, whereas the formation of a second layer is observed at higher temperatures. No evidence of further distinct layer formation can be detected even though the amount adsorbed strongly increases with temperature.

Furthermore, methyl chloride and methyl bromide exhibit similarities in molecular adsorption area on MgO . A molecular area of $\sigma = 22.8 \pm 1.0 \text{ \AA}^{-2}$ was determined for CH_3Br on MgO at 176.7K. Comparison with the results presented earlier show that this is within 3% of the value obtained for methyl chloride.

b) The 2D compressibility of methyl bromide on MgO

The 2D isothermal compressibility was calculated to gain more information about the behavior of the second layer for isotherms at 173.80 K and higher. This is shown in Figure 4.12. Clearly recognizable are the 2D compressibility features corresponding to the second layer formation. The peaks are displaced towards lower difference in chemical potential with decreasing temperature. This observation can be used to determine the onset temperature for the 2nd layer formation. The position of the compressibility peaks as a function of the chemical potential difference was plotted versus temperature (Figure 4.13). A linear fit to these data (four point) can be used to estimate $T_{2\text{nd}}=172.0 \text{ K}$ as layering temperature, however it needs to be considered that at 172.50 K no evidence of a second layer is found. Because only such a limited number of data points is available, the layering temperature for the second layer is estimated to $T_{2\text{nd}}=173.0 \pm 1.0 \text{ K}$.

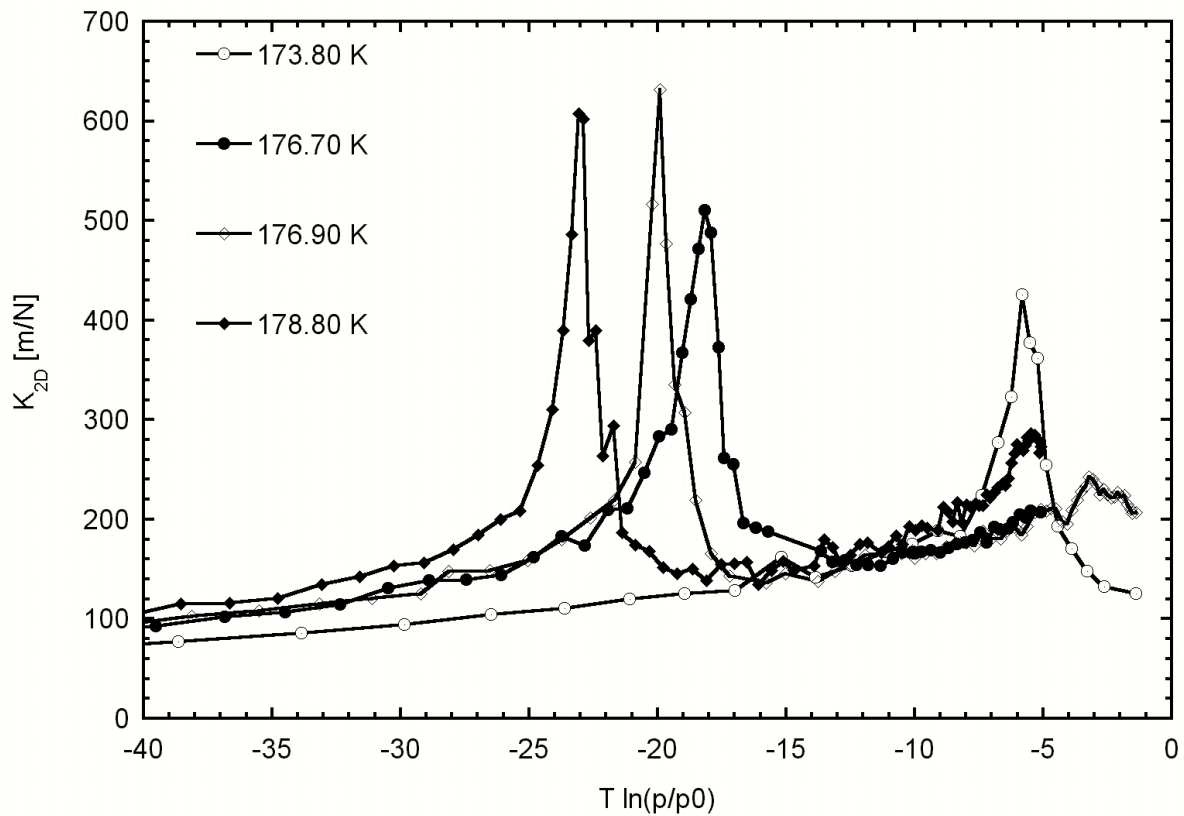


Figure 4.12: 2D compressibility of the second adsorption step of CH_3Br on MgO .

There is a distinct difference in the behavior of the height and width of these 2D compressibility features when compared to the $\text{CH}_3\text{Cl}/\text{MgO}$ case. With increasing temperature no linear decrease was observed for the height of the K_{2D} feature. It seems to stay more or less fixed. Furthermore, the peak width is essentially constant for all four K_{2D} features.

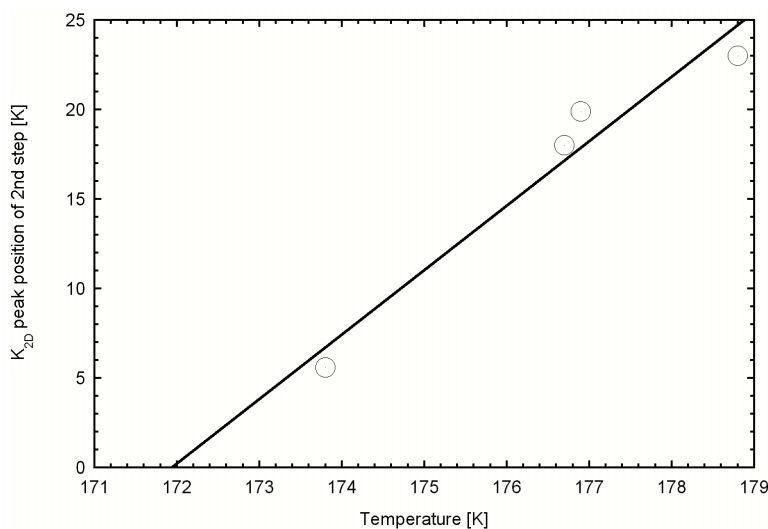


Figure 4.13: Position of the maximum of the 2D compressibility corresponding to the second step of CH_3Br on MgO as a function of temperature. The error bars are typically: ± 0.5 K along the x-axis and ± 2 K along y.

c) The isosteric heat of adsorption

The isosteric heat of adsorption was calculated for methyl bromide on MgO (Figure 4.14). The isotherms at 173.80K, 176.70K and 178.80K were used to calculate it. Due to the uncertainty of the temperature determination, it is necessary to calculate Q_{st} from two isotherms different in temperature by a few degrees in order to minimize the error propagated. The isosteric heat of adsorption is inversely proportional to the temperature difference between these isotherms.

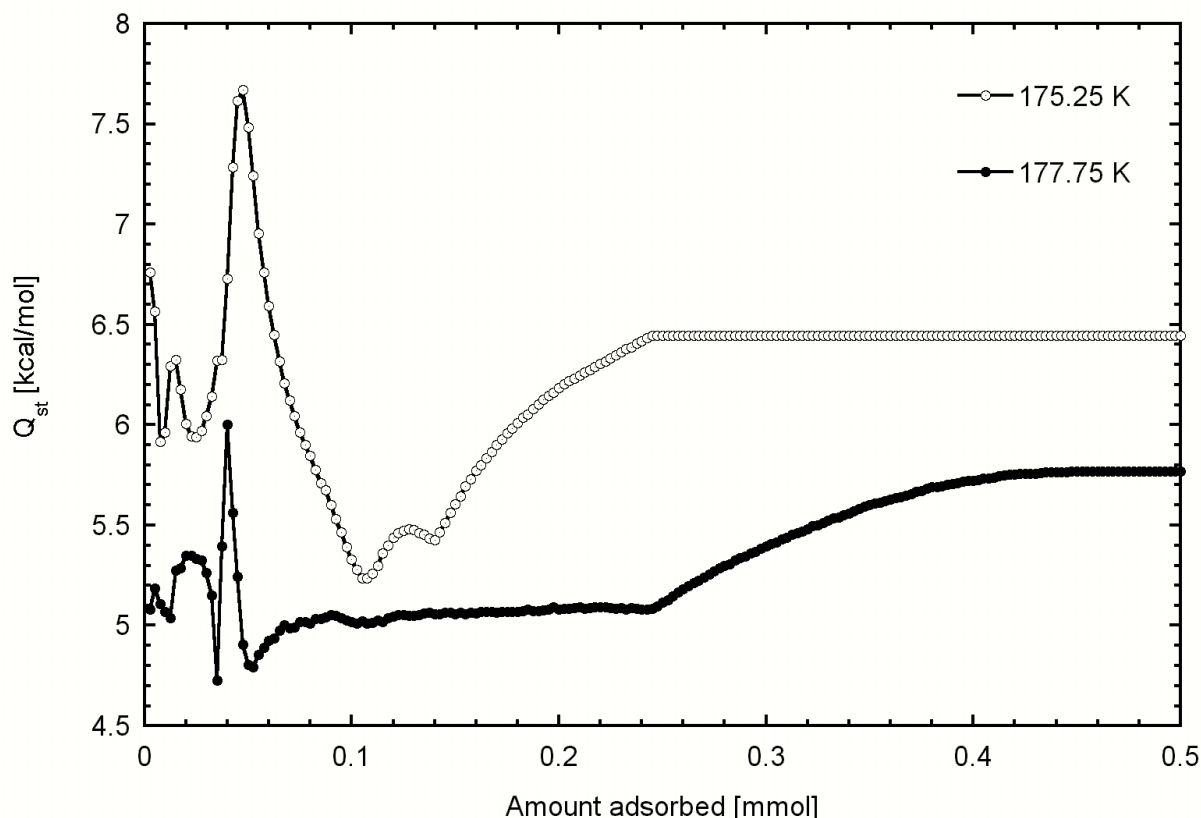


Figure 4.14: Isosteric heat of adsorption of CH_3Br on MgO versus the amount adsorbed.

At high coverage $Q_{st}=6.2\pm 1.0$ kcal/mol as determined by averaging the linear portions in Figure 4.14. Despite a very limited data set, this value is close to the literature value of methyl bromide of $Q_{st}=5.71$ kcal/mol at 276.6 K [CRC73].

d) The film growth of methyl bromide near T_{triple}

Some general comments are made about the behavior of the film growth near the triple point. Over a relatively small temperature interval ($172.50\text{K} \leq T \leq 178.80\text{K}$), a ten-fold increase (from 0.04 mmol to 0.40 mmol) in the amount adsorbed is observed in the neighborhood of the bulk chemical potential. This observation, the similarity to the case of $\text{CH}_3\text{Cl}/\text{MgO}$ and

the behavior of the isotherms at temperatures above 180K (i.e. not reaching the SVP), indicate that the system CH_3Br on MgO most likely exhibits triple point wetting.

4.1.3 Methyl iodide on magnesium oxide

The thermodynamic properties of Iodomethane on MgO were studied using multiple sets of adsorption isotherms between 175-225 K. Figure 4.15 displays a typical set in this temperature region. Similar problems and difficulties already discussed for CH_3Br , apply to CH_3I (i.e. no low temperature bulk vapor pressure data were available).

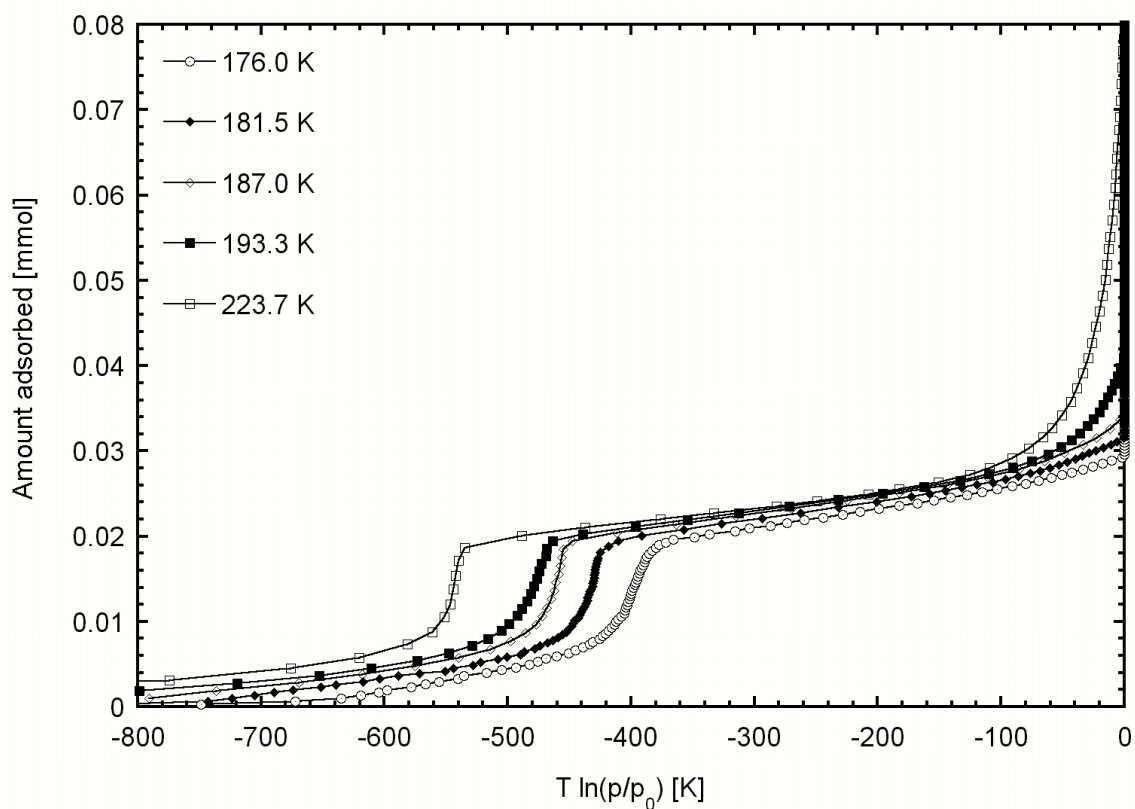


Figure 4.15: Set of adsorption isotherms of methyl iodide on MgO. The amount adsorbed is plotted versus the difference in chemical potential between the film and the bulk phase of methyl iodide.

a) General description

The isotherms show the formation of a single layer between $-600 \text{ K} \leq T \ln(p/p_0) \leq -400 \text{ K}$. The position of the step moves towards the bulk chemical potential with decreasing temperature. After the completion of the monolayer only small additional amounts are adsorbed at high temperatures, e.g. the maximum amount adsorbed before the bulk chemical potential is

reached is about four times the monolayer capacity at the highest temperature of 223.7K. It is interesting to note that this is clearly above the bulk triple point of CH_3I $T_{\text{triple}} = 206.70 \text{ K}$, so it can be concluded that methyl iodide does not exhibit triple point wetting on magnesium oxide. Furthermore, no evidence for the formation of distinct layers beyond the monolayer is observed.

The molecular area of CH_3I on MgO was determined to $\sigma = 25.2 \text{ \AA}^2$ at 206.5K, about 10% larger than the value obtained for methyl chloride.

b) Isosteric heat of adsorption

The isosteric heat of adsorption was calculated for multiple isotherms and is shown in Figure 4.16. One notices that at high coverages all the heats converge into the small interval around $Q_{\text{st}} = 7.83 \pm 0.60 \text{ kcal/mol}$. Even though Q_{st} was calculated using a rather large temperature interval, it should still be representative set, because the isotherms exhibited only small variations over this whole temperature range.

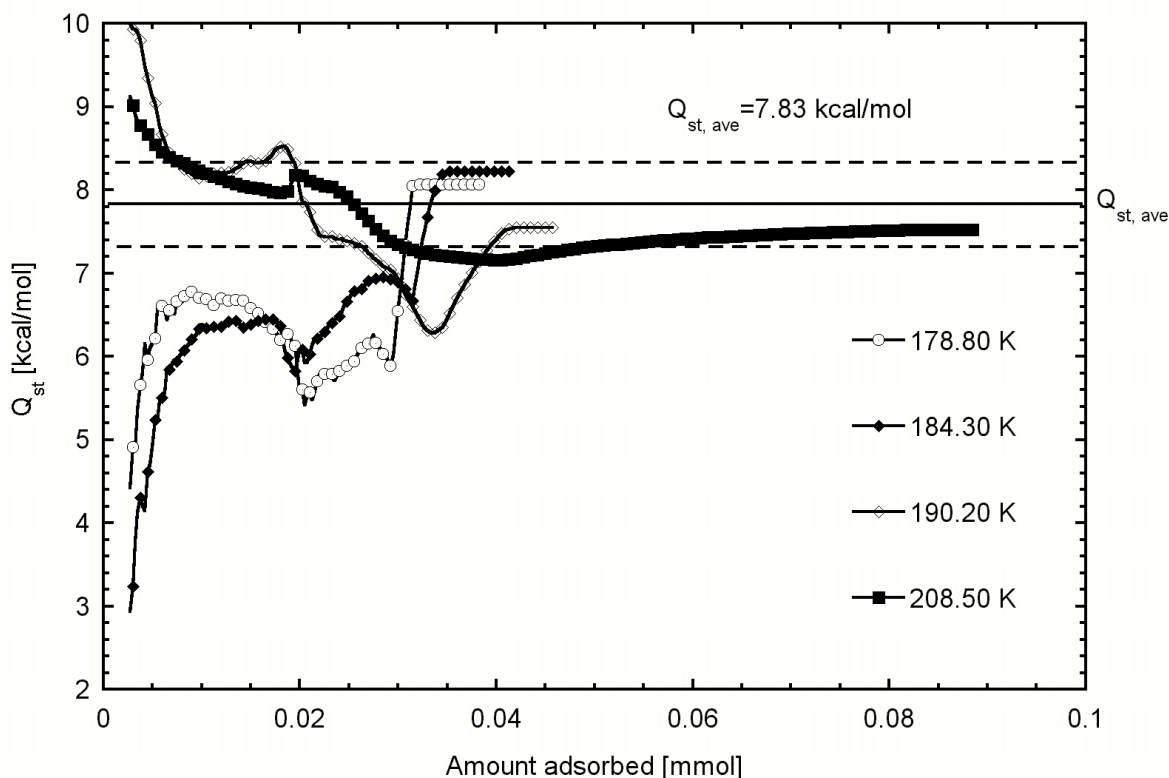


Figure 4.16: Isosteric heat of adsorption of CH_3I on MgO .

4.2 Adsorption isotherms on BN

Volumetric isotherms were also used to determine the monolayer capacities of the methyl halides and thermodynamic quantities of methyl chloride on BN. Before use, BN (Alfa Aesar, 99.5%, metal basis) samples were prepared as described in Chapter 3. The surface area of these powders was determined to be about $8 \text{ m}^2/\text{g}$ using the monolayer capacity of a Krypton isotherm. This allowed also performing a test of the sample quality before beginning adsorption experiments with the methyl halides.

4.2.1 Monolayer capacities of methyl halides on boron nitride

Determination of the monolayer capacity is an important 1st step to perform before the structural investigations of adsorbed films is undertaken. The molecular area is a valuable piece of information to incorporate when trying to derive the number of molecules per unit cell of possible solutions for the 2D structures. A monolayer height comparison between krypton and methyl halide isotherms is used to estimate the molecular areas on the substrate BN. This is displayed in Figure 4.17a,b.

The values for the adsorption areas obtained from these investigations are summarized in Table 4.2. They are comparable to values for the methyl halides on MgO (see previous section) and graphite (e.g. [Buc89], [Cla91] and [Mor91]). It should be pointed out that the molecular area obtained for methyl chloride on BN is close to the value of the low-density (LD) phase of CH_3Cl on graphite (see next chapter). This suggests that over the observed temperature range the CH_3Cl molecules most likely arrange with their C-Cl axis parallel to the BN surface.

Adsorbate	Molecular area on graphite [\AA^2]	Molecular area on boron nitride [\AA^2]	Molecular area on MgO [\AA^2]
CH_3Cl	19.50 [LD] 13.80 [HD]	20.7 ± 1.0	23.3 ± 1.0
CH_3Br	21.05	21.4 ± 1.0	22.8 ± 1.0
CH_3I	22.25	25.8 ± 1.0	25.2 ± 1.0

Table 4.2: Molecular areas of the methyl halides adsorbed on graphite, boron nitride and magnesium oxide. The values for CH_3Cl [Mor91], CH_3Br [Cla91] and CH_3I [Buc89] on graphite are calculated using diffraction data. All other values were estimated using adsorption isotherms.

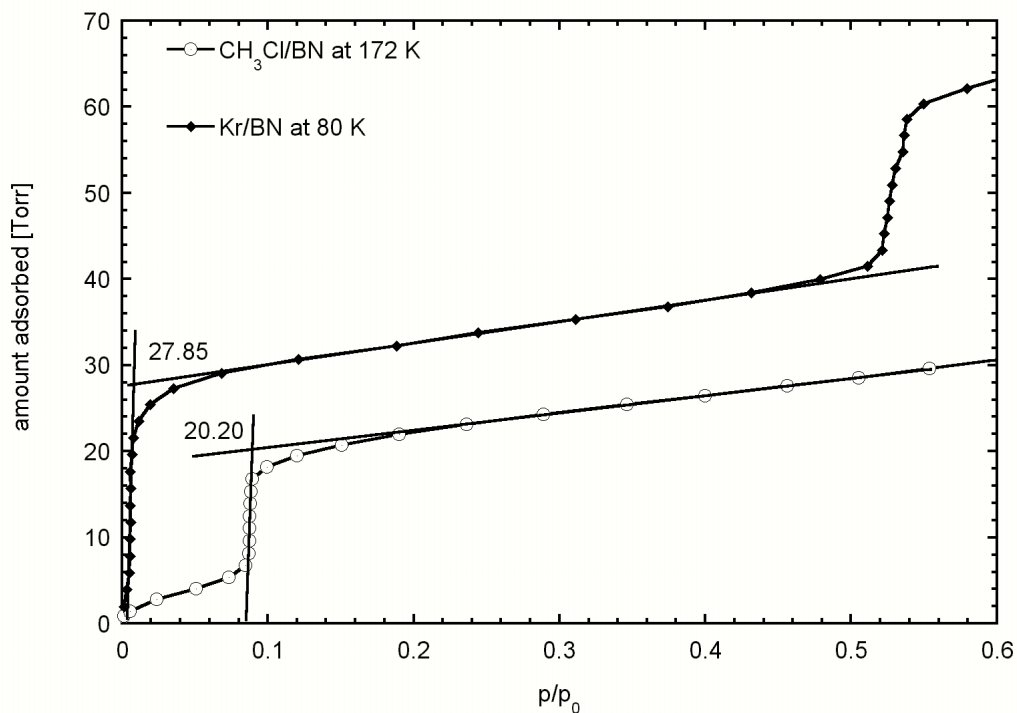


Figure 4.17a: Monolayer height comparison between Kr and CH_3Cl adsorbed on BN.

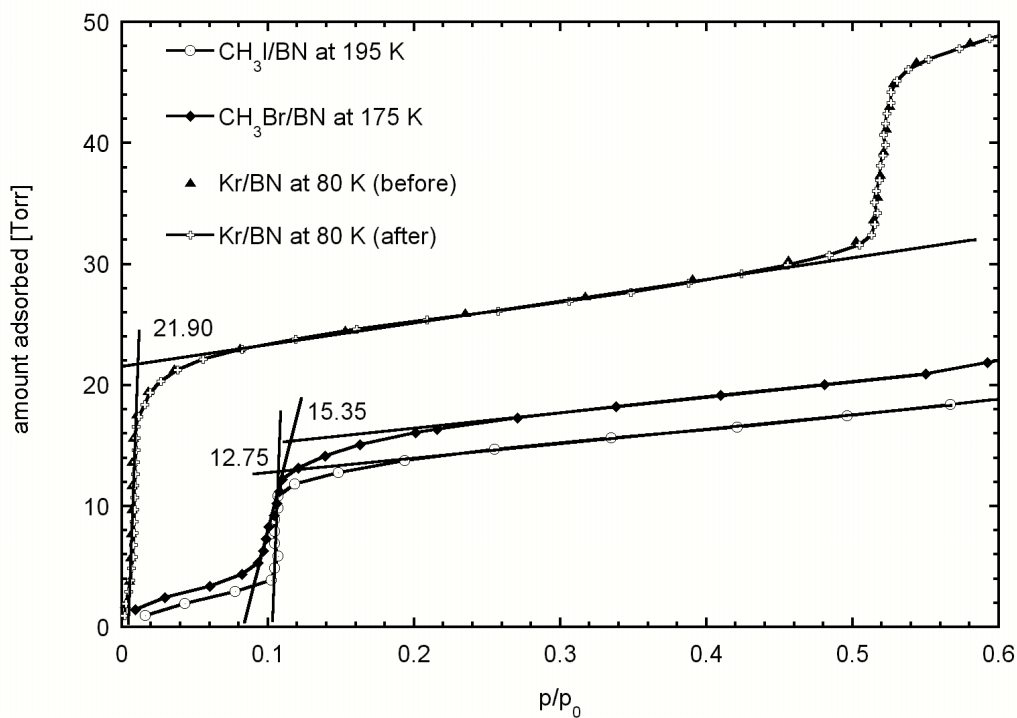


Figure 4.17b: Monolayer height comparison between Kr, CH_3Br and CH_3I adsorbed on BN.

4.2.2 Methyl chloride on boron nitride

The investigation of methyl chloride on BN with adsorption isotherms concentrated on the search of a low-density to high-density phase transition. Methyl chloride on graphite exhibited such a phase transition at temperatures below 145K as indicated by heat capacity [Ina91], adsorption isotherm [Bah95] and neutron and x-ray powder diffraction measurements [Shi91], [Mor91].

The isotherm measurements show no evidence of such a phase transition in the temperature interval between 142K and 173K. The isotherms (Figure 4.18) indicate that only a single layer of CH_3Cl forms before the bulk vapor pressure is reached. At the highest temperatures, the formation of a second layer adsorbed is observed. Attempts to measure isotherms below 142K failed because of the low vapor pressures involved. From these measurements it can only be concluded, that if a high-density phase of methyl chloride exists on BN, it must appear at temperatures lower than on graphite.

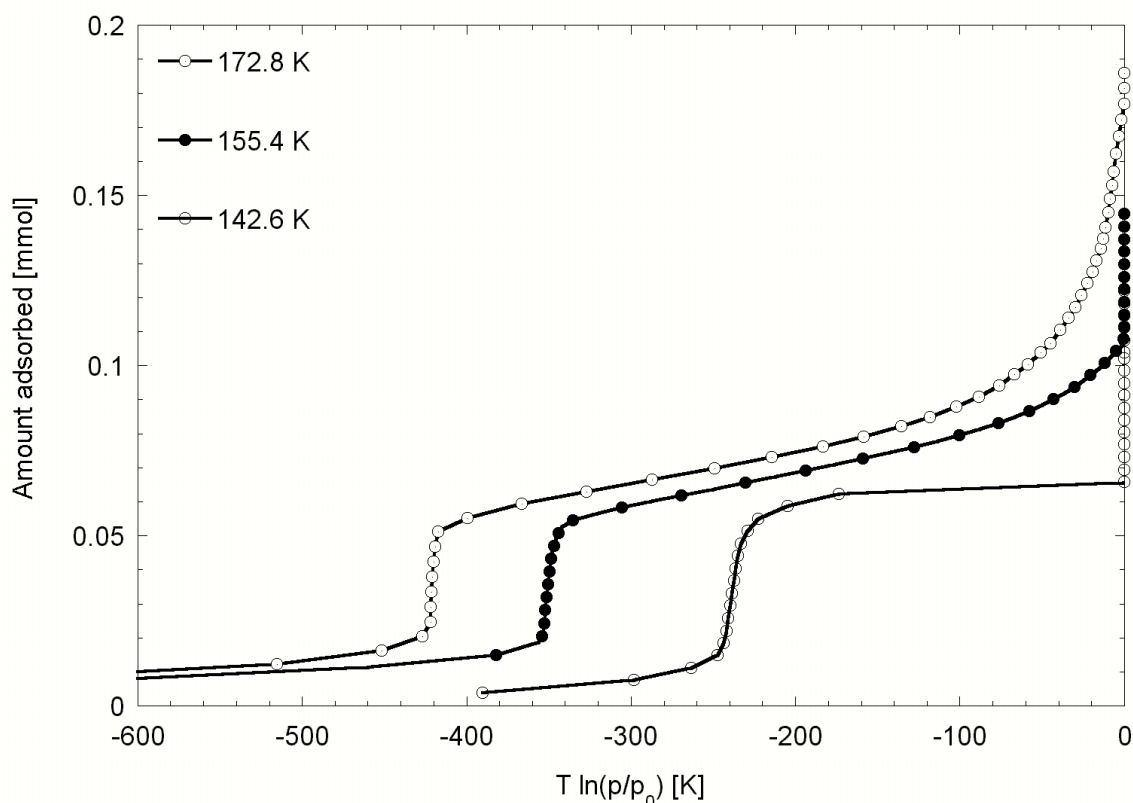


Figure 4.18: Adsorption isotherms of methyl chloride on BN. The amount adsorbed is plotted as a function of the chemical potential difference between film and bulk CH_3Cl .

The available isotherm data was used to calculate the heat of adsorption of methyl chloride on BN (Figure 4.19). Near the formation of bulk material $Q_{st} = 7.56 \pm 0.50$ kcal/mol was deter-

mined. This is consistent with the value obtained for CH_3Cl on MgO ($Q_{\text{st}} = 7.58$ kcal/mole, previous section). Although the isotherms are recorded with large temperature differences, it seems possible to get a reasonable estimate of the bulk heat of vaporization using this technique. On the other hand, the characteristic maximum of the heat of adsorption after monolayer completion cannot be observed due to the limited amount of data points in this region of the isotherms. For example, the sharp drop off in the low temperature heat at $\Omega \approx 0.06$ ml is due to the discontinuity in the isotherm at 142.6K indicated by the sudden appearance of the bulk vapor pressure at this coverage.

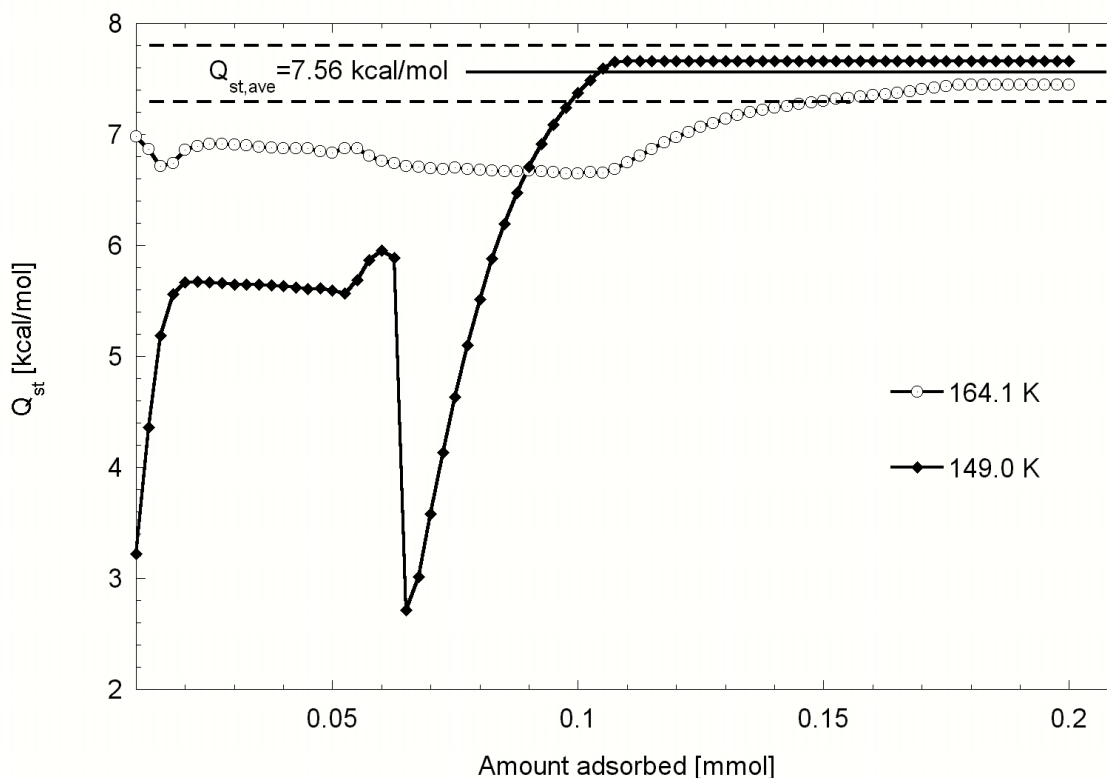


Figure 4.19: Isothermic heat of adsorption of methyl chloride on boron nitride as a function of the amount adsorbed.

Chapter 5

Structural investigations

This chapter presents the results of structural investigations of monolayers of methyl halides adsorbed on magnesium oxide and boron nitride. These thin films were examined with x-ray powder diffraction at X7B at the NSLS. The layout of this beamline is described in chapter 3. The x-ray sample cells were filled with powder (about 0.2g in the case of BN and about 0.4g of MgO) and a calibration isotherm (Kr on BN or CH₄ on MgO) was run to establish the gas capacity and quality of the sample. These in situ adsorption measurements make it possible to determine what the surface area occupied per adsorbed molecule is, a quantity which helps later when trying to restrict the number of molecules in proposed unit cells.

All measurements were undertaken with x-ray wavelengths around $\lambda = 0.94 \text{ \AA}$ (the actual energy resolution was $\Delta E/E = 2 \times 10^{-4}$, but the precise wavelengths varied between experiments). The distance between the sample and the Mar345 detector was held fixed at $d_{\text{MAR345}} = 365 \text{ mm}$ to allow the recording of wave vectors up to $Q_{\text{max}} = 3.0 \text{ \AA}^{-1}$.

This chapter is divided into three main parts. The first two sections describe the results of measurements on the hexagonal substrates, graphite and boron nitride. Starting, the known monolayer structures of methyl halides adsorbed on graphite are summarized. Then the experimentally investigations of adsorbed films of methyl halides on boron nitride are presented. Finally, measurements of monolayer films of methyl halides on MgO are discussed.

5.1 Methyl halides on graphite: A summary

A summary of the structures of monolayer films of the polar methane derivative (CH_jR_{4-j}, R=F, Cl, Br, I and j=0, 1, 2, 3, 4) physisorbed on graphite has been presented by Knorr [Kno92]. A brief summary of the structures of CH₃Cl, CH₃Br and CH₃I on graphite is presented here because those are used to make comparisons to the structures of methyl halides on boron nitride later on.

5.1.1 Methyl chloride on graphite

CH_3Cl on graphite is a well-characterized system. It has been studied using He atom scattering [Rui88], heat capacity measurements [Ina91], adsorption isotherm techniques [Bah95], x-ray diffraction measurements [Shi91], [Gri96] and a combined study of x-ray and neutron diffraction [Mor91].

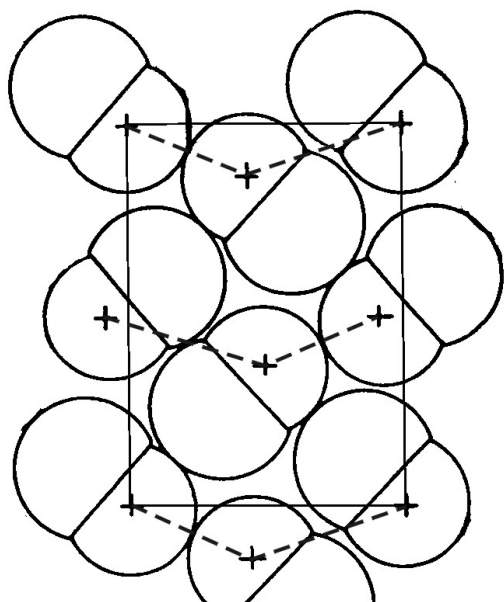


Figure 5.1a: LD phase of CH_3Cl on graphite. Four molecules are lying with the C-Cl axis parallel to the graphite surface in two zigzag rows [Kno92].

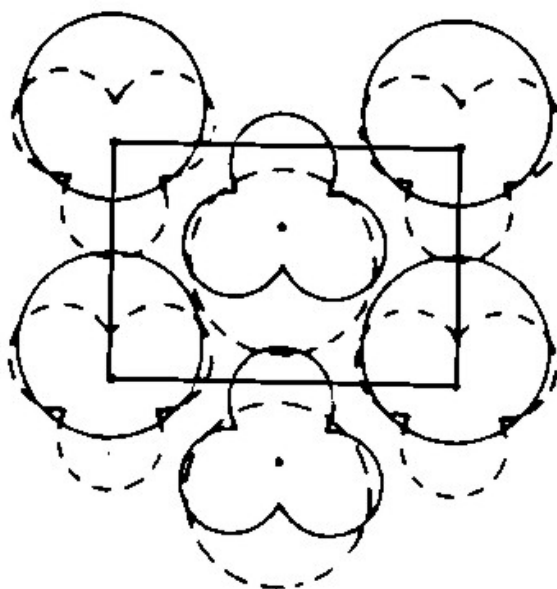


Figure 5.1b: HD phase of methyl chloride on graphite. The unit cell contains two molecules in an up-down configuration [Kno92].

At low temperatures, it was found that CH_3Cl forms two different solid structures. CH_3Cl forms a unit cell ($|\vec{A}| = 10.14\text{\AA}$, $|\vec{B}| = 7.71\text{\AA}$ and $\gamma = 91.2^\circ$ at 32K) containing four molecules with the C-Cl axis almost parallel to the graphite surface at low coverages. This is referred to as the low-density (LD) phase (see Fig. 5.1a). The molecules arrange in a herringbone pattern in response to an in-plane intermolecular dipole moment. A high-density phase (HD) forms at lower temperatures and higher coverages (see Fig. 5.1b). The HD phase is a nearly centered rectangular unit cell ($|\vec{A}| = 4.26\text{\AA} = \sqrt{3}a_c$, $|\vec{B}| = 6.44\text{\AA}$ at 25K) with two molecules in an up-down configuration. The cell is commensurate with the substrate along \vec{A} . In the other direction, it is incommensurate and expands significantly with temperature.

This system exhibits some interesting 2D behavior. For example, the HD phase appears to lose its long-range order (i.e. melts) along the direction incommensurate with the substrate a few degrees below the other (commensurate) direction and an intermediate phase forms [Gri94]. This behavior will be discussed later on.

5.1.2 Methyl bromide on graphite

Substantially less information is available concerning the adsorption properties of methyl bromide on graphite. The monolayer structure of CH_3Br on graphite has been investigated using a combined neutron and x-ray diffraction study [Cla91]. The complicated diffraction patterns could only be explained by assuming that the molecules arrange in a large unit cell on the graphite surface. It was concluded that methyl bromide forms a rectangular unit cell with the lattice constants of $|\vec{A}|=30.35\text{\AA}$ and $|\vec{B}|=5.55\text{\AA}$, that is incommensurate with the graphite basal planes. The cell contains eight molecules aligned in four zigzag rows lying with the C-Br axis parallel to the graphite surface (see Fig. 5.2a). This configuration has no net dipole moment and is similar to the (010) plane of the bulk crystal of methyl bromide ([Kaw73] and [Ger86]).

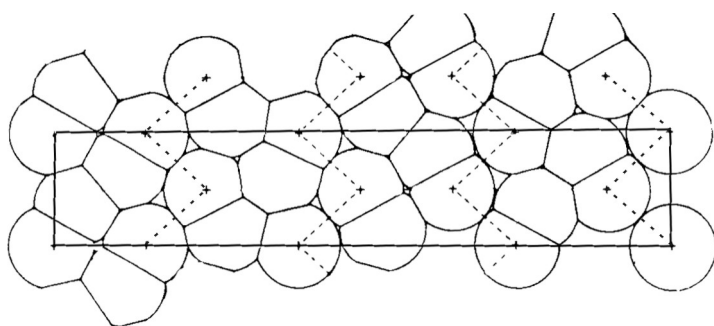


Figure 5.2a: Monolayer structure of CH_3Br on graphite. Eight molecules are arranged in four zigzag rows [Kno92].

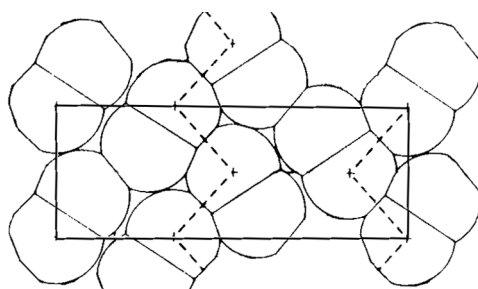


Figure 5.2b: The structure of methyl iodide on graphite. The unit cell contains four molecules with the C-I axis parallel to the surface [Kno92].

5.1.3 Methyl iodide on graphite

The structure of a monolayer of CH_3I on graphite has been studied using neutron and x-ray diffraction [Buc89]. While the x-ray diffraction study suggested that methyl iodide forms an oblique unit cell containing two molecules, this model could not be used to explain the neutron diffraction data. A larger rectangular unit cell with the lattice parameters of $|\vec{A}|=15.40\text{\AA}$ and $|\vec{B}|=5.78\text{\AA}$ incommensurate with the graphite surface was proposed satisfying both diffraction data sets. This unit cell contains four molecules of methyl iodide arranged in two zigzag rows parallel to the graphite surface. The layer resembles the (010) plane of a methyl iodide crystal [Kwa73] and a schematic view is displayed in Figure 5.2b.

5.2 Methyl halides on boron nitride

In this section the investigations of films of methyl halides on BN are described. As mentioned earlier the hexagonal form of boron nitride is a layered material with unit cell dimensions similar to graphite. The in-plane lattice constants differ by less than 2% ($a_{\text{graphite}} = 2.457 \text{ \AA}$ to $a_{\text{BN}} = 2.505 \text{ \AA}$) whereas the basal plane separation is $c_{\text{graphite}} = 6.690 \text{ \AA}$ and $c_{\text{BN}} = 6.656 \text{ \AA}$ (this is a difference smaller than 0.5%). Additional information about boron nitride is provided in Chapter 3.

The system CH_3I adsorbed on BN is used to explain, how the raw data was analyzed. It discusses difficulties that can occur and how those problems have to be overcome in order to solve these structures. Continuing, the measurements of methyl bromide and methyl chloride on boron nitride are presented.

5.2.1 Methyl iodide on BN

Two reasons make CH_3I on boron nitride a good example to explain how the experimental data was processed. First, CH_3I films have the strongest diffraction signal of the methyl halides, since the x-ray diffraction signal is roughly proportional to the square of the number of electrons (17 for chlorine, 35 for bromine and 53 for iodine) in the illuminated volume. Secondly, the difficulty of the data analysis was increased due to the appearance of additional diffraction features. The outlined data reduction method is used to analyze all other measurements of the adsorbed films of methyl halides later on.

X-ray powder diffraction is a powerful method to study crystal structures or observe structural phase transitions. To study the structure of adsorbed films, difference measurements are used to separate the weak signal of the adsorbed film from the strong response of the underlying substrate. Because the diffraction pattern from the empty substrate is usually temperature dependent, ‘background’ measurements are performed at several different temperatures. After the ‘backgrounds’ are completed, the gas (adsorbate) is added to sample the cell and diffraction measurements with the gas adsorbed onto the substrate are performed.

Since the beam intensity in a synchrotron is time dependent, a normalization has to be performed before the background measurements can be subtracted from the measurements made after the gas was deposited. Normalization with respect to the total number of counts or exposure time was not possible due to the decay of the stored information on the image plate and the change in beam intensity over time, respectively.

However, it was found that a normalization of the intensity of the first substrate peak (the (002) reflection of BN or the (111) reflection of MgO) to $I_{\text{max}}=1000$ counts gave good results. This normalization method introduces a small error resulting in a constant offset because the signal of the adsorbed film overlaps with the signal of the bulk reflection. This er-

ror is negligible since the ratio of substrate signal and film signal is of the order $I_{\text{substrate}}/I_{\text{film}} \approx 1000$ (see differences later). In addition, other methods of normalization were tried, but did not produce as good results. In order to compensate for small misalignments of the detector position, the background scans were slightly shifted in Q to improve the subtraction. This follows closely a method described by Grieger [Gri94].

Because no previous isotherm data was available as the diffraction measurements on the system CH_3I on BN were performed, the CH_3I coverage is expressed in terms of the estimated monolayer height of the Krypton calibration isotherm at 85K. The methyl iodide on BN coverages investigated were $\Omega_1=0.51$ and $\Omega_2=0.60$ equivalents of Kr. Later, it was found that a coverage of $\Omega=0.58$ equivalent of Kr was comparable to the monolayer height of CH_3I on BN at 195K (see Chapter4). An example of the background subtraction for both coverages of CH_3I on boron nitride at 125K is displayed in Figure 5.3. The intensity of the (002) reflection of boron nitride at $Q_{(002)} \approx 1.89\text{\AA}^{-1}$ is so strong (normalized to $I_{\text{max}}=1000$) that the region $1.82\text{\AA}^{-1} \leq Q \leq 1.96\text{\AA}^{-1}$ does not provide reliable data.

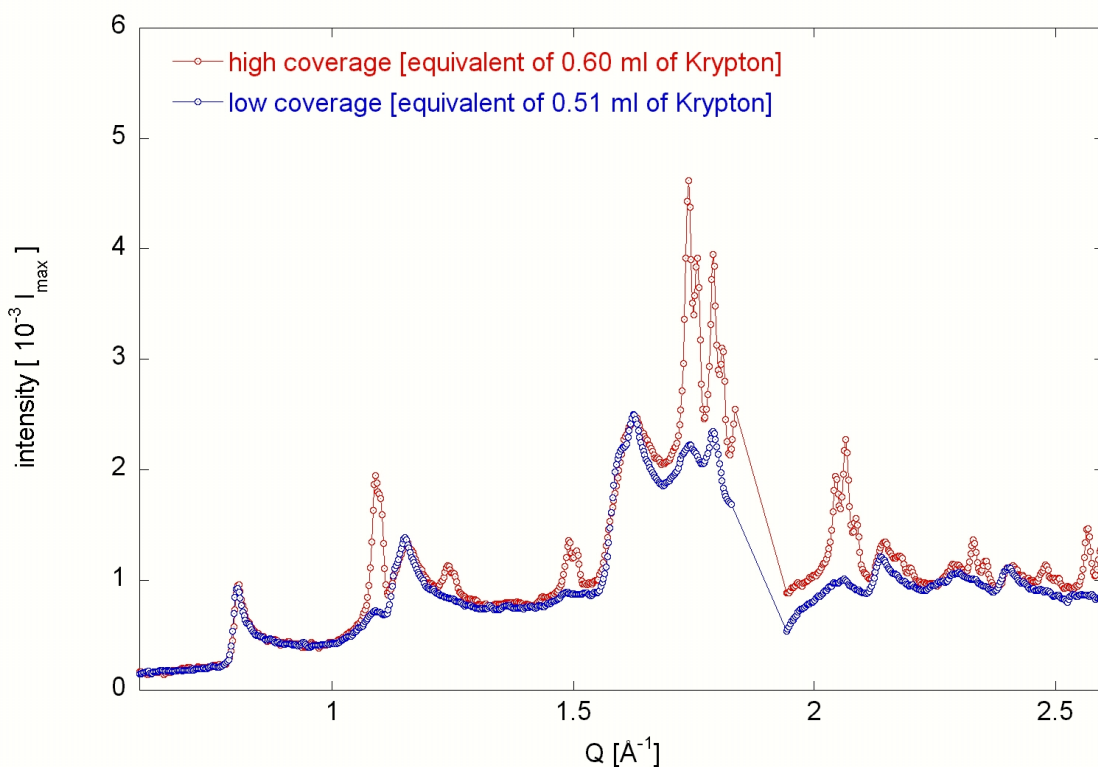


Figure 5.3: Difference pattern of methyl iodide on boron nitride at 125K over the Q range of $0.6\text{\AA}^{-1} \leq Q \leq 2.6\text{\AA}^{-1}$. The intensity is expressed in parts per thousand of the (002) reflection of BN.

Several comments concerning these two difference patterns are in order. Two distinct sets of reflections are recognizable in Fig. 5.3. The peaks at $Q \approx 0.80\text{\AA}^{-1}, 1.13\text{\AA}^{-1}, 1.62\text{\AA}^{-1} \dots$ stay con-

stant in intensity for the two different coverages and show the asymmetric Warren lineshape characteristic for 2D systems. The other set of peaks at $Q \approx 1.10\text{\AA}^{-1}, 1.24\text{\AA}^{-1}, 1.50\text{\AA}^{-1} \dots$ increases in intensity and split up as a function of coverage. The latter peaks have a symmetric profile indicating the formation of 3D crystallites. This leads to the conclusion that the recorded difference patterns are a superposition of two phases, a 2D CH_3I film and 3D crystallites.

In order to determine the structure of the 2D phase it is useful to separate the pattern into its components. Table 5.1 lists the positions of the 3D peaks. They can be identified as reflections of methyl iodide crystals. Figure 5.4 displays a calculated bulk powder pattern of CH_3I in comparison with the difference pattern of the higher coverage of CH_3I at 125K. The splitting of these peaks has its origin in the formation of bulk CH_3I on the inside of both beryllium windows.

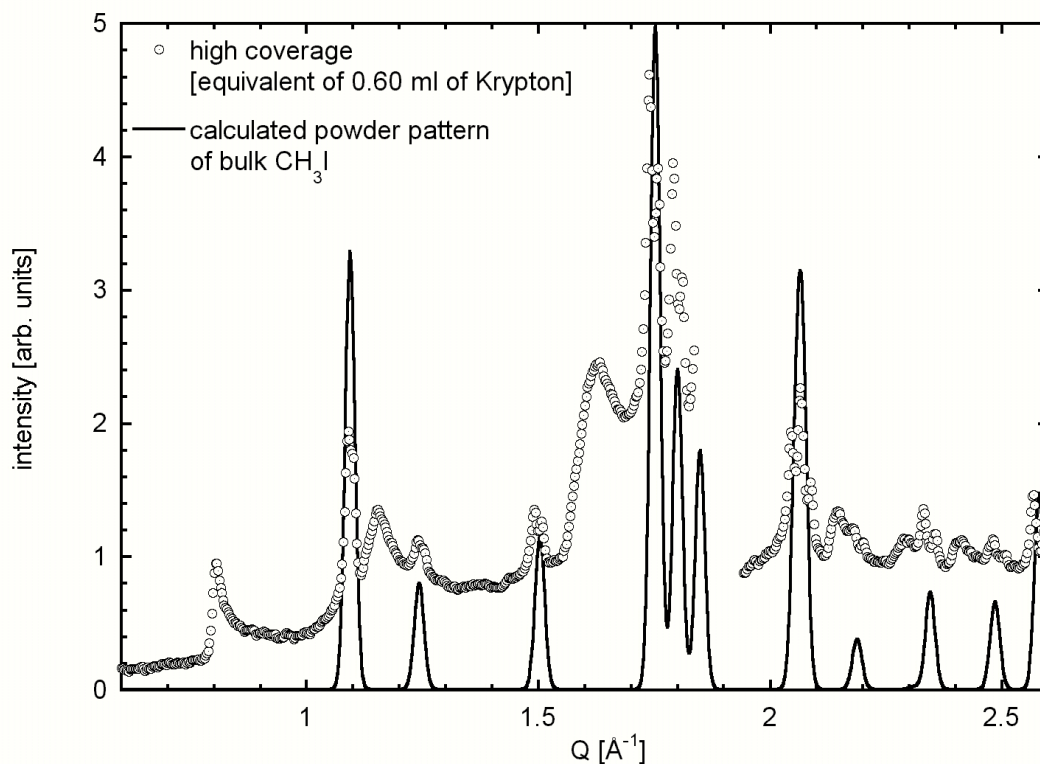


Figure 5.4: The experimental diffraction pattern of the higher coverage of CH_3I on BN in comparison to a calculated x-ray powder diffraction pattern of bulk methyl iodide. All reflections of the bulk pattern can be identified in the diffraction pattern of the adsorbed film.

The fact that the intensity of the asymmetric reflections, presumably from the adsorbed film on the boron nitride, remains constant, suggests that only a limited amount of methyl iodide can be adsorbed on the substrate. This observation agrees with the later thermodynamic in-

vestigation. There only one distinct layer of CH_3I adsorbed on the substrate before the formation of bulk material started (Chapter 4). Figure 5.4 shows that the investigated coverage equivalents of $\Omega_1=0.51\text{mnl}$ and $\Omega_2=0.60\text{mnl}$ of Kr exceeded the monolayer capacity for CH_3I on BN.

#	$Q_{\text{est}}[\text{\AA}^{-1}]$	$Q_{\text{CH}_3\text{I}}[\text{\AA}^{-1}]$	(hkl)
1	1.09	1.0929	(011)
2	1.24	1.2421	(002)
3	1.50	1.5013	(101)
4	1.75	1.7500	(111)
5	1.80	1.7985	(020)
6	N/A	1.8469	(102)
7	2.06	2.0542	(112)
		2.0688	(013)
8	2.19	2.1858	(022)
9	2.34	2.3107	(103)
		2.3428	(121)
10	2.49	2.4796	(113)
		2.4842	(004)
11	2.58	2.5779	(122)

Table 5.1: Estimated peak positions of reflections whose intensity increased with coverage and the corresponding reflections of bulk methyl iodide [Kwa73].

In order to estimate the monolayer coverage of CH_3I on BN a linear extrapolation of the intensity of bulk peaks versus coverage was performed and the monolayer coverage of CH_3I on BN was estimated to be $\Omega_{\text{max}}=0.485\pm 0.010$ equivalent krypton monolayer at 125K. Two bulk peaks, the (011) and the (101), were used (Table 5.2) because they are easy to separate from the Warren lineshape like peaks. At higher coverages bulk condensation occurs.

(hkl)	(011)	(101)
$I_{\text{est}} [\Omega_1=0.51]$	0.335	0.190
$I_{\text{est}} [\Omega_2=0.60]$	1.430	0.560
Ω_{Max}	0.489	0.480

Table 5.2: Estimated intensity of bulk reflections at the different coverages to determine the maximum possible coverage of CH_3I on BN.

The next step of the data reduction process requires removing the bulk diffraction peaks. This is a difficult task because some of these peaks overlap with the monolayer film features and location and intensity are temperature dependent. In addition, the profiles of the peaks are also broader and slightly displaced in Q as compared to an ideal bulk sample of methyl iodide because only thin crystalline films of CH_3I adsorbed on the Beryllium windows.

However, the first peak of the adsorbed film on boron nitride at $Q = 0.797 \text{ \AA}^{-1}$ shows a clear Warren lineshape like profile. It can be used to make a few general observations about the nature of the CH_3I film on boron nitride since no bulk peaks appear in the immediate vicinity of it.

Using the formulas developed in Chapter 2.1 to model a Warren lineshape to this single diffraction peak, the following general properties are obtained:

1. The coherence length of the film is estimated to $L_G=270\text{\AA}$.
2. The intensity distribution function can be modeled by a simple Gaussian function.
3. The powder is nearly isotropic.

Using these parameters, a Warren lineshape is also fit to the peak next following in Q that has been unambiguously identified as a reflection due to the 2D film (Figure 5.3). This makes it possible to remove the bulk peaks between these two 2D reflections as a sum of Gaussian and Lorentzian functions. This procedure is then continued throughout the entire Q range.

The difference patterns shown in Figure 5.5 were obtained after a careful subtraction of the bulk peaks following this method. These data clearly illustrate the temperature dependence of the methyl iodide film adsorbed on boron nitride between 125K and 157K. A dramatic change in the diffraction pattern is observed between 152K and 154K. As the temperature increases the well defined, sharp peaks (Table 5.3) broaden. This indicates that a transition from a phase with long-range order (presumably a 2D solid) into one with short-range order (fluid/liquid like) occurs. The sharp diffraction peaks are no longer visible in the difference pattern at 157K. Only a broad peak from a disordered phase is observed. This high temperature scan can be modeled as a sum of two broad Gaussian distributions and a linear part. A closer look at Figure 5.5 revealed that the scattered intensity of the lowest temperature scans is also a sum of multiple contributions. First, the same linear background can be observed for all scans. Second, a fraction of the scattered intensity is contributed from a disordered phase underneath the Warren lineshape like diffraction profiles even at low temperatures. A model of the high temperature scan was used to estimate and to remove the contributions due to the disordered phase and the linear part from the other patterns, before the analysis of the long-range ordered phase continued.

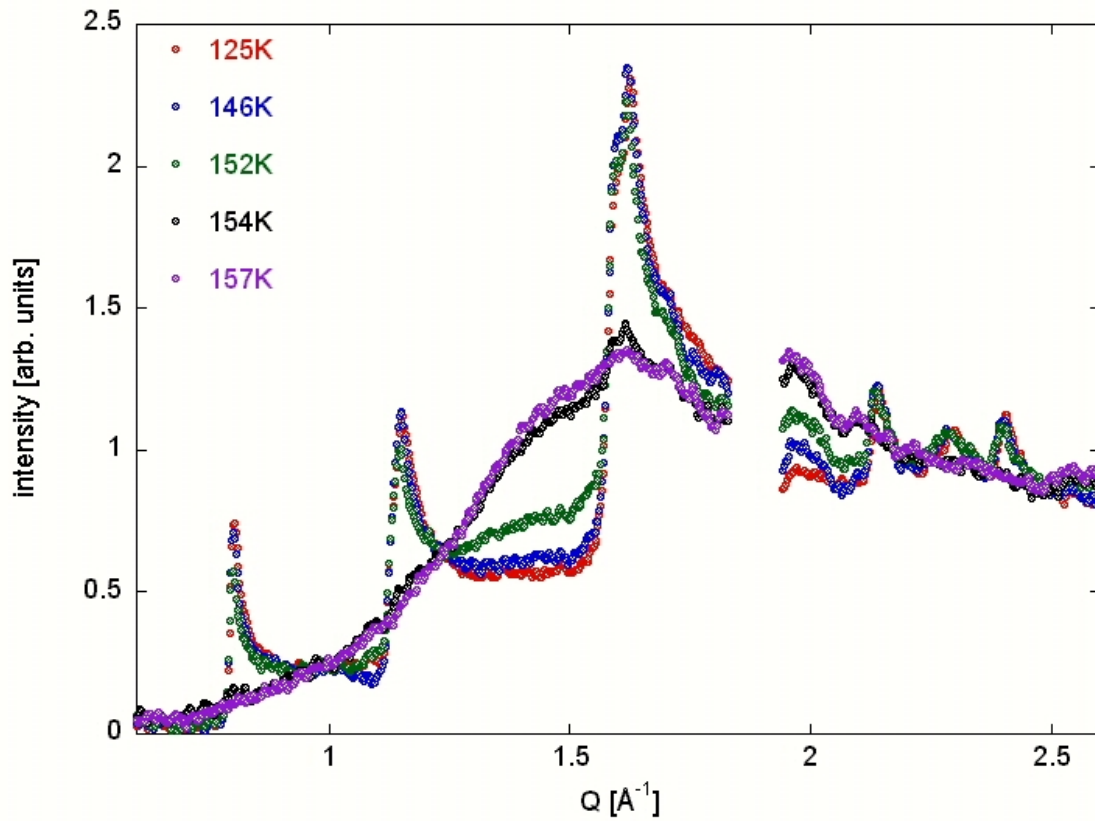


Figure 5.5: Difference scans of the lower coverage for different temperatures after the CH_3I bulk peaks are removed.

The long range ordered phase:

In the next step of the data reduction process the properties of the long range ordered 2D phase are extracted. Figure 5.6 shows this component of the diffracted intensity for different temperatures between 125K and 157K. The diffraction patterns have been offset by 0.1 counts for illustration purposes only. Six diffraction peaks are clearly identified, three at low wave vectors below the (002) bulk reflection of BN and three at higher Q values.

For comparison, Figure 5.7 shows the x-ray diffraction pattern of CH_3I on graphite of Bucknall et al. [Buc89]. Strong similarities are observed between the two diffraction patterns, e.g. three diffraction peaks below the (002) graphite or BN reflection (even with similar intensity distributions) and a characteristic triplet of reflections at higher Q values. While this is not a surprising result since boron nitride and graphite are very similar substrates, there are some small but important differences.

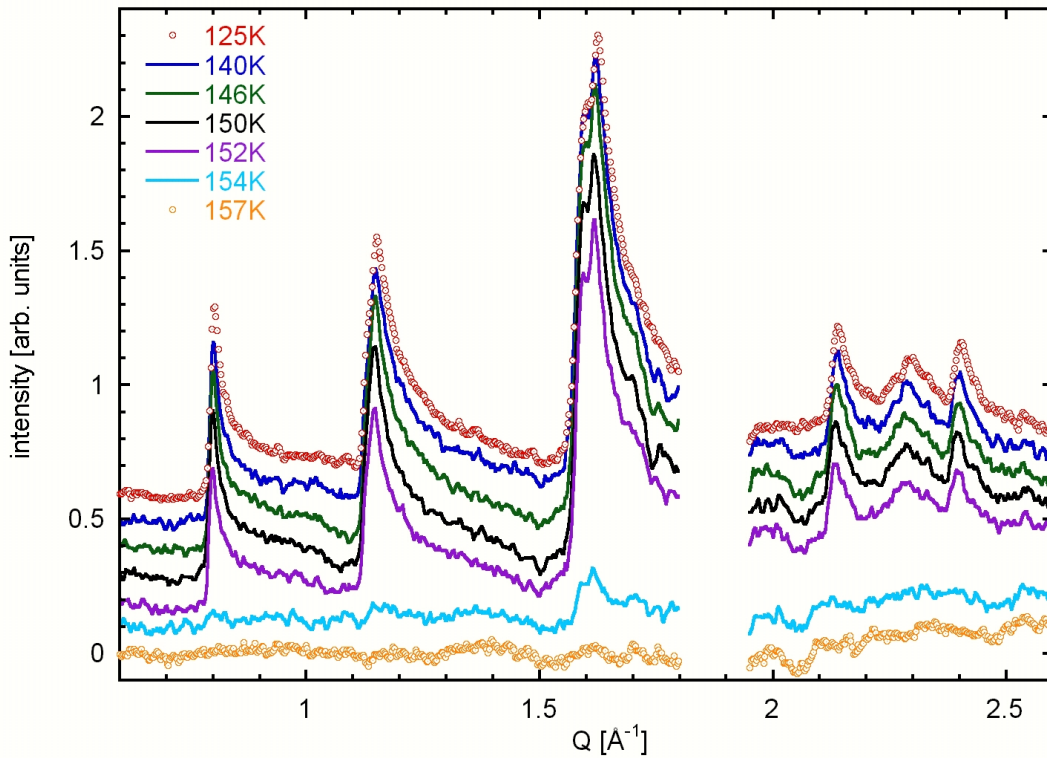


Figure 5.6: Melting of the solid phase of CH_3I on BN. The intensity distribution of the reflections is shown over the Q range between 0.6\AA^{-1} and 2.6\AA^{-1} and for temperatures between 125K and 157K. The scans were shifted by 0.1 counts for illustration purposes.

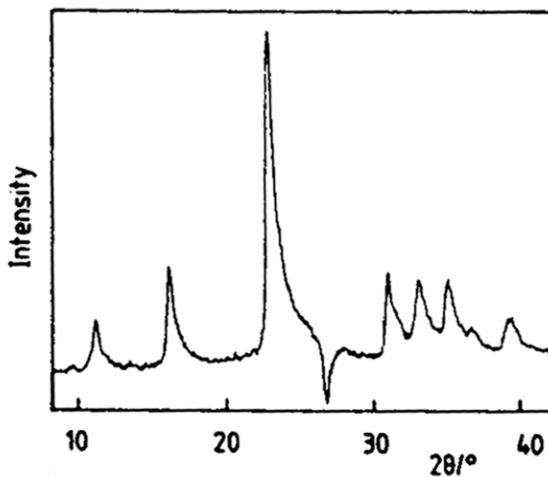


Figure 5.7: X-ray diffraction pattern of CH_3I on graphite at 110K. The figure is from Bucknall et al. [Buc89] showing the intensity over a relevant region in 2θ .

First, it appears that methyl iodide does not form a rectangular unit cell. The reflection at $Q \approx 1.14\text{\AA}^{-1}$ shows a shoulder in the vertical rise indicating that it may be the superposition of two reflections. This splitting is more evident at higher wavevectors (e.g. $Q \approx 1.60\text{\AA}^{-1}$ and $Q \approx 2.27\text{\AA}^{-1}$), where multiple reflections are clearly resolved. The following positions of re-

flections have been determined (Table 5.3) leading to a unit cell with the lattice parameter $|\vec{A}| = (5.90 \pm 0.05) \text{ \AA}$, $|\vec{B}| = (15.78 \pm 0.05) \text{ \AA}$ and $\gamma = 91.5^\circ \pm 0.5^\circ$.

While the unit cell dimensions are related to the positions of the diffracted peaks, the intensity variation of the diffracted peaks is determined by the position and orientation of the molecules within the unit cell. Since the dimensions of the unit cells of CH_3I on BN and graphite are comparable, it is assumed that both cells contain the same number of molecules (i.e. four molecules).

	Index (h, k)	$Q_{\text{cal}} [\text{\AA}^{-1}]$	$Q_{\text{est}} [\text{\AA}^{-1}]$	Intensity [est.]
1	(0,2)	0.797	0.800	21.0
2	(1,-1)	1.127	1.135	40.0
	(1,1)	1.147		
3	(1,-3)	1.580	1.600	100.0
	(0,4)	1.593		
	(1,3)	1.622		
4	(2,0)	2.131	2.130	30.0
5	(1,-5)	2.234	2.240	13.0
	(2,-2)	2.255		
6	(1,5)	2.283	2.290	17.0
	(2,2)	2.294		
7	(0,6)	2.390	2.390	30.0

Table 5.3: Position and intensities of reflections of the diffraction signal from a monolayer methyl iodide on boron nitride. The intensities are proportional to the multiplicity m times the square of the structure factor F over Q ($I \approx m \cdot F^2 / Q$) since these are powder-integrated values.

An estimate of the intensity of every reflection is a difficult task because the large overlap due to the Q -dependence of the lineshape of the reflections. Nevertheless, it was possible to determine the sum of intensity of reflections that are positioned close in Q after an approximation of Warren profiles to the diffraction pattern had been carried out. Table 5.3 summarizes the obtained values for the intensities. The positions of the reflections have been calculated using the determined unit cell of CH_3I on BN.

The distribution of the intensity of the reflections shown in Table 5.3 is determined by the arrangement of the molecules within the unit cell. In order to decide where the molecules reside, the four molecules are shifted on a fine grid ($0.2 \text{ \AA} \times 0.2 \text{ \AA}$) within the unit cell and the corresponding intensities are calculated for each configuration. Initially, only the four iodine atoms are shifted to reduce the number of parameters and the calculation time. This is a good approximation because the majority of the scattered intensity comes from these atoms.

If a configuration of molecules was found with similar intensities to the experimental ones (i.e. all intensities of the reflections agreed within $\pm 20\%$), it was marked and maps of possible positions within the unit cell were created. Once the estimation using only the iodine atoms converged, the calculation was repeated using the entire CH_3I molecule. It was assumed that the molecule is positioned with the C-I axis parallel (like CH_3I on graphite) to the surface. Furthermore, each of the molecules was rotated around an axis perpendicular to the surface in steps of 15 degree at or near the estimated positions of the previous calculation. A good agreement was obtained by positioning four methyl iodide molecules into the unit cell at the following positions (Table 5.4):

#	Fractional coordinates	Orientation φ
1	(0.00, 0.00)	$135^\circ \pm 15^\circ$
2	$(0.00 \pm 0.05, 0.30 \pm 0.03)$	$315^\circ \pm 15^\circ$
3	$(0.50 \pm 0.05, 0.50 \pm 0.03)$	$45^\circ \pm 15^\circ$
4	$(0.50 \pm 0.05, 0.80 \pm 0.03)$	$225^\circ \pm 15^\circ$

Table 5.4: Molecule position and orientation φ of the four methyl iodide molecules within the unit cell on BN.

The angle φ describes the orientation of a methyl iodide molecule around a normal to the plane of the unit cell. An orientation of $\varphi=0$ would indicate that the molecule is parallel to \vec{A} , i.e. the methyl group pointing along the direction of \vec{A} .

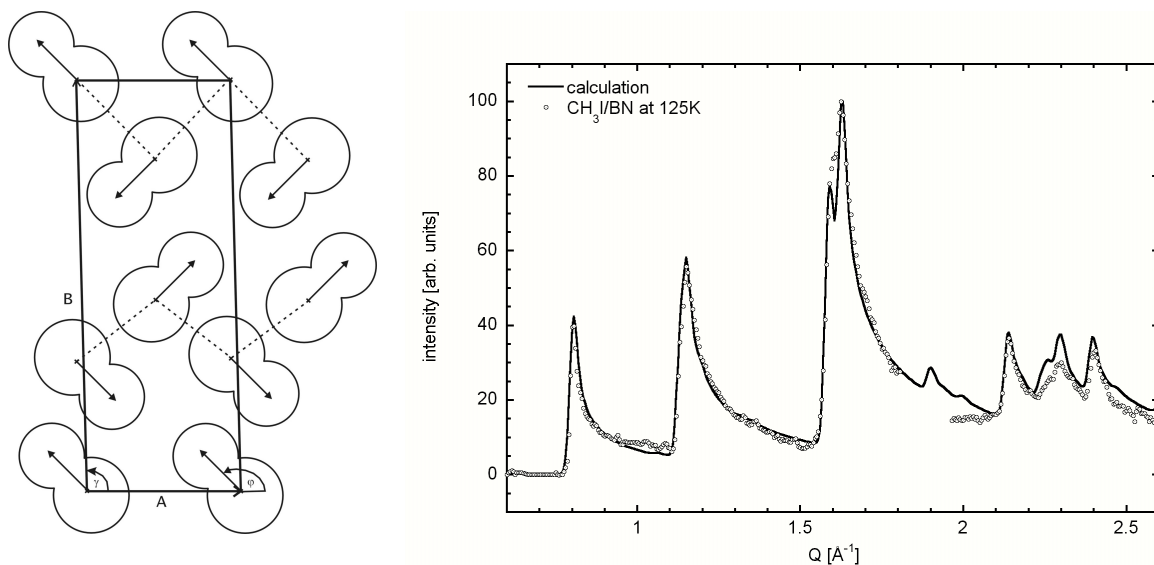


Figure 5.8: Schematic view of the unit cell constructed to explain the diffraction pattern of methyl iodide on BN [left]. The arrows are pointing away from the iodine atoms of the molecules. The graph on the right hand side shows a calculation of a diffraction signal from this configuration of molecules in comparison with the experimental data at 125K.

This layout in the unit cell produces no net overall dipole moment in the layer and is essentially identical to the graphite case and reproduces the (010) plane of a methyl iodide crystal. Figure 5.8 shows the setup of the CH₃I molecules in the unit cell and a calculation of the corresponding diffraction signal.

In the calculation a Debye-Waller factor, $DWF \approx \exp(-\sigma^2 Q^2)$, was included to improve the fit. It describes the effects of thermal vibration of the molecules on the observed diffraction peaks. The best estimate was a displacement of $\sigma = 0.27 \text{ \AA}$. It should be pointed out that no preferred order of the powder particles was observed. This is surprising because BN is composed of small flat plates (Chapter 3). A highly preferentially ordered sample would result in a change of the tail of the Warren lineprofile (i.e. a faster drop off resulting in a more 3D like shape of the reflection), which was not detected. The calculation confirmed the preliminary findings that the intensity distribution function could be modeled by a Gaussian function only and that the coherence length of the adsorbed film was $L_G = 270 \text{ \AA}$.

The melting of the 2D solid phase:

It was mentioned above that a dramatic change in the diffraction patterns was observed between 152K and 154K (Figure 5.5). The temperature dependence of the position and intensity of reflections of the solid phase (Figure 5.6) can be used to characterize this transition more quantitatively. The position and intensity of three reflections [(0,2), (1,3) and (2,0)] was examined with increasing temperature. These reflections were chosen in order to see if the changes are similar in both unit cell directions. The temperature dependence of intensity and position of these three reflections are shown in Figures 5.9a,b. In both plots, the behavior is normalized relatively to the low temperature scan at 125K.

Figure 5.9a displays a sudden decrease in intensity at around $153 \pm 1 \text{ K}$ for all investigated reflections. This means that the long-range order is lost in both directions of the unit cell at the same time and is characteristic for a first order melting transition.

In addition, a small expansion of the unit cell with temperature could be observed as shown in Figure 5.9b. Even though the data has large errors, it is possible to determine an average expansion of the unit cell to $d(T) = d(125 \text{ K}) / (1 - 0.00014 (T [^\circ\text{K}] - 125 \text{ K}))$ in the range between 125K and 153K by fitting a straight line to the position as function of temperature.

As a summary of these investigations it can be stated that the observed long range ordered phase of CH₃I is likely a 2D solid, which is similar in structure to the (010) plane of bulk crystals of methyl iodide and the adsorbed CH₃I film on graphite. This solid structure is incommensurate with the BN substrate and it appears that it undergoes a first order melting transition at $153 \pm 1 \text{ K}$.

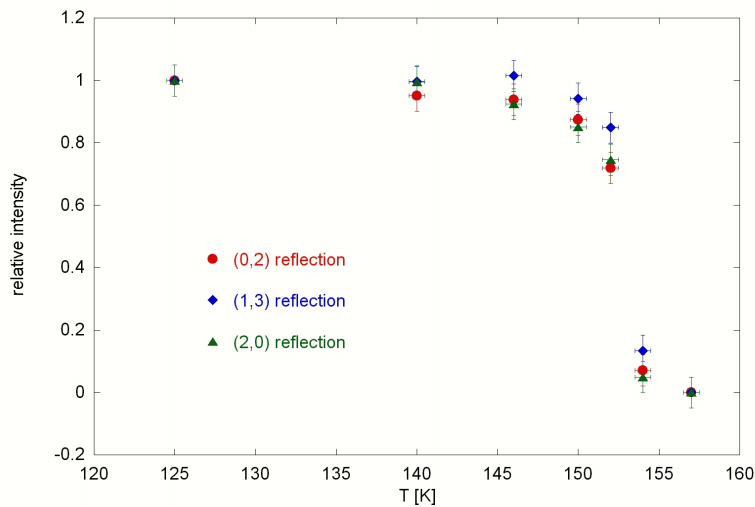


Figure 5.9a: Temperature dependence of the maximum intensity of reflections.

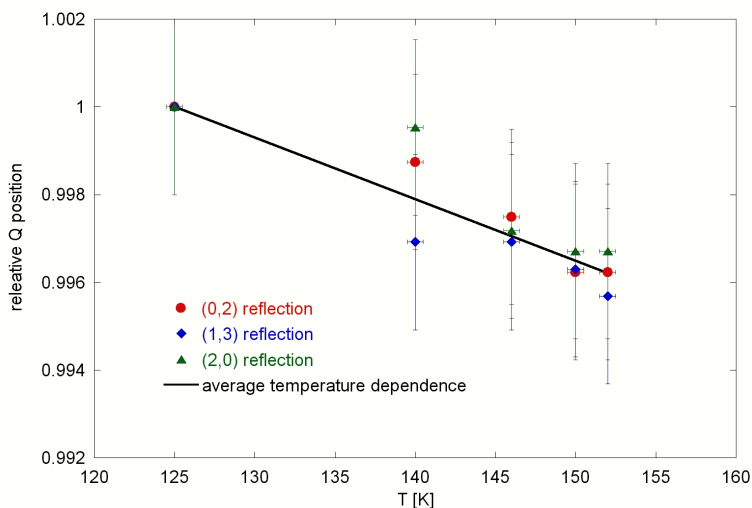


Figure 5.9b: Temperature dependence of the position of reflections.

5.2.2 Methyl bromide on BN

A single coverage (0.69 monolayer of Krypton equivalent) was investigated at temperatures of 50, 75, 100, 125 and 150K to determine the monolayer structure of CH_3Br . A difference scan at 100K is shown in Figure 5.10. The graph displays data within the interval of $1.1 \text{ \AA}^{-1} \leq Q \leq 2.6 \text{ \AA}^{-1}$. No additional diffraction signal of the adsorbed film was observed at lower wave vectors even though the measurements reached to $Q = 0.6 \text{ \AA}^{-1}$. This diffraction pattern exhibits a strong Warren lineshape like reflection at $Q \approx 1.7 \text{ \AA}^{-1}$ and two smaller peaks at $Q \approx 1.45 \text{ \AA}^{-1}$ and $Q \approx 2.35 \text{ \AA}^{-1}$. In addition one observes that the diffraction pattern below the (002) reflection of BN and at higher wave vectors do not smoothly connect. This may in-

indicate that another reflection may be present under the dominant scatter of the (002) BN diffraction peak that is due to the CH_3Br film.

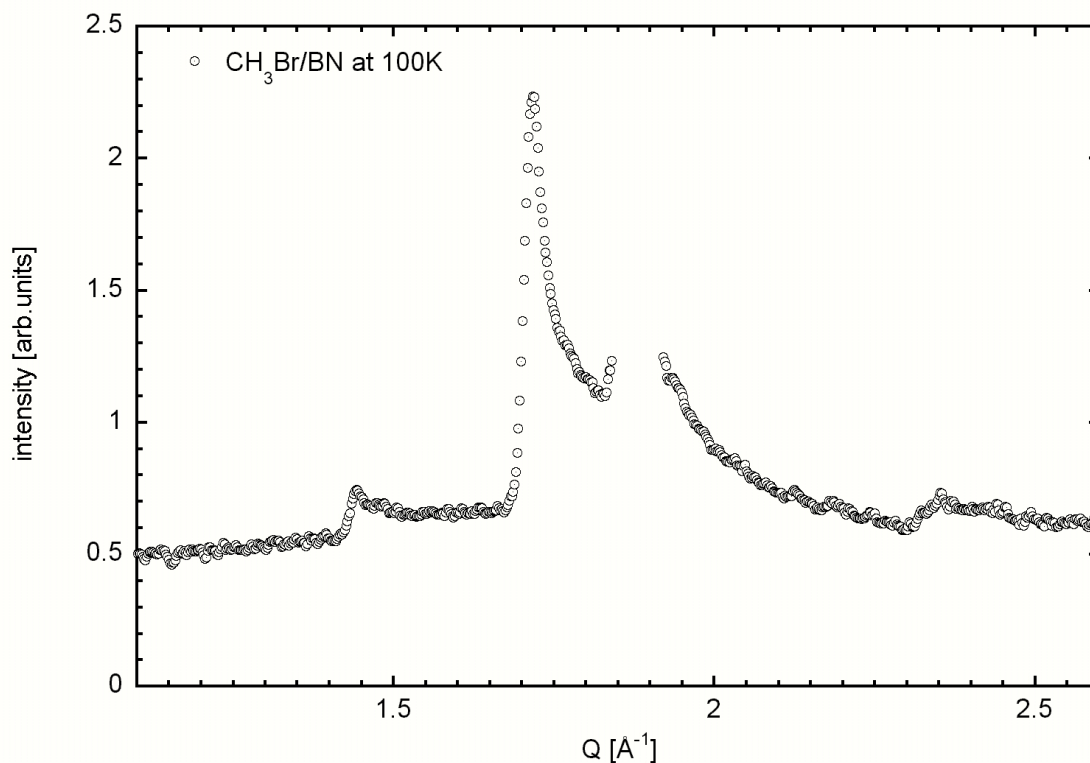


Figure 5.10: Difference pattern of a monolayer of methyl bromide on BN at 100K. The region $1.82\text{\AA}^{-1} \leq Q \leq 1.96\text{\AA}^{-1}$ does not provide reliable data because the strong (002) BN reflection is located there.

For the solution of the structure of CH_3Br on BN one can once again compare to structures of methyl halides on graphite. The x-ray pattern of the HD phase of methyl chloride on graphite exhibits strong similarities to the pattern shown in Figure 5.10. The HD phase of CH_3Cl on graphite is a small, almost centered, rectangular unit cell containing two molecules (see Section 5.11). In addition to the scattered intensity from the 2D solid phase, the difference scans contain a disordered phase and a diffuse background. Although these contributions are small (compared to the CH_3I case), they still have to be taken into consideration when trying to analyze the data. After accounting for these contributions, the following positions and intensities have been estimated for the monolayer CH_3Br on BN (Table 5.5).

Following a procedure similar to that for CH_3I on BN, a rectangular unit cell with the lattice parameter $|\vec{A}| = (4.38 \pm 0.05)\text{\AA}$ and $|\vec{B}| = (6.76 \pm 0.05)\text{\AA}$ was found, which results in good agreement with the experimentally determined positions of the reflections.

#	Index (h,k)	$Q_{\text{cal}} [\text{\AA}^{-1}]$	Intensity [est.]	Intensity [cal.]
1	(0,1)	0.929	0.0	0.00
2	(1,0)	1.435	10.0	10.33
3	(1,1)	1.709	100.0	100.00
4	(0,2)	1.859	55.0	50.26
5	(1,2)	2.348	10.0	9.00

Table 5.5: Experimentally determined and calculated positions and intensities of diffraction peaks of a monolayer CH_3Br on BN. The position and intensity of the (0,2) reflection of the adsorbed film are more uncertain because the presence of the strong (002) BN peak.

This unit cell contains two molecules in an up-down configuration similar to $\text{CH}_3\text{Cl}/\text{Gr}$ case, because the size of the unit cell and the x-ray diffraction pattern are similar. Before the search for the molecular configuration within the unit cell is started, it should be pointed out that the (1,0) and the (1,2) reflection are not extinguished. This is an indication that the unit cell is not centered.

Once again, an interactive search was used to determine the molecular positions within the unit cell that resulted in calculated intensities that best reproduced the experimental intensities. The first molecule was fixed at the origin of the unit cell with the methyl group pointing away from the surface fixing the orientation of the methyl group of the second molecule towards the surface. The position of the second molecule was then shifted on a very fine grid (1000 steps in each direction) within the unit cell and a structure factor calculation was performed for each step. This calculation produced the following solution:

While the first molecule resides at the origin, the second molecule is located at $(0.620 \pm 0.02, 0.50 \pm 0.03)$ in reduced unit cell dimensions. The molecules are in an up-down configuration. The agreement between model and experiment is good so that a possible tilt of the molecules is not considered.

A lineshape calculation of this molecular configuration gives the positions and intensities summarized in Table 5.5 and the Figure 5.11 displays the agreement between model and experiment. The coherence length of the adsorbed film was found to be 270\AA and the BN powder was isotropic (in agreement with the measurements on CH_3I on BN). As for CH_3I on BN the fit was improved including the effects of the Debye-Waller factor. The displacement due to temperature vibrations was estimated to be $\sigma = 0.20\text{\AA}$.

The structure reported here is probably not the only one that can be used to explain the x-ray diffraction pattern since only four reflections are recorded and the pattern is dominated by scattering from the bromine atoms. However, several arguments in favor of this solution can be made.

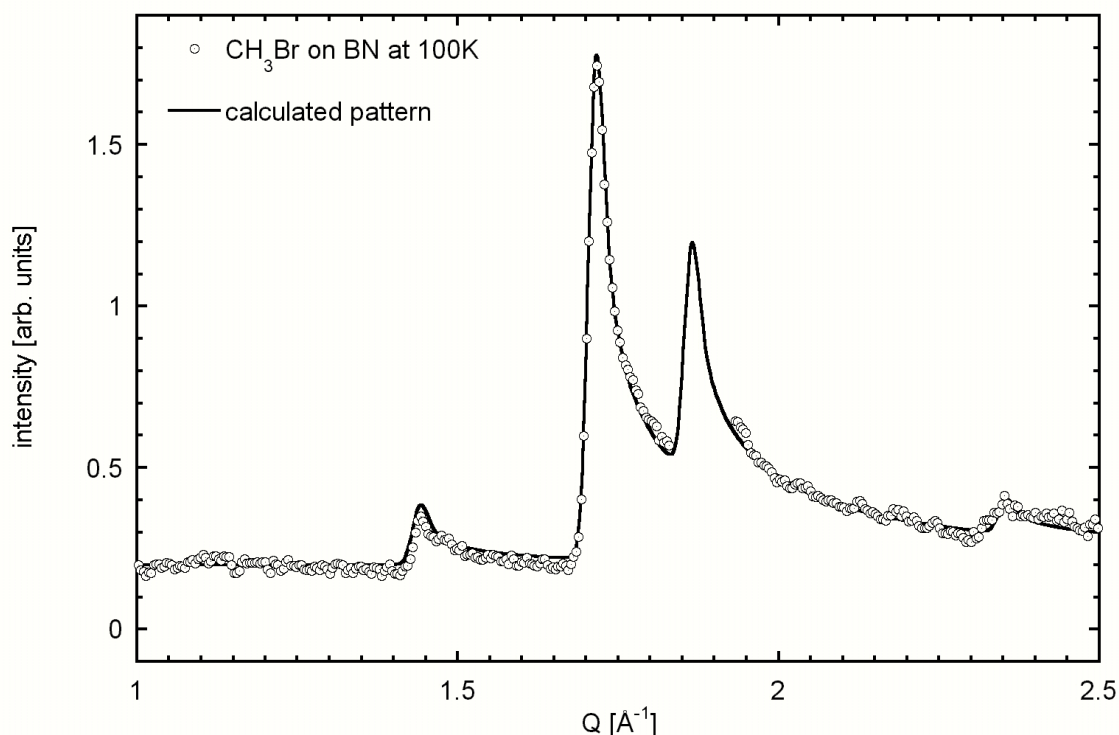


Figure 5.11: The solid phase of CH_3Br on boron nitride. Experimental data at 100K and calculation based on a rectangular unit cell containing two molecules.

First, the unit cell is probably too small to allow a molecular arrangement with the C-Br axis parallel to the surface. The area per molecule is only $\sigma_{\text{CH}_3\text{Br}} = 14.8 \text{ \AA}^2$ which is a very small value compared to the area occupied by methyl halide molecules lying flat on graphite, which are $\sigma_{\text{CH}_3\text{Cl}} = 19.5 \text{ \AA}^2$ for CH_3Cl , $\sigma_{\text{CH}_3\text{Br}} = 21.0 \text{ \AA}^2$ for CH_3Br and $\sigma_{\text{CH}_3\text{I}} = 22.5 \text{ \AA}^2$ for CH_3I (see [Mor91], [Cla91] and [Buc89]). Second, this configuration has no net dipole moment, which is energetically favorable. Third, this structure is very similar to the HD phase of methyl chloride on graphite. This last point is appealing since the structure presented here resembles planes of the bulk crystal (both methyl bromide and methyl chloride have a similar bulk phase [Kwa73], [Ger86]). But, the question remains why this structure is so different from the structure of methyl bromide on graphite (see Section 5.1.2, eight molecules are arranged in a herringbone structure). Two possible explanations can account for this difference. First, it could be possible that methyl bromide can form both a low-density **and** a high-density phase on boron nitride (i.e. like methyl chloride on graphite). In this case, the low-density phase was not observed on boron nitride because neither coverage dependent diffraction studies nor extended thermodynamic studies due to the extremely low saturated vapor pressure have been undertaken. The other possibility is that the slightly larger hexagons ($\sim 2\%$ as com-

pared to graphite) and the bi-atomic composition of the underlying BN substrate make it possible for the CH₃Br molecules to arrange in an up-down configuration.

The unit cell is nearly commensurate with the BN substrate in one direction. The mismatch in this dimension ($\sqrt{3}a_{\text{BN}} = 4.338\text{\AA}$) is less than 1% and within the accuracy of our measurements. A similar one-dimensional commensurability was detected for the HD phase of CH₃Cl on graphite.

The melting of this solid structure occurs between 125K and 150K. Unfortunately, only a few temperatures were investigated so it is not possible to narrow this interval or to analyze the behavior in more detail. However, the melting temperature of CH₃Cl on graphite was determined to $T_{\text{M}}=148\text{K}$, a value consistent with the results observed here.

5.2.3 Methyl chloride on BN

The structure of a methyl chloride film on BN was investigated at a single coverage equivalent of 0.67 monolayer of Krypton at 85K and measurements were performed at 50K, 75K, 100K, 125K and 150K. Figure 5.12 shows the difference patterns. The statistics of this data set is significantly poorer than the one for the methyl bromide or methyl iodide data. With this experiment the limit to detect and resolve the signal due to the adsorbed film was approached.

At 150K, only a very broad background from a disordered phase is observed. The diffraction data at 125K show a characteristic Warren lineshape like reflection at $Q \approx 1.733\text{\AA}^{-1}$ and the tail of a 2D reflection at $Q \approx 1.90\text{\AA}^{-1}$. Additional pairs of diffraction peaks are observed at $Q \approx 1.78\text{\AA}^{-1}$ and at $Q \approx 1.95\text{\AA}^{-1}$ in the low temperature scans. These extra reflections can be explained by the formation of bulk crystals of CH₃Cl on the Beryllium windows and have been identified as (111) and (200) reflection. This makes the analysis of the data even more difficult. However, those difference patterns exhibit similarities to diffraction data of the HD phase of methyl chloride on graphite. Exploiting this fact, the analysis of this data set can proceed.

Figure 5.13 shows how various components were removed from the raw difference scan before a model of the 2D structure on BN could be developed. In a first step, the broad diffuse background was removed from the differences. The second step removed bulk reflections of methyl chloride and another broad disordered phase centered at $Q \approx 1.90\text{\AA}^{-1}$. A similar disordered phase as for CH₃Cl on BN was observed and subtracted for methyl chloride on graphite, e.g. [Gri94] and [Str98]. The bulk reflections are easy to explain, however, the nature of the broad disordered phase is much harder to understand. A explanation to account for such a large percentage (~40%) of CH₃Cl molecules remaining disordered with an average molecule-molecule distance of around 3.8\AA (assuming a hexagonal close packed system) is

that the system was investigated in a two phase coexistence region (2D solid plus fluid/liquid like).

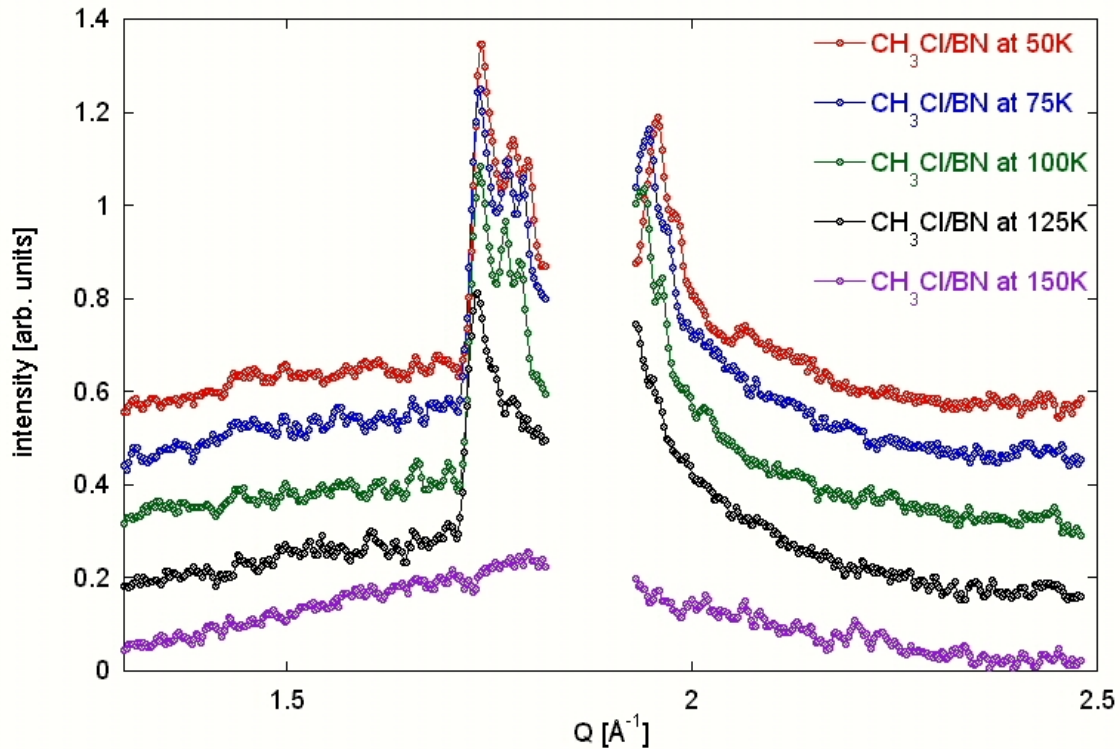


Figure 5.12: Difference data of methyl chloride on BN. For greater clarity the data were offset by a small amount.

After a careful subtraction of these bulk peaks of CH_3Cl , two reflections with Warren line-shapes are observable, a strong reflection at $Q \approx 1.733 \text{ \AA}^{-1}$ and a second reflection at $Q \approx 1.940 \text{ \AA}^{-1}$. Parts of this second peak are hidden under the strong (002) reflex of the boron nitride and were overlapped by scatter from the very near (200) bulk reflections of methyl chloride.

The second peak is most prominent at 50K since the 2D structure exhibits significant temperature dependence and the peaks move to slightly higher wavevectors as the temperature is decreased. It is possible to determine the two peak positions and to construct a similar rectangular unit cell with extended lattice distances as in the case on graphite. This analysis indicates that CH_3Cl on BN forms a rectangular unit cell at 50K with the following dimensions: $|\vec{A}| = 4.38 \text{ \AA}$ and $|\vec{B}| = 6.45 \text{ \AA}$.

The length of \vec{A} is within the experimental errors of the commensurate value of $\sqrt{3}a_{\text{BN}} = 4.338 \text{ \AA}$ (as in the case of methyl bromide on BN). An investigation of the peak shift with temperature indicates that the unit cell expands only in direction of \vec{B} . The length

of the lattice vector \vec{B} can be estimated to $|\vec{B}| = 6.53\text{\AA}$ at 125K and for other temperatures it can be determined by a linear interpolation between the two estimated values.

A comparison of the unit cell dimensions of CH_3Cl on graphite and BN indicates that the structure is locked to the substrate in direction of \vec{A} (both structures are (almost) commensurate in this direction) and an expansion is only possible with the substrate.

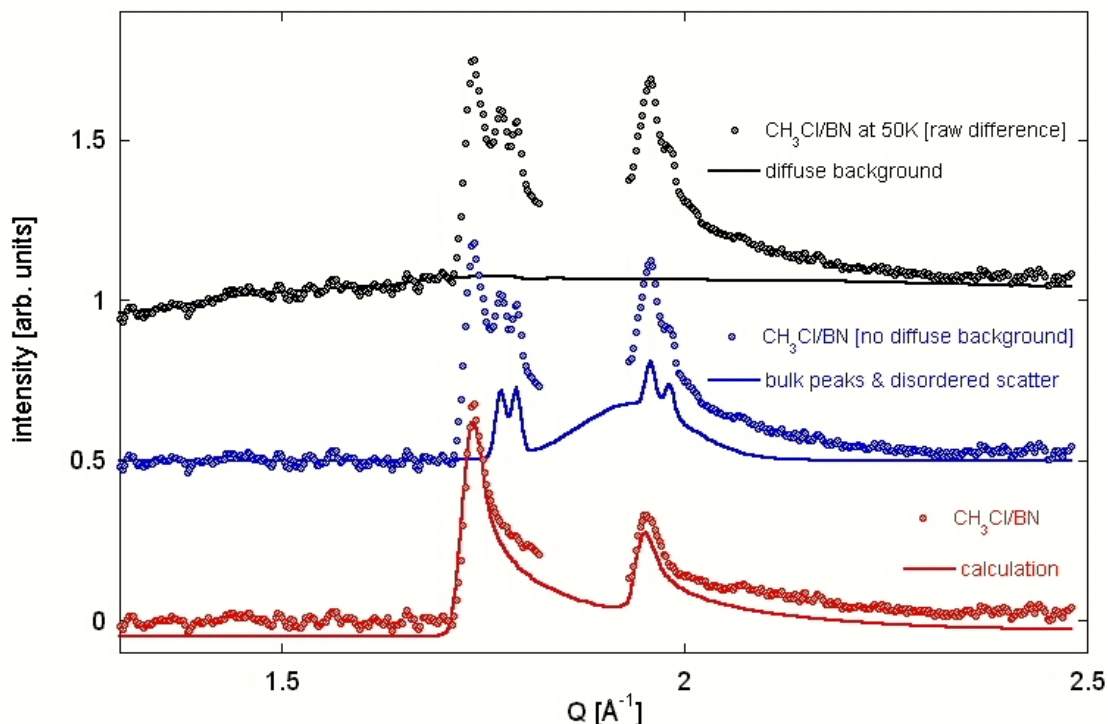


Figure 5.13: Estimated contributions to the difference patterns of CH_3Cl on BN. The scan at 50K is used as an example. A) A broad diffuse background is removed [top]. B) Bulk reflections and a second broad disordered phase centered at $Q \approx 1.90\text{ \AA}^{-1}$ are subtracted from the difference pattern [middle]. C) The remaining pattern is compared to a calculated pattern of a centered rectangular unit cell containing two molecules in an up-down configuration [bottom].

However, in the other direction, a large temperature dependence is observed. The adsorbate-adsorbate interaction seems to dominate in that direction. It is interesting to note, that the dimensions of the unit cells on graphite and BN are practical identical over a large temperature range (6.45\AA on BN and 6.46\AA on graphite at 50K and 6.53\AA on BN and 6.52\AA on graphite at 125K) excluding a strong influence of the substrates.

Some additional observations are helpful in determining the position of the second molecule within the unit cell. The (1,0), (0,1) and (1,2) reflection are extinguished indicating an almost centered position of the second molecule in the rectangular unit cell.

The results of methyl iodide and methyl bromide indicated that the intensity distribution function (Equation 2.16) of adsorbed films on BN could be modeled by a simple Gaussian function. The powder seemed to be isotropic and the coherence length of the film was around 270Å. Using these results the third step in Figure 5.13 shows a calculated pattern for the unit cell of CH₃Cl on BN mentioned above with two molecules at (0, 0) and (0.5, 0.5) in an up-down configuration in comparison with the experimental pattern after all these corrections.

It should be mentioned that the experimental data indicate a ratio of intensities between the two observed reflections of $I_{(11)}/I_{(02)} \approx 1$ if no disordered phase was subtracted from the difference patterns. However, no configuration of two molecules in an up-down configuration could explain this ratio. In the up-down model, the intensity of the (11) reflection cannot exceed 60% of the intensity of the (02) reflection.

However, the statistics of the available data is probably not good enough to further analyze the nature of the broad disordered background. If better data becomes available, it might be possible to develop models with higher certainty and other interesting question could be investigated. For example, it would be interesting to see if a LD phase could be observed on BN as on graphite and if so, to study the phase transition between these two phases in more detail.

5.3 Methyl halides on magnesium oxide

The study of 2D structures of adsorbed methyl halides films on the (100) surface of magnesium oxide provides an intriguing contrast to the investigations discussed in the previous section. The interactions of polar molecules with the four-fold, ionic (100) MgO surface introduce new aspects into phenomena like 2D electrical ordering.

From the practical perspective, one problem is encountered in studying adsorbed films of methyl halides on MgO with x-ray powder diffraction. The signal from the MgO substrate is roughly 3-4 times stronger than the signal from the boron nitride samples due to the higher electron density making it more difficult to separate the signal of the adsorbed film from the background.

Already in the beginning of this chapter it was mentioned that a normalization of the (111) reflection of the MgO ($I_{MgO(111)} = 1000$) is performed before the difference is taken between background measurements and the measurements of the adsorbed film are calculated. The main reason to use this reflection ($Q_{111} = 2.584 \text{ \AA}^{-1}$) is that the intensity is about 25 times weaker than the intensity of the (200) reflection ($Q_{200} = 2.984 \text{ \AA}^{-1}$). For most measurements the MAR 345 detector was positioned in a way that the Debye-Scherrer cone of the (200) reflection was just outside of the active area of the detector. This allowed longer exposure times before the image plate response saturated.

In this section, the measurements of adsorbed methyl halides films on MgO are discussed. It begins with an examination of the temperature and coverage dependent properties of methyl iodide films. After the CH_3I films this section is concluded by describing the investigations of properties of the monolayer structures of CH_3Br and CH_3Cl films.

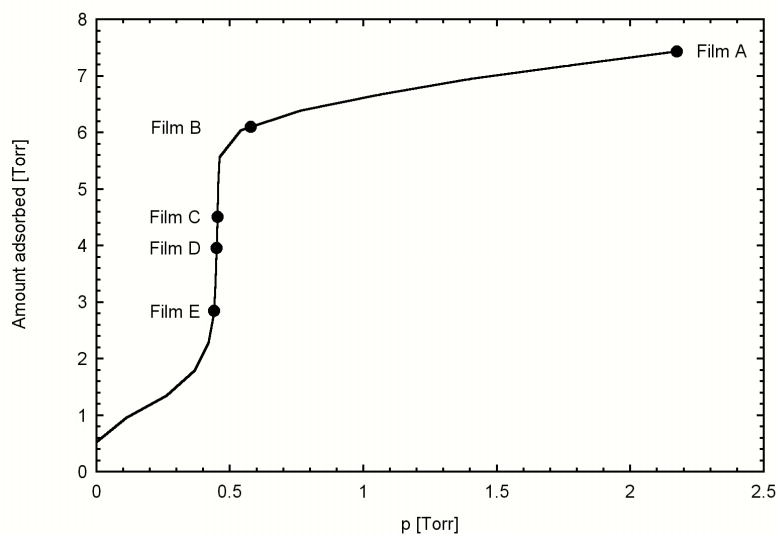


Figure 5.14: Isotherm of methyl iodide on MgO at 225K. The amount adsorbed in Torr is plotted against the vapor pressure in Torr. The dosing volume was $V_{\text{dos}} = 58.9 \text{ cm}^3$. The markers indicated the coverages that were temperature dependent investigated.

5.3.1 Methyl iodide on MgO

To study the structural properties of methyl iodide on MgO as a function of coverage and temperature a series of films of different surface coverages were prepared. The markers on the isotherm in Figure 5.14 indicate the coverages that were investigated.

Films are identified according to the amount adsorbed. Film A corresponds to the highest coverage, while Film E to the lowest. The coverages have been determined using the point B method. This resulted in the following values:

	Film A	Film B	Film C	Film D	Film E
Ω [mnl]	1.17	0.96	0.71	0.63	0.45

Table 5.6: Coverages of the methyl iodide on MgO films in monolayer [mnl].

Most films were studied between 125-175 K, but this temperature range was extended for some films to even lower temperatures (25 K or 75 K). Figure 5.15 displays the temperature dependence using a subset of the difference scans from film B between 125-150K. An example of the coverage dependence of methyl iodide on MgO at 125 K is shown in Figure 5.16. The temperature dependent behavior is discussed first

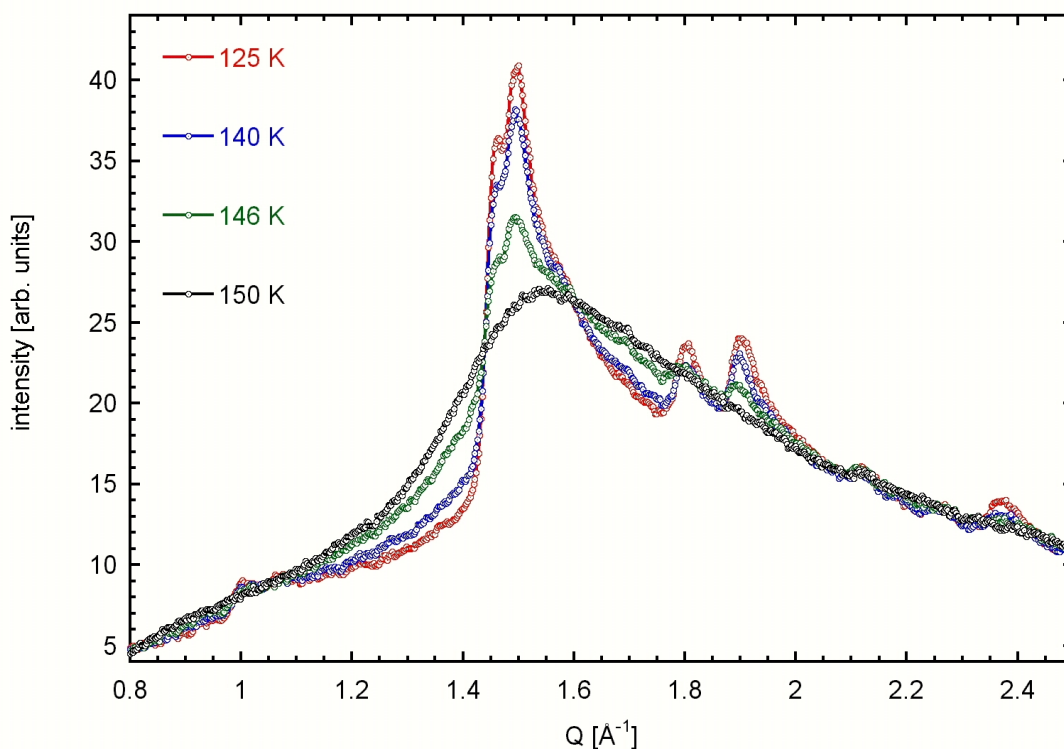


Figure 5.15: Difference scans of film B of methyl iodide adsorbed on MgO over the temperature range between 125 K and 150 K.

The temperature dependent spectra in Figure 5.15 are reminiscent of the behavior of methyl iodide on boron nitride (Figure 5.5). There is little variation in the spectra below 146K. Multiple Warren lineshape like diffraction features (see Table 5.8) are observed. However, at around 146 K a significant change in the difference pattern takes place. A drop in the peak intensity ($Q \approx 1.5 \text{ \AA}^{-1}$) and a broadening of the peaks is observed. This trend continues as the temperature is increased until only a broad feature is observed.

Another interesting variation in the diffraction lineshape features is readily observable in the coverage dependent difference spectra (Figure 5.16). At the lowest coverage, no evidence of Warren lineshape like features is observed. The difference pattern exhibits only a broad diffuse signal centered at $Q \approx 1.5 \text{ \AA}^{-1}$. All other traces show a pronounced Warren lineshape appearance.

No evidence of bulk formation of methyl iodide on MgO is found (in contrast to the measurements of CH_3I on BN). This makes the preliminary data reduction less labor intensive. However, the main focus of the data analysis is centered on the determination of the 2D unit cell and in establishing the location of the molecular positions within it. This task is more difficult because there is no similar system (like BN/graphite) available to use as starting point and small modifications of known structures do not lead to successful solutions for the 2D structure of CH_3I on MgO.

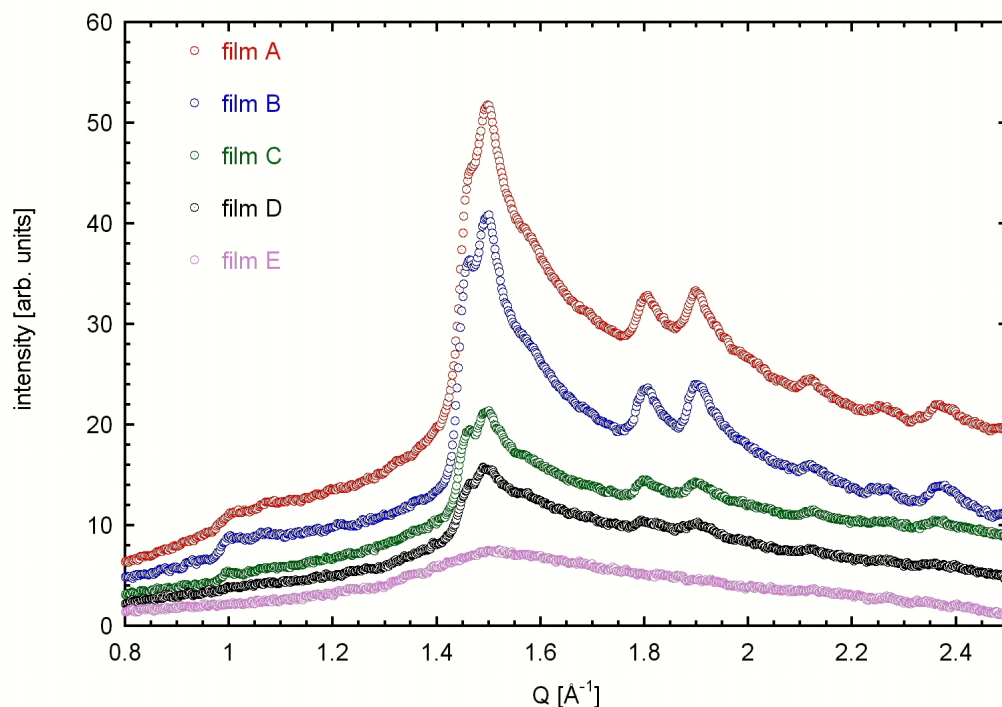


Figure 5.16: Coverage dependent difference spectra of methyl iodide adsorbed on MgO at 125K.

a) The determination of the position and intensity of the reflections

The attempt to solve the monolayer structure of CH₃I adsorbed on MgO begins by performing a detailed analysis of the difference spectra of film B at 125 K (Figure 5.17). This difference pattern shows the sharpest Warren lineshape like reflections and the coverage is below monolayer completion so multilayer effects are excluded. The analysis is concentrated on wavevectors below $Q = 2.5 \text{ \AA}^{-1}$ to avoid places where the pattern is affected by the strong substrate reflections. It should be noted that two reflections are present at Q values ($Q \approx 2.837 \text{ \AA}^{-1}$ and $Q = 3.336 \text{ \AA}^{-1}$) above the MgO (111) and MgO (200) reflections respectively.

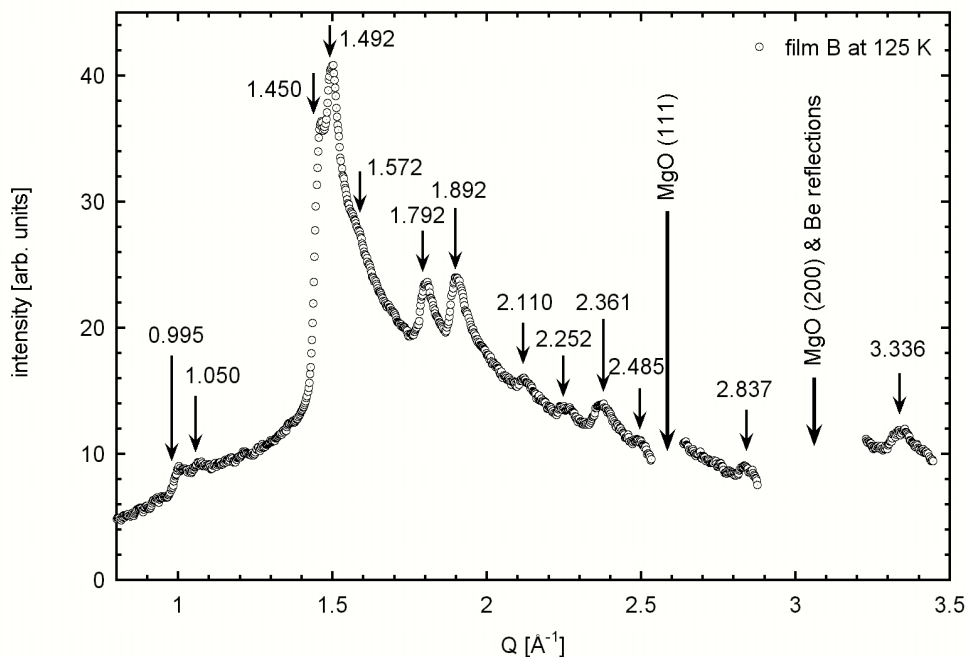


Figure 5.17: X-ray diffraction difference spectra from film B at 125K. Preliminary estimates of the positions of the Warren lineshape like reflections are indicated. Data in the regions of $Q \approx 2.584 \pm 0.07 \text{ \AA}^{-1}$ and $Q \approx 3.05 \pm 0.15 \text{ \AA}^{-1}$ is not accessible because the background signal is very strong.

The data reduction started by assuming the diffraction pattern is a superposition of a broad diffuse background and a highly ordered 2D phase (similar to methyl iodide on BN). These two parts of the difference pattern have to be separated to improve the initial estimates of the peak positions and intensities of the 2D reflections. Inspection of Figure 5.15 suggests that the difference pattern at 150K might be a good trace to use to separate these phases. It is assumed that the 2D solid part of the difference pattern could be separated as:

$$I_{\text{solid film B}}[T(\text{K})] = I_{\text{film B}}[T(\text{K})] - a \cdot I_{\text{film B}}[150\text{K}] - \text{const.} \quad 5.1$$

The variable a , $0 \leq a \leq 1$, describes the ratio of the disordered phase to the total difference spectra and the constant offset is estimated as the mean intensity value in the region of $0.80 \text{ \AA}^{-1} \leq Q \leq 0.95 \text{ \AA}^{-1}$. Figure 5.18 displays the obtained temperature dependent patterns for the solid phase of film B.

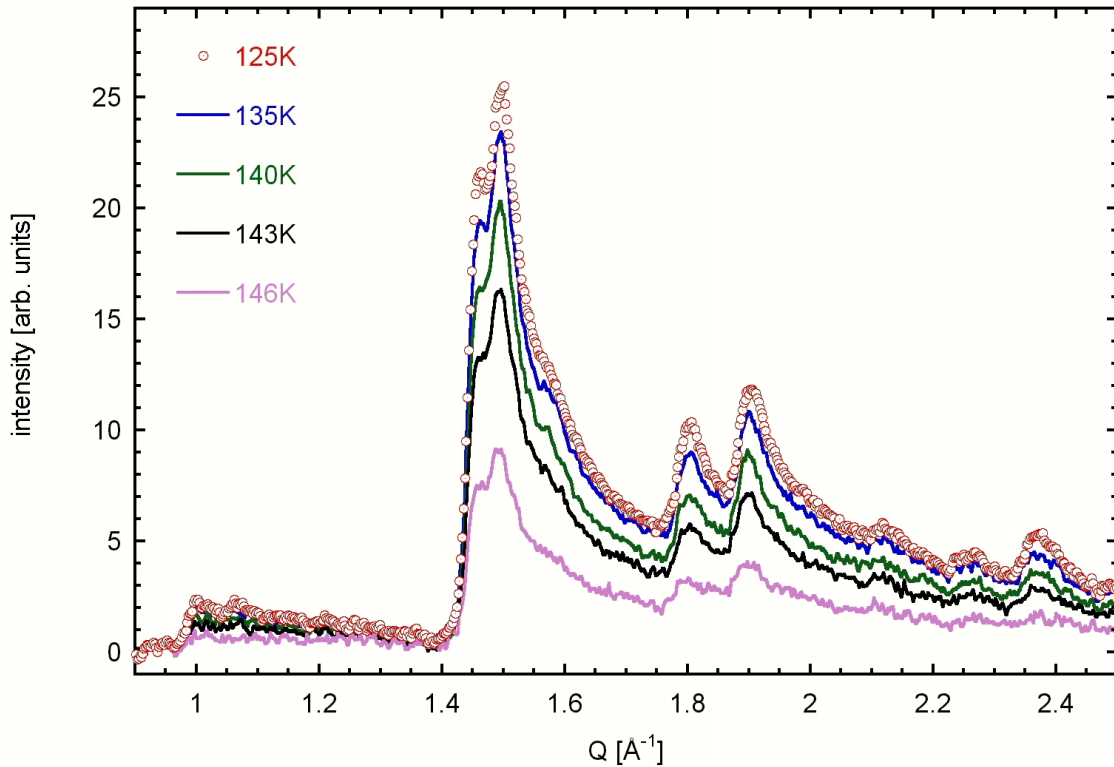


Figure 5.18: Temperature dependence of the 2D solid phase of film B of methyl iodide on MgO.

Table 5.7 summarizes the values obtained from these calculations.

T [K]	solid part (1-a) [%]	disordered part a [%]	const. offset
125	51±3	49±3	2.6390
135	47±3	53±3	2.3202
140	39±3	61±3	2.0100
143	32±3	68±3	1.5606
146	17±3	83±3	0.8504
150	0	100	0.0000

Table 5.7: Solid and disordered phase parameters derived for film B using Equation 5.1. The diffraction pattern at 150 K was assumed to be the model for the disordered component.

The next step in the analysis was to fit Warren lineshape like profiles to the solid part of film B difference patterns. Figure 5.19 illustrates this procedure. The objective is to determine reliable values for the positions and intensities of the reflections.

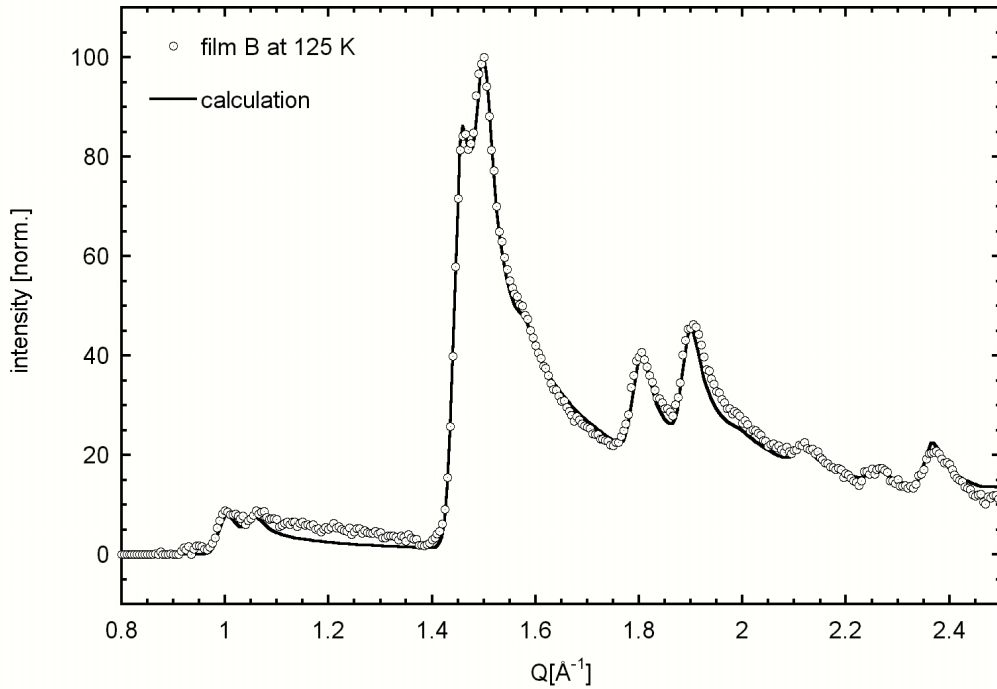


Figure 5.19: Solid part of film B at 125 K and a calculation of Warren lineshape like profiles.

In performing this analysis, an isotropic distribution of the MgO particles in the powder was assumed and the intensity of the Braggrod was characterized using a Gaussian intensity distribution function (Equation 2.27). A total of 12 reflections were detected in the Q range of $0.8 \text{ \AA}^{-1} \leq Q \leq 2.5 \text{ \AA}^{-1}$. The coherence length was found to be $L_G = 210 \pm 10 \text{ \AA}$. In addition, a Debye-Waller factor was included. The best estimate resulted in a molecule displacement of $\sigma = 0.285 \text{ \AA}$.

$Q [\text{\AA}^{-1}]$	0.995	1.050	1.450	1.492	1.573	1.796	1.892
$I [Q]$	5.0	3.0	100.0	74.0	7.0	36.5	46.5
$Q [\text{\AA}^{-1}]$	1.989	2.110	2.252	2.359	2.487	2.834	3.334
$I [Q]$	2.5	10.0	9.0	31.5	3.5	N/A	N/A

Table 5.8: Positions and intensities of the Warren lineshape like reflections used to model the difference pattern of film B of methyl iodide on MgO. The intensities are not directly proportional to the multiplicity m times the square of the structure factor F . Instead, they are proportional to $I \approx m \cdot F^2 / Q$.

The positions and intensities used in the calculation are listed in Table 5.8. The error ε of the assigned peak position should be linear in Q because of line broadening at higher wave vectors. It was estimated to $\varepsilon \leq 0.005 \cdot Q$. The error in determining the intensities is greater and more complicated to estimate due to the Q dependence of the reflections and effects of the Debye-Waller factor at large Q values. The overlap of the two strongest reflections (at $Q = 1.450 \text{ \AA}^{-1}$ and $Q = 1.492 \text{ \AA}^{-1}$) is another fact increasing the difficulty to determine the exact values of the intensities. However, the intensities can be determined with respect to the sum of these two reflections with a high certainty (see Table 5.9) similar to the case of CH_3I on BN. The error is of the order of the greater value of 10% or ± 5 counts.

$Q [\text{\AA}^{-1}]$	0.786	1.025	1.475	1.573	1.796	1.892	1.989
$I [Q]$	<10.0	<10.0	100.0	5.0	25.0	35.0	<5.0
$Q [\text{\AA}^{-1}]$	2.110	2.252	2.359	2.487	2.834	3.334	
$I [Q]$	8.0	7.5	30.0	<5.0	N/A	N/A	

Table 5.9: Estimated intensities of the Warren lineshape like reflections normalized to the sum of the two strong reflections at $Q = 1.450 \text{ \AA}^{-1}$ and $Q = 1.492 \text{ \AA}^{-1}$. The intensities are proportional to $I \approx m \cdot F^2$.

b) Search for the 2D unit cell of CH_3I on MgO

A closer look at Table 5.8 reveals that several of the positions of the 2D reflections are very near to or exactly at commensurate positions on MgO. For example, the position of the (10) reflection of a 1×1 structure of the adsorbed molecules would be $Q_{10} = 2.110 \text{ \AA}^{-1}$ or the position of the (10) reflection of a $\sqrt{2} \times \sqrt{2} R 45^\circ$ structure would be $Q_{10} = 1.492 \text{ \AA}^{-1}$. In addition, some reflections are simple multiples of others or are connected via other simple relations. Table 5.10 provides an overview of these relationships.

#	$Q [\text{\AA}^{-1}]$	Relationship
1	0.995	$2 \cdot 0.497 = 0.994$
	1.492	$3 \cdot 0.497 = 1.491$
	1.989	$4 \cdot 0.497 = 1.988$
	2.487	$5 \cdot 0.497 = 2.485$
2	1.050	$1 \cdot 1.050 = 1.050$
	2.110	$2 \cdot 1.050 = 2.110$

Table 5.10: Relationships between the positions of some of the reflections determined for the solid phase of methyl iodide on MgO.

Recognition of these ‘algebraic coincidences’ led to search for a commensurate structure of methyl iodide on MgO, which could explain all the observed reflections. While it was tempt-

ing to think that the solution was simple, it was soon realized that none of the simple superstructures (e.g. square or very small) allowed predicting all the peak positions. A computer program was written that could test if any commensurate structures existed that could reproduce the observed reflections.

#	$ \bar{A} $ [Å]	$ \bar{B} $ [Å]	γ [degree]	Area [Å ²]
1	8.4226	13.317	108.43	106.41
2	8.4226	17.867	135.00	106.41
3	8.4226	24.556	149.04	106.41
4	13.317	13.317	143.13	106.41
5	13.317	17.867	154.43	106.41
6	13.317	25.268	161.57	106.41
7	13.317	30.368	164.47	106.41
8	17.867	24.556	165.96	106.41
9	17.867	30.368	168.69	106.41
10	8.4226	25.268	90.00	212.82
11	8.4226	26.635	108.43	212.82
12	8.4226	30.368	123.69	212.82
13	8.4226	35.734	135.00	212.82
14	13.317	16.845	108.43	212.82
15	13.317	17.867	116.57	212.82
16	13.317	24.556	139.40	212.82
17	13.317	26.635	143.13	212.82
18	13.317	35.734	154.43	212.82
19	16.845	17.867	135.00	212.82
20	16.845	24.556	149.04	212.82
21	17.867	26.635	154.43	212.82
22	8.9335	29.927	95.711	266.02
23	8.9335	30.368	101.31	266.02

Table 5.11: Part of the list of possible solutions of the 2D unit cell of methyl iodide on MgO found to reproduce all experimentally determined reflections.

The program imposed some restrictions in trying to find a structure solution. First, the investigated Q range was limited to $Q_{\max} = 2.5 \text{ \AA}^{-1}$. Second, an uncertainty in the positions of the peak was included. The difference between experimentally estimated and calculated position had to be less than the linear error mentioned above. Third, the size of the unit cell was restricted. The maximum side length of the 2D structure was limited to 50 \AA . Finally, the program limited the Miller indices h, k to be less than 16.

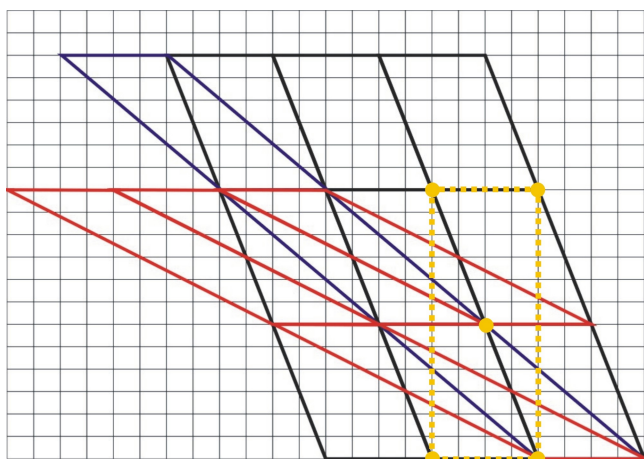


Figure 5.20: Schematic sketch of some solutions (#1 (black), #2 (blue) and #3 (red)) of 2D unit cells of methyl iodide on MgO (see table 5.10). The underlying square grid simulates the (100) surface of MgO (each square has a side length of 2.11\AA). In addition solution #10 is shown (orange) to visualize its relationship to solution #1.

On the very first run of this structure searching computer program so many commensurate structures were found that reproduced all observed 2D reflections that the suspicion, that methyl iodide forms a commensurate structure on MgO was confirmed. However, with so many solutions, a set of criteria had to be developed to decide which of these possibilities had higher probabilities to be the ‘*final*’ solution. It was decided to sort the solutions in the following way.

$Q [\text{\AA}^{-1}]$	#1	#10	#22
	(h,k)	(h,k)	(h,k)
0.995	(0,2)	(0,4)	(1,3)
1.050	(1,1), (1,-2)	(1,3)	(0,5)
1.450	(1,2), (1,-3)	(1,5)	(2,1)
1.492	(2,-1), (0,3)	(0,6), (2,0)	(2,-3)
1.573	(2,0), (2,-2)	(2,2)	(1,-7), (2,-4)
1.793	(2,1), (2,-3)	(2,4)	(2,-6)
1.893	(1,3), (1,-4)	(1,7)	(1,8)
1.989	(0,4)	(0,8)	(2,6)
2.110	(2,2), (2,-4)	(2,6)	(0,10), (3,-1)
2.252	(3,-1), (3,-2)	(3,1)	(2,-9)
2.359	(3,0), (3,-3)	(1,9)	(1,-11), (3,-6)
	(1,4), (1,-5)	(3,3)	(3,4)
2.487	(2,3), (2,-5)	(2,8), (0,10)	(1,11)
	(0,5)		

Table 5.12: List of Miller indices of the 2D reflections for the three possible unit cell.

The first criterion was the size of the unit cell. Next, the angle between the unit vectors of the unit cell was considered. Angles close to 90 degree were considered to have a higher probability. Table 5.11 lists a small portion of the solutions obtained after this method. Most of

these solutions are identical with others and by applying geometrical arguments one can quickly reduce the manifold of solutions. This is demonstrated graphically by using the first three solutions of Table 5.11 in Figure 5.20. By identifying the equivalent solutions the entries in Table 5.11 can be reduced to three, number 1, 10 and 22. In fact even solutions #1 and #10 can be easily connected. Solution #10 can be interpreted as a centered rectangular version of two unit cells of the form of #1 (see Figure 5.20).

Once the number of possibilities is reduced, the next step is to index the reflections. This is done for these three unit cells in Table 5.12. Identification of extinction rules is the starting point for the search for symmetries within the unit cell. Closer examination of the three cases listed above produces the following information. Unit cell #1 shows no evidence of higher symmetry and this choice of unit cell does not predict any additional reflections in the investigated Q range. Only the three low order reflections (1,0), (0,1) and (1,-1) which are located at $Q \leq 0.8 \text{ \AA}^{-1}$ ($Q_{(0,1)} = 0.497 \text{ \AA}^{-1}$ and $Q_{(1,0),(1,-1)} = 0.786 \text{ \AA}^{-1}$), which is outside the experimentally accessible range, are not observed.

For unit cell #10 only reflections, with an even sum of the Miller indices h, k , are predicted. This is strong evidence of a centered unit cell and confirms the interpretation of the relationship between cells #1 and #10. Including the symmetry restriction ($h+k$ even), only two reflections are predicted at low wavevectors ($Q \leq 0.8 \text{ \AA}^{-1}$). These are $Q_{(0,2)} = 0.497 \text{ \AA}^{-1}$ and $Q_{(1,1)} = 0.786 \text{ \AA}^{-1}$. This unit cell does not predict that additional reflections should be observed in the investigated Q range either.

Although unit cell #22 can reproduce all the observed reflections, no symmetry rules are found by indexing them. The shortcoming of this solution is that many additional reflections are predicted to exist in the Q range studied. This means that the configuration of the molecules within the unit cell needs to be adjusted so that all these unobserved reflections will be extinguished in order to account for the observed diffraction pattern. While technically possible, this solution seems less likely. On this basis, this unit cell was eliminated as a solution for the methyl iodide structure on MgO.

Since the unit cell #1 and #10 are closely related to one another, it is customary to choose the unit cell with the higher symmetry. This is the centered rectangular unit cell #10, with $|\vec{A}| = 8.423 \text{ \AA}$ (width) and $|\vec{B}| = 25.268 \text{ \AA}$ (depth).

c) Search for the molecule configuration

Analysis of the thermodynamic investigations of CH_3I on MgO (see Chapter 4.1.3) indicated that the molecular adsorption area at 200K to be $\sigma = 25.2 \text{ \AA}^2$. Even though the thermodynamic measurements were performed at much higher temperatures, they can be used as a guide for determining the number of molecules within the unit cell. The molecular areas of methyl iodide on graphite and boron nitride are useful points to keep in mind. These were determined to be:

$$\sigma_{\text{CH}_3\text{I}/\text{graphite}} = 22.25 \text{ \AA}^2 \text{ [Buc89]} \text{ and } \sigma_{\text{CH}_3\text{I}/\text{BN}} = 23.25 \text{ \AA}^2.$$

It is also important to consider that the molecular areas of the up-down structures of the methyl halides on graphite or BN are about 15 \AA^2 [e.g. $\text{CH}_3\text{Cl}/\text{graphite}$, $\text{CH}_3\text{Cl}/\text{BN}$ and $\text{CH}_3\text{Br}/\text{BN}$]. Combining this information one can conclude that the unit cell most likely contains 8, 10 or 12 molecules. These choices can be used to estimate the molecular areas of: $\sigma_8 = 26.60 \text{ \AA}^2$, $\sigma_{10} = 21.28 \text{ \AA}^2$ and $\sigma_{12} = 17.73 \text{ \AA}^2$ respectively.

The centered character of the unit cell requires that the cell contain an even number of molecules. Additional support for this assumption is given by the fact that the dipolar interaction between methyl iodide molecules reduces the likelihood of an odd number of molecules in the cell. All known structures of methyl halides on graphite [Kno92] and BN (Chapter 5.1 and 5.2) contain an even number of molecules in the unit cell as well.

Whereas the estimated molecular areas for a unit cell containing 8 or 10 molecules are large enough to account for a molecular arrangement where the dipole moments are parallel to the surface, a unit cell containing twelve molecules would probably have some of the dipole moments perpendicular to the surface.

Once the number of molecules in the cell is restricted the next step in the data analysis is to locate the positions of the molecules within the unit cell. The programs described earlier (5.2) were modified to perform this task by including the centered character of the unit cell. Once again, the data analysis proceeded by allowing the molecules to move on grid in the unit cell and a structure factor calculation is performed for each configuration.

Again some assumptions are needed to reduce the number of possible solutions. First, one molecule is fixed at the origin of the unit cell and another molecule in the center. By using the van der Waals radius and bulk solid CH_3I as a guide a minimum distance between iodine atoms is established. Again, the structures of CH_3I on graphite and BN are used as a guide. The minimum iodine-iodine distance is around 3.83 \AA on graphite (a value close to the bulk value of 3.8 \AA) and 4.04 \AA on BN. It seems reasonable to eliminate solutions that predict an iodine-iodine distance smaller than a minimum distance of $d_{\text{min}} = 3.5 \text{ \AA}$. Imposing a maximum distance restriction between molecules is more complicated because the electrostatic nature of the intermolecular interaction tends to favor the formation of herringbone like structures (i.e. zig-zag rows). This arrangement results in larger distances between iodine atoms in adjacent rows. This is combined by the difficulty in determining the arrangement of the molecules in the cell. Contrary to the long and narrow unit cells on graphite or BN, the width of the unit cell of 8.423 \AA is large enough to position two molecules along \vec{A} at almost the same depth (fraction of \vec{B}). Keeping in mind that the scattered intensity related to the disorder in the system is centered at around $Q \approx 1.5 \text{ \AA}^{-1}$ and assuming a close packed phase forms, an average molecule distance of 4.9 \AA can be estimated. With all these considerations in mind, we introduced a maximum iodine-iodine nearest neighbor distance of 6.3 \AA . Thus, each iodine atom was restricted to be within a 3.5 \AA to 6.3 \AA range of another iodine atom.

Finally, only iodine atoms were taken into account when performing the structure factor calculation since the contributions of these atoms clearly dominate the signal due to the large x-ray scattering cross sections (large number of electrons).

Even with all these restrictions, no molecule configuration could be found that was able to reproduce all determined intensities of the recorded x-ray reflections. Probably the main reason why this 'brute' force method failed can be attributed to the relatively high number of free parameters, which did not allow moving the molecules on a fine enough grid. The intensity distribution is sensitive to molecule movements of the order of 0.2 Å within the unit cell. The resulting number of permutations did not allow solving this problem in reasonable amounts of computation time.

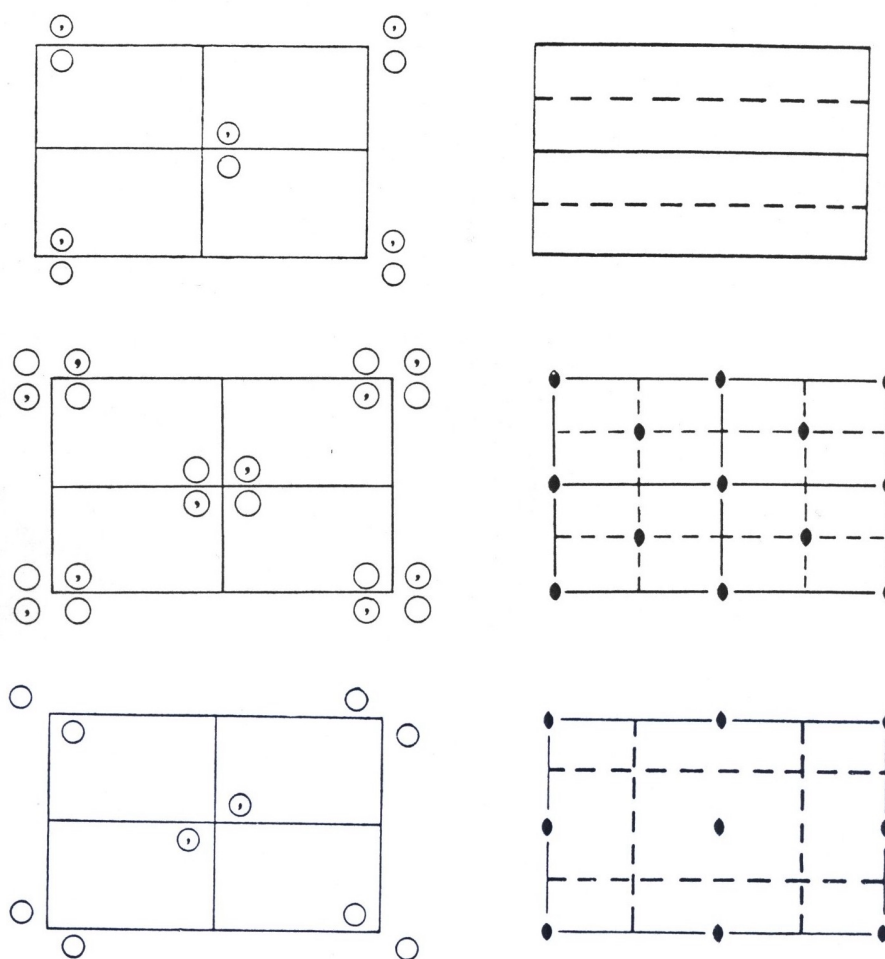


Figure 5.21: Space groups of **cm** (top), **c2mm** (middle) and **p2gg** (bottom) symmetry [Int83]. The right side of the images indicates the symmetry elements, mirror planes (—), glide planes (---) and rotations points (●), from the cells on the left side.

A better way to solve this problem is to use space groups. In two dimensions, 17 plane groups exist and seven of these groups are rectangular. The number of 'independent' molecules within the unit cell can be reduced because symmetry conditions restrict the positional

placement of molecules. Hence symmetry conditions force the placement of ‘*dependent*’ molecules at specific positions relative to ‘*independent*’ molecules. The ‘*International tables of crystallography*’ [Int83] are a good reference for locating the details of those restrictions.

Because indexing the diffraction peaks for the proposed unit cell detected only reflections with an even sum of the Miller indices h, k , only three of the seven rectangular plane groups seem reasonable to describe the 2D solid phase of CH_3I on MgO . These are the two centered plane groups **cm** (#5) and **c2mm** (#9) and the space group with **p2gg** (#8) symmetry (Figure 5.21). The latter possibility was included, because it predicts only 5 additional reflections (with $h+k=\text{odd}$ and $h, k \neq 0$) in the investigated Q interval.

Each of these space groups provides multiple ways to place 8-12 molecules into the unit cell (Table 5.13). Some of the possibilities can be excluded quickly because either the size of the unit cell or the van der Waals radius of the methyl iodide molecule make such molecule configurations sterically impossible. A separate computer program was written for each of the remaining possibilities.

	8 molecules		10 molecules		12 molecules	
cm symmetry	2b	4	2b, a	5	3b	6
	b, 2a	4	b, 3a	5	2b, 2a	6
					b, 4a	6
p2gg symmetry	2c	4	2c, b	4	3c	6
	c, b, a	2	2c, a	4	2c, b, a	4
c2mm symmetry	f	2	f, b	2	f, e	3
	2e	2	f, a	2	f, d	3
	e, d	2	2e, b	2	f, c	2
	e, c	1	2e, a	2	f, b, a	2
	e, b, a	1	e, c, b	1	2e, d	3
	d, c		e, c, a	1	2e, c	2
					2e, b, a	2
					e, d, c	2

Table 5.13: Possibilities to place 8-12 molecules into a rectangular 2D unit cell of one of the plane group **cm**, **p2gg** and **c2mm**. The Wyckoff notation is used to describe the molecules within the unit cell [Int83]. For example, the possibility ‘2e, d’ in **c2mm** symmetry has three ‘*independent*’ molecules, two of type e and one of type d. Each of these molecules generates three additional ‘*dependent*’ molecules, so that a total of 12 molecules is described. Finally, the number of free parameters is given.

By performing structure factor calculations using only the iodine atoms it became evident, that it is not possible to arrange 8 or 10 molecules within this unit cells in the symmetries mentioned above to reproduce the observed diffraction pattern. Some solutions were found if the unit cell contained 12 molecules. Good agreement with the experimental data was obtained for one of the possibilities in the high symmetry space group, $c2mm$, which is now described. The configuration of molecules within the unit cell was given by the combination of ‘2e, d’ (Figure 5.22a,b).

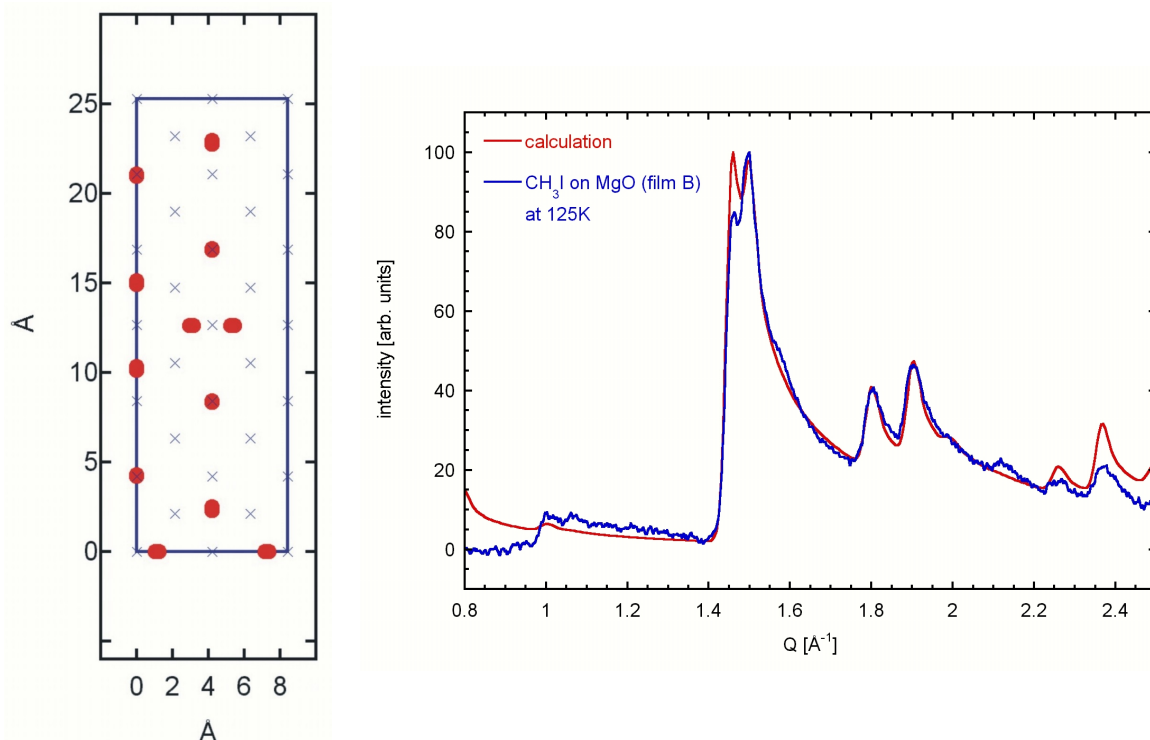


Figure 5.22a,b: Possible configuration of 12 iodine atoms (red markers) within the unit cell (blue rectangle) in $c2mm$ symmetry [left]. The blue crosses are guidance to visualize the underlying substrate. The plot on the right hand side shows a calculation (red line) of a diffraction pattern from this configuration of molecules. The experimental data of CH_3I on MgO (film B) at 125K is shown in the blue curve.

This combination has three ‘independent’ molecules, which in fractional coordinates of the unit cell are located at (Table 5.14):

#	Fractional coordinates	
1	(0.000, 0.175)	e
2	(0.000, 0.425)	e
3	(0.175, 0.000)	d

Table 5.14: Fractional coordinates of the three independent molecules.

For the two ‘*independent*’ molecules of type ‘e’ the following rule is used to locate the three dependent atoms:

$$(0, y) \qquad (0, -y) \qquad \left(\frac{1}{2}, y + \frac{1}{2}\right) \qquad \left(\frac{1}{2}, \frac{1}{2} - y\right)$$

For the third ‘*independent*’ molecule (type ‘d’) four molecules are located at:

$$(x, 0) \qquad (-x, 0) \qquad \left(x + \frac{1}{2}, \frac{1}{2}\right) \qquad \left(\frac{1}{2} - x, \frac{1}{2}\right)$$

A few comments are appropriate in discussing the results presented here. The average grid size used in these calculations was $0.15 \text{ \AA} \times 0.15 \text{ \AA}$. It should also be noted that only the iodine atoms were included in the search for possible molecule configurations within the unit cell (Figure 5.22a) and in the calculation of the resulting Warren lineshape (Figure 5.22b). The main features of the experimental diffraction pattern are well reproduced by the calculated pattern. While the differences at high wavevectors can probably be explained by an imperfect background subtraction in the vicinity of the (111) MgO reflection, the effects of the beam stop might influence the x-ray diffraction pattern at low wavevectors. In addition, the rise in intensity in the calculated pattern appearing at low wavevectors has its origin in the (0,2) reflection, which is located at $Q_{(0,2)} = 0.497 \text{ \AA}^{-1}$. This Q regime was not accessible in the measurements.

While using the iodine atoms only is already a good approximation the effect of the methyl groups on the intensity distribution should not be neglected. Including this contribution should be an effect of the order of 10% and might well produce an even better agreement between experiment and calculation. In addition, the relatively close distance of approach ($d = 2.95 \text{ \AA}$) between nearest neighbors of type ‘d’ (which is of some concern) might increase. However, including these effects results in a huge increase in computation time.

The search for a unit cell and a configuration of molecules that is able to explain the observed diffraction pattern for the solid phase of CH_3I on MgO, can be summarized in the following way:

- a) The position of the diffraction peaks can be reproduced using a large rectangular unit cell. The cell is centered and commensurate ($2 \cdot \sqrt{2} \times 6 \cdot \sqrt{2}$) with the underlying substrate.
- b) The unit cell most likely contains 12 molecules. The molecular area of $\sigma_{12} = 17.73 \text{ \AA}^2$, which is identical to the molecular area of CH_4 on MgO, indicates that in order to fulfill sterically restrictions at least some of the molecules are arranged in an up-down configuration.

d) Melting of the solid phase

It was noted earlier that the difference pattern of CH_3I on MgO near 146K consisted of two phases (Figure 5.15 and Figure 5.18). One phase is presumably a 2D solid phase and the

other a disordered (liquid like) phase. It was also indicated that at temperatures above 146 K a difference pattern characteristic of a disordered phase is recorded for film B. It is probable that a melting of the solid phase takes place near this temperature. This melting transition was investigated in more detail. For this purpose, the solid and the disordered phase for the other films are separated, too.

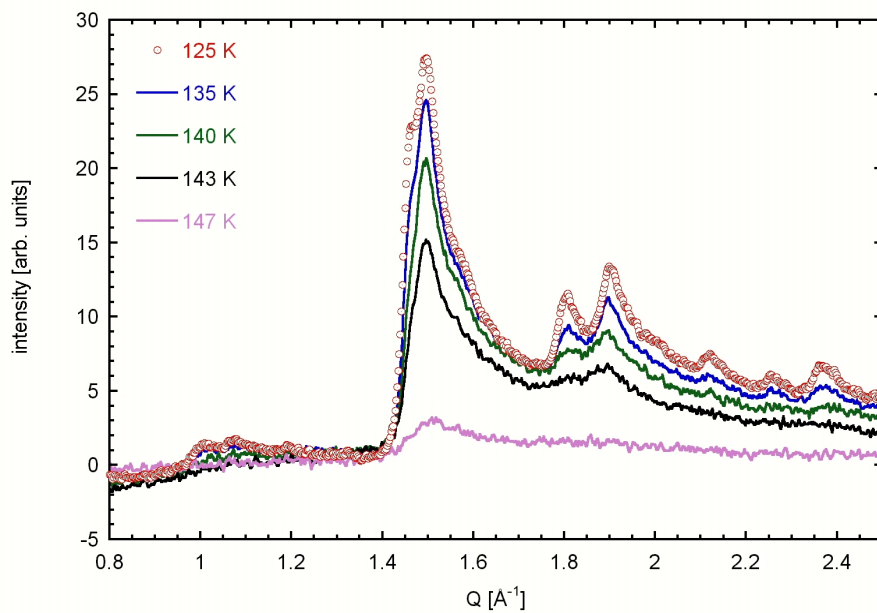


Figure 5.23: Temperature dependence of the 2D solid phase of film A of CH₃I on MgO.

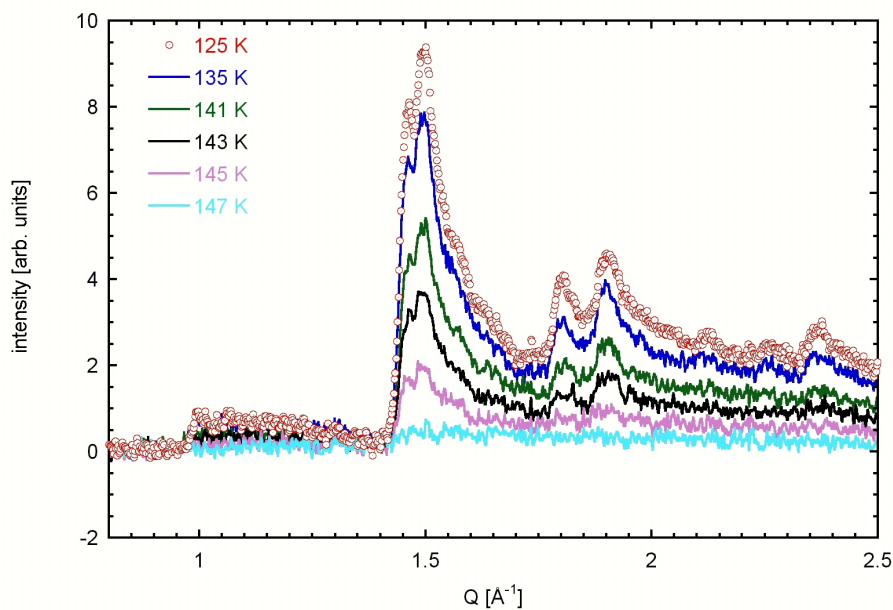


Figure 5.24: Temperature dependence of the 2D solid phase of film C of CH₃I on MgO.

At high temperature (150 K), only a broad disordered feature existed. This trace was scaled and then subtracted from the lower temperature scans to obtain the solid phase (Equation 5.1). The temperature dependence of the solid phase of the films A, C and D are displayed in the Figures 5.23-5.25 respectively. These are similar to Figure 5.18, where the temperature dependent behavior of the solid phase of film B was displayed. No evidence of a solid phase was found in film E. Only a broad disordered phase was detected between 25 K and 175 K.

A few general comments about these figures are appropriate. First, the intensity of the solid phase is coverage dependent. However, only a portion of the total intensity belongs to the solid phase. The intensities that can be associated with the solid phases of film A and B are almost identical. Second, all difference patterns exhibit the same features for the 2D solid phase. All the reflections found for film B can be detected in any other of the x-ray diffraction difference patterns. This is a strong indication that only one solid phase forms. Third, the intensity of the solid phase disappears for all coverages in the temperature interval 145–150 K.

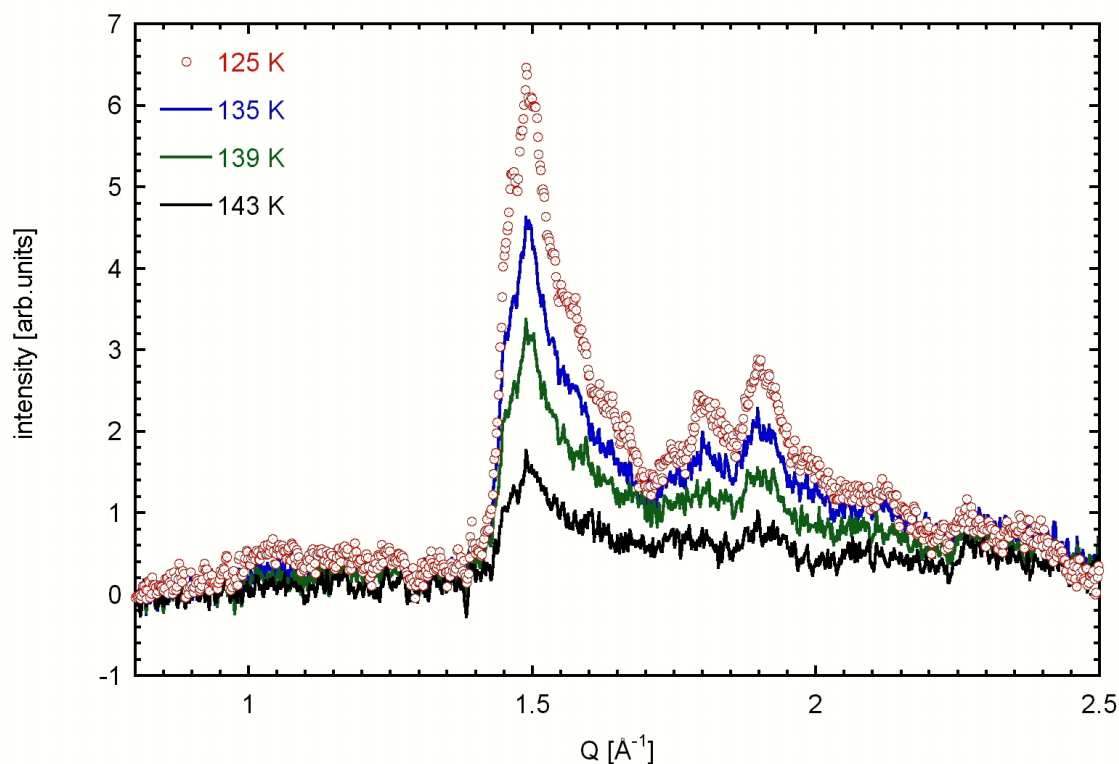


Figure 5.25: Temperature dependence of the 2D solid phase of film D of CH₃I on MgO.

Finally, the melting (disordering) of the CH₃I solid phase was explored. The fraction of the intensity of the solid phase was normalized to monolayer coverage ($\Omega \cdot [1 - a]$, see Equation 5.1) and plotted versus temperature for all films studied. This plot is shown in figure 5.26. It is remarkable that the temperature dependence of all the films is similar. The fraction of the

solid phase monotonically decreases with increasing temperature and disappears for all coverages at the melting temperature of CH_3I on MgO determined to $T_{\text{melt}}=147.0\pm 1.0$ K. It is interesting to note that the curves for film A and B are almost identical. This indicates that the adsorbed film is likely to be liquid like at coverages above a monolayer.

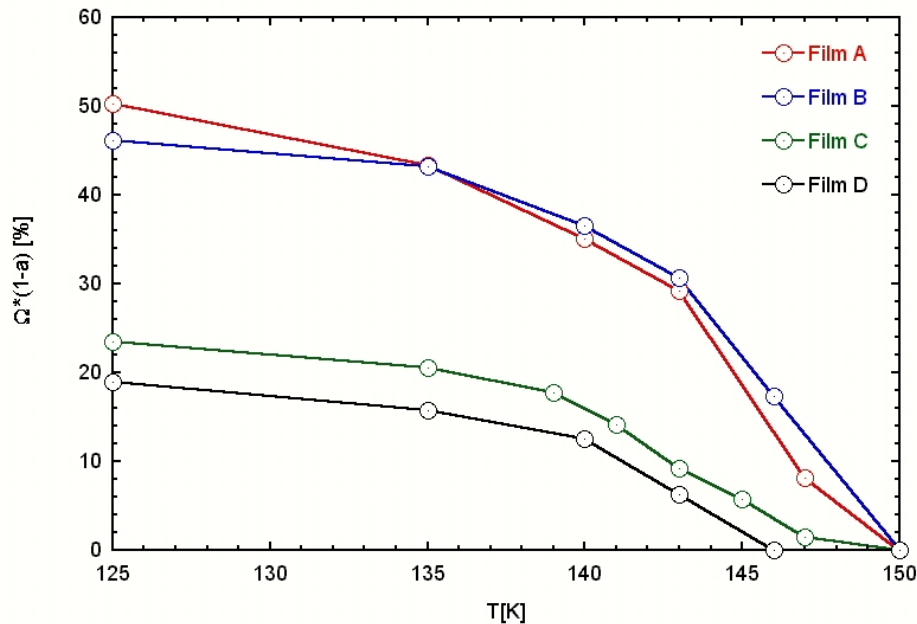


Figure 5.26: Melting curves of CH_3I on MgO . The temperature dependence of the coverage corrected intensity of the solid phase of methyl iodide on MgO is plotted versus T [K].

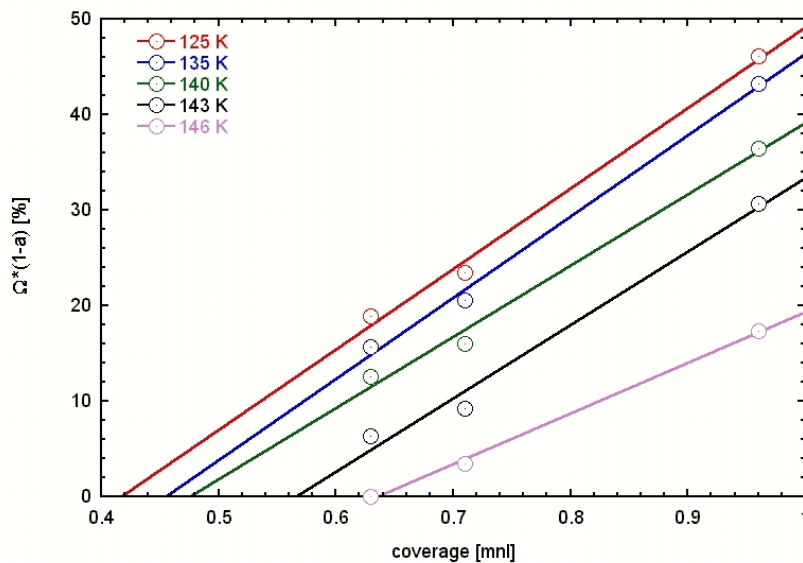


Figure 5.27: The product of the film coverage and the fraction of the solid phase intensity is plotted against coverage for different temperatures to determine the minimum coverage needed to form the solid phase as intersection of linear fits with the x-axis.

In order to establish where the onset of the ordered 2D solid phase takes place the following aid was used. Figure 5.27 displays the coverage times the fraction of the solid intensity

($\Omega \cdot [1 - a]$) as a function of coverage for different temperatures of film B, C and D. The intersection with the x-axis of a linear fit through this data indicates the minimum coverage needed to form the solid phase as a function of temperature. Clearly visible is the increase of this coverage in temperature as expected from the difference pattern of the solid phase.

d) Phase diagram of methyl iodide on MgO

The information presented above is sufficient to propose a phase diagram of methyl iodide on MgO for coverages up to 1.2 mnl (Figure 5.28). First, only a disordered phase ($\text{fluid}_{1\text{st}}$) is observed at low coverages (below ~ 0.4 mnl). Second, a two-phase coexistence of the disordered phase and a 2D solid phase ($\text{solid}_{1\text{st}}$) is observed in the approximate coverage region of $0.4 \text{ mnl} \leq \Omega \leq 1.0 \text{ mnl}$ and temperature region of $125 \text{ K} \leq T \leq 148 \text{ K}$. CH_3I seems to form an adsorbed solid phase until monolayer completion is reached.

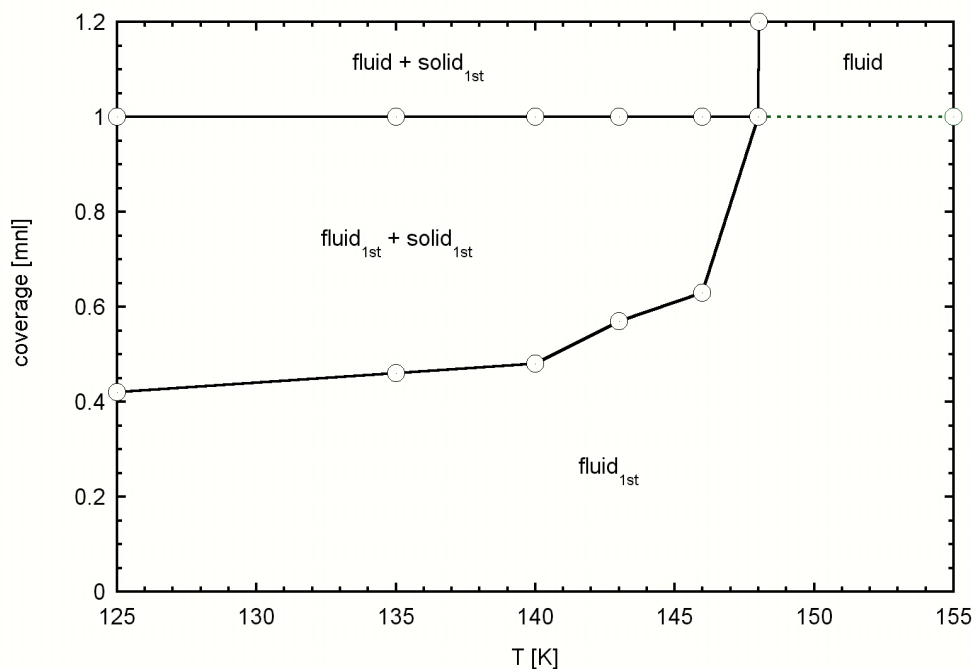


Figure 5.28: Phase diagram of CH_3I on MgO. The coverage in monolayer is plotted against the temperature in K.

Third, additional particles (i.e. for coverages above monolayer completion) are adsorbed into a disordered phase (fluid) at temperatures below 148 K. This region is probably best characterized by a coexistence of a first layer fluid ($\text{fluid}_{1\text{st}}$) and a disordered/liquid like second layer. However, using only this x-ray diffraction data it is not possible to distinguish between these two disordered phases. This part of the phase diagram is still a coexistence region of disordered and solid phases. Finally, only a broad disordered feature was detected in the x-ray diffraction data at coverages above a monolayer and temperatures above 148 K. This suggests a fluid like phase (fluid). The dotted line in the phase diagram is just to indicate

suggests a fluid like phase (fluid). The dotted line in the phase diagram is just to indicate that some molecules populate the second layer from this point on and is not meant to say anything about the order of the transition.

5.3.2 Methyl bromide and methyl chloride on MgO

This section presents investigations of the structural properties of monolayer films of CH_3Br and CH_3Cl on MgO. It will be shown that both adsorbates exhibit a similar behavior and thus can be analyzed together.

#	Ω_1	Ω_2	Ω_3	Ω_4	Ω_5	Ω_6	Ω_7	Ω_9	Ω_{11}	Ω_{13}
[mnl]	0.1	0.18	0.27	0.37	0.46	0.55	0.64	0.82	0.99	1.12

Table 5.15: Estimated coverages for the measurements of CH_3Cl on MgO displayed in Figure 5.29

Figure 5.29 displays x-ray diffraction pattern of CH_3Cl on MgO as a function of coverage. The scans were taken at different points along an isotherm at 175K and the data of the individual scans are offset by 0.1 counts per trace for illustration purposes. The final coverage, $\Omega_{\text{max}} = 1.12 \text{ mnl}$, slightly exceeded the estimated monolayer coverage. The other coverages that were investigated are summarized in Table 5.15:

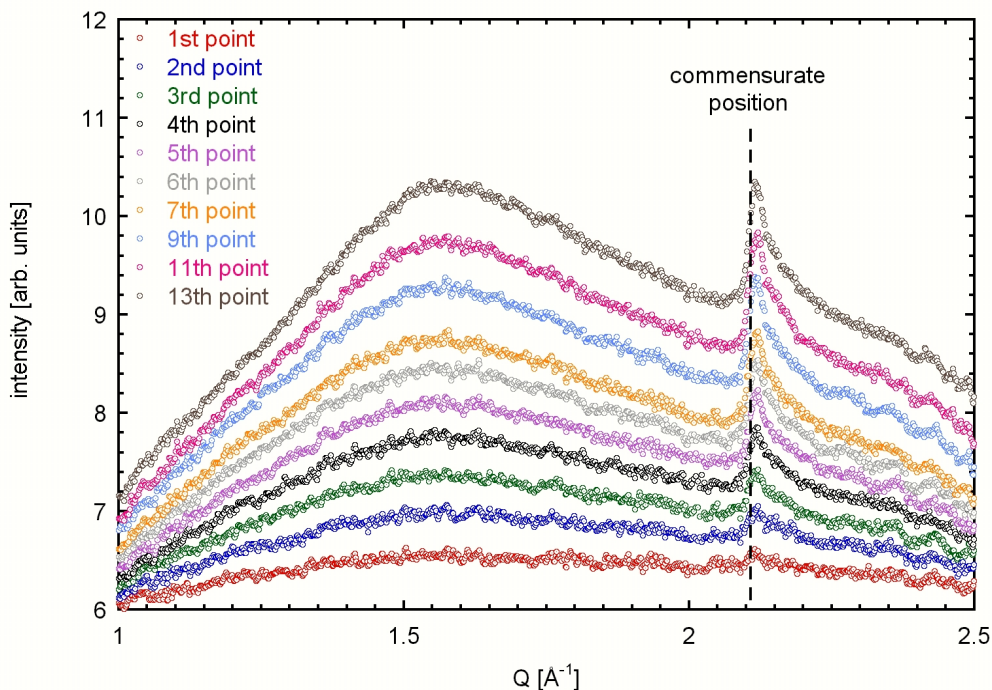


Figure 5.29: X-ray diffraction pattern of CH_3Cl on MgO as a function of coverage at 175K.

Two prevalent features characterize the difference diffraction patterns in Figure 5.29; a very broad feature centered at $Q \approx 1.55 \text{ \AA}^{-1}$ and a sharp Warren lineshape like profile at $Q_{comm} = 2.11 \text{ \AA}^{-1}$, which is a commensurate position on MgO. Both features grow in height as the coverage increases.

In the next step of these measurements, the sample was cooled and the temperature dependent behavior of the 1.12ml coverage of CH_3Cl on MgO was monitored. A series of scans at different temperatures is displayed in Figure 5.30. Again, an offset, of 0.4 counts, is applied to visually separate the data. Some comments concerning this figure are in order. First, a shift of the broad disordered feature towards higher wave vectors was observed indicating an arrangement of higher density with decreasing temperature as expected. Second, the height of the 2D reflection at $Q_{comm} = 2.11 \text{ \AA}^{-1}$, which does not show positional temperature dependence increases with decreasing temperature. Finally, new peaks appear in these patterns between 110K and 120K. In addition to the two features already described above, four other reflections are observed near $Q_1 = 1.415 \text{ \AA}^{-1}$, $Q_2 = 1.489 \text{ \AA}^{-1}$, $Q_3 = 1.606 \text{ \AA}^{-1}$ and $Q_4 = 1.706 \text{ \AA}^{-1}$.

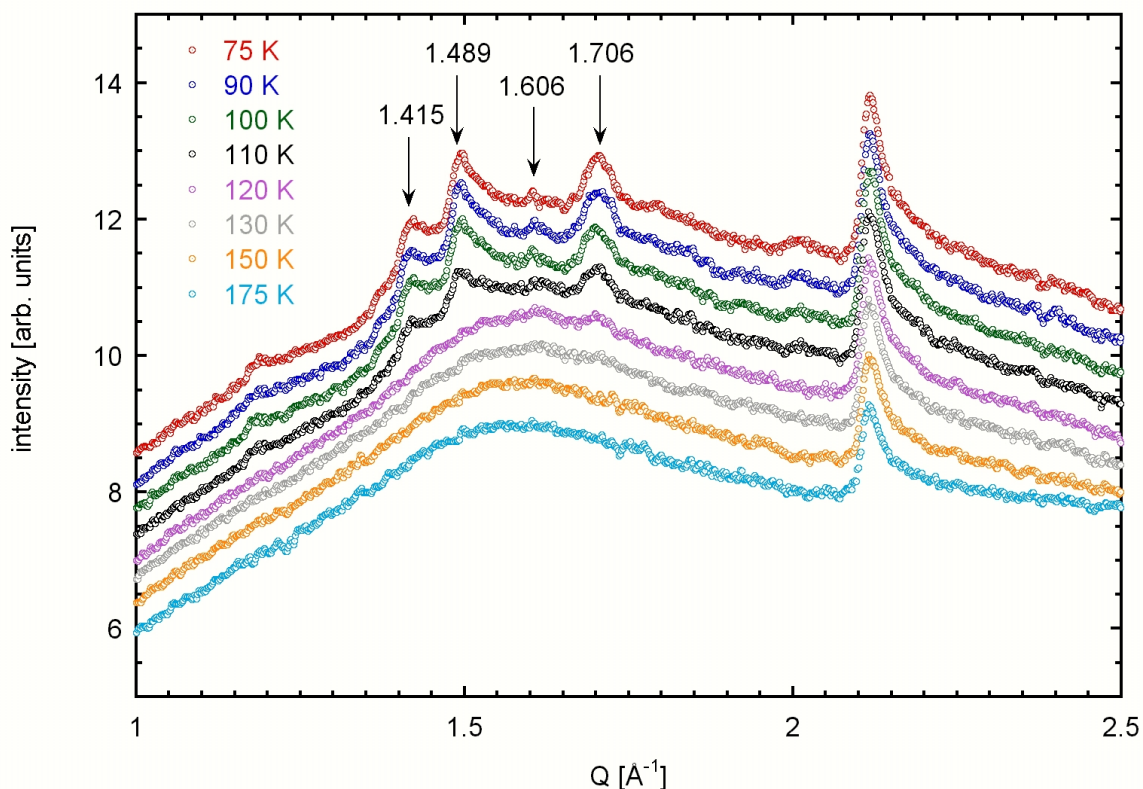


Figure 5.30: X-ray diffraction pattern showing the temperature dependence of the highest coverage of CH_3Cl on MgO between 75K and 175K.

In order to investigate the nature of these extra reflections, two more measurements were undertaken. First, the CH_3Cl coverage was reduced to $\Omega_2 = 0.90$ mnl. The second measurement was performed again with the coverage of $\Omega_{\text{max}} = 1.12$ mnl to see if the first results could be reproduced. The results of these measurements are displayed in Figure 5.31a,b.

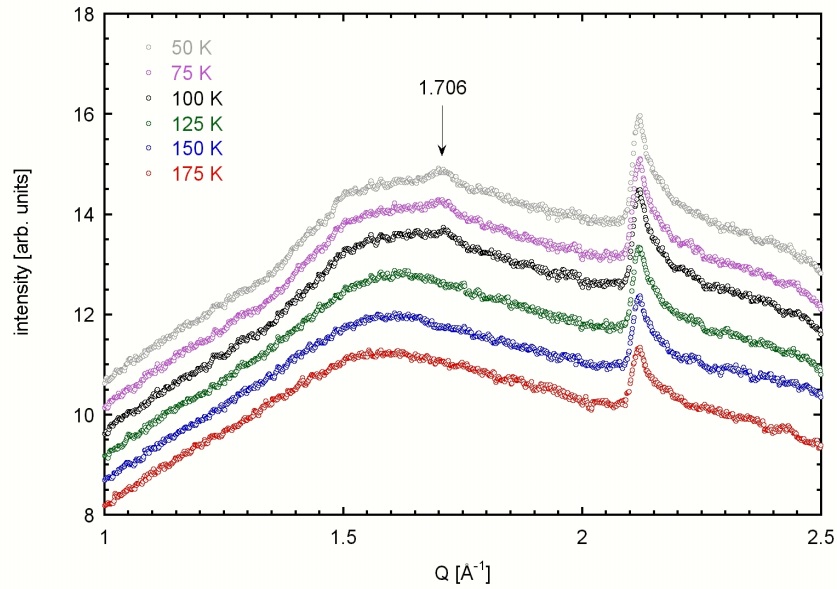


Figure 5.31a: X-ray diffraction pattern showing the temperature dependence of a CH_3Cl film on MgO with coverage $\Omega_2 = 0.90$ mnl

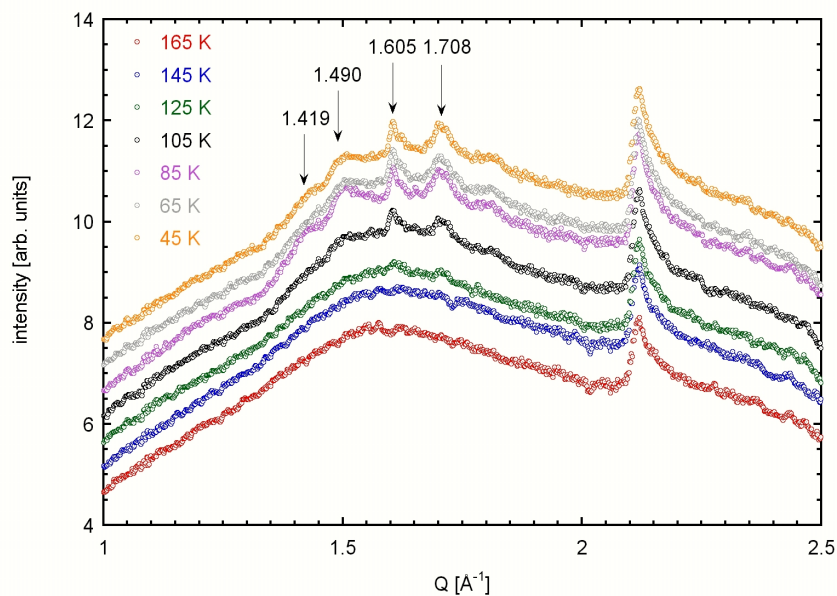


Figure 5.31b: X-ray diffraction pattern showing the temperature dependence of a CH_3Cl film on MgO with coverage $\Omega_{\text{max}} = 1.12$ mnl

Whereas the low coverage scans show only the appearance of the reflection at $Q_4 = 1.706 \text{ \AA}^{-1}$, all four reflections are observed for a second time in the high coverage measurement, but the reflection at $Q_3 = 1.606 \text{ \AA}^{-1}$ is more pronounced. Already the scan at 125K showed evidence of the two reflections at Q_3 and Q_4 , which is evidence that both these reflections belong together. It was found that these two features are probably the (100) and (002) reflection of bulk of hexagonal ice ($Q_{100} = 1.6041 \text{ \AA}^{-1}$ and $Q_{002} = 1.7055 \text{ \AA}^{-1}$) condensed on the outside of the beryllium windows due a tiny leak of the outside vacuum can. However, the nature of the two other features cannot be explained so easily since they are **neither** bulk reflections of CH_3Cl or belong to a different ice phase. Both features are more pronounced in Figure 5.30, where both seem to exhibit a triangular shape with a stronger rise at low wave vectors reminiscent of the Warren lineshape (especially the reflection at $Q_2 = 1.489 \text{ \AA}^{-1}$). This could become an important fact since this position is very close to another (highly) commensurate position at $Q_{comm} = 1.492 \text{ \AA}^{-1}$.

However, before the analysis of all the observed features is started in more detail, the x-ray diffraction pattern of measurements of adsorbed films of CH_3Br on MgO are presented. Two different coverages, $\Omega_1 = 0.89 \text{ mnl}$ and $\Omega_2 = 0.97 \text{ mnl}$, were investigated. Temperature dependent measurements of these investigations are shown in Figures 5.32 and 5.33.

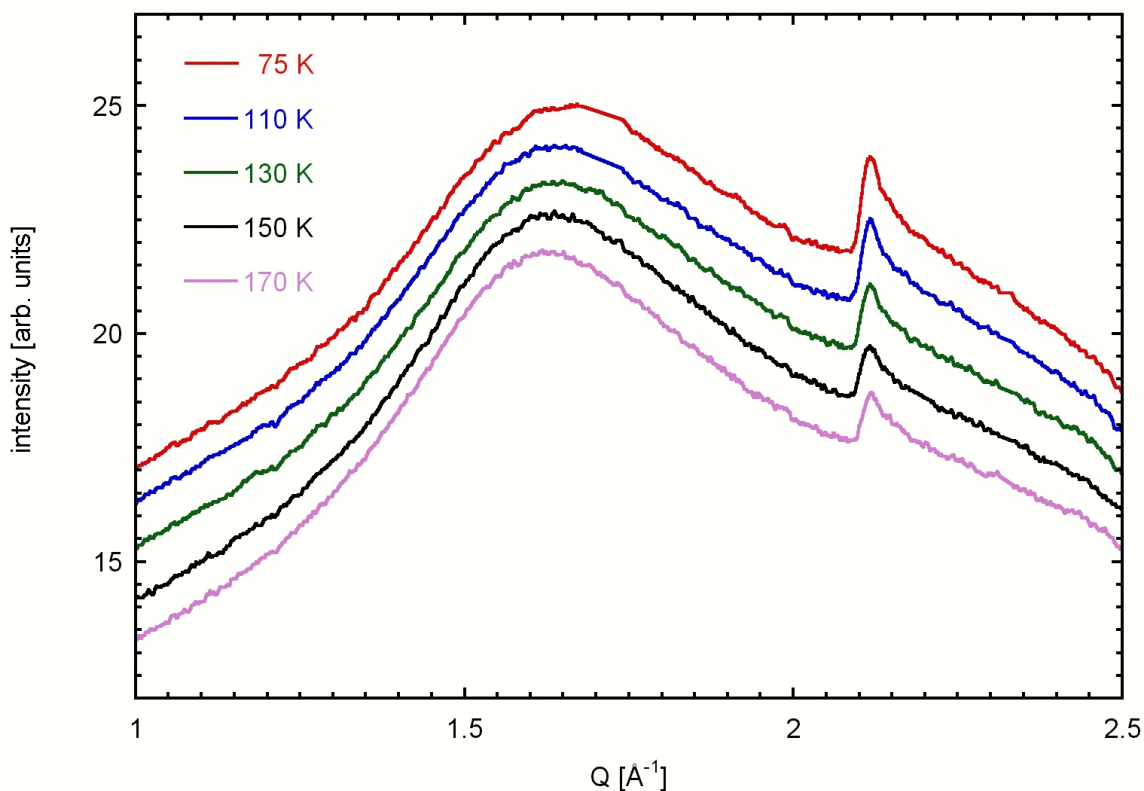


Figure 5.32: Temperature dependent difference scans of CH_3Br on MgO ($\Omega_1 = 0.89 \text{ mnl}$).

As indicated above, the x-ray diffraction patterns of CH_3Cl and CH_3Br are very similar at temperatures above 120K (see Figure 5.30). A broad feature centered at $Q \approx 1.6 \text{ \AA}^{-1}$ and a sharp Warren lineshape profile at $Q_{\text{comm}} = 2.110 \text{ \AA}^{-1}$ are apparent. Both features exhibit some temperature dependence. The broad Gaussian like feature moves towards higher wavevectors and the height of the 2D lineshape increases as the temperature decreases.

However, unlike CH_3Cl no evidence for additional reflections at lower temperature is observed for CH_3Br on MgO. Thus, the high temperature (HT) diffraction pattern of CH_3Cl on MgO and the diffracted signal of CH_3Br on MgO are investigated before it is attempted to understand the low temperature (LT) features of methyl chloride on magnesium oxide.

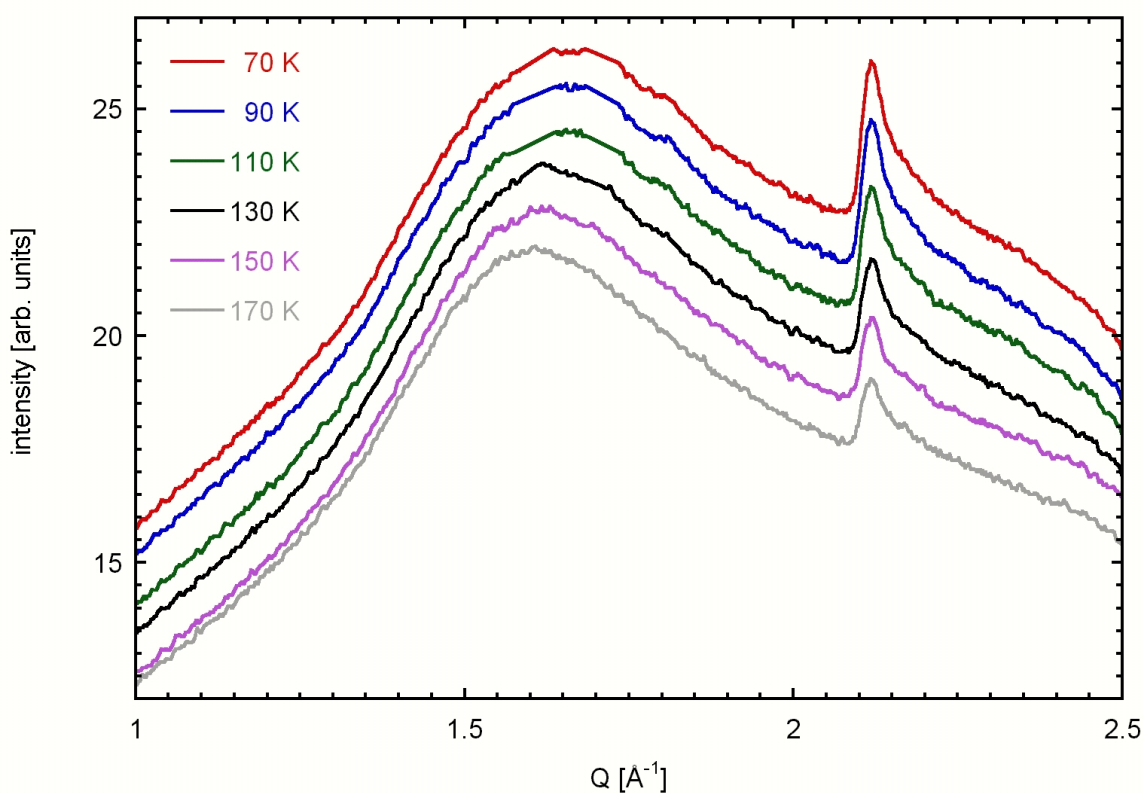


Figure 5.33: Temperature dependent difference scans of CH_3Br on MgO ($\Omega_2 = 0.97 \text{ mnl}$).

Both, the coverage dependent measurements of the isotherm run and the temperature dependent investigations indicate, that these two methyl halides can form at least one distinct layer on magnesium oxide. Both films have x-ray diffraction features of a disordered phase and a 2D solid phase at the same time.

The appearance of the broad Gaussian like diffraction feature is an indication for the fact, that a large portion ($\sim 80\% - 90\%$ of the total diffracted intensity is contained in this feature) of the molecules remains disordered on the surface and forms a disordered possibly 'liquid like' or 'amorphous solid' layer. However, the sharp Warren lineshape at

$Q_{\text{comm}} = 2.110 \text{ \AA}^{-1}$ indicates that the remaining portion of the molecules has long-range order. The coherence length of this 2D reflection is $L_G \approx 200 \text{ \AA}$, if a Gaussian only intensity distribution is used to model its shape (see chapter 2.1).

A detailed structure analysis of this long-range ordered reflection is not warranted for the following reasons. First, only one reflection is observed and second, it is unclear if both features, the broad disordered one and the sharp Warren profile, belong to the same phase or not. Nevertheless, a few comments about possible arrangements of the molecules within a presumably solid phase are appropriate. Naturally, it is possible to index the 2D reflection at $Q_{\text{comm}} = 2.110 \text{ \AA}^{-1}$ using a square plane group. There are three 2D space groups with square symmetry (**p4**, **p4mm** and **p4gm**).

It is unlikely that it is the (1,0) reflection of a square unit cell, since it would correspond to a square cell with a length of $|\vec{A}| = 2.984 \text{ \AA}$. This results in a molecular area per molecule of $\sigma = 8.90 \text{ \AA}^2$, significantly smaller than the molecular area of CH_3Cl in the HD phase on graphite of $\sigma = 13.80 \text{ \AA}^2$ [Mor91].

Similar arguments can be made for the attempt to index this peak as (1,1) or (2,0) reflection. Even though the corresponding side lengths of the squares are $|\vec{A}| = 4.22 \text{ \AA}$ and $|\vec{A}| = 5.96 \text{ \AA}$, the resulting molecular areas are not necessarily different since the cells need to contain more molecules in order to extinguish the resulting reflections at lower wave vectors.

At this point, it is clear that additional investigations of CH_3Cl and CH_3Br on MgO need to be performed before further attempts to solve the nature of this phase (presumably commensurate solid in at least one direction) are undertaken. Neutron powder diffraction and/or single crystal (e.g. LEED) measurements would be helpful since they can add another perspective to this problem. However, it should be clear that the large disordered component of molecules might introduce nearly unsolvable problems.

Some comments can be made concerning the observed LT reflections of CH_3Cl on MgO. The appearance of an additional reflection at $Q_2 = 1.489 \text{ \AA}^{-1}$ could be explained by the loss of at least one symmetry element in the 2D solid phase since it is close to the commensurate position of $Q_{\text{comm}} = 1.492 \text{ \AA}^{-1}$ and within the resolution of the measurements of $\varepsilon \leq 0.005 \cdot Q$ as determined for CH_3I on MgO. A probable explanation would be the freezing of a free rotating molecule and its corresponding arrangement to compensate the in-plane dipole moment of the layer to a vanishing value. However, it is more difficult to formulate a consistent picture if the other observed reflection at $Q_1 = 1.415 \text{ \AA}^{-1}$ is included.

Below, several points of the investigations of CH_3Cl and CH_3Br on MgO that were established with a high degree of certainty are summarized.

- CH_3Cl and CH_3Br adsorb on MgO in a similar fashion. They exhibit a powder diffraction pattern comprised of a broad disordered feature and a 2D reflection

($Q_{\text{comm}} = 2.110 \text{ \AA}^{-1}$) of long-range order, which indicates a phase commensurate with the underlying MgO substrate.

- CH_3Cl on MgO undergoes some structural phase transition between 110K and 120K. This transition is indicated by the appearance of two additional reflections at $Q_1 = 1.415 \text{ \AA}^{-1}$ and $Q_2 = 1.489 \text{ \AA}^{-1}$ (the latter is close to another commensurate position at $Q_{\text{comm}} = 1.492 \text{ \AA}^{-1}$).
- No evidence for the disappearance of the 2D reflection is observed between 75K and 175K.

Chapter 6:

Summary and interpretation

In this chapter, the results of this thesis are summarized and interpreted. The goal of this work was to gain a better picture of the interactions of polar molecules under influence of different substrate geometries. Structural properties and thermodynamic quantities of adsorbed films of three methyl halides (CH_3Cl , CH_3Br and CH_3I) on boron nitride and magnesium oxide were investigated.

In the past, the majority of studies of adsorbed films using x-ray and neutron powder diffraction and volumetric isotherm techniques were performed with graphite as substrate. However, in recent years the availability of large quantities of other powders of comparable high quality increased significantly (e.g. high quality powders of metal oxides [Kun01]). This has opened the door to make comparisons of the behavior of adsorbate particles under the influence of different substrates, which might lead to better understanding of adsorbate-adsorbate and adsorbate-substrate interactions in 2D films in general.

A great number of studies were performed on properties of adsorbed films of polar methane derivatives on graphite and a summary of the results is available [Kno92]. The use of polar molecules as adsorbate is motivated by the search for electrostatic ordering in two dimensions. The three investigated molecules offer the possibility to vary two important parameters of this property, molecular size and dipole moment, systematically.

Summary:

In order to study and understand the properties of thin adsorbed films of methyl halides on BN and MgO, the powder diffraction theory of 2D systems was extended. The Schildberg algorithm [Sch88] as latest development to describe the characteristic Q-dependent profile ('Warren lineshape') of 2D reflections was modified and improved in two aspects.

First, an improved powder averaging function $P(u, \theta_{Mos})$, which is able to describe the effects of preferred orientation for all values of θ_{Mos} was derived. Secondly, it was shown that the implementation of the \vec{Q} -dependent structure factor $S(Q, u, \omega)$ is a rather difficult task. The simple, quadratic Taylor expansion, used so far, cannot reproduce the oscillatory cosine part of the structure factor in all cases. This is especially true for larger 2D structures

of systems that exhibit shorter coherence lengths. However, formulas were derived to overcome this problem using Lagrange polynomials and a sum of integrals of smaller interval sizes.

In addition, diffraction experiments were performed on the system xenon on graphite to determine if the use of image plate detectors is possible and/or useful to study thin adsorbed films with XPD. This technique offers some great advantages over conventional experiments using sodium iodide (point) detectors or PSDs (line detectors). Comparable results were obtained using scan times reduced by a factor of 10. This is possible because the signal of the total diffracted cone is integrated. Furthermore, effects like preferred orientation or diffracted signal from impurities ('dirt' spots) are directly visible on the integrated image enabling the researcher to account for them.

The results obtained for the three studied methyl halides (CH_3Cl , CH_3Br and CH_3I) are summarized in tables 6.1-6.3. The tables are constructed in two sections. Starting, information concerning the structure of 2D solids on the three substrates graphite, boron nitride and magnesium oxide is presented and then the thermodynamics quantities are described.

a) Methyl chloride

Methyl chloride forms two solid structures on graphite, an LD and a HD phase. The HD phase of CH_3Cl on graphite forms a rectangular unit cell that is commensurate in one direction. A structure similarly to this phase is observed for CH_3Cl on BN. The cell is also 1D commensurate and thus slightly expanded along that direction. The lattice parameter along the other direction is nearly identically for CH_3Cl on graphite and BN over a large temperature interval. The cell contains two molecules in an up-down arrangement.

The LD phase of CH_3Cl on graphite illustrates another way to compensate for an in-plane dipole moment. Four molecules arrange themselves in a herringbone pattern with the C-Cl axis parallel to the surface. Even though no evidence of a LD phase of CH_3Cl on BN was found in the (not coverage dependent) diffraction experiments, the isotherm measurements indicate that a phase of lower density, similar to the LD phase of CH_3Cl on graphite, might be possible on BN, too.

A simple model cannot explain the diffraction pattern of CH_3Cl (and CH_3Br) on MgO. It appears that about 80% of the diffracted intensity arises from disordered molecules (i.e. a broad Gaussian like feature). The appearance of a sharp 2D reflection, which is at a commensurate position, indicates that the remaining molecules have long-range order and register with the substrate. An interesting aspect of future studies (preferable single crystal diffraction experiments) would be to reveal the nature of this observed diffraction pattern. The question remains if here just a single phase or a two-phase coexistence was investigated. Direct methods like atomic force microscopy (AFM) might also reveal how the diffraction pattern can be translated into a picture of CH_3Cl (or CH_3Br) molecules on the MgO surface.

Methyl chloride		
<i>Structural investigations</i>		
Graphite [Rui88], [Mor91], [Shi91], [Gri96]	LD phase (incommensurate) $ \vec{A} = 10.14 \text{ \AA}$ $ \vec{B} = 7.71 \text{ \AA}$ $\gamma = 91.2^\circ$ 4 molecules, herringbone	HD phase (1D commensurate) $ \vec{A} = 4.26 \text{ \AA} = \sqrt{3} \cdot a_{\text{graphite}}$ $ \vec{B} = 6.53 \text{ \AA} \text{ (145K)}$ $\gamma = 90.0^\circ$ 2 molecules, up-down
BN	???, isotherm measurements indicate that a phase of lower density might exist	HD phase (1D commensurate) $ \vec{A} = 4.38 \text{ \AA} \approx \sqrt{3} \cdot a_{\text{BN}}$ $ \vec{B} = 6.53 \text{ \AA} \text{ (125K)}$ $\gamma = 90.0^\circ$ 2 molecules, up-down
MgO	observation of a broad disordered feature, which contains ~80% of the intensity (molecules) and a sharp Warren lineshape like profile at a commensurate position $Q_{\text{comm}} = 2.110 \text{ \AA}^{-1}$	
<i>Thermodynamic investigations</i>		
Graphite [Bah95]	a) formation of up to two distinct adsorbed layer near the triple point b) LD-HD phase transition at around 145K c) molecular area determined to $\sigma = (20.0 \pm 1.0) \text{ \AA}^2$ for LD phase d) probable triple point wetting (not investigated in detail)	
BN	a) formation of up to two distinct adsorbed layer near the triple point b) no evidence of LD-HD phase transition above 142K c) molecular area determined to $\sigma = (20.7 \pm 1.0) \text{ \AA}^2$ (indication for LD phase) d) probable triple point wetting (though not investigated in detail)	
MgO	a) formation of up to two distinct adsorbed layer near the triple point b) estimated layering temperature for the 2 nd layer $T_{2\text{nd}} = 158.9 \text{ K}$ c) molecular area determined to $\sigma = (23.3 \pm 1.0) \text{ \AA}^2$ d) triple point wetting	

Table 6.1: Summary of structural and thermodynamic properties of CH_3Cl adsorbed on graphite, boron nitride and magnesium oxide.

Methyl chloride exhibits similar film growth processes on all three substrates. Isotherm measurements show evidence of two distinct adsorbed layers near the triple point and also indicate that triple point wetting is likely. In addition, CH_3Cl probably undergoes a LD-HD phase transition on both hexagonal substrates. Although the isotherm experiments on BN

show no evidence for this phase transition above 142K, they observed a molecular area of $\sigma = (20.7 \pm 1.0) \text{ \AA}^2$ in the monolayer regime. On the other hand the diffraction patterns can only be explained by a phase of higher density, $\sigma = 14.3 \text{ \AA}^2$. Further information needs to be gathered to settle this issue.

b) Methyl bromide

Methyl bromide	
<i>Structural investigations</i>	
Graphite [Cla91]	$ \vec{A} = 30.35 \text{ \AA}$, $ \vec{B} = 5.55 \text{ \AA}$, $\gamma = 90.0^\circ$, 8 molecules, herringbone
BN	<div style="display: flex; justify-content: space-between;"> <div style="width: 45%;"> ???, isotherm measurements indicate that a phase of lower density might exist </div> <div style="width: 50%;"> HD phase (1D commensurate) $\vec{A} = 4.38 \text{ \AA} \approx \sqrt{3} \cdot a_{\text{BN}}$ $\vec{B} = 6.76 \text{ \AA}$ (100K) $\gamma = 90.0^\circ$ 2 molecules, up-down </div> </div>
MgO	observation of a broad disordered feature, which contains ~80% of the intensity (molecules) and a sharp Warren lineshape like profile at a commensurate position $Q_{\text{comm}} = 2.110 \text{ \AA}^{-1}$
<i>Thermodynamic investigations</i>	
Graphite	Not available
BN	a) molecular area determined to $\sigma = (21.4 \pm 1.0) \text{ \AA}^2$ (indication for LD phase)
MgO	a) formation of up to two distinct adsorbed layer near the triple point b) estimated layering temperature for the 2 nd layer $T_{2\text{nd}} = (173.0 \pm 1.0) \text{ K}$ c) molecular area determined to $\sigma = (22.8 \pm 1.0) \text{ \AA}^2$ d) triple point wetting

Table 6.2: Summary of structural and thermodynamic properties of CH₃Br adsorbed on graphite, boron nitride and magnesium oxide.

While analysis of the isotherm measurements determine a molecular area of $\sigma = (21.4 \pm 1.0) \text{ \AA}^2$ for CH₃Br on BN comparable to the LD phase of CH₃Cl on graphite, analysis of the x-ray diffraction results favor a structure similar to the HD phase of CH₃Cl on graphite (i.e. a 1D commensurate rectangular unit cell containing two molecules in an up-down configuration). The cell is slightly (~4%) expanded along the direction incommensurate with the substrate as compared to the cell of CH₃Cl on BN, most likely to compensate for the larger diameter of the bromine atoms.

Combining the larger molecular area of $\sigma = (21.4 \pm 1.0) \text{ \AA}^2$ determined from the analysis of the isotherm measurements and the fact that CH_3Br on graphite forms in a herringbone structure, indicates the possibility that other solid structures form on each hexagonal substrate: CH_3Br could form in a solid phase of lower density (i.e. herringbone arrangement) on BN and a HD phase (up-down) might also be possible on graphite. The later possibility is especially interesting, because if such a HD phase does not exist, the diameter of the bromine atom may **just** be too large to allow an up-down molecule configuration on the graphite surface.

Determination of the thermodynamic quantities and properties of methyl bromide is a challenging task. With the scope of a limited number of volumetric isotherms performed on MgO, CH_3Br displays a very similar behavior to CH_3Cl on MgO. The appearance of two distinct layers on MgO and a substantial increase in film thickness near the triple point indicate that triple point wetting probably takes place. Due to the difficulties introduced by the low vapor pressure of CH_3Br , only the molecular area was determined with BN as substrate.

c) Methyl iodide

Analysis of the diffraction studies revealed that CH_3I forms a 2D solid phase on each of the three investigated substrates. Again, the structures on graphite and BN are similar. The unit cell obtained on BN is slightly expanded in both directions when compared to the graphite cell. This can be related directly to the different lattice parameter of the substrates. Four molecules form in a herringbone arrangement with the C-I axis parallel to the surface. Both cells are incommensurate with the substrate and reassemble the (010) plane of bulk methyl iodide.

CH_3I on MgO forms in a two-phase coexistence of a disordered phase and a 2D solid phase at coverages above 0.4 monolayers and at temperatures below 147K. A large centered rectangular unit cell, which is commensurate with the underlying MgO substrate and contains 12 molecules, makes up the solid phase. It undergoes a first order melting transition at $T_{\text{melt}} = (147.0 \pm 1.0) \text{ K}$. Further diffraction experiments are needed to locate the exact arrangements of the methyl groups in the unit cell. A possible method to accomplish this is an elastic neutron diffraction experiment. Here, the contributions of the CD_3 groups would be dominant.

Methyl iodide exhibits a different film growth on MgO compared to CH_3Cl and CH_3Br . Thermodynamic measurements reveal that only one distinct layer forms before bulk-like behavior becomes evident. No signs of triple point wetting are observed. The molecular areas observed on BN ($\sigma = (25.8 \pm 1.0) \text{ \AA}^2$) and MgO ($\sigma = (25.2 \pm 1.0) \text{ \AA}^2$) are similar and large enough for an in-plane arrangement of the molecules.

Methyl iodide	
<i>Structural investigations</i>	
Graphite [Buc89]	$ \vec{A} = 15.40\text{\AA}$, $ \vec{B} = 5.78\text{\AA}$, $\gamma = 90.0^\circ$, 4 molecules, herringbone, incommensurate
BN	$ \vec{A} = 15.78\text{\AA}$, $ \vec{B} = 5.90\text{\AA}$, $\gamma = 91.5^\circ$, 4 molecules, herringbone, incommensurate
MgO	two phase coexistence of a disordered phase (~50% of molecules) and a large solid phase commensurate with the MgO ($ \vec{A} = 8.42\text{\AA} = 2 \cdot \sqrt{2} \cdot a_{\text{MgO}}$, $ \vec{B} = 25.27\text{\AA} = 6 \cdot \sqrt{2} \cdot a_{\text{MgO}}$ and $\gamma = 90.0^\circ$) containing 12 molecules melting transition of the solid phase at $T_{\text{melt}} = (147.0 \pm 1.0)\text{K}$
<i>Thermodynamic investigations</i>	
Graphite	Not available
BN	a) molecular area determined to $\sigma = (25.8 \pm 1.0)\text{\AA}^2$
MgO	a) formation of only one distinct adsorbed layer (i.e. no evidence of other layering transitions) b) molecular area determined to $\sigma = (25.2 \pm 1.0)\text{\AA}^2$

Table 6.3: Summary of structural and thermodynamic properties of CH_3I adsorbed on graphite, boron nitride and magnesium oxide.

Interpretation:

The results of the x-ray diffraction experiments of CH_3Cl and CH_3Br on MgO are rather strange in nature. Reproducible measurements produce features characteristic of a disordered **and** a long-ranged ordered phase are observed simultaneously. The results are only very weakly coverage and temperature dependent making it difficult to decide if only one phase or a two-phase coexistence was observed.

A similar diffraction pattern was noted in earlier studies for CH_3Cl on graphite in a small temperature interval when the HD phase starts to melt [Gri96], [Str98]. In those studies it was found that first long-range spatial order was lost along the direction of the unit cell that is incommensurate with the graphite. Over an interval of a few degrees an intermediate phase is observed signaled by the appearance of a broad Gaussian like feature and the remaining (0,2) sharp 2D reflection of the HD phase, before this peak also broadens at higher temperatures and finally disappears. Two models were proposed to explain this phase, a coexisting hexagonal phase or a liquid-crystalline phase.

While this behavior on graphite was present only over a narrow temperature interval, it seems that it is dominant for CH_3Cl and CH_3Br on magnesium oxide. The facts that the (100) surface of MgO is ionic and has a four-fold symmetry different to the hexagonal surfaces of graphite and BN and especially the commensurate position of the observed 2D reflection reduce the probability that the model of a coexisting hexagonal phase can describe the observed phase. It is more likely that the molecules arrange on parallel rows of $a_{\text{MgO-2D}} = 2.9778\text{\AA}$ distance, where the distance between molecules on the rows is highly disordered. A similar structure was observed for the low coverage structure of tetramethyltin on graphite [Ass98]. At this time however the experimental results do not provide sufficient information to substantiate this model.

Other experiments currently performed with a variety of different molecules (e.g. H_2S , SO_2 , NO , ...) on MgO also display similar diffraction features, so that it is of great importance to understand the nature of this phase (e.g. [Fre01] and [Kim01]). There is even a possibility that the catalytic properties of MgO are responsible for a dissociation of the adsorbed molecules. However, future experiments utilizing other methods (most notable direct methods such as AFM) are needed to complete the picture of adsorbed films of methyl halides and/or other polar molecules on MgO. In addition to structural information future experiments should also address the dynamic properties of these thin adsorbed films. Here, the combination of order-disorder is an intriguing problem to investigate.

Comparisons between adsorbed films on graphite and BN have proved to be of great value, even though most of the observed properties and structures are similar. Even the small differences are helpful to gain a better picture of adsorbed films. Furthermore, circumstantial evidence was found that some new properties and structures of methyl halides on graphite that have not been investigated yet might exist.

Appendices

Appendix A: The prefactors W of the Lagrange polynom:

$$W_4 = f_1 - 4f_2 + 6f_3 - 4f_4 + f_5 \quad \text{A1}$$

$$\begin{aligned} W_3 = & -f_1 \cdot (x_2 + x_3 + x_4 + x_5) + 4f_2 \cdot (x_1 + x_3 + x_4 + x_5) \\ & - 6f_3 \cdot (x_1 + x_2 + x_4 + x_5) + 4f_4 \cdot (x_1 + x_2 + x_3 + x_5) \\ & - f_5 \cdot (x_1 + x_2 + x_3 + x_4) \end{aligned} \quad \text{A2}$$

$$\begin{aligned} W_2 = & 1 f_1 \cdot (x_2(x_3 + x_4 + x_5) + x_3(x_4 + x_5) + x_4x_5) \\ & - 4f_2 \cdot (x_1(x_3 + x_4 + x_5) + x_3(x_4 + x_5) + x_4x_5) \\ & + 6f_3 \cdot (x_1(x_2 + x_4 + x_5) + x_2(x_4 + x_5) + x_4x_5) \\ & - 4f_4 \cdot (x_1(x_2 + x_3 + x_5) + x_2(x_3 + x_5) + x_3x_5) \\ & + 1 f_5 \cdot (x_1(x_2 + x_3 + x_4) + x_2(x_3 + x_4) + x_3x_4) \end{aligned} \quad \text{A3}$$

$$\begin{aligned} W_1 = & -1 f_1 \cdot (x_2(x_3x_4 + x_3x_5 + x_4x_5) + x_3x_4x_5) \\ & + 4f_2 \cdot (x_1(x_3x_4 + x_3x_5 + x_4x_5) + x_3x_4x_5) \\ & - 6f_3 \cdot (x_1(x_2x_4 + x_2x_5 + x_4x_5) + x_2x_4x_5) \\ & + 4f_4 \cdot (x_1(x_2x_3 + x_2x_5 + x_3x_5) + x_2x_3x_5) \\ & - 1 f_5 \cdot (x_1(x_2x_3 + x_2x_4 + x_3x_4) + x_2x_3x_4) \end{aligned} \quad \text{A4}$$

$$\begin{aligned} W_0 = & 1 f_1 \cdot (x_2x_3x_4x_5) - 4f_2 \cdot (x_1x_3x_4x_5) \\ & + 6f_3 \cdot (x_1x_2x_4x_5) - 4f_4 \cdot (x_1x_2x_3x_5) + 1 f_5 \cdot (x_1x_2x_3x_4) \end{aligned} \quad \text{A5}$$

Appendix B: The 15 solutions of the 15 integrals over ω :

a) For the Gaussian intensity distribution function:

$$\int_a^b J_G(Q, u, \omega) d\omega = \frac{1}{\pi} \cdot A_G \cdot \exp\left(-A_G \cdot (u Q - Q_0)^2\right) \quad \text{B1}$$

$$\times \sqrt{\frac{\pi}{4 C_G}} \cdot \left(\operatorname{erf}\left(b\sqrt{C_G}\right) - \operatorname{erf}\left(a\sqrt{C_G}\right)\right)$$

$$\int_a^b \omega \cdot J_G(Q, u, \omega) d\omega = \frac{1}{\pi} \cdot A_G \cdot \exp\left(-A_G \cdot (u Q - Q_0)^2\right) \quad \text{B2}$$

$$\times \frac{1}{2 C_G} \cdot \left(\exp\left(-a^2 C_G\right) - \exp\left(-b^2 C_G\right)\right)$$

$$\int_a^b \omega^2 \cdot J_G(Q, u, \omega) d\omega = \frac{1}{\pi} \cdot A_G \cdot \exp\left(-A_G \cdot (u Q - Q_0)^2\right) \quad \text{B3}$$

$$\times \left(\begin{array}{l} \sqrt{\frac{\pi}{16 C_G^3}} \cdot \left(\operatorname{erf}\left(b\sqrt{C_G}\right) - \operatorname{erf}\left(a\sqrt{C_G}\right)\right) \\ + \frac{1}{2 C_G} \cdot \left(a \cdot \exp\left(-a^2 C_G\right) - b \cdot \exp\left(-b^2 C_G\right)\right) \end{array} \right)$$

$$\int_a^b \omega^3 \cdot J_G(Q, u, \omega) d\omega = \frac{1}{\pi} \cdot A_G \cdot \exp\left(-A_G \cdot (u Q - Q_0)^2\right) \quad \text{B4}$$

$$\times \frac{1}{2 C_G^2} \cdot \left(\begin{array}{l} \left(1 + a^2 C_G\right) \cdot \exp\left(-a^2 C_G\right) \\ - \left(1 + b^2 C_G\right) \cdot \exp\left(-b^2 C_G\right) \end{array} \right)$$

$$\int_a^b \omega^4 \cdot J_G(Q, u, \omega) d\omega = \frac{1}{\pi} \cdot A_G \cdot \exp\left(-A_G \cdot (u Q - Q_0)^2\right) \quad \text{B5}$$

$$\times \frac{1}{8} \cdot \left(\begin{array}{l} \frac{1}{C_G^2} \left(+2 a \cdot \left(3 + 2 a^2 C_G\right) \cdot \exp\left(-a^2 C_G\right) \right) \\ -2 b \cdot \left(3 + 2 b^2 C_G\right) \cdot \exp\left(-b^2 C_G\right) \right) \\ + \sqrt{\frac{9 \pi}{C_G^5}} \left(\operatorname{erf}\left(b\sqrt{C_G}\right) - \operatorname{erf}\left(a\sqrt{C_G}\right)\right) \end{array} \right)$$

b) For the Lorentzian intensity distribution function:

$$\int_a^b J_L(Q, u, \omega) d\omega = \frac{1}{\pi} \cdot \frac{A_L}{\ln(1 + A_L \cdot Q_{Max}^2)} \times \frac{1}{\sqrt{D_L \cdot C_L}} \left(\arctan\left(b \sqrt{\frac{C_L}{D_L}}\right) - \arctan\left(a \sqrt{\frac{C_L}{D_L}}\right) \right) \quad \text{B6}$$

$$\int_a^b \omega \cdot J_L(Q, u, \omega) d\omega = \frac{1}{\pi} \cdot \frac{A_L}{\ln(1 + A_L \cdot Q_{Max}^2)} \times \frac{1}{2 C_L} \cdot \left(\ln(D_L + b^2 C_L) - \ln(D_L + a^2 C_L) \right) \quad \text{B7}$$

$$\int_a^b \omega^2 \cdot J_L(Q, u, \omega) d\omega = \frac{1}{\pi} \cdot \frac{A_L}{\ln(1 + A_L \cdot Q_{Max}^2)} \times \left(\sqrt{\frac{D_L}{C_L^3}} \cdot \left(\arctan\left(a \sqrt{\frac{C_L}{D_L}}\right) - \arctan\left(b \sqrt{\frac{C_L}{D_L}}\right) \right) + \frac{b-a}{C_L} \right) \quad \text{B8}$$

$$\int_a^b \omega^3 \cdot J_L(Q, u, \omega) d\omega = \frac{1}{\pi} \cdot \frac{A_L}{\ln(1 + A_L \cdot Q_{Max}^2)} \times \frac{1}{2 C_L^2} \cdot \left(D_L \cdot \left(\ln(D_L + a^2 C_L) - \ln(D_L + b^2 C_L) \right) + C_L \cdot (b^2 - a^2) \right) \quad \text{B9}$$

$$\int_a^b \omega^4 \cdot J_L(Q, u, \omega) d\omega = \frac{1}{\pi} \cdot \frac{A_L}{\ln(1 + A_L \cdot Q_{Max}^2)} \times \left(\sqrt{\frac{D_L^3}{C_L^5}} \cdot \left(\arctan\left(b \sqrt{\frac{C_L}{D_L}}\right) - \arctan\left(a \sqrt{\frac{C_L}{D_L}}\right) \right) + \frac{(a-b) \cdot D_L}{C_L^2} + \frac{b^3 - a^3}{3 C_L} \right) \quad \text{B10}$$

c) For the Lorentzian Square intensity distribution function:

$$\int_a^b J_S(Q, u, \omega) d\omega = \frac{1}{\pi} \cdot A_S \cdot \left(\frac{1}{\sqrt{4 D_S^3 \cdot C_S}} \cdot \begin{pmatrix} \arctan \left(b \sqrt{\frac{C_S}{D_S}} \right) \\ -\arctan \left(a \sqrt{\frac{C_S}{D_S}} \right) \end{pmatrix} + \frac{1}{2 D_S} \cdot \left(\frac{b}{D_S + b^2 C_S} - \frac{a}{D_S + a^2 C_S} \right) \right) \quad \text{B11}$$

$$\int_a^b \omega \cdot J_S(Q, u, \omega) d\omega = \frac{1}{\pi} \cdot A_S \cdot \frac{(b^2 - a^2)}{2 (D_S + a^2 C_S) \cdot (D_S + b^2 C_S)} \quad \text{B12}$$

$$\int_a^b \omega^2 \cdot J_S(Q, u, \omega) d\omega = \frac{1}{\pi} \cdot A_S \cdot \left(\frac{1}{\sqrt{4 C_S^3 \cdot D_S}} \cdot \begin{pmatrix} \arctan \left(b \sqrt{\frac{C_S}{D_S}} \right) \\ -\arctan \left(a \sqrt{\frac{C_S}{D_S}} \right) \end{pmatrix} + \left(\frac{a}{2 C_S \cdot D_S + 2 a^2 C_S^2} - \frac{b}{2 C_S \cdot D_S + 2 b^2 C_S^2} \right) \right) \quad \text{B13}$$

$$\int_a^b \omega^3 \cdot J_S(Q, u, \omega) d\omega = \frac{1}{\pi} \cdot A_S \times \left(\frac{1}{2 C_S^2} \cdot \begin{pmatrix} \ln(D_S + b^2 C_S) \\ -\ln(D_S + a^2 C_S) \end{pmatrix} + \frac{D_S}{2 C_S^2} \cdot \begin{pmatrix} \frac{1}{D_S + b^2 C_S} \\ -\frac{1}{D_S + a^2 C_S} \end{pmatrix} \right) \quad \text{B14}$$

$$\int_a^b \omega^4 \cdot J_S(Q, u, \omega) d\omega = \frac{1}{\pi} \cdot A_S \cdot \left(\sqrt{\frac{9 D_S}{4 C_S^5}} \cdot \begin{pmatrix} \arctan \left(a \sqrt{\frac{C_S}{D_S}} \right) \\ -\arctan \left(b \sqrt{\frac{C_S}{D_S}} \right) \end{pmatrix} + \frac{1}{C_S^2} \cdot (b - a) + \frac{D_S}{2 C_S^2} \cdot \left(\frac{b}{D_S + b^2 C_S} - \frac{a}{D_S + a^2 C_S} \right) \right) \quad \text{B15}$$

References

- [Abr72] **M. Abromowitz, I. A. Stegun**
Handbook of mathematical functions
Dover Publications Inc., New York, 1972
- [Alk91] **M.T. Alkhafaji and A.D. Migone**
Vapor-Pressure study of the melting of two-dimensional Argon adsorbed on BN
Phys. Rev. B, **43**, (1991), 8741
- [Alk92] **M. T. Alkhafaji and A. D. Migone**
Multilayer adsorption isotherm study of Ar films on Boron Nitride
Phys. Rev. B, **45**, (1992), 8767
- [Alk94] **M. T. Alkhafaji, P. Shrestha and A.D. Migone**
Adsorption-isotherm Study of Monolayer Films of N₂ on BN
Phys. Rev. B, **50**, (1994), 15
- [Alm98] **A. L. Almeida, J. B. L. Martins, C. A. Taft, E. Longo, W. A. Lester Jr.**
Ab initio and semiempirical studies of the adsorption and dissociation of water on pure, defective, and doped MgO(001) surfaces
J. Chem. Phys., **109**, (1998), 3671-3685
- [Ass98] **B. Asmussen, M. Strzelczyk, W. Press, J. Z. Larese**
Low coverage structure of tetramethyltin adsorbed on graphite
Surface Science, **406**, (1998), 138-148
- [Aud92] **P. Audibert, M. Sidoumou, J. Suzanne**
CO adsorbed on MgO(100): A high-resolution LEED study
Surface Science Letters, **273**, (1992), L467-L471
- [Bah95] **A. Bah, N. Dupont-Pavlovsky**
Thermodynamic characterization of a methyl chloride film adsorbed on graphite
Surface Science, **338**, (1995), 293-299

- [BET38] **S. Brunauer, P. H. Emmet, E. Teller**
Adsorption of gases in multimolecular layers
Journal of the American chemical Society, **60**, (1938), 309
- [Bie87] **M. Bienfait, J. P. Coulomb, J. P. Palmari**
Diffusivity of a two-dimensional lattice fluid: CH₄ adsorbed on MgO(100)
Surface Science, **182**, (1987), 557-566
- [Bir86] **R. Birgeneau, P. M. Horn**
Two-dimensional rare gas solids
Science, **232**, (1986), 329
- [Boj99] **M. J. Bojan, G. Stan, S. Curtarolo, W. A. Steele, M. W. Cole**
Wetting transitions of Ne
Physical review E, **59**, (1999), 864-873
- [Bru45] **S. Brunauer**
The adsorption of gases and vapors
Clarendon Press, (1945)
- [Bru97] **L. W. Bruch, Milton W. Cole, and E. Zaremba**
Physical Adsorption: Forces and Phenomena
Int. Series of Monographs on Chemistry, Vol. 33. Clarendon: New York, 1997
- [Buc89] **R. E. Bucknall, S. M. Clarke, R. A. Shapton, R. K. Thomas**
The structure of methyl iodide monolayer adsorbed on graphite
Molecular Physics, **67**, (1989), 439-446
- [Bur53] **R. D. Burbank**
The crystal structure of methyl chloride at -125°
J. Am. Chem. Soc., **75**, (1953), 1211-1214
- [Che93] **E. Cheng, M. W. Cole, W. F. Saam, J. Treiner**
Wetting transitions of classical liquid films: A nearly universal trend
Physical review B, **48**, (1993), 18214-18221
- [Chi98] **A. Chizmeshya, M. W. Cole, E. Zaremba**
Weak binding potentials and wetting transitions
Journal of Low Temperature Physics, **110**, (1998), 677-684

- [Cla91] **S. M. Clarke, R. K. Thomas**
The structure of bromomethane monolayer adsorbed on graphite
Molecular Physics, **72**, (1991), 413-423
- [Col94] **M. W. Cole, E. Cheng, C. Carraro, W. F. Saam, M. R. Swift, J. Treiner**
Weak adsorption and prewetting transitions
Physica B, **197**, (1994), 254-259
- [Cou84] **J. P. Coulomb, T. S. Sullivan, O. E. Vilches**
Adsorption of Kr, Xe and Ar on highly uniform MgO smoke
Physical review B, **30**, (1984), 1381
- [Cou85] **J. P. Coulomb, K. Madih, B. Croset, H. J. Lauter**
Evidence of a square two-dimensional solid of methane physisorbed on the (100) surface of magnesium oxide
Physical Review Letters, **54**, (1985), 1536
- [CRC] **D. R. Lide** (editor in chief)
CRC Handbook of Chemistry and Physics
CRC Press, Inc., **73rd edition**, 1992-1993
- [Das75] **J. G. Dash**
Films on solid surfaces
Academic Press, New York, (1975)
- [Das78] **J. G. Dash, R. Ecke, J. Stoltenberg, O. E. Vilches, O. J. Whittmore Jr.**
Uniform magnesium oxide smoke
Journal of Physical Chemistry, **82**, (1978), 1450
- [Day93] **P. Day, M. LaMadrid, M. Lysek, D. Goodstein**
Multilayer krypton phase diagram
Physical Review B, **47**, (1993), 7501-7507
- [Deg88] **D. Degenhardt**
Struktur und Phasenübergänge von adsorbierten Monolagen auf MgO-Pulver
Dissertation, 1988, Universität Kiel, Germany
- [Dia99] **A. Diama and A. D. Migone**
Multilayer adsorption of Kr on BN
Phys. Rev. B, **60**, (1999)

- [Die85] **S. Dietrich, M. Schick**
Critical wetting of surfaces in systems with long-range forces
Physical review B, **31**, (1985), 4718-4720
- [Die97] **S. Dietrich, M. Schick**
Wetting at a solid-liquid-liquid-vapor tetra point
Surface Science, **382**, (1997), 178-181
- [Dim85] **P. Dimon, P. M. Horn, M. Sutton, R. J. Birgeneau, D. E. Moncton**
First order and continuous melting in a two-dimensional system: Monolayer xenon on graphite
Physical review B, **31**, (1985), 437
- [Dol86] **W. A. Dollase**
Correction of intensities for preferred orientation in powder diffractometry: Application of the March model
J. Appl. Cryst., **19**, (1986), 267-272
- [Dut81] **P. Dutta, S. K. Sinha**
Analytic form of the static structure factor for a finite two-dimensional harmonic lattice
Physical review Letters, **47**, (1981), 50
- [Ein96] **T. L. Einstein**
Interactions between adsorbate particles
in 'Handbook of Surface Science', edited by W. N. Unertl
Elsevier Science B. V., (1996), 577-650
- [Emm37] **P. H. Emmet, S. Brunauer**
J. Amer. Chem. Society, **59**, (1937), 1553
- [Fer96] **D. Ferry, A. Glebov, V. Senz, J. Suzanne, J. P. Toennies, H. Weiss**
Observation of the second ordered phase of water on the MgO(100) surface: Low energy electron diffraction and helium atom scattering studies
J. Chem. Phys., **105**, (1996), 1697-1701
- [Fer97] **D. Ferry, A. Glebov, V. Senz, J. Suzanne, J. P. Toennies, H. Weiss**
The properties of a two-dimensional water layer on MgO(001)
Surface Science, **377-379**, (1997), 634-638

- [Fer98] **D. Ferry, S. Picaud, P. N. M. Hoang, C. Girardet, L. Giordano, B. Demirdjian, J. Suzanne**
Water monolayers on MgO(100): structural investigations by LEED experiments, tensor LEED dynamical analysis, and potential calculations
Surface Science, **409**, (1998), 101-116
- [Fre00] **A. E. Freitag, J. Z. Larese**
Layer growth of methane on magnesium oxide: An adsorption isotherm study
Physical Review B, **62**, (2000), 8360
- [Fre01] **A. E. Freitag**
personal information
Materials Science group, Chemistry Dept., BNL
- [Fre46] **J. Frenkel**
Kinetic theory of liquids
Clarendon, Oxford, (1946)
- [Fuj91] **I. Fujii, Y. Morimoto, Y. Higuchi, N. Yasuoka**
Evaluation of x-ray diffraction data from protein crystals by use of an imaging plate
Acta Cryst., **47**, (1991), 137-144
- [Gay85] **J. M. Gay, J. Suzanne, R. Wang**
The melting of submonolayer ethane adsorbed on graphite
Journale de Physique Lettres, **46**, (1985), 425
- [Ger82] **S. J. Gregg, K. S. W. Sing**
Adsorption, surface area and porosity
Academic Press, London (1982)
- [Ger86] **P. N. Gerlach, B. H. Torrie, B. M. Powell**
The crystal structures and phase transitions of methyl bromide
Molecular Physics, **57**, (1986), 919-930
- [Gio98] **L. Giordano, J. Goniakowski, J. Suzanne**
Partial dissociation of water molecules in the (3×2) water monolayer deposited on the MgO(100) surface
Physical Review Letters, **81**, (1998), 1271-1273

- [Git84] **F. T. Gittes, M. Schick**
Complete and incomplete wetting by adsorbed solids
Physical Review B, **30**, (1984), 209-214
- [Gor48] **W. Gordy, J. W. Simmons, A. G. Smith**
Microwave determination of the molecular structures and nuclear couplings of the methyl halides
Physical Review, **74**, (1948), 243-249
- [Gri94] **S. Grieger**
Phasenuebergaenge von CH₃Cl physisorbiert auf Graphite
Dissertation, 1994, Universität Kiel, Germany
- [Gri96] **S. Grieger, W. Press**
Existence of a liquid-liquid phase transition in CH₃Cl adsorbed on graphite
Europhysics Letters, **33**, (1996), 193-198
- [Gro97] **B. Groh, S. Dietrich**
Orientational order in dipolar fluids consisting of nonspherical hard particles
Physical review E, **55**, (1997), 2892-2901
- [Gui94] **A. Guinier**
X-Ray Diffraction
Dover Publications, Inc., New York, 1994
- [Hal48] **G. D. Halsey Jr.**
J. Chem. Phys., **16**, (1948), 931 & J. Chem. Phys., **17**, (1949), 520
- [Hal78] **B. I. Halperin, D. R. Nelson**
Theory of two-dimensional melting
Physical Review Letters, **41**, (1978), 121
- [Hal91] **C. J. Hall, R. A. Lewis, B. Parker, J. Worgan**
2D detectors for synchrotron x-ray sources, some comparative tests
Nuclear instruments and methods in physics research, **310**, (1991), 215-219
- [Ham94] **A. P. Hammersley, S. O. Svensson, A. Thompson**
Calibration and correction of distortions in 2D detector systems
Nucl. Instr. Meth., **A346**, (1994), 312-321

- [Ham97] **A. P. Hammersley**
Fit2D: An introduction and overview
ESRF Internal Reports, (1997)
- [Har99] **J. H. Harris, D. J. Harris, S. C. Parker**
Atomistic simulation of steps on the MgO(100) surface
Surface Science Letters, **422**, (1999), L183-L187
- [Hei83] **P. A. Heiney, P. W. Stephens, R. J. Birgeneau, P. M. Horn, D. E. Moncton**
X-ray scattering study of the structure and freezing transition of monolayer xenon on graphite
Physical Review B, **28**, (1983), 6416-6433
- [Hei92] **J. Heidberg, D. Meine**
Polarized infrared spectra of CO₂ adsorbed on the MgO(100) single crystal surface
Surface Science Letters, **279**, L175-L179
- [Hei95] **J. Heidberg, B. Redlich, D. Wetter**
Adsorption of water vapor on the MgO(100) single crystal surface
Ber. Bunsenges. Phys. Chem., **99**, (1995), 1333-1337
- [Hen94] **V. E. Henrich, P. A. Cox**
The surface science of metal oxides
Cambridge University Press, (1994)
- [Hil49] **T. L. Hill**
J. Chem. Phys., **17**, (1949), 590 & J. Chem. Phys., **17**, (1949), 668
Adv. Catal., **4**, (1952), 211
- [Hol97] **S. A. Holt, C. F. Jones, G. S. Watson, A. Crossley, C. Johnston, C. J. Sofield, S. Myhra**
Surface modification of MgO substrates from aqueous exposure: An atomic force microscopy study
Thin Solid Films, **292**, (1997) 96-102
- [Hon86] **H. Hong, R. J. Birgeneau, M. Sutton**
Low-temperature structures of xenon on graphite in the one- to two-layer regime
Physical Review B, **33**, (1986), 3344-3348

- [Ina91] **A. Inaba, H. Chihara**
Phase transitions in CH₃Cl monolayers physically adsorbed on the surface of graphite
Journal of the physical society of Japan, **60**, (1991), 17-20
- [Int74] *International Tables for X-Ray Crystallography*
Volume IV, Table 2.2B, page 101
The Kynoch Press, Birmingham, England, 1974
- [Int83] **T. Hahn**
International tables for crystallography, volume A, space group symmetry
Kluwer Academic Publishers, Dordrecht, (1983)
- [Ito91] **M. Ito, Y. Amemiya**
X-ray energy dependence and uniformity of an imaging plate detector
Nuclear instruments and methods in physics research, **310**, (1991), 369-372
- [Jin89] **A. J. Jin, M. R. Bjurstrom, M. H. W. Chan**
Thermodynamic evidence of first-order melting of Xe on graphite
Physical Review Letters, **62**, (1989), 1372-1375
- [Joh97] **D. E. Johnson, J. M. Phillips, J. Z. Larese**
Search for evidence of commensurate argon on graphite films near monolayer completion
Physical Review B, **56**, (1997), 6462-6465
- [Joh99] **D. E. Johnson, J. Z. Larese**
Wetting and adsorption of ammonia on magnesium oxide
Physical review B, **59**, (1999), 8247-8251
- [Jor85] **J. L. Jordan, J. P. McTague, J. B. Hastings, L. P. Passell**
An X-ray diffraction study of krypton adsorbed on MgO(100) surfaces
Surface Science Letters, **150**, (1985), L82-L92
- [Kaw73] **T. Kawaguchi, M. Hijikigawa, Y. Hayafuji, M. Ikeda, R. Fukushima, Y. Tomite**
The crystal structures of methyl bromide and methyl iodide
Bul. Chem. Soc. Japan, **46**, (1973), 53-56

- [Kim01] **J. Y. Kim**
personal information
Materials Science group, Chemistry Dept., BNL
- [Kje76] **J. K. Kjems, L. Passell, H. Taub, J. G. Dash, A. D. Novaco**
Neutron scattering study of nitrogen adsorbed on basal-plane-oriented graphite
Phys. Rev. B **13**, (1976) 1446
- [Kno92] **K. Knorr**
Monolayers of polar methane derivatives physisorbed on graphite
Physics Reports, **214**, (1992), 113-157
- [Kno98] **K. Knorr, S. Fassbender, A. Warken, D. Arndt**
Melting of monolayers of some halomethanes and haloethanes physisorbed on graphite
Journal of Low Temperature Physics, **111**, (1998), 339-348
- [Kos73] **J. M. Kosterlitz, D. J. Thouless**
Ordering, metastability and phase transition in two-dimensional systems
Journal of Physics C, **6**, (1973), 1181
- [Kri84] **J. Krim, J. G. Dash, J. Suzanne**
Triple point wetting of light molecular gases on Au(111) surfaces
Physical Review Letters, **52**, (1984), 640-643
- [Kun01] **W. Kunmann, J. Z. Larese**
Method for the generation of variable density metal vapors which bypasses the liquidus phase

U.S. Patent No.: **US 6,179,897**, Jan. 30th, 2001
- [Lah92] **Y. Larher**
Monolayer adsorption of Ar, Kr, Xe and CH₄ on layered halides
in 'Surface properties of layered structures', edited by G. Benebek,
Kluwer Academic Publishers, (1992), 261-315
- [Lan37] **L. D. Landau**
Zur Theorie der Phasenumwandlungen I
Physikalische Zeitschrift der Sowjetunion, **11**, (1937), 26

- [Lar88] **J. Z. Larese, L. Passell, B. Ravel**
Oriental ordering of ethylene on graphite
Can. J. Chem., **66**, (1988), 633-636
- [Lar97] **J. Z. Larese, M. Y. M. Lee**
Combined neutron diffraction and adsorption isotherm study of the anomalous wetting properties of NH₃ on graphite
Physical Review Letters, **79**, (1997), 689-691
- [Lar97] **J. Z. Larese**
Structure and dynamics of physisorbed phases
Current opinion in solid state & materials science, **2**, (1997), 539-545
Surface Science
- [Lar98] **J. Z. Larese**
Neutron scattering studies of the structure and dynamics of methane adsorbed on MgO(100) surfaces
Physica B, **248**, (1998), 297-303
- [Lar99] **J. Z. Larese, M. Sprung, A. Freitag, J. Hanson**
X-ray diffraction studies of adsorbed films
NSLS Newsletter, July 1999
- [Li96] **W. Li, P. Shrestha, A.D. Migone, A. Marmier and C. Girardet**
Monolayer Kr films adsorbed on BN
Phys. Rev. B, **54**, (1996), 8833
- [Lys91] **M. Lysek, M. LaMadrid, P. Day, D. Goodstein**
Adsorption hysteresis, capillary condensation, and melting in multilayer methane films on graphite foam
Langmuir, **8**, (1992), 898-900
- [MAR] **MAR345 detector system**
<http://www.marresearch.com>
- [MAT] **Matheson**
Gas Data Book (6th edition)
<http://www.mathesongas.com>

- [May90] **V. Mayagoitia, F. Rojas**
Dual site-bond description of heterogeneous surfaces
Physical Review B, **41**, (1990), 7150-7155
- [May96a] **V. Mayagoitia, F. Rojas, I. Kornhauser, E. Ancona, G. Zgrablich, R. J. Faccio**
Two-fold description of topological disordered surfaces
Langmuir, **12**, (1996), 207-210
- [May96b] **V. Mayagoitia, F. Rojas, I. Kornhauser, E. Ancona, G. Zgrablich, R. J. Faccio, B. Gilot, C. Guiglion**
Refinements of the twofold description of porous media
Langmuir, **12**, (1996), 211-216
- [McT79] **J. P. McTague, A. D. Novaco**
Substrate-induced strain and Orientational ordering in adsorbed monolayers
Physical Review B, **19**, (1979), 5299
- [Mec96] **K. R. Mecke, J. Krim**
Adsorption isotherms and thermal fluctuations
Physical Review B, **53**, (1996), 2073-2082
- [Mel95] **J. M. Meldrim and A. D. Migone**
Vapor-pressure-isotherm Study of Monolayer CO films adsorbed on BN
Phys. Rev. B, **51**, (1995), 4435
- [Mig93] **A. D. Migone, M. T. Alkhafaji, G. Vidali and M. Karimi**
Thermodynamic study of Argon films adsorbed on Boron Nitride
Phys. Rev. B, **47**, (1993), 6685
- [Miy86] **J. Miyahara, K. Takahashi, Y. Amemiya, N. Kamiya, Y. Satow**
A new type of x-ray area detector utilizing laser stimulated luminescence
Nuclear instruments and methods in physics research, **246**, (1986), 572-578
- [MMM] **Martin Marietta Magnesia Specialities Inc.**
http://www.martinmarietta.com/corpsite/about_mmm/magnesia/mag_kids.asp
- [Mor91] **K. Morishige, Y. Tajima, S. Kittaka, S. M. Clarke, R. K. Thomas**
The structure of chloromethane monolayers adsorbed on graphite
Molecular Physics, **72**, (1991), 395-411

- [Mur96] **Z. Mursic, M. Y. M. Lee, D. E. Johnson, J. Z. Larese**
A computer-controlled apparatus for performing high-resolution adsorption isotherms
Review Sci. Instrum., **67**, (1996), 1886-1890
- [NBS] **F. D. Rossini, D. D. Wagman, W. H. Evans, S. Levine, I. Jaffe**
NBS Circ. 500 (1952)
- [Nel79] **D. R. Nelson, B. I. Halperin**
Dislocation-mediated melting in two-dimensions
Physical review B, **19**, (1979), 2457
- [NIST] **NIST Chemistry WebBook**
NIST Standard Reference Database Number 69 - February 2000 Release
<http://webbook.nist.gov/chemistry/>
- [Opp92] **A. Oppermann**
Strukturuntersuchungen am Adsorbatsystem Methylchlorid auf Graphit mittels Röntgenbeugung
Dissertation, 1998, Universität Kiel, Germany
- [Pan83] **R. Pandit, M. E. Fischer**
Wetting transitions near bulk triple points
Physical Review Letters, **51**, (1983), 1772-1775
- [Pei34] **R. E. Peierls**
Bemerkungen ueber Umwandlungstemperaturen
Helvetia Physica Acta, Suppl. II, **7**, (1934), 81
- [Pei36] **R. E. Peierls**
Statistical theory of adsorption with interaction between the adsorbed atoms
Proceedings of the Cambridge philosophic society, **32**, (1936), 471
- [Phi93] **J. M. Phillips, Q. M. Zhang, J. Z. Larese**
Why do vertical steps reappear in adsorption isotherms?
Physical Review Letters, **71**, (1993), 2971-2974
- [Phi97] **J. M. Phillips, J. Z. Larese**
Microscopic structure and transitions in xenon multilayer films
Physical Review B, **56**, (1997), 15938-15946

- [Pic93] **S. Picaud, A. Lakhlifi, C. Girardet**
NH₃ physisorbed on MgO(100) substrate: Potential calculations revisited
J. Chem. Phys., **98**, (1993), 3488-3495
- [Pre86] **W. H. Press, S. A. Teukolsky, W. T. Vetterling, B. P. Flannery**
Numerical Recipes - The Art of scientific computing,
Cambridge University Press, (1986-1992), 2nd edition
- [Rui88] **J. C. Ruiz-Suarez, M. L. Klein, M. Moller, P. A. Rowntree, G. Scoles, J. Xu**
Structure of physisorbed overlayers of dipolar molecules: A combined study by atomic beam scattering and molecular dynamics
Physical Review Letters, **61**, (1988), 710-713
- [Sch88] **H. P. Schildberg**
Strukturuntersuchungen der zweidimensionalen Quantengase ³He, ⁴He und D₂ adsorbiert auf Graphit mit Neutronenstreuung
Dissertation, (1988), Universitaet Kiel
- [Sch89] **H. P. Schildberg, H. J. Lauter**
Lineshape calculations for two-dimensional powder samples
Surf. Sci. **208**, (1989) 507
- [Shi91] **A. R. B. Shirazi, K. Knorr**
CH₃Cl mono- and submonolayers physisorbed on graphite
Surface Science, **243**, (1991), 303-308
- [Shi93] **A. R. B. Shirazi, K. Knorr**
Monolayers of C₂F₆ on graphite
Molecular Physics, **78**, (1993), 73-81
- [Shr92] **N. D. Shrimpton, M. W. Cole, W. A. Steele, M. H. W. Chan**
Rare Gases on graphite
in 'Surface properties of layered structures', edited by G. Benebek,
Kluwer Academic Publishers, (1992), 219-260
- [Shr94] **P. Shrestha, M. T. Alkhafaji, M. M. Lukowitz, G. Yang and A. D. Migone**
Adsorption Studies on Boron Nitride Substrates
Langmuir, **10**, (1994), 3244-3249

- [Shr96] **P. Shrestha and A. D. Migone**
Adsorption isotherm study of multilayer N₂ films on BN
Phys. Rev. B, **54**, (1996), 17102
- [Sid92] **M. Sidoumou, T. Angot, J. Suzanne**
Ethane adsorbed on MgO(100) single crystals: A high-resolution LEED study
Surface Science, **272**, (1992), 347-351
- [Sid94] **M. Sidoumou, V. Panella, J. Suzanne**
Interaction of ammonia molecules with the MgO(100) surface: Application to the measure of the effective ionic surface charge
J. Chem. Phys., **101**, (1994), 6338-6343
- [Sin87] **S. Sinha**
Adsorbed monolayers and intercalated compounds
Methods of experimental Physics, **23**, (1987), 1-83
- [Ste84] **P. W. Stephens, P. A. Heiney, R. Birgeneau, P. M. Horn, D. E. Moncton, G. S. Brown**
High-resolution x-ray-scattering study of the commensurate-incommensurate transition of monolayer Kr on graphite
Phys. Rev. B **29**, (1984) 3512
- [Sto68] **G. H. Stout, L. H. Jensen**
Heavy atom methods & Trial and error methods
in 'X-ray structure determination: A practical guide
The MacMillan group, NY, (1998), 270-314
- [Str97] **M. Strzelczyk, N. Haack, B. Asmussen, W. Press, J. Z. Larese**
Structures and phase diagrams of tetramethyltin and tetramethyllead adsorbed on graphite
Surf. Sci. **376**, (1997) 339
- [Str98] **M. Strzelczyk**
Struktur und Dynamik von Adsorbatmoleculen auf Graphite und Magnesiumoxid
Dissertation, 1998, Universität Kiel, Germany

- [Sue95] **J. Süßenbach**
Phasendiagramme von Metall-Tetramethylverbindungen adsorbiert auf Graphite (001) im Submonolagenbereich
Dissertation, 1995, Universität Kiel, Germany
- [Suk97] **K. G. Sukhatme, J. E. Rutledge, P. Taborek**
Wetting near triple points
Physical Review Letters, **80**, (1997), 129-132
- [Suz93] **J. Suzanne, V. Panella, M. Sidoumou**
The structure of CO₂ monolayers on MgO(100) single crystal surfaces
Surface Science Letters, **293**, (1993), L912-L916
- [Suz96] **J. Suzanne, J. M. Gay**
The structure of physically adsorbed phases
in 'Handbook of Surface Science', edited by W. N. Unertl
Elsevier Science B. V., (1996), 503-576
- [Tau77] **H. Taub, K. Carneiro, J. K. Kjems, L. Passell, J. P. McTague**
Neutron scattering study of ³⁶Ar monolayer films adsorbed on graphite
Physical Review B, **16**, (1977), 4551-4568
- [Tho69] **A. Thomy, X. Duval**
Adsorption de molecules simples sur graphite
Journal de Chemie Physique, **67**, (1969), 1101
- [Tho94] **A. Thomy, X. Duval**
Stepwise isotherms and phase transitions in physisorbed films
Surface Science, **299**, (1994), 415
- [Tra92] **M. Trabelsi, J. P. Coulomb**
Thermodynamic study of ethane thin films adsorbed on MgO(100) powder
Surface Science, **272**, (1992), 353-357
- [War41] **B. E. Warren**
X-Ray Diffraction in Random Layer Lattices
The Physical Review **59**, (1941) 693
- [War69] **B. E. Warren**
X-Ray Diffraction
Dover Publications, Inc., New York, 1969, 1990

- [Wol96] **R. A. Wolfson, L. M. Arnold, P. Shrestha, and A. D. Migone**
Comparative Study of the Substrate Quality of BN Powders
Langmuir, **12**, (1996), 2868
- [You62] **D. M. Young, A. D. Crowell**
Physical adsorption of gases
Butterworths, London, (1962)
- [You79] **A. P. Young**
Melting and the vector coulomb gas in two dimensions
Physical Review B, **19**, (1979), 1855
- [Youn93] **H. S. Youn, X. F. Meng, G. B. Hess**
Multilayer adsorption of xenon, Krypton and Argon on graphite: An ellipsometry study
Physical Review B, **48**, (1993), 14556-14576

Parts of this thesis have already been published or have been submitted for publication:

- **M. Sprung, J. Z. Larese**
Adsorption isotherm studies of methyl chloride on MgO
Physical Review B, **61**, (2000), 13155-13158
- **M. Sprung, J. Z. Larese**
Melting transition of monolayer methyl iodide adsorbed on magnesium oxide
NSLS Activity Report 1998
- **M. Sprung, A. E. Freitag, J. Hanson, J. Z. Larese**
Adsorption of methyl bromide on Boron nitride
NSLS Activity Report 1999
- **J. Z. Larese, M. Sprung, A. E. Freitag, J. Hanson**
X-ray diffraction studies of adsorbed films
NSLS Newsletter, July 1999

Lebenslauf

Michael Sprung
Reußstr. 30
24340 Eckernförde

geboren am 29.07 1970 in Eckernförde
als Sohn von Elke und Wilfried Sprung

Deutsche Staatsbürgerschaft

- | | |
|-------------------|--|
| 1977-1981 | Besuch der Richard-Vosgerau-Schule in Eckernförde |
| 1981-1990 | Besuch der Jungmannschule in Eckernförde |
| 26/05/1990 | Allgemeine Hochschulreife |
| 07/1990 – 07/1991 | Grundwehrdienst |
| 11/1991 | Immatrikulation an der Christian-Albrecht-Universität zu Kiel
für den Studiengang Physik |
| 11/1993 | Vordiplom Physik |
| 11/1995 – 12/1996 | Anfertigung der Diplomarbeit bei Prof. Dr. W. Press
am Institut für Experimentalphysik, Abteilung Festkörperphysik,
zum Thema <i>Untersuchung des Benetzungsverhaltens von Alkoholfilmen auf Silizium</i> |
| 02/1997 | Diplom in Physik |
| 04/1997 – 03/1998 | Research Collaborator in der Materials Science Group von Dr.
Larese am Brookhaven National Laboratory |
| seit 04/1998 | Anfertigung der vorliegenden Dissertation unter der Anleitung von
Dr. Asmussen in der Arbeitsgruppe von Prof. Dr. W. Press, am Insti-
tut für Experimentalphysik, Abteilung Festkörperphysik, in Ver-
bindung mit der Materials Science Group von Dr. Larese am Brook-
haven National Laboratory |

Eidesstattliche Versicherung

Hiermit versichere in an Eides Statt, daß die vorliegende Dissertation – abgesehen von der Beratung durch meine wissenschaftlichen Lehrer – nach Inhalt und Form meine eigene Arbeit ist. Sie hat weder ganz noch zum Teil an einer anderen Stelle im Rahmen eines Prüfungsverfahrens vorgelegen.

Kiel, am 30. April 2001

.....
(Michael Sprung)

Danksagung/Acknowledgements

I would like to express my thanks to the people, who made it possible for me to work on my PhD thesis, while spending most of my time in the vicinity of the greatest city on earth, New York. This combination was a dream come true for me. My special thanks go to my two advisors, John Larese and Bernd Asmussen.

I would like to thank John for offering me the possibility to work in his group at Brookhaven National Laboratory, for giving me the opportunity to work in a great environment with ‘state of the art’ equipment, and for making the best of the very sad situation related to the HFBR. In addition, he acted as a mentor in many different areas. Thanks, John!

Bernd möchte ich für die Bereitschaft danken, einen ‘long distance’-Studenten zu betreuen. Sein Wissen zum Thema physisorbierter Filme und seine Diskussionsbereitschaft haben mir sehr geholfen. Desweiteren möchte ich ihm danken, daß er die Sisyphus-Arbeit, meinen Schreibstil ‘geradezubiegen’, auf sich genommen hat. Vielen Dank, Bernd!

Mein weiterer Dank gilt Herrn Prof. Dr. Press für die Aufnahme in seine Gruppe und die vielen nützlichen Ratschläge, sei es zum Thema der Arbeit oder zu den kleinen Problemen des täglichen Lebens (Krankenversicherung, ...).

I want to thank all the members of the Materials Chemistry group, Walter Kunnmann for all his (in the beginning barely understandable) fascinating stories related to chemistry, history of Long Island and/or the Lab, Dave Johnson for helping me to get started working with all of the equipment, Curt Koehler (the 3rd) for his great support, Jae Yong Kim for giving me the feeling that I might not be a hopeless case in interacting with Asian people, and especially Andrea Freitag. You’re a great person!

In addition I want to thank Jon Hanson for his support at X7B, Connie, Dick and the people of the machine shop for their help in preparing and repairing of equipment, and the front office (Jeannie, Sabrina and Lois) for helping this poor German student to survive at BNL.

Natürlich möchte ich mich auch bei den Mitgliedern der Kieler-Arbeitsgruppe bedanken. Danke, dass ihr mich voll integriert habt und mir nie das Gefühl gegeben habt, nicht dazu zugehören. Vielen Dank auch an den (B)V(F)B Fan, dessen nette kleine Fragen (wie viele Seiten?!?) für den ‘*nötigen*’ Druck gesorgt haben.

Furthermore, I would like to thank all my friends in the states and here in Germany for making this the time of my life (so far!). My special thanks goes to my three roommates, Jun,

Laurent (I still miss you) and Dieter. Without the friendship between us, life would have been much different.

Mein abschließender Dank geht an meine Familie, die mich immer tatkräftig unterstützt hat. Insbesondere, möchte ich mich für die letzten Monate bedanken, als sie (wegen mir) einige 'kleinere' Entbehrungen (z. B. kein Auto) aufnehmen mußten. Ich hoffe, es war nicht zu schlimm. Danke!

This work was supported by the U.S. Department of Energy, Materials Science Division under Contract No. DE-AC02-98CH10886.